DOE/NV/25946--2758

FY2015 Annual Report

Site-Directed Research & Development

Strategic Opportunity Research
Exploratory Research

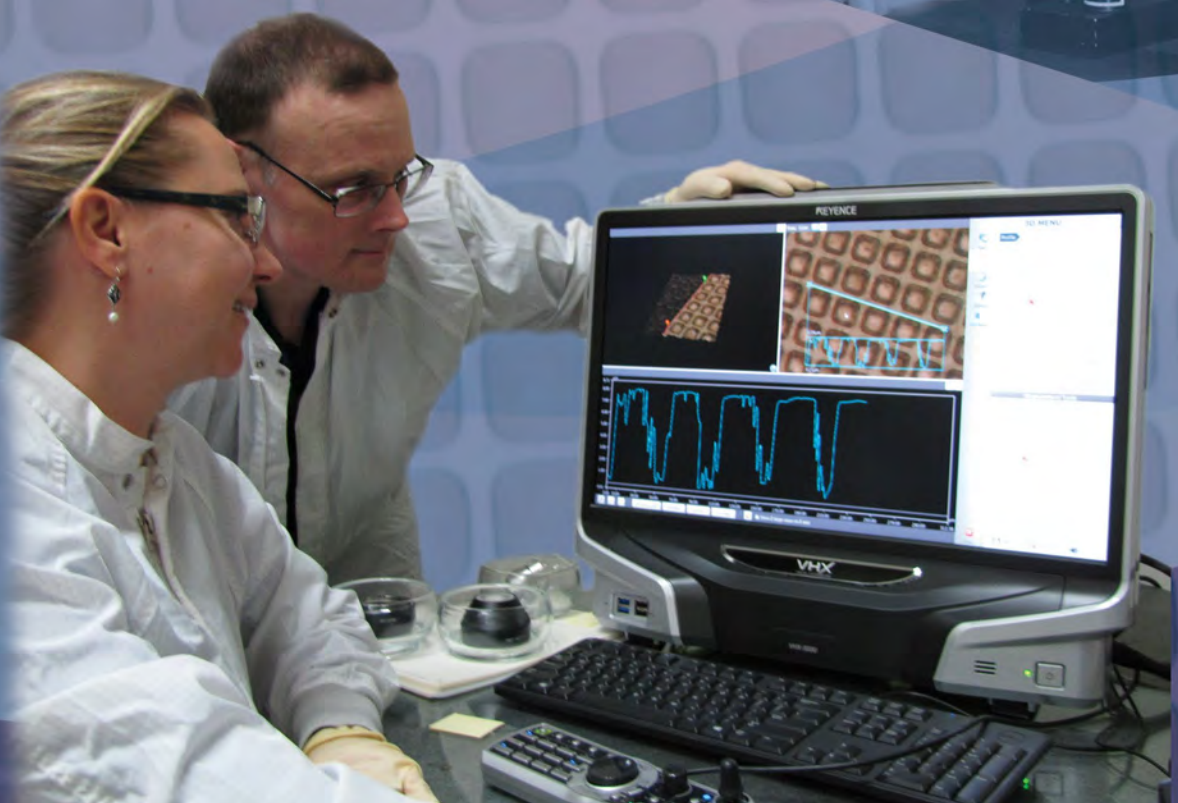

NNSA
Nevada National Security Site

Availability Statement

Available for sale to the public from:

U.S. Department of Commerce
National Technical Information Service
5301 Shawnee Road
Alexandria, VA 22312
Telephone: 800.553.6847
Fax: 703.605.6900
E-mail: orders@ntis.gov
Online ordering: http://www.ntis.gov/help/ordermethods.aspx

Available electronically at http://www.osti.gov/bridge

Available for a processing fee to the U.S. Department of Energy and its contractors in paper, from:

U.S. Department of Energy
Office of Scientific and Technical Information
P.O. Box 62
Oak Ridge, TN 37831-0062
Telephone: 865.576.6401
Fax: 865.576.5728
E-mail: reports@adonis.osti.gov
Online ordering: http://www.osti.gov/reportform.html

DOE/NV/25946--2758

Nevada National Security Site

Site-Directed Research and Development

Fiscal Year 2015 Annual Report

This work was done by National Security Technologies, LLC, under Contract No. DE-AC52-06NA25946 with the U.S. Department of Energy, and supported by the Site-Directed Research and Development Program.

Report Date: April 2016

Contents

Unpublished Summaries

Available from SDRD Program Office, Las Vegas, NV 89193-8521

Advanced Data Analysis Techniques for Nuclear Weapons Physics Modeling, R. Berglin

Concurrent Transceiver with Ultra-High-Speed Fourier Transforms for Unrealized SIGINT Applications, D. Seastrand

A perspective:
"Can-do"
woven into the fabric of the NNSS

Many of us have spent a large portion of our professional careers deep in a "can-do" environment, an idiom for getting the job done at all costs. We (falsely) believed that an emphasis on safety, security, and compliance only added layers of ineffectiveness to our ever-demanding schedule-driven programs. But within the past decade, our culture has shifted to a more fundamental approach to safety, security, and compliance. This is truly of the utmost importance, for without this we would cease to exist as an organization and be unable to execute the critical work necessary to support our mission to the nation.

The Nevada National Security Site, from its beginnings as the Nevada Test Site, has historically conducted large, complex, hazardous, nuclear tests; the can-do approach was a historical tactic that met the urgency of the times. We got it done, and our customers knew we could. In this modern era, however, high thresholds of risk acceptance that were once tolerated have to be seen through a different lens. Our workforce, engaged in increasingly high-hazard activities, is learning and adopting new ways to deliver yet not compromise safety, security, and our environment.

Today we are still an evolving organization; a new generation of leaders is building a stronger foundation to sustain the national security mission. I recently attended an NSTec future leaders briefing called "Connecting with the Workforce." Those who attended represented our entire organization from staff, to supervisors, to managers. I walked away fully convinced that the future of NSTec is bright, given the collaborative, professional, and insightful dialogue. We were given an exercise (based on one developed by Apple Inc.) to define the NSTec Golden Circle, starting with our core, the Why:

- **Why: Our Purpose**
  What is our cause? What do we believe?
  In an ever-changing world, we protect the nation from ever-changing threats.

- **How: Our Process**
  Specific actions we take to realize our "Why."
  Promote a culture of safety, security, and quality in the world's largest laboratory.

- **What: The Results**
  What do we do? The result of "Why."
  Develop, test, evaluate, and deploy technologies to defeat national and global threats.

Most organizations begin by defining the "What" aspect, whereas high-performance organizations begin from the core principle, the "Why." I see a bright and ever changing future filled with challenges and addressing emerging issues from a new perspective. We "can-do" this by coupling innovative ideas in science, technology, and engineering to core principles and modern needs in safety, security, and compliance.

Raffi Papazian
Vice President for Program Integration

This page left blank intentionally

Investing for the Future

In 2015 the Site-Directed Research and Development (SDRD) Program implemented the first-ever increase in SDRD funding based on our assessment of the benefit and impact it would have to our mission. Without a doubt it has been a measurable success, contributing the amplifying impact we see with targeted R&D investment. Our principal motivation, as described in the FY 2014 annual report, was to drive **new strategic long-term research** that is vital to the Nevada National Security Site (NNSS) and our national security missions. The two strategic research areas chosen were dynamic materials science and unmanned aerial sensor systems and platforms. This report highlights the first full year of those efforts; the reports of two Strategic Opportunity Research projects make up the first section of this annual report.

By enabling enhanced strategic research with larger investments, we have brought people and highly specialized tools together to address scientific challenges in these key areas. Heretofore our program was predominantly driven by individuals whose inherent curiosity seeded discovery and fueled exploratory concepts. However, in the past few years we have been building the foundation **to strategically assess mission needs and opportunities** that align our capabilities to the overall national security mission and then drive desired outcomes. Our legacy capabilities in remote sensing combined with new paradigms for emergency response and consequence management help drive the need to develop advanced aerial sensor platforms that do not currently exist. Likewise, dynamic materials science is a critical area of scientific research for which basic physics issues are still unresolved. New methods of characterizing materials in extreme states are vitally needed, and these efforts are paving the way with new knowledge.

Projects selected in FY 2015 for our Exploratory Research portfolio exhibit a strong balance of NNSS mission relevance. Geoscience, seismology, and techniques for detecting underground nuclear events are still essential focus areas. Many of the project reports in the second major section of this annual report, Exploratory Research, are ongoing continuations in multi-year lifecycles. Diagnostic techniques for stockpile and nuclear security science figured prominently as well, with a

"Ground Truth and Discovery III"

The third annual year-end review of SDRD projects was held in September 2015. Once again, the review showcased the various efforts and results achieved to a growing audience. Due to this expanded interest, a new format was implemented to include strategic opportunity research projects and two parallel concurrent sessions in the afternoon. We believe this venue for presenting and discussing R&D results has become indispensably important given the complexity of projects, the extended collaborations, and geographic separation between some of our sites. In addition, members of our advisory board were in attendance to review and assess projects as part of our ongoing advisory activities.

"I found the talks fascinating and was impressed by the breadth of topics covered."
—E. Rose

"I was impressed with diagnostics of implosion physics . . . also looking forward to further results on detecting nuclear detonations."
—G. Yonas

Dr. Larry Franks Recognized by IEEE for Lifetime Achievements

Dr. Larry Franks received the Lifetime Achievement Award at the November 2015 IEEE/RTSD (Room-Temperature Semiconductor Detectors) Conference at San Diego in recognition of his many contributions to the development of semiconductor radiation detectors. The international award is given annually for either a single seminal development or lifetime contributions.

Past recipients include Dr. Paul Siffert, CRNLP, Strasbourg, France; Professor Emeritus Michael Schieber, Hebrew University, Israel; Dr. Ralph James, former Associate Director, Brookhaven National Laboratory; Professor Zhong He, University of Michigan; Professor Arnold Burger, Fisk University; Professor Michael Federle, Albert-Ludwigs–Universitaet Frieburg, Germany; and Dr. Aleksey Bolotnikov, Brookhaven National Laboratory.

Dr. Larry Franks (center, with Dr. Ralph James [left] and Professor Michael Federle [right]) receives a lifetime achievement award for his extensive contributions to semiconductor radiation detectors development at the November 2015 IEEE Conference

Jeffrey Koch Named FY 2015 MVPI

Jeffrey Koch (right) of Livermore Operations (LO) receives the Most Valuable Principal Investigator (MVPI) Award from Chief Technology Officer, Christopher Deeney

Koch's work on high Miller-index crystals has opened up new areas in which hard x-ray spectroscopy can be applied to high-temperature plasma physics, and instituted a new lab, the HEX lab at Livermore Operations (LO), where calibrations are now possible at energies not achievable previously. Moreover, this accomplishment may lead to technological breakthroughs in high-energy density physics—a major mission thrust area for NSTec. He has also spurred another significant innovation, x-ray Doppler velocimetry to diagnose the plasma conditions in high-temperature fusion implosions. Beyond Jeff's technical contributions, his role with SDRD program development and management as an SDRD Site Representative for LO has had a profound influence on the quality and number of innovative proposals he helps staff generate.

SDRD to Stockpile Stewardship Success: Observation of Phase Transition Kinetics

Certification of our nation's aging stockpile requires complex weapons performance models that predict the behavior of designs and components without the benefit (and cost) of testing. At the core of these calculations are material models, or equations of state that govern how a material behaves under extreme dynamic conditions. A material can transform to other phase states (liquid or gas), and many materials have multiple distinct high-pressure solid phases. Determining the location of phase boundaries is difficult, and it has been a long-standing goal of the Nuclear Weapons Laboratories community. As a material changes phase, a change in crystal or electronic structure, thermal conductivity, dielectric constants, optical reflectance, or other quantities could be used to indicate a phase transition. Many of these characteristics are difficult to observe dynamically.

Surface reflectance is one of the more accessible properties of a metal in a shock experiment. We began looking at the relationship between reflectance and material phase in an FY 2004 SDRD project.[1] *Our initial results allowed us to transition this work to Science Campaign 2 funding, where we continued to develop our techniques with Los Alamos National Laboratory (LANL) collaborators, culminating in a summary article that illustrates the correlations between reflectance and material phase.*[2] *In a series of more recent experiments, our group developed integrating sphere reflectance techniques to determine the emissivity and temperature of shocked tin,*[3] *and the dynamic reflectance measured in those experiments showed pronounced changes while reverting phase. More importantly, these experiments showed indications that the reflectance changes lagged behind the stress changes (i.e., that kinetics slowed the phase transition). Our FY 2015 SDRD project investigated these observations in depth.*

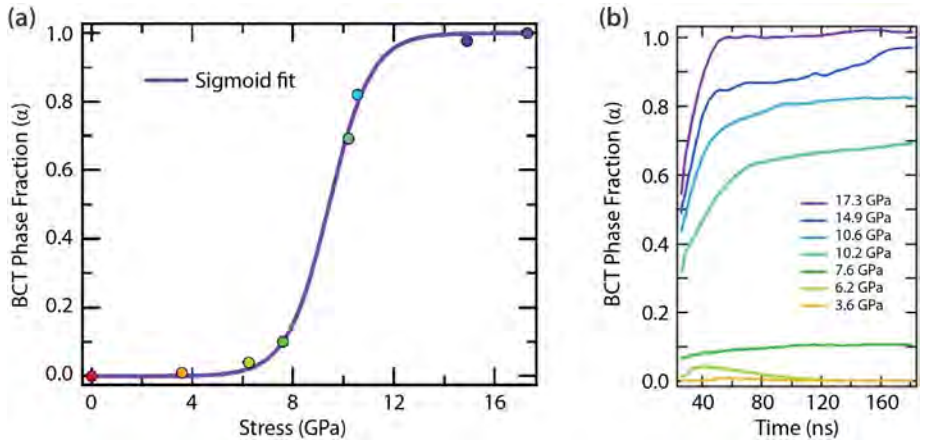

(a) Inferred phase fraction versus stress from our experiments. (b) Phase fraction versus time for seven different peak stresses.

In this project, we developed a methodology to obtain the dynamic phase-fraction of shocked materials using optical reflectance. Our method extrapolates the low-pressure and high-pressure behaviors of two isomorphic phases and finds the phase fraction that best matches the measured reflectance to six spectral channels. The figure shows the results of this analysis. In it, we see the β to BCT transition begins at 6 GPa and completes at 12 GPa, which is more gradual than indicated by velocimetry. The time required for the shocked material to reach equilibrium in a final mixed phase varies with stress—from tens to hundreds of nanoseconds. In FY 2016 we plan to apply our newly developed techniques and investigate zirconium phase transitions with LANL collaborators.

[1] Stevens, G. D., W. D. Turley , L. R. Veeser, "Optical diagnostics for phase changes," in *Nevada Test Site–Directed Research, Development, and Demonstration*, FY 2004, Bechtel Nevada, Las Vegas, Nevada, 2005, 281–286.

[2] Stevens, G. D., W. D. Turley, L. R. Veeser, B. J. Jensen, P. A. Rigg, "Reflectance changes during shock-induced phase transformations in metals," *Rev. Sci. Instrum.* **81** (2010) 065101-1–065101-12.

[3] La Lone, B. M., G. D. Stevens, W. D. Turley, D. B. Holtkamp, A. J. Iverson, R. S. Hixson, L. R. Veeser, "Release path temperatures of shock-compressed tin from dynamic reflectance and radiance measurements," *J. Appl. Phys.* **114,** 6 (2013) 063506-1–063506-14.

Contributed by G. D. Stevens

few key efforts coming to fruition, such as phase transition detection (see vignette on page vii). In other areas, modeling efforts toward better understanding plasma focus physics has also started to pay dividends to major program needs.

New Initiatives and Project Selection

This past fiscal year marked the 13th anniversary of Congressional authorization of the SDRD program and with it one of the most significant initiatives to date. For the first time in program history, we raised the investment level to create strategic opportunity research. An increase of 0.5% was applied in FY 2015 to fund these projects, above and beyond the approximate 2% utilized for the exploratory research projects that have thus far formed the core of our program. Overall, our SDRD investment rate is currently 2.5%, yielding a program size of approximately $9.2M. Commensurate with this increase were some long anticipated enhancements that could not have been accomplished without increased funding.

SDRD to Global Security Success: Compton Crosstalk Method for Directional Detection

The Compton crosstalk directional method was a 1-year SDRD project in FY 2013.[1] *The project demonstrated that the direction to a gamma source can be inferred by a covariance analysis of the data streams from a pair of ordinary radiation detectors. The covariance method extracts and estimates correlated gamma events, and the correlated data are processed to infer the direction to the gamma source, as well as to construct second-order spectra, useful for isotope identification. The asymmetry of the energy distributions of Compton-scattered gammas between the two detectors is the quantity of interest, and although the energy distributions are broad for close-packed detectors, the asymmetry of those distributions allows remarkable precision in estimating the direction back to a gamma source. The work has been published in* Review of Scientific Instruments,[2] *and the technique is currently being implemented in NSTec's Janus and EagleRay devices.*

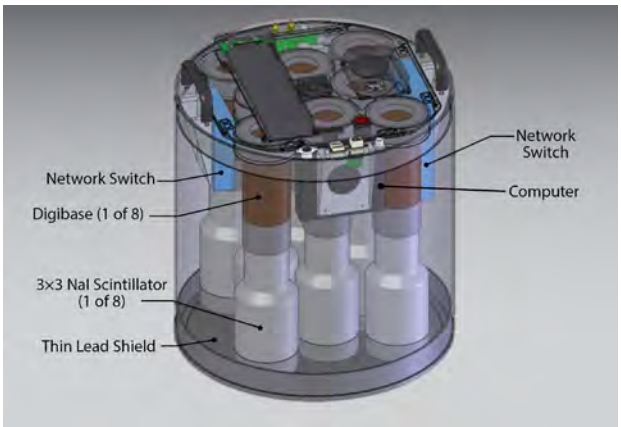

Janus is a directional gamma detector employing the occlusion method (i.e., inter-detector shadowing), and it consists of eight 3×3 thallium-doped sodium iodide detectors (see figure) capable of list-mode data streaming. The Compton crosstalk method is being implemented side-by-side with the occlusion method, and results of both are compared. The occlusion method is faster, but less precise, and depending upon particular conduct of operations, one method may be favored.

[1] Trainham, R., J. Tinsley, "Covariance processing of energy asymmetry of Compton crosstalk for directional gamma sensing," in *Site-Directed Research and Development*, FY 2013, National Security Technologies, LLC, Las Vegas, Nevada, 2014, 137–147.

[2] Trainham, R., J. Tinsley, "Directional gamma sensing from covariance processing of inter-detector Compton crosstalk energy asymmetries," *Rev. Sci. Instrum.* **85** (2014) 063504.

Contributed by R. Trainham

New Tools for Effective R&D: Integrated Feedback

In FY 2014 we implemented feedback reports to individual lead principal investigators (PIs) on all non-selected proposals. In FY 2015 we carried this concept further by integrating feedback directly into the pre-proposal phase. Peer review comments were highly effective in helping PIs refine ideas in the early pre-proposal phase and often gave new insight into how to effectively overcome technical challenges. Integrated feedback was used about 50% in our first year of its availability. This type of front-end feedback is hoped to be more effective than the traditional comments often shared "after-the-fact" in proposal evaluations.

Revised two-phase SDRD proposal process with integrated feedback

In 2015, for the FY 2016 call, we implemented a **new two-phase hybrid proposal process** consisting of a pre-proposal (idea phase) followed by an invited proposal. In the pre-proposal phase, principal investigators are encouraged to submit ideas in a standardized, succinct format that presents the proposed project's essence and impact. In addition, during the pre-proposal phase, proposers have the opportunity to obtain feedback to hone the idea. Our intent was to spark creativity and open the way for submission of many more innovative ideas—our ultimate goal was to **capture as many good ideas as possible**.

Given the rigor needed to write a typical proposal for SDRD, and to shift the bulk of the effort to the most probable project selection, we implemented an invited proposal process after pre-proposal evaluation. Based on actual FY 2016 data, we have seen enhanced program effectiveness and efficiencies gained as a result of this new implementation. Pre-proposal submissions (128) were up by 12% over FY 2015's one-phase proposal process and helped reverse a downward trend. We were particularly encouraged by the increase, as it occurred during a staff voluntary separation plan that affected our technical workforce who regularly submit SDRD proposals. We invited 62 full proposals, and by most measures quality was consistently higher across our evaluation criteria elements.

FY 2015 Annual Report Synopsis

The reports that follow are for project activities that occurred from October 2014 through September 2015. Project lifecycle is indicated under the title as well as the original proposal number (in the following format: site abbreviation--ID #--originating fiscal year, e.g., STL-##-YR). Each report details the discoveries, achievements, and challenges encountered by our principal investigators. As SDRD, by definition, invests in "high-risk" and hopefully "high-payoff" research, the element of uncertainty is inherent. While many of our efforts are "successful" and result in positive outcomes or technology utilization, some fall short of expectations, but cannot be construed as "failure" in the negative

sense. The latter is a natural and valid part of the process of advanced research and often leads to unforeseen new pathways to future discovery. Regardless, either result advances our knowledge base and increases our ability to identify solutions and/or avoid costly and unwarranted paths for future challenges.

In summary, the SDRD program continues to provide an unfettered mechanism for innovation that returns multi-fold to our customers, to national security, and to the general public. The program is a vibrant R&D innovation engine, benefited by its discretionary pedigree, enhanced mission spectrum, committed resources, and sound competitiveness to yield maximum taxpayer benefit. The 26 projects described exemplify the creativity and ability of a diverse scientific and engineering talent base. The efforts also showcase an impressive capability and resource that can be brought to find solutions to a broad array of technology needs and applications relevant to the NNSS mission and national security.

Acknowledgments

A number of individuals contribute significantly to make SDRD successful year after year. Without their support much of this would not be possible. My sincere gratitude goes out to Michele Vochosky, Katharine Kelly Streeton, and Sierra Cory, for compiling, editing, and publishing this report; Gomersall Design and Boone Printing for graphic design, printing, and binding; Emma Gurr for efforts in cost accounting and Tom Graves for project management support; Newell Ramsey, Kathy Gallegos, and Samantha Hixson for information system support; Janet Lux for compiling financial data for reporting requirements; Larry Franks, Rob Hixson, and Lynn Veeser for exceedingly valuable technical guidance and support; and SDRD site representatives and review committee: Frank Cverna, Daniel Frayer, Paul Guss, Jeff Koch, Eric Machorro, Michael Mohar, Sanjoy Mukhopadhyay, Mike Haugh, and Jerry Stevens. Special thanks again to members of our external advisory board, Larry Franks, Carl Ekdahl, Damon Giovanielli, Ralph James, Paul Rockett, Evan Rose, and Gerry Yonas, who graciously give their time and provide ongoing, valuable recommendations.

Howard A. Bender III
SDRD Program Manager

Strategic Opportunity Research

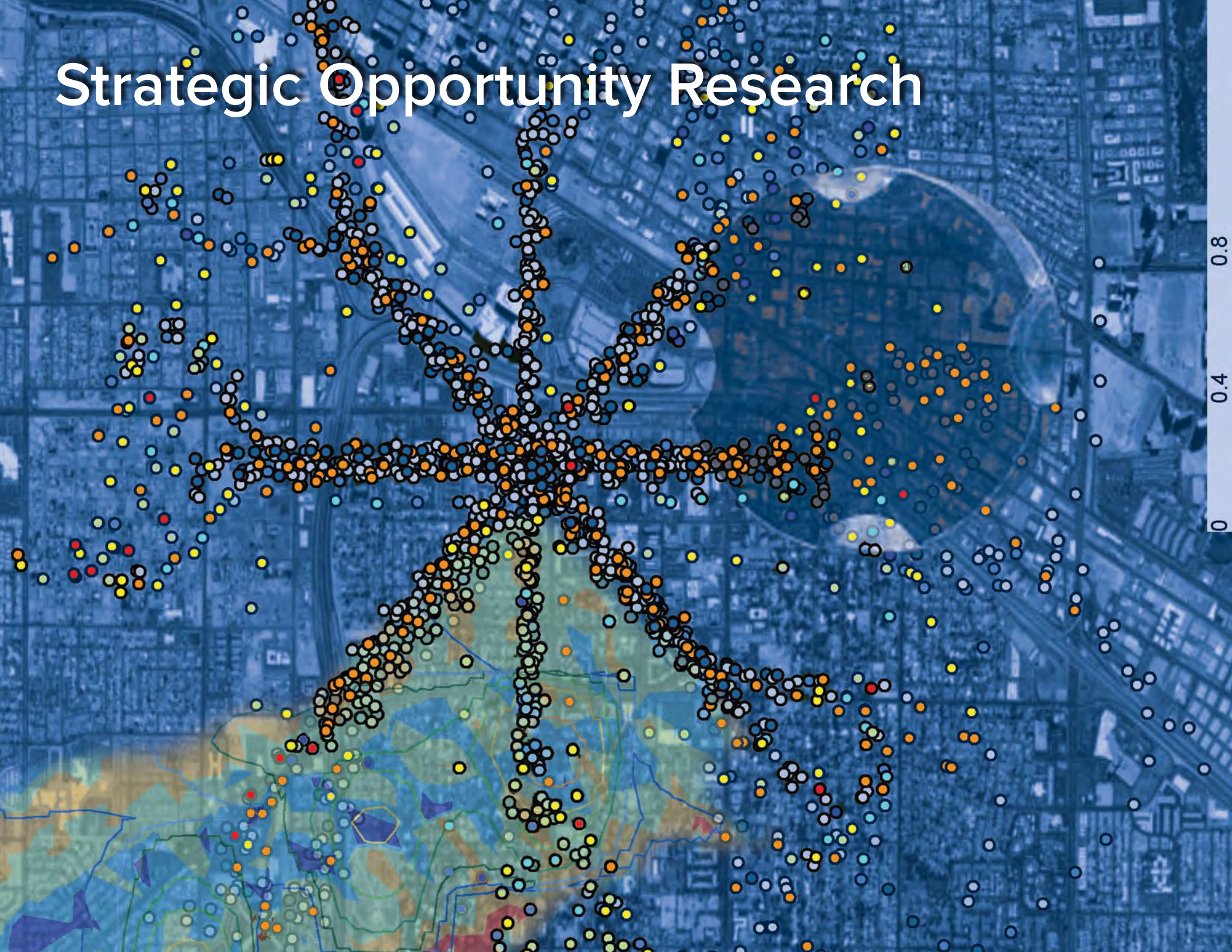

Multiple Unmanned Aircraft System for Remote Contour Mapping of a Nuclear Radiation Field

RSLN-15-15 | Continuing in FY 2016 | Year 1 of 3

Paul Guss,[1,a] Karen McCall,[a] Rick Fischer,[b] Michael Lukens,[a] Mark Adan,[a] Ki Park,[a] Roy Abbott,[c] Tanushree Luke,[a] Russell Malchow,[a] Sanjoy Mukhopadhyay,[b] Paul Oh,[d] Pareshkumar Brahmbratt,[d] Eric Henderson,[d] Jinlu Han,[e] Justin Huang,[e] and Casey Huang[e]

Nuclear radiation detection and monitoring are very important to public safety, particularly so for nuclear disasters involving radioactive contamination. Among the advantages an unmanned aircraft system (UAS) has are fast deployment, low-altitude flying that enhances sensitivity, wide area coverage, no radiation exposure health safety restriction, and the ability to access highly hazardous or radioactive areas. Additionally, the UAS can be configured with the nuclear detecting sensor optimized to measure the radiation associated with the event. For this project, small UAS (sUAS) platforms were obtained for the installation of sensor payloads for radiation detection and electro-optical systems that were specifically developed for UAS research, development, and operational testing. The sensor payloads were optimized for the contour mapping of a nuclear radiation field, which will result in a formula for low-cost UAS platform operations with built-in formation flight control. The focus of the FY 2016 work is to continue developing the algorithms and to initiate the sUAS comprehensive testing using the Sandstorm platforms.

[1] gusspp@nv.doe.gov, 702-295-1552
[a] Remote Sensing Laboratory–Nellis; [b] Remote Sensing Laboratory–Andrews; [c] Special Technologies Laboratory; [d] University of Nevada, Las Vegas; [e] Astroflight

Background

Unmanned aircraft systems (UASs) have many advantages and provide significant operational benefits. It is a common argument that UASs are better suited to "4D" tasks: the dull, dirty, dangerous, and deep (Barnhart 2012a). The "dull" aspect refers to repetitive missions or missions that require persistence, and so are better suited to autonomous systems than humans. "Dirty" refers to environments in which there are nuclear, biological, and chemical threats. The tasks deemed "dangerous" are those in which there is a high risk to the aircraft and aircrew. "Deep" tasks are those that are beyond the range of current manned aircraft (Franklin 2008). Low-cost UASs (Di 2011a) are becoming increasingly popular in both research and practical applications, leading to a new, potentially significant service product known as UAS-based personal remote sensing (Chao 2009). Lately, UAS research is becoming a notable area with a growing number of papers focused on system modeling, navigation, flight control, path planning, and other topics. And with the rapid development of electronics and wireless communication technology, civilian remote sensing becomes practical by installing inexpensive sensors on UASs to measure and collect temperature and humidity data, as well as images, in real time.

UASs are used for personal remote sensing for applications in many different areas, such as water management, forest fire detection, wetland monitoring, and

crop identification (Chao 2009). Compared with a single UAS, the cooperative UAS system performs with more safety and efficiency (Geramifard 2011; Han 2013a, 2014a). Compared with satellite remote sensing, UASs provide equivalent or higher-resolution imagery and are more affordable than satellites (Chao 2012). Multiple UASs can share information with each other by wireless communication (Abdessameud 2010), so optimal algorithms like gradient searching can be implemented (Gan 2011). Multi-UAS systems with advanced cooperative control algorithms can offer advantages over a single UAS, especially when time-urgent tasks are involved, such as detecting nuclear radiation as part of consequence management operations. Multi-UASs reduce the time it takes to complete a task and the demand for capacity on one UAS because they operate in a distributed manner that increases the redundancy and robustness of the entire system (Nemra 2010).

Advantages of UASs are evident in situations where the people's safety may be jeopardized, such as pollutant diffusion, radiation leakage, and forest fire (Casbeer 2005). In March 2011, an earthquake occurred in Japan, and the subsequent tsunami led to a significant event in part due to the nuclear radiation from a damaged nuclear power plant. In such extremely dangerous conditions, it was difficult to access the area close to the nuclear radiation leakage site to perform high-fidelity measurements of the nuclear radiation around the nuclear plant. However, if UASs equipped with radiation detection instruments could have been deployed, precise radiation data would have been collected nearby but outside the high-radiation area. Some corporations and institutes, Honeywell and Virginia Tech in particular, have begun research to enable UAS access to potentially contaminated areas (Ford 2010, Carey 2011). Furthermore, if multiple UASs in a specified formation can conduct the radiation contour mapping in 3-D space, which is quite important for analyzing the safety factor around a damaged nuclear plant, the data would be extremely beneficial (Han 2013b).

UASs are an effective platform for intelligence, surveillance, and reconnaissance as well as tracking, border security, counter insurgency, attack and strike, target identification and designation, communications relay, electronic attack, law enforcement and security applications, environmental monitoring and agriculture, remote sensing, aerial mapping, and meteorology. The central tenet of the UAS is that the cockpit does not have an operator onboard the aircraft; therefore, control of the aircraft must take place by other means. The approach to command and control can be separated into three distinct forms: (1) ground control or remote piloting, (2) semi-autonomous control, and (3) autonomous control.

A small UAS (sUAS) system (maximum weight of 55 lb) can employ sensors to not only perform remote sensing, but also to assist with the autonomous or semi-autonomous navigation and operation of the sUAS (Beard 2012). Under autonomous control, the onboard computer is in control—not a human being (Gupta 2013). Goplen (2015) has enumerated the types of data that UASs collect for U.S. Geological Survey use and archives: 3-D modeling, color infrared orthophotography, contour map generation, digital surface models, feature extraction, keyhole markup language, normalized difference vegetation index, orthophotography point cloud generation, and volumetric measurements.

UAS designs are usually one of two types: fixed-wing (Di 2011a) and rotary-wing, which are also called vertical takeoff and landing (VTOL) UASs. Fixed-wing UASs can cooperate (Di 2011b) to fulfill the requirements of many practical applications (Han 2013b, 2014b, 2014c) and are popular for tasks requiring endurance (Chao 2010). Compared with fixed-wing UASs, VTOL UASs have particular advantages, such as hovering capability and little space restriction for takeoff and landing, which are beneficial for applications in search and surveillance as well as static image capturing or remote sensing.

UAS payloads may be either sensors or cargo (Barnhart 2012b). For sUASs, typically, the payloads are sensors; larger UASs are typically cargo carriers. Still, it is interesting to note that Amazon is performing their testing for cargo delivery using sUASs (Gabbee 2013, Duncan

2015). Designers of electro-optical sensor payloads for sUASs are under intense pressure to evolve their technologies to keep pace with the fast-moving trends in the sUAS industry. Perhaps in no other market are needs for ever-smaller, lighter, and less expensive payloads as urgent as they are in the sUAS business. Small size, weight, and power consumption—known by its ubiquitous acronym SWaP—is a paramount concern (Keller 2013). The Federal Aviation Administration (FAA) has issued a proposed sUAS rule to develop a set of guidelines and limits for sUAS usage throughout the United States (FAA 2015).

Project

The motivation of this work is to detect the level of nuclear radiation in a timely way through efficient use of multiple low-cost UASs. Two different scenarios of radiation detection tasks are explored. We demonstrated contour mapping through simulation and validated waypoint detection by the experimental flight test.

Our project scope included taking measurements on the ground to determine the response (counts per second [cps] per gigabecquerel [GBq]) of the detector as a function of source-to-detector distance. We mounted a detector on a sUAS and operated it initially in the cps mode to perform field and flight tests to demonstrate that the equipment was functioning as designed. Operation of the radiation detector was tested using different unshielded sources. The equipment should easily detect unshielded ^{137}Cs and ^{192}Ir point sources whose activities correspond to those mentioned in the HASS (high-activity sealed radioactive sources) directive (HASS 2003). HASS values for ^{137}Cs and ^{192}Ir are 20 and 10 GBq, respectively. The purpose of this directive is to prevent exposure of workers and the public to ionizing radiation arising from inadequate control of high-activity sealed radioactive sources and orphan sources. The equipment can also be used to detect radioactive "hot spots" on the ground, but manned aircraft are better for mapping fallout in wide areas (Pollanen 2009).

Figure 1. July 7, 2015, sUAS demonstration at the NNSS Area 25 test location adjacent to the "MX Racetrack." Insets (clockwise from top right) show flight path on computer, sUAS procurement evaluation team, positioning sUAS for takeoff, and a sUAS in flight.

Our objective is to demonstrate the potential of this technology using a radiological field, which has not been done before. We proposed to do this for two UASs in the first year. Use of multiple UASs to detect the nuclear radiation will be the guiding objective for future development work for monitoring the normal operation of a nuclear reactor and deploying in a nuclear event or anomaly, a case to which multiple UASs is particularly well suited. Using multiple low-cost UASs more efficiently addresses both scenarios of primary concern (i.e., nuclear radiation detection and contour mapping of the nuclear radiation). Eventually our results will be used in a comparative analysis and assessment of results of older-generation systems for acquiring similar data (Han 2013b, 2014b).

We acquired two fixed-wing Sandstorm UASs this year and will acquire data in the follow-on years (Figure 1). The systems are capable of performing normal and operational scenario flight maneuvers. The systems are self-contained, have an independent capability to control or terminate the aircraft, use autonomous waypoint navigation, support line-of-sight operations, and have the flexibility to integrate commercially available off-the-shelf and government-furnished sensors that are interchangeable. The systems' control, telemetry, and subsystems shall meet minimum federal requirements for aerial flight missions. The system shall provide real-time sensor data and metadata for processing and recording. The system includes a ground control station. Flight performance and command and control specifications are reported in Tables 1 and 2, respectively.

Table 1. Flight performance specifications

Performance Area Description	Requirements for Small UAS (55 lb max)
Payload (minimum)	10 lb (4" × 4" × 4", 0.04 ft^3)
Endurance	1 hr (minimum)
Weight of Vehicle (Gross Takeoff Weight)	55 lb (maximum to include 10 lb payload)
Operating Altitude	100–1000 ft
Speed	<70 knots
Launch Method	For unprepared environment or remote locations, using runway, catapult, or vertical method
Launch/Recovery Area Requirements	500 ft wide by 500 ft long (maximum)
Fuel Type	No requirement
Operational Temperature	10°F–110°F
Operating Environment	Day and night aircraft lighting; water-resistant (light rain, snow, mist) vehicle
Operations Crew Requirements	Maximum of 4 crew members, not including observer
sUAS Assembly	<4 hr with 4-person team

Table 2. Command and control station specifications

Requirement	Minimum Requirements
Control Guidance System	Manual and pre-programmed
Telemetry Option/ Data Link	Long-range, beyond line of sight
Communications Range	Communication range (transmitter/receiver) command and control of 2 nautical miles line of sight
Downlink Frequency	Secure digital data link
Emergency Procedures	Aircraft must be able to land immediately. Programmable loss of link capability: return to launch and land immediately, or land at a specified rally point.
Flight Area Control Authority	Direct pilot control authority, semi-autonomous flight modes
Flight Planning	Software must be able to program multiple GPS waypoints within flight line–modifiable options
Operations Crew	Maximum of 2, not including observer
Ready to Launch	<2 hr with 2-person team

UNLV Drones and Autonomous Systems Laboratory (DASL)

The University of Nevada, Las Vegas (UNLV) allocated a portion of their robotics facility, the Drones and Autonomous Systems Laboratory (DASL), located a quarter mile from the contiguous real estate constituting the main UNLV campus, for this work. Two Da-Jiang Innovations Science and Technology Co., Ltd (DJI) S1000 sUAS platforms to demonstrate the multi-sUAS radiation-sensing mission along with the detector system to use with the drones were prepared. Figures 2 and 3 show the DJI S1000 sUAS platform that UNLV procured for this project for flight-testing and the current condition of the DASL workspace. Figures 4 and 5 show the transmitter/receiver station acquired for the transmission of the data sent by the two Safecast units, shown in Figure 4, left.

Safecast System

Safecast's bGeigie Nano (on the left in Figure 4) is a mobile radiation detector that uses an LND, Inc., 7317 2" pancake Geiger-Müeller tube to measure alpha, beta, and gamma radiation. It uses an internal lithium-ion battery for approximately 40 hours of operation while remaining very compact. The bGeigie Nano incorporates a GPS receiver and can send data wirelessly over Wi-Fi, Bluetooth, and other protocols with the addition of an XBee module from Digi Corporation. XBee modules use Digi's own ZigBee-based protocol to provide a fast point-to-multipoint or peer-to-peer network infrastructure.

We performed data tracking studies with the Safecast detector system in the lab, on foot, and while driving about Nellis Air Force Base and Las Vegas. We flew the Safecast system to obtain comparison baseline

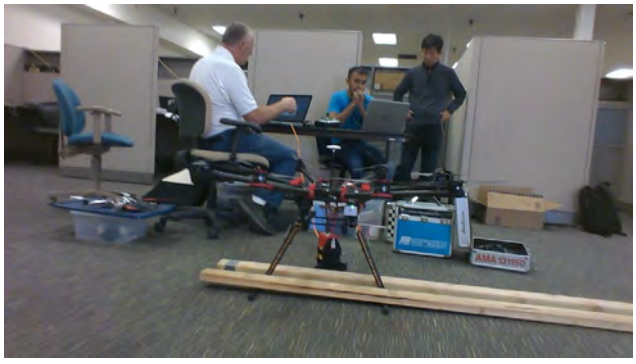

Figure 2. DASL team members (l. to r.) Eric Henderson and Paresh Brahmbhatt show NSTec's Ki Park the algorithm for the DJI S1000 sUAS platform

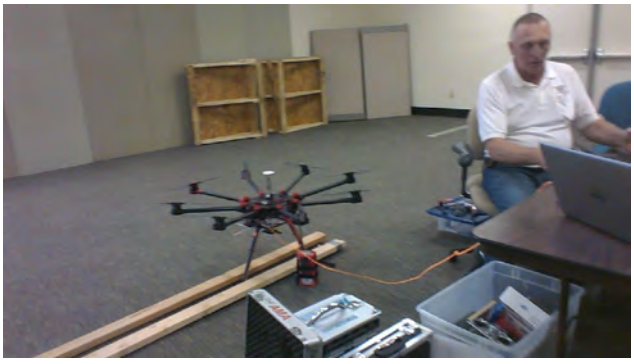

Figure 3. DASL team member Eric Henderson programs the "mow-the-lawn" algorithm for the DJI S1000 sUAS platform

Figure 4. Safecast system interfaced to RaptorX

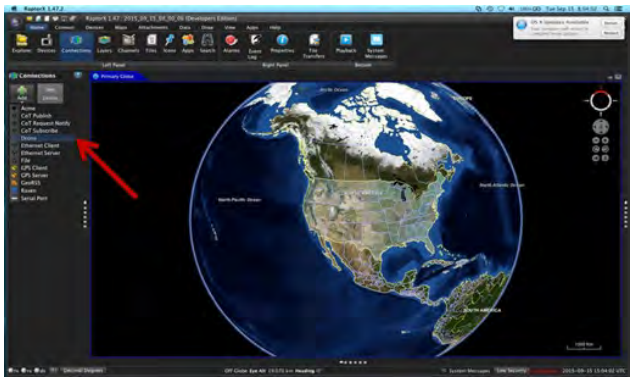

Figure 5. Selecting the XBee-PRO 900 receiver with RaptorX

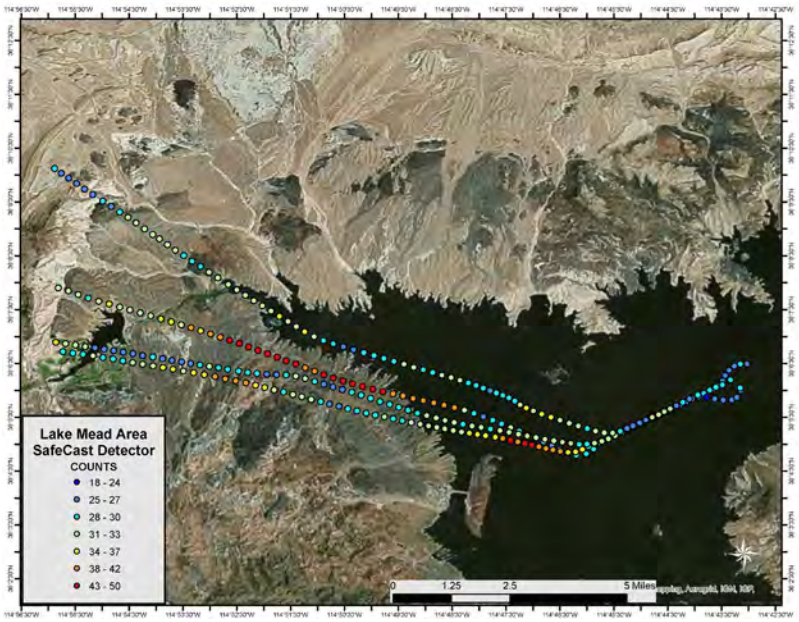

Figure 6. Safecast data acquired over the Lake Mead Test Line

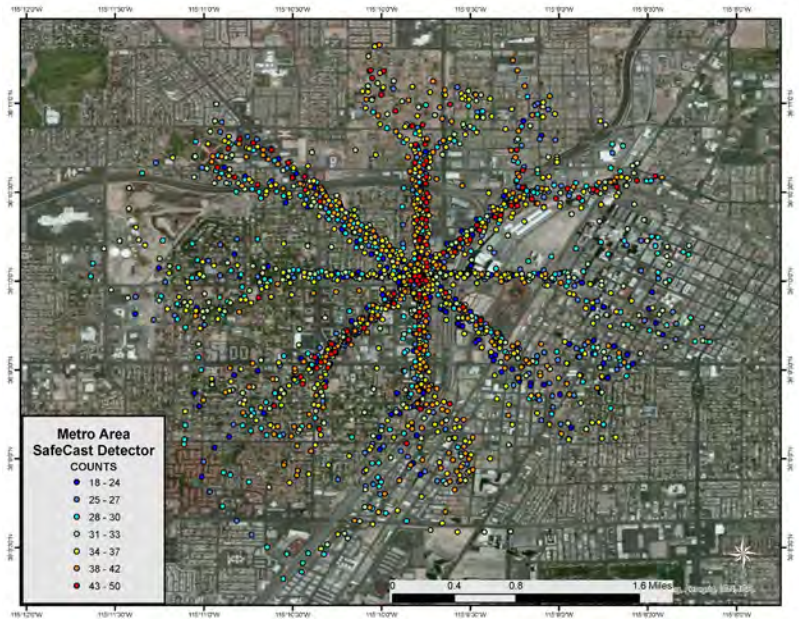

Figure 7. Safecast data gathered over the interstate highway and Rancho Boulevard in Las Vegas, Nevada

information between it and the Aerial Measuring System (AMS)/Advanced Visualization and Integration of Data (AVID) system (Joines 2013). Next, we prepared for several AMS aerial flights using the Radiation Solutions, Inc. (RSI) system (RSI 2007). We flew the Safecast system alongside the RSI system on two notable aerial flights. The first was the Lake Mead Test Line, for which there is an abundance of historical baseline data (Figure 6). The test line is especially well characterized, tested, and flown with AMS. We also flew the Safecast over Las Vegas (Figure 7). We took advantage of and leveraged against testing and evaluation processes for the U.S. Department of Homeland Security Domestic Nuclear Detection Office (DNDO) Airborne Radiological Enhanced-Sensor System (ARES) and flew the Safecast simultaneously with the ARES system onboard RSL–Nellis helicopters for calibration and normalization methods (NSTec 2012).

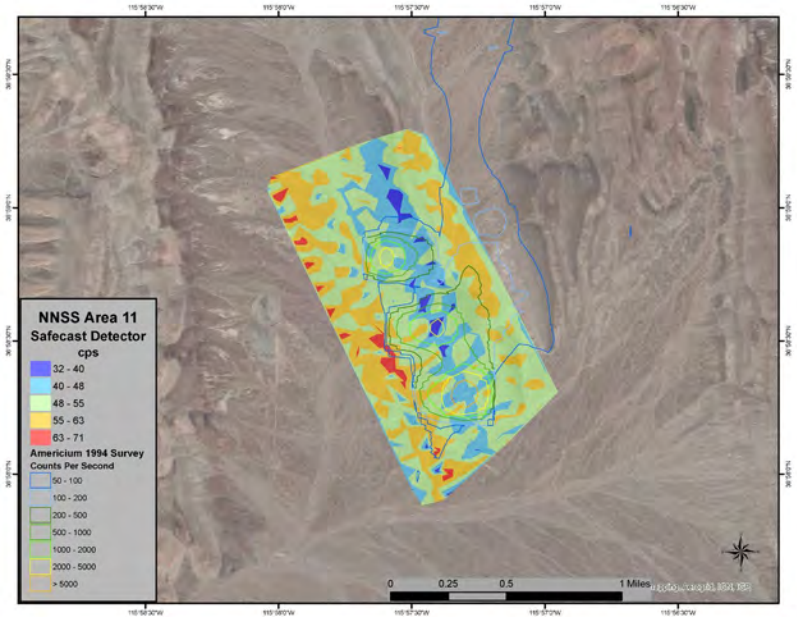

Figure 8. Safecast data for NNSS Area 11 Aerial Measurements Survey

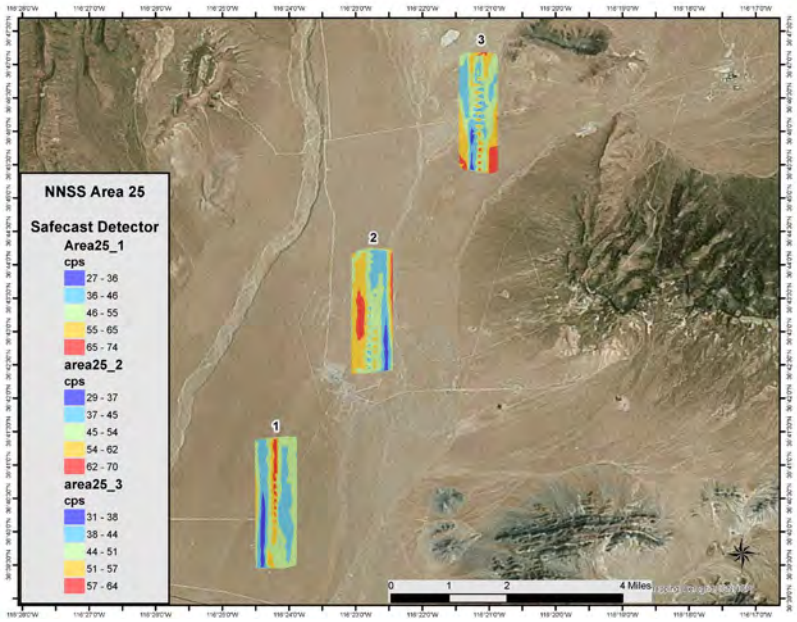

Figure 9. Safecast data for NNSS Plutonium Valley Aerial Measurements Survey

A source was placed outside in a controlled area in central Las Vegas to test the DNDO ARES system in an urban environment. The ARES, RSI/AVID, and Safecast systems were flown over this source. Preliminary results indicate that the ^{137}Cs radiation source was seen by the RSI/AVID system and by the DNDO ARES system but not by the Safecast system. This is not necessarily a surprise, though it is still slightly disappointing. Our proposal stated that initially the UAS would be capable of spotting point sources that met the HASS criteria (HASS 2003); we note that the sources used for these tests were significantly lower in intensity than those specified by the HASS criteria. We also flew the Safecast system at the NNSS Area 11 and at Plutonium Valley, Area 25 (Figures 8 and 9, respectively). Figures 6 through 12 include examples of data acquired with the Safecast system. We continue to assess the aerial Safecast data. In general, we saw a good correlation between the RSI/AVID and Safecast systems.

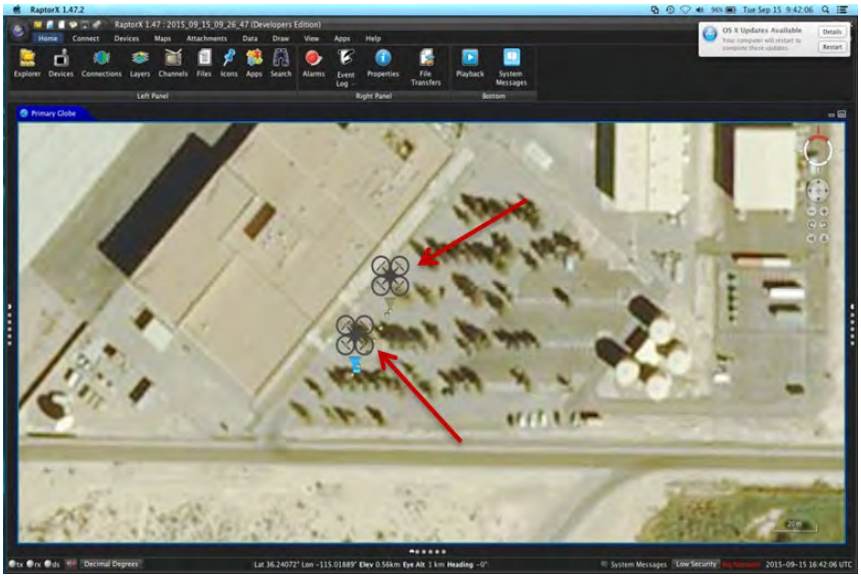

Figure 10. Multiple Safecast bGeigie Nanos systems with the XBee-PRO XSC 900 transceiver as displayed by RaptorX

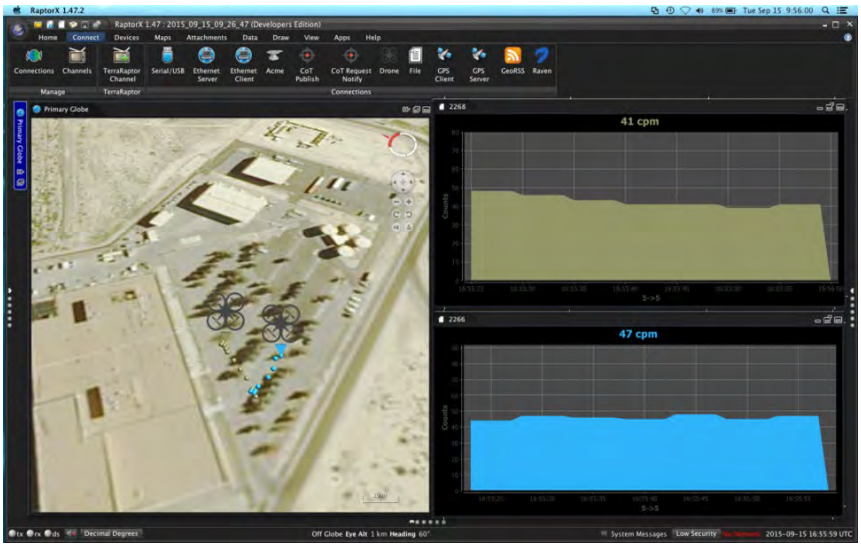

Figure 11. View of the strip charts of data acquired with the Safecast system

Figure 12. The RaptorX system was adjusted to accept radiological data streams from two sUAS simultaneously, and to plot their respective breadcrumb data

Integration to RaptorX

We determined the communication requirements to transmit detector data. The transmitter system we obtained is depicted in Figure 4. We made remarkable progress in setting up the real-time transmission system for the Safecast. We acquired the transmitter/receiver hardware and successfully demonstrated the integration of this hardware with RaptorX software (Figure 5) (RaptorX 2015). After this real-time system was demonstrated, we began the integration of UNLV and Remote Sensing Laboratory (RSL) assets for this project with the RaptorX software.

RaptorX is a 3-D geographic information system application with extensive plugin architecture for integrating a variety of georeferenced data. The application, developed by the Special Technologies Laboratory (STL), provides a completely extensible software platform to perform command and control for a vast array of sensors. RaptorX is built on the platform-independent Java programming language, allowing users to run it on Windows, Mac, or Linux machines. It uses as much license-free and open-source technologies as possible. One of the main attractions of RaptorX is the application programming interface (API). The RaptorX API allows independent developers and organizations to create software extensions to integrate their specialized hardware and software products into the RaptorX application. A graphical user interface was created through the RaptorX API for the wireless reception and real-time monitoring of radiation and location data. Two Safecast detector systems were transported about the RSL parking lot to test the setup. They were simultaneously attached to RaptorX, and the breadcrumbs were plotted individually. Figures 10–12 illustrate the mapping, strip chart, and alarming features using RaptorX.

Safecast Telemetry for Unmanned Aircraft

Using a transmitter/receiver board for the Safecast system (Figure 13) and the XBee-PRO XStream Compatible (XSC) 900 MHz RF module (Figure 14), we were able to set up the radio transmission. The system accommodates two Safecast systems transmitting data simultaneously from each of two separate sUAS (Figure 4).

The operation and configuration of the XBee-PRO 900 transceivers is an important aspect of the system. The XBee-PRO transceivers (Figure 14) are well suited for fast and easy point-to-point networking because of their nearly drop-in readiness. However, to ensure that the bGeigie Nanos and the base computer do not receive interference from other XBee-PRO 900 modules, the destination and source addresses were changed. In this case, the source address corresponds to the bGeigie Nano, and the destination address corresponds to the base computer. The destination address of the receiver module is the source address of the transmitter module, and vice versa. This allows

Figure 13. Transmitter/receiver board for Safecast system

Figure 14. XBee-PRO XSC 900 MHz RF module

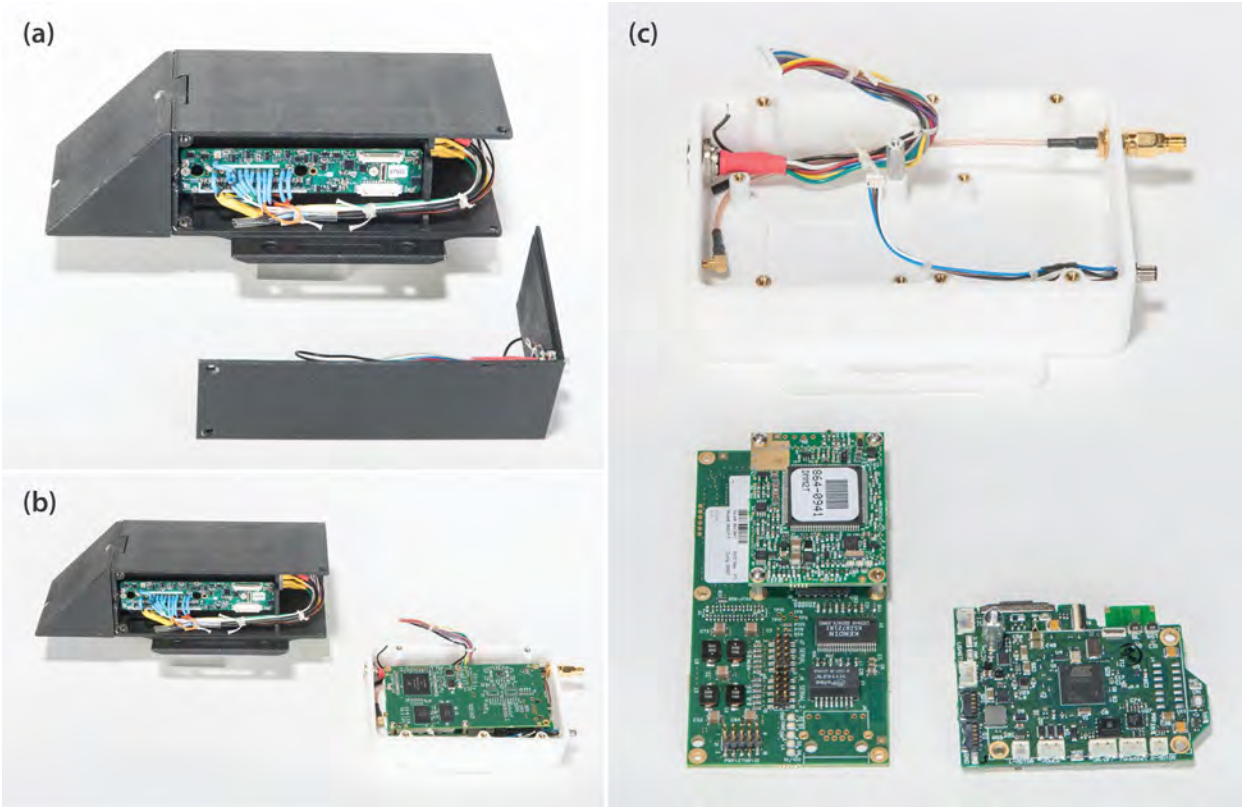

Figure 15. Radiation detector and transmission system built for this sUAS project. (a) Bluetooth/900 MHz downlink and multichannel analyzer, (b) 1" × 2.5" NaI:Tl detector and electronics, and (c) transmitter module and Ethernet interface case, 900 MHz Ethernet interface, and main controller and detector electronics.

two-way communication between the two devices. In our configuration, data are not sent to the bGeigie Nano. That capability opens up the prospect of using RaptorX to control a sUAS flight in a future configuration of the system. If the bGeigie Nanos necessitated control through the RaptorX plugin, a possible modification of its firmware would be required.

Spectral Unit with Real-Time Data Telemetry for Unmanned Aircraft

We prepared a low-power multichannel analyzer/spectra transmitter device (Figure 15), which when combined with the 1" × 1" thallium-doped sodium iodide (NaI:Tl) detector enables a sUAS to collect and transmit real-time isotopic gamma ray spectra. The government off-the-shelf radiation detection system is a low-power mobile spectral detector system. This device not only integrates into the STL RaptorX package, but it also interfaces with the RSI/AVID system. This is a critical milestone on the proof-of-concept pathway to demonstrate and to achieve the technology to autonomously perform a radiological survey using a sUAS. The device was built using spare parts from other similar RSL Spectral Unattended Detector (SpUD) units. The next step is to set up a 900 MHz radio to replace the range-limited Bluetooth currently in place. We shall acquire benchmarking data for Physical Sciences, Inc. (PSI), to construct isotope identification algorithms (Cosofret 2014). Figure 15 shows the system. It collects a 1024-channel spectra at 0–3 MeV and sends the spectra acquired at 1 Hz to either a RaptorX or AVID computer ground station for real-time mapping, breadcrumb tracking, or isotope identification.

Poisson-Clutter Split (PCS) Algorithms for Unmanned Aircraft

As mentioned, one goal of this study is to evaluate the effectiveness of conducting radiological/nuclear mapping with multiple UASs, each containing a custom lightweight air sampling system (Perajarvi 2008) and a radiation detector. The concept is to detect radiation in the environment and to create contour map products of nuclear radiation fields using a sUAS as a platform. The equipment will be capable of locating highly radioactive sources on the ground using a commercial radiation detector with a cylindrical probe mounted to the UAS. The project includes both field and flight tests to demonstrate that the equipment is functioning as designed.

We subsequently wish to improve the analysis and interpretation of radiation data collected by these multiple UASs by using advanced data processing algorithms. We are investigating the effectiveness of the Poisson Clutter Split (PCS) algorithm, developed by PSI (Cosofret 2014), which determines a statistical estimation of the background for sparse data acquisitions, thus being an ideal tool for our UAS environments. We are collaborating with PSI to implement the PCS algorithm to UAS-collected data and then adjust it based on data collection findings. This algorithm will be used to analyze and interpret the data collected by the onboard radiation detectors in real time. The algorithm is well tested and executed, so the implementation of the PCS algorithm for improved detection and discrimination capabilities of the UAS collected data within this SDRD project is relatively straightforward—it does involve collection of detector response data, which we plan to do in FY 2016. Implementation of the PCS algorithm is in its earliest stages, and we expect to improve the sensitivity of our sUAS-based detector system with its employment.

Conclusion

This project scope is to engineer a UAS swarm concept for remote sensing with several UASs, originally expecting to work with one UAS in FY 2015. However, we received authorization to acquire two UAS platforms on February 26, 2015, and did acquire two Sandstorm UASs from Unmanned Systems Incorporated. In FY 2015, we prepared a real-time radiation data acquisition, storage, and transmission system that interfaces to AVID and/or RaptorX systems. The preliminary field trials described above look promising and illustrate the potential to make significant remote sensing radiological measurements using sUAS platforms. We are also in the process of incorporating algorithms to improve real-time data analysis. In FY 2016, we will continue development of the algorithms and the initiation of a comprehensive sUAS remote sensing operations program using the Sandstorm platforms.

Acknowledgments

We would like to thank Michael Madlener, Michael Howard, Bogdan Cosofret, Colin Okada, Raymond Keegan, and Ding Yuan for their contributions to this work.

References

Abdessameud, A., A. Tayebi, "Formation stabilization of VTOL UASs subject to communication delays," 49th IEEE Conference on Decision and Control, Atlanta, Georgia, December 15–17, 2010, 4547–4552.

Barnhart, R. K., B. Hottman, D. M. Marshall, E. Shappee, *Introduction to Unmanned Aircraft Systems*, RCR Press, Boca Raton, Florida, 2012a, 2.

Barnhart, R. K., B. Hottman, D. M. Marshall, E. Shappee, *Introduction to Unmanned Aircraft Systems*, RCR Press, Boca Raton, Florida, 2012b, 24.

Beard, R. W., T. W. McLain, S*mall Unmanned Aircraft Theory and Practice*, Princeton University Press, Princeton, New Jersey, 2012, 288.

Carey, B., "Honeywell's micro-UAV monitors damaged nuclear plant," AIN Online (May 2011), http://www.ainonline.com/aviation-news/defense/2011-05-02/honeywells-micro-uav-monitors-damaged-nuclear-plant, accessed January 12, 2012.

Casbeer, D., R. Beard, T. Mclain, S.-M. Li, R. Mehra, "Forest fire monitoring with multiple small UASs," American Control Conference, Portland, Oregon, June 8–10, 2005.

Chao, H., A. M. Jensen, Y. Han, Y. Chen, "AggieAir: Towards low-cost cooperative multispectral remote sensing using small unmanned aircraft systems," in *Advances in Geoscience and Remote Sensing*, G. Jedlovec, ed., InTech, Vukovar, Croatia, 2009, 463–490, https://www.researchgate.net/publication/221905354_AggieAir_Towards_Low-cost_Cooperative_Multispectral_Remote_Sensing_Using_Small_Unmanned_Aircraft_Systems, accessed January 5, 2016.

Chao, H. Y., Y. C. Cao, Y. Q. Chen, "Autopilots for Small Unmanned Aerial Vehicles: A Survey," *International Journal of Control, Automation, and Systems* **8**, 1 (2010) 36–44.

Chao, H., Y. Chen, "Remote sensing and actuation using unmanned vehicles," *IEEE Book Series on Systems Science and Engineering*, Wiley-IEEE Press, 2012, 206.

Cosofret, B. R., K. Shokhirev, P. Mulhall, D. Payne, B. Harris, "Utilization of advanced clutter suppression algorithms for improved standoff detection and identification of radionuclide threats," *Proc. SPIE* **9073** (2014) 907316.

Di, L., Y. Chen, "Autonomous flying under 500 USD based on RC aircraft," *Proc. of 2011 ASME/IEEE International Conference on Mechatronic and Embedded Systems and Applications*, Washington, D.C. (2011a).

Di, L., H. Chao, J. Han, Y. Chen, "Cognitive multi-UAS formation flight: Principle, low-cost UAS testbed, controller tuning and experiments," *Proc. of 2011 ASME/IEEE International Conference on Mechatronic and Embedded Systems and Applications*, Washington, D.C. (2011b).

Duncan, J. S., *Exemption No. 11290*. FAA Letter, Attn: P. Misener, Amazon. Regulatory Docket No. FAA−2014−0474. United States Department of Transportation (2015, April 8), http://www.faa.gov/uas/legislative_programs/section_333/333_authorizations/media/amazon_com_11290.pdf, accessed April 15, 2015.

FAA, "Operation and Certification of Small Unmanned Aircraft Systems," Small UAS Notice of Proposed Rulemaking, Billing Code 4910-13-P, Department of Transportation, Federal Aviation Administration, 14 CFR Parts 21, 43, 45, 47, 61, 91, 101, 107, and 183, FAA Federal Register 80, 35, Monday, February 23, 2015, Proposed Rules (February 23, 2015), http://www.gpo.gov/fdsys/pkg/FR-2015-02-23/pdf/2015-03544.pdf, accessed May 5, 2015.

Ford, J., "UAV for nuclear scouting missions," *The Engineer* (March 5, 2010), http://www.theengineer.co.uk/uav-for-nuclear-scouting-missions/, accessed September 30, 2015.

Franklin, M., "Unmanned combat air vehicles: Opportunities for the guided weapons industry?" Royal United Services Institute for Defence and Security Studies (2008), https://rusi.org/sites/default/files/200808_op_unmanned_combat_air_vehicles.pdf, accessed January 6, 2016.

Gabbee, "Amazon testing drone delivery system," *YouTube*, December 2, 2013, https://www.youtube.com/watch?v=Le46ERPMlWU, accessed April 11, 2015.

Gan, S. K., S. Sukkarieh, "Multi-UAS target search using explicit decentralized gradient-based negotiation," IEEE International Conference on Robotics and Automation, Shanghai, China, May 9–13, 2011.

Geramifard, A., J. Redding, N. Roy, J. P. How, "UAS cooperative control with stochastic risk models," American Control Conference, San Francisco, California, June 29–July 1, 2011.

Goplen, S. E., J. L. Sloan, "National unmanned aircraft systems project office," U.S. Geological Survey Fact Sheet, FS-2015–3013, 2015.

Gupta, S. G., M. M. Ghonge, P. M. Jawandhiya, "Review of unmanned aircraft system (UAS)," *International Journal of Advanced Research in Computer Engineering and Technology*, **2**, 4 (2013) 1646–1658, http://www.uxvuniversity.com/wp-content/uploads/2014/04/Review-of-Unmanned-Aircraft-System-UAS.pdf, accessed January 6, 2016.

Han, J., Y. Q. Chen, "Cooperative source seeking and contour mapping of a diffusive signal field by formations of multiple UAVs," *Proc. IEEE 2013 International Conference on Unmanned Aircraft Systems*, Atlanta, Georgia, 2013a.

Han, J., Y. Xu, L. Di, Y. Q. Chen, "Low-cost multi-UAS technologies for contour mapping of a nuclear radiation field," *J. Intell. Robot. Syst.* **70** (2013b) 401–410.

Han, J., Y. Q. Chen, "Multiple UAV formations for cooperative source seeking and contour mapping of a radiative signal field," *J. Intell. Robot. Syst.* **74** (2014a) 323–332.

Han, J., L. Di, C. Coopmans, Y. Q. Chen, "Pitch loop control of a VTOL UAS using fractional order controller," *J. Intell. Robot. Syst.* **73** (2014b) 187–195.

Han, J., "Cyber-physical systems with multi-unmanned aerial vehicle-based cooperative source seeking and contour mapping," Doctoral Thesis, Utah State University, 2014c.

HASS, "The Council of the European Union Council Directive 2003/122/ EURATOM of 22 December 2003 on the control of high-activity sealed radioactive sources and orphan sources," *Official Journal of the European Union*, December 31, 2003.

Joines, C., et al., "An extensible architecture for supporting next-generation aerial radiological measurements," in *Site-Directed Research and Development*, FY 2012, National Security Technologies, LLC, Las Vegas, Nevada, 2013, 159–167.

Keller, J., "Electro-optical sensor payloads for small UAVs," 2013, http://www.militaryaerospace.com/articles/print/volume-24/issue-10/technology-focus/electro-optical-sensor-payloads-for-small-uavs.html, accessed April 14, 2015.

Nemra, A., N. Aouf, "Robust cooperative UAS visual SLAM," 2010 IEEE 9th International Conference on Cybernetic Intelligent Systems, Reading, United Kingdom, September 1–2, 2010.

NSTec Remote Sensing Laboratory, *An Aerial Radiological Survey of the California Bay Area*, TARD-ATD-0006v.1, U.S. Department of Homeland Security, Domestic Nuclear Detection Office, Las Vegas, Nevada, 2012, http://www.ci.berkeley.ca.us/uploadedFiles/Clerk/Level_3_-_General/2013-HQFO-00353%20Document.pdf, accessed September 30, 2015.

Perajarvi, K., J. Lehtinen, R. Pollanen, H. Toivonen, "Design of a sampler for a small-size unmanned aerial vehicle," *Rad. Prot. Dosim.* **132** (2008) 328–333.

Pollanen, R., H. Toivonen, K. Perajarvi, T. Karhunen, T. Ilander, J. Lehtinen, K. Rintala, T. Katajainen, J. Niemela, M. Juusela, "Radiation surveillance using an unmanned aerial vehicle," *Applied Radiation and Isotopes* **67** (2009) 340–344.

RaptorX, https://raptorx.org, 2015, accessed September 30, 2015.

Radiation Solutions, Inc. (RSI), RS-500 "Advanced digital gamma-ray spectrometer," 2007, http://www.radiationsolutions.ca/index.php?id=38, accessed September 30, 2015.

This page left blank intentionally

Enhanced Dynamic Materials Research

LAO-19-15 | Continuing in FY 2016 | Year 1 of 3

Robert S. Hixson,[1,a] Brandon La Lone,[b] Gerald D. Stevens,[b] Dale Turley,[b] and Lynn R. Veeser[a]

We have initiated a research program in dynamic materials properties to address some key unresolved shock physics issues. Fundamental shock physics research requires a condition of uniaxial strain to be maintained to be able to interpret results, and this requires large-diameter targets and impactors. To do this we have procured a new research-quality propellant launcher, which will be installed at the gas launcher and small-scale explosives campus located at the NSTec Special Technologies Laboratory (STL). This new launcher, with a maximum velocity of 2 km/s, will allow us to move dynamic materials research in the direction needed to improve the fundamental physics models used in large hydrodynamic codes routinely used to simulate dynamic events. Specifically, this new capability will allow research to be done at much higher stress states than currently possible, greatly expanding the region over which fundamental information is available and over which physics models are validated. In FY 2015 we fielded experiments on single-crystal copper using the existing STL launcher; the results are helping us begin to understand the effects of grain structure in metals. Our first experiments performed in collaboration with the California Institute of Technology on their two-stage gas gun have allowed us to quantitatively measure the melt curve of tin upon shock release by determining its temperature as a function of shock stress. Finally, we have begun doing hydrodynamic simulations of experimental designs on shocked gallium. In FY 2016 we will install the 40 mm bore propellant launcher; continue, and perhaps finish, the tin melt curve research; continue the single-crystal copper work to obtain accurate shock wave velocities; and perform our first gallium experiments in collaboration with Los Alamos National Laboratory.

[1] hixsonrs@nv.doe.gov, 505-663-2022

[a] New Mexico Operations–Los Alamos; [b] Special Technologies Laboratory

Background

This strategic SDRD project has several focus areas. First, we are developing the capability to reach higher pressures in our shock experiments; to this end we are in the process of obtaining a larger-bore (40 mm) propellant launcher. Second, we aim to understand the properties of single-crystal metals, specifically how their response as a function of crystalline orientation contributes to polycrystalline response. This research complements the earlier work of Minich (2004). Third, our project will improve temperature measurements sufficiently to begin to measure the melt curve of tin. Finally, we intend to investigate gallium (Ga) metal, a metal with a complex phase diagram. Scientists at Los Alamos National Laboratory (LANL) are beginning to do dynamic research on Ga, and we will be teaming with them. Progress has been made on all these goals in FY 2015, as described in this report.

Project

Propellant Launcher

The existing gas launcher at the Special Technologies Laboratory (STL) has now been upgraded to have a 38 mm bore, allowing a broader range of fundamental shock experiments to be done. This launcher has an upper performance limit of 700–800 m/s, which is suitable for low stress regime research. However, one of our key goals is to reach stress states that are roughly equivalent to those occurring with high explosive (HE) detonation. To attain this performance requires a higher impact speed. We therefore looked in detail at propellant launcher systems that were roughly equivalent in tube bore but had a much higher impact speed capability. We have ordered a 40 mm propellant launcher from Physics Applications, Inc. that can reach impact velocities of about 2 km/s. This launcher is scheduled to be delivered, installed at STL, and test fired in FY 2016.

Single-Crystal Metal Physics

Metals used in engineering applications are polycrystalline in nature, composed of small "grains" of single-crystal metal. If such samples are not made correctly, it is possible to have grains oriented in a way that is not purely random. This can cause preferred orientation in some direction or directions and lead to a very fundamental question concerning the propagation of stress waves in such a sample: will the wave speeds be the same in all directions? To answer this requires a study of single-crystal metal samples.

Most shock compression research done to date has focused on polycrystalline materials, which are assumed to be isotropic. However, single crystals are typically anisotropic to some degree so may respond differently when shocked along different crystal orientations. The most fundamental measurement to characterize such anisotropic response is the velocity of shock waves, including both elastic and plastic waves. Other important properties are compressive and tensile strength. Finally, for materials with phase transformations, it is reasonable to ask if the transformation stress depends on shock direction. In our first experiment series, we attempted to answer a few of these questions for a cubic metal—copper—which has a relatively simple single-crystal system but has a relatively large Zener anisotropy ratio, which can be written in terms of the cubic elastic constants as

$$2C_{44}/(C_{11} - C_{12}) = 3.2. \quad \textbf{(1)}$$

In the elastic regime, isotropic materials have the simplest response. Elastic properties are the same in all directions, and the constitutive relation is also simple, described in Equation 2, where λ and μ are called the Lamé constants. The elastic response of isotropic solids depends upon only these two constants.

Slightly more complex are single-crystal solids with cubic structure (either simple, face centered, or body centered). For this class of material, the elastic response is governed by three elastic constants, C_{11}, C_{12}, and C_{44}. Then the constitutive relation is described in Equation 3.

$$\begin{bmatrix} \sigma_{xx} \\ \sigma_{yy} \\ \sigma_{zz} \\ \sigma_{yz} \\ \sigma_{zx} \\ \sigma_{xy} \end{bmatrix} = \begin{bmatrix} \lambda+2\mu & \lambda & \lambda & 0 & 0 & 0 \\ \lambda & \lambda+2\mu & \lambda & 0 & 0 & 0 \\ \lambda & \lambda & \lambda+2\mu & 0 & 0 & 0 \\ 0 & 0 & 0 & \mu & 0 & 0 \\ 0 & 0 & 0 & 0 & \mu & 0 \\ 0 & 0 & 0 & 0 & 0 & \mu \end{bmatrix} \begin{bmatrix} \varepsilon_{xx} \\ \varepsilon_{yy} \\ \varepsilon_{zz} \\ \varepsilon_{yz} \\ \varepsilon_{zx} \\ \varepsilon_{xy} \end{bmatrix}, \quad \textbf{(2)}$$

$$\begin{bmatrix} \sigma_{xx} \\ \sigma_{yy} \\ \sigma_{zz} \\ \sigma_{yz} \\ \sigma_{zx} \\ \sigma_{xy} \end{bmatrix} = \begin{bmatrix} C_{11} & C_{12} & C_{12} & 0 & 0 & 0 \\ C_{12} & C_{11} & C_{12} & 0 & 0 & 0 \\ C_{12} & C_{12} & C_{11} & 0 & 0 & 0 \\ 0 & 0 & 0 & C_{44} & 0 & 0 \\ 0 & 0 & 0 & 0 & C_{44} & 0 \\ 0 & 0 & 0 & 0 & 0 & C_{44} \end{bmatrix} \begin{bmatrix} \varepsilon_{xx} \\ \varepsilon_{yy} \\ \varepsilon_{zz} \\ \varepsilon_{yz} \\ \varepsilon_{zx} \\ \varepsilon_{xy} \end{bmatrix} \quad (3)$$

For solids with less symmetry, the number of required elastic constants increases. For cubic symmetry, the bulk modulus K is an invariant of the elastic constant matrix

$$K = \frac{C_{11} + 2C_{12}}{3}. \quad (4)$$

We also know that $K = \rho_0 C_b^2$, where C_b is the bulk sound velocity and ρ_0 is density. This implies that the bulk sound speed does not depend upon direction in crystals with cubic symmetry in the elastic regime. Because the y-intercept of the plastic shock Hugoniot is approximately equal to C_b, the Hugoniots in the various directions might be expected to have close to the same y-intercept in U_s-u_p space. For materials with linear Hugoniots in U_s-u_p space, the slopes might still be different; this should be examined in more detail, both theoretically and experimentally. But the directional elastic Hugoniots, as well as the Hugoniot elastic limit (HEL), may still be expected to be different in general.

Therefore, it makes sense to carefully measure shock properties in the [100], [110], and [111] directions for a cubic system. We chose copper because it is a relatively easy metal for which to obtain both polycrystalline and single-crystal samples, some dynamic research has been done with single-crystal samples (Jones 1969, Kanel 1992, Schwartz 2002, Minich 2004, Chau 2010), and we have experience in doing research on polycrystalline copper samples. Some of the work done by these researchers is especially relevant to ours. Minich (2004) looked at spall response of copper single crystals, Chau (2010) examined relatively high-stress plastic wave speeds, and the early work of Jones (1969) describes strength properties and active slip systems. As mentioned above, it is important to make careful measurements of several fundamental shock properties as a function of orientation, namely (1) both elastic and plastic wave velocities, (2) dynamic strength in compression, or HEL, and (3) spall strength.

Measurements this year were done at relatively low shock stress with a goal of looking at elastic response from low stress up to the overdrive stress to examine elastic response in detail. Then, above the overdrive stress, in future years we will go as high as possible with existing experimental platforms to look at plastic shock response. Finally, we have measured dynamic tensile strength (spall) at low stress (primarily in the [100] orientation), and will go to higher stress if required. Although some work has already been done on single-crystal copper, nothing this comprehensive has yet been published.

Based on the above considerations and other work, we expect to observe different wave speeds in the elastic regime but plastic wave speeds that fall on the polycrystalline Hugoniot. We also expect to observe different spall and compressive strength responses in the different orientations. In addition, we expect spall strength to increase with increasing final stress state.

STL Gas Launcher Experiments

We executed a campaign of seven experiments on the 13 mm bore STL gas gun in March of 2015 to initiate this research. We used targets of polycrystalline and single-crystal copper in the [100], [110], and [111] orientations. Samples for the March shots were limited to 2 mm in thickness to avoid edge-release effects given the small diameter required. To get the spall to occur roughly midway through the target, we made

the impactor of the same material as the target and roughly half its thickness. This arrangement produces symmetric impact and allows for the simplest analysis of the results. In August, after the 38 mm barrel was installed on the gun, we fielded five [100] experiments with similar samples of 2 and 4 mm thicknesses but 25 mm diameters. Analysis of these latest shots has just begun, so the results discussed here are preliminary.

The first series of experiments at STL were done with VISAR and photonic Doppler velocimetry (PDV) diagnostics at the back of the target to measure projectile velocity and approximate tilt. The experiment geometry is shown in Figure 1. The target had machined cutouts to enable measuring shock arrival time at a target location close to the impact interface (Figure 2). PDV probes, pointed at the cutouts, provided fiducial times for the shock arriving at that sample location. The average arrival time at the cutouts was compared with the arrival time at the center of the sample free surface to determine the shock velocity. Measuring the impact time turns out to be somewhat difficult, as corrections are needed for differences in measured sample thickness at each cutout location, as well as timing corrections to the measured arrival times. For this initial series, some samples were not flat and parallel to required tolerances, so an unknown uncertainty was introduced.

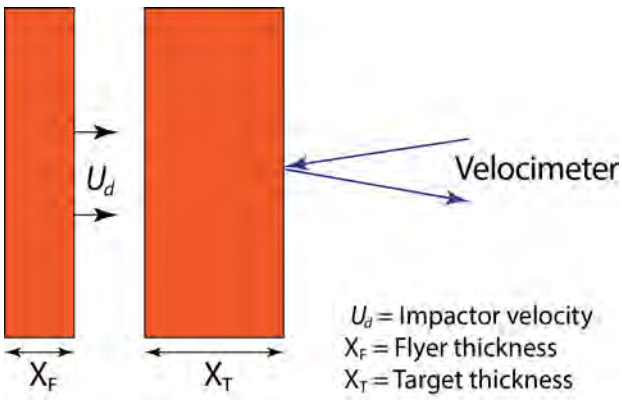

Figure 1. Experiment design

The 38 mm diameter barrel on the second set of experiments allowed us to use larger-diameter (25 mm) samples and impactors, which in turn allowed thicker targets (~4 mm) and impactors (~2 mm). We also abandoned the cutouts on the targets in favor of electrical pins that were flush with the target's impact surface. These changes improved the data quality. Details of all the experiments are given in Table 1, along with preliminary values for measured quantities. Velocities are in km/s. The spall strength shown is an estimate done using the momentum shock jump condition

Figure 2. Copper sample, showing cutouts for measuring shock arrival time at the target used in initial experiments. Impact pins replaced the cutouts in our second series of shots.

$$\sigma_{spall} \cong \frac{1}{2}\rho_0 C_b u_{fs}, \quad (5)$$

where u_{fs} is the measured free surface pullback velocity, and C_b is the bulk sound speed. Peak stress values are calculated using the polycrystalline Hugoniot, $U_s = 3.94 + 1.498\ u_p$.

Typical uncertainty on velocimetry data is ~1% in velocity and ~1 ns in timing. We are still quantifying the real uncertainties in these experiments, so no error bars are shown for them in Table 1.

We note that in an earlier LANL polycrystalline copper spall experiment (called CUSPALL), an estimated spall strength of about 13.5 kbar was obtained for a peak stress of 57 kbar and a sample thickness of 4 mm (Hixson 2015). The larger spall strength for shot 150304 may be a result of its higher strain rate during

Table 1. First analysis of copper experiments. Uncertainties, when determined, are shown in parentheses below the value in the first row.

Experiment (bore diameter)	Target Thickness (mm)	Crystal Orientation	Impactor Velocity, U_d (km/s)	Shock Velocity, U_s (km/s)	Longitudinal Sound Speed, C_L (measured)	Longitudinal Sound Speed, C_L (ultrasonic)	Decrease in Free Surface Velocity δu_{fs} (spall)	Spall Stress, σ_{spall} (kbar)	Peak Stress, σ_{peak} (kbar)
150304 (13 mm)	2.01	Polycrystalline	0.609	4.43	4.75	4.72 (0.023)	0.108	18.95	119.5
150305 (13 mm)	1.928	100	0.608	4.27	4.35	4.410	0.148	25.90	119.30
150306 (13 mm)	2.178	110	0.500	4.22	5.28	5.010	0.107	18.73	96.32
150313 (13 mm)	1.874	111	0.501	4.33	5.34	5.200	0.084	14.70	96.53
150324 (13 mm)	1.684	100	0.502	4.24	4.37	4.410	0.116	20.30	96.74
150325 (13 mm)	2.005	110	0.390	4.59	4.49	5.010	0.126	22.10	73.70
150325-2 (13 mm)	1.994	111	0.384	3.86	5.29	5.200	0.086	15.05	72.49
150819-1 (38 mm)	3.941	100	0.299	4.14	--	4.365	0.093	16.24	55.50
150819-2 (38 mm)	2.050	100	0.600	4.56	--	4.394	0.135	23.57	117.4
150820-1 (38 mm)	3.946	100	0.601	4.38	--	4.362	0.117	20.43	117.7
150820-2 (38 mm)	2.040	100	0.297	3.88	--	4.373	0.115	20.08	55.10
150818-2 (38 mm)	3.949	100	0.281	4.16	↑	4.358	0.091	15.89	52.00

release into tension. This result needs to be checked for reproducibility. We also checked our spall strength results against prior data reported by Minich (2004), whose results are shown in Figure 3.

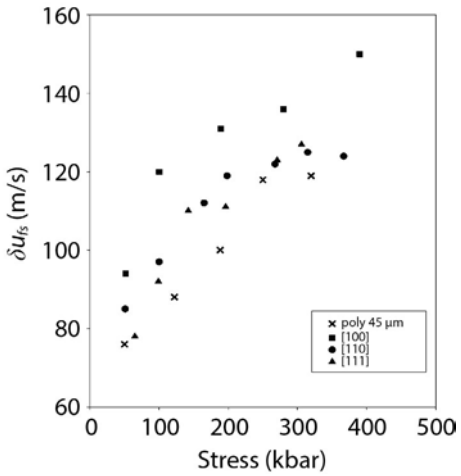

Figure 3. Spall strengths in copper from Minich (2004) show a monotonic increase with stress. The [100] orientation is stronger than polycrystalline or other grain orientations. Data shown as open squares that had silicate impurities increase the number of impurity sites, which affect dislocation dynamic processes.

Our experiments were done at three stress levels, approximately 119, 96, and 73 kbar. Only at the 96 kbar level were all three orientations tested, but no polycrystalline sample was tested at this stress. We note one difference between our results and those of Minich—we used much thinner (2 mm) samples for our first series, whereas Minich used 5 mm samples. Our second shot series used 4 mm samples, which allows a more direct comparison with Minich's work. We might expect our results for thin samples to have a higher strain rate when going into tension and therefore, in general, have a higher spall strength.

[100] Orientation

The [100] time-resolved velocimetry data from the second experimental series, which was done exclusively for this orientation, yielded quality data. (Essentially

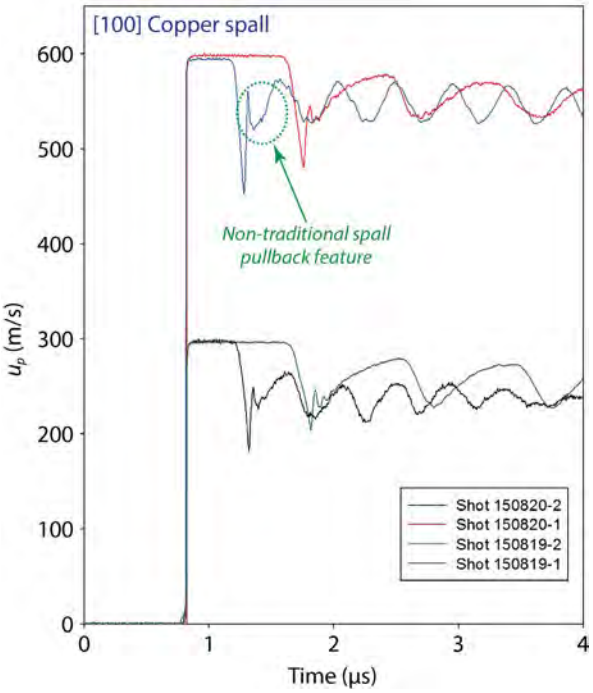

Figure 4. Time-resolved velocimetry for data copper [100] orientation; the non-traditional pullback feature requires further study

all of the data from the first shot series with thinner samples in the [100] orientation had issues and are not shown.) The 4 mm thick samples (150819-1, 150820-1, 150818-2) yielded data of the highest quality, showing good reproducibility and well-defined spall signatures, all of which have a non-traditional pullback signature. Further study will enhance our understanding of this feature. The time-resolved data for this orientation are shown in Figure 4.

The spall signature (Figure 5) was analyzed to find the change in free surface velocity from peak to minimum and compared with Minich's results.

[110] Orientation

In Figure 6 we show a plot of time-resolved velocimetry in the [110] orientation for shot 150306, the only experiment in this orientation in which we have confidence. We can also compare the particle velocity change (pullback) we found to Minich's data for this orientation. The plot in Figure 7 shows that experiment 150306 (present data) agrees reasonably well with Minich's work.

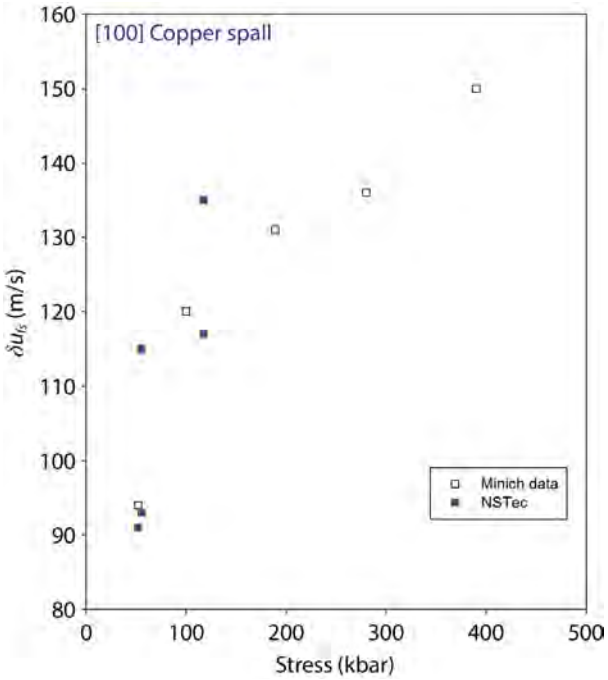

Figure 5. Decrease in free surface velocity between the beginning of stress release and the start of the spall signature (pullback) for the [100] orientation for our August campaign only as compared to Minich (2004)

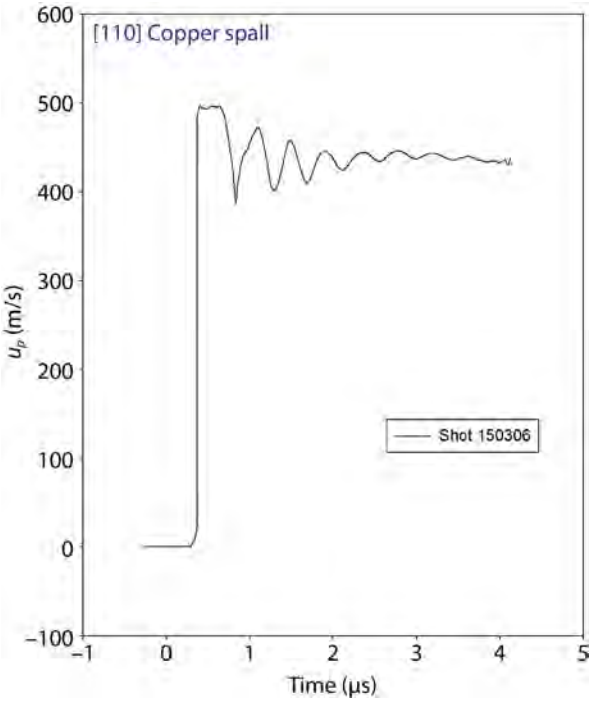

Figure 6. Velocimetry for the [110] orientation for shot 150306

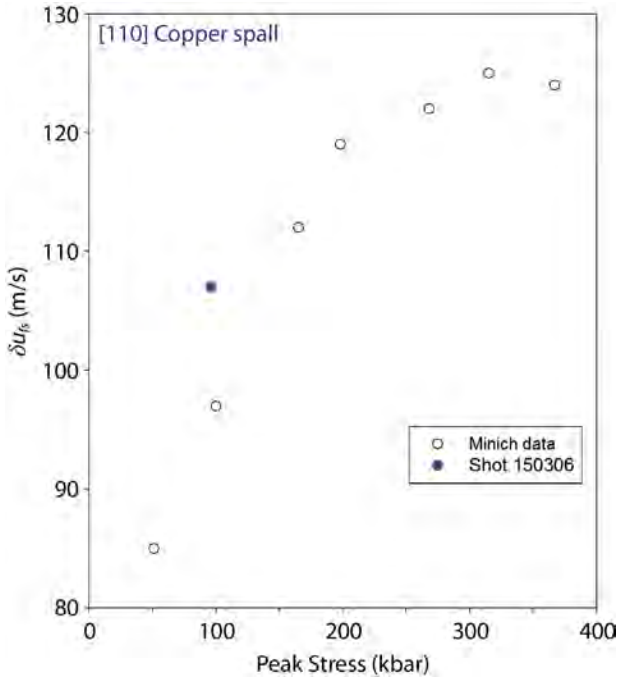

Figure 7. Decrease in free surface velocity between the beginning of stress release and the start of the spall signature (pullback) for the [110] orientation, comparing shot 150306 to Minich (2004)

[111] Orientation

Figure 8 shows a plot of time-resolved velocimetry in the [111] orientation, while Figure 9 compares the measured pullbacks to Minich's data (2004).

For the [111] orientation, we observe the Minich results to show a relatively large increase in spall strength with impact stress. After error bars are assigned, we expect there to be reasonable agreement between our results and that of Minich. We note that this appears to be the weakest orientation for dynamic tension. This conclusion warrants a closer look at the underlying physics. On the other hand, the [100] orientation appears to be the strongest. Perhaps spall in polycrystalline samples depends greatly on the crystals having [111] orientation.

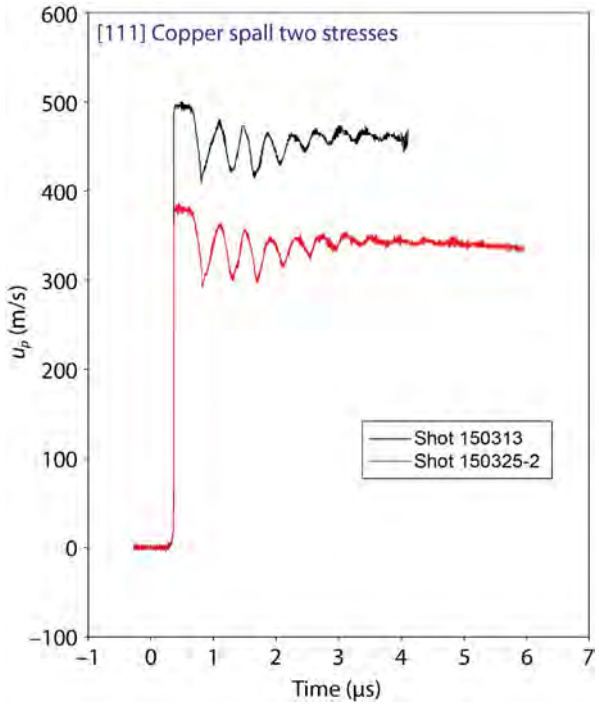

Figure 8. Velocimetry data for the [111] orientation

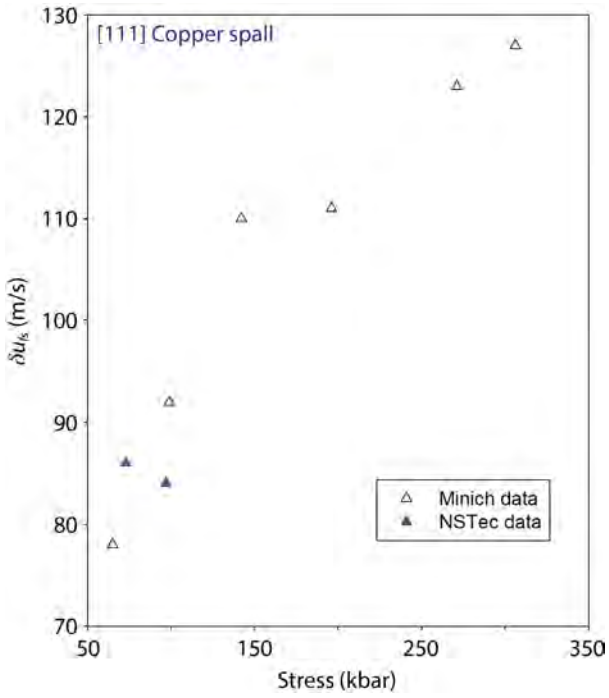

Figure 9. Decrease in free surface velocity between the beginning of stress release and the start of the spall signature (pullback) for the two [111] orientation shots compared to Minich (2004)

Polycrystalline Copper

We performed experiment 150304 on a sample of copper that was 2 mm thick. CUSPALL had been done with half-hard copper but with a 4 mm thick target and a lower peak stress. Grain sizes were not characterized for either. Results are compared in Table 2.

Figure 10 shows data from shot 150304 and the CUSPALL shot, clearly done at different stresses. The spall signature for shot 150304 is much larger than for the older experiment done at lower stress and with a thicker target. Minich's data (2004) show a clear trend of spall strength increasing with peak stress, and we are curious to see how shot 150304 compares to those results. Because we did not do preshot characterization of our polycrystalline copper material, we must assume that the grain size is "nominal" for as-received oxygen-free high thermal conductivity metal. This would place an estimate of grain size at 30–60 μm. Shown in Figure 11 is a plot of our results along with the 45 μm grain results of Minich.

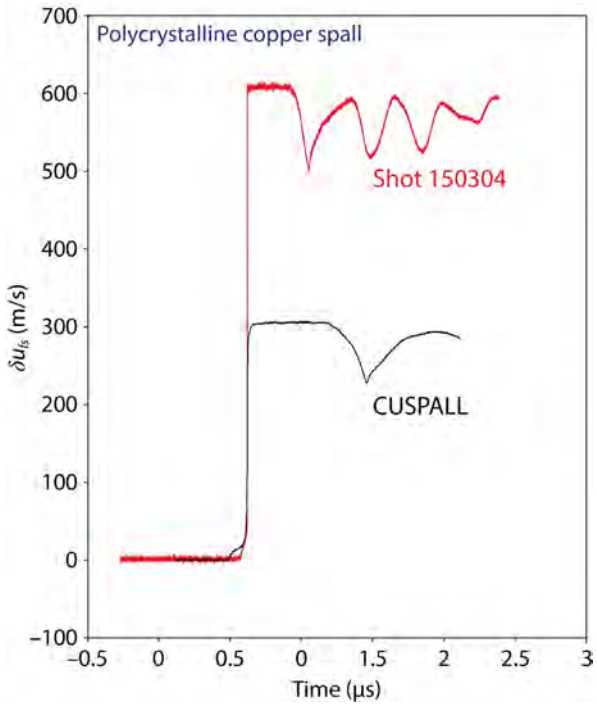

Figure 10. Overplot of polycrystalline time-resolved data

Table 2. Polycrystalline copper data

Shot	Target Thickness (mm)	Impactor Velocity, U_d (m/s)	Peak Stress, σ_{peak} (kbar)	Decrease in Free Surface Velocity, δu_{fs} (m/s)	Spall Stress, σ_{spall} (kbar)
150304	2.01	609.0	119.5	108	18.95
CUSPALL (LANL)	4.00	307.7	57.30	77	13.50

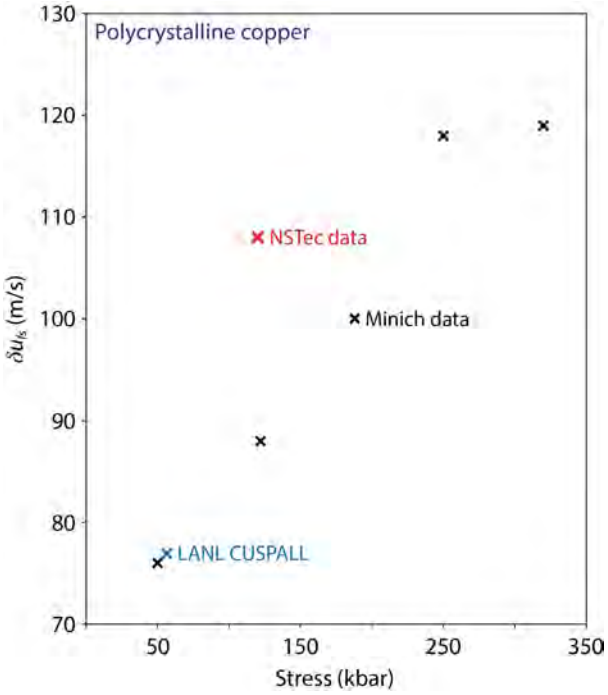

Figure 11. Decrease in free surface velocity between the beginning of stress release and the start of the spall signature (pullback) for polycrystalline copper. Black crosses are from Minich (2004), the red cross is our measurement (120 kbar), and the blue cross is the LANL CUSPALL measurement (57 kbar).

Wave Speed Data

One of the major goals of this project is to determine if either elastic or plastic shock velocities depend upon crystalline orientation. From ultrasonic sound speed measurements (including our own), it is clear that small amplitude elastic waves travel at different velocities in all of the orientations we have studied. Johnson (1974) predicts that plastic waves at low pressure travel at the same bulk sound speed in the [100] and [111] orientation but at a different velocity in the [110] orientation (specifically for the sodium chloride structure). We note that as Johnson says, plastic shock wave velocities approach the bulk sound speed in the low stress regime. The bulk sound speed for many materials is close to the U_s intercept for U_s-u_p Hugoniots. At higher stress, it is less clear what will happen. Chau (2010) concludes that the single-crystal Hugoniot points are the same as the polycrystalline Hugoniot. But Chau's research looked only at relatively high stresses.

We wish to do credible research that sheds light on this issue. But to do so means we need to make very accurate measurements of shock velocity. This is always a challenge, especially at such a low stress. Cutouts were made in our targets to create steps to measure the shock speed in our first experiment series (Figure 2), and impact pins were used for our second series. We performed an initial analysis of wave speeds using the PDV data on the lower steps or impact pins to give a time fiducial that can be combined with the free surface arrival time data to obtain an average shock velocity through the sample. This was our first attempt to do this using these techniques. We compare these data with the polycrystalline Hugoniot from Mitchell (1981) in Table 3. These results are shown plotted with the Mitchell polycrystalline Hugoniot in Figure 12.

Although Johnson (1974) leaves open the possibility that wave speeds may be systematically different in the [110] orientation, the high-pressure work of Chau (2010) concludes that there is no directional dependence, even though at some stress levels their data show scatter that is outside of their stated error bars. Our data show no clear trends, except that we observe three shots with shock velocities that are significantly off of the Mitchell Hugoniot, while all others fall within about 2% of the polycrystalline value. Two of the three shots are in the [100] orientation and one in the [111].

Table 3. Preliminary wave speed results

Experiment	Crystal Orientation	Shock Velocity, U_s (km/s)	Velocity, u_p (km/s)	Shock Velocity, U_s (from Mitchell 1981)	% Difference
150306	110	4.22	0.256	4.31	2.0
150313	111	4.33	0.251	4.31	0.5
150325-2	111	3.86	0.192	4.22	8.6
150820-2	100	3.88	0.148	4.16	6.7
150820-1	100	4.38	0.301	4.38	0.0
150819-2	100	4.56	0.299	4.38	3.9
150819-1	100	4.14	0.149	4.16	0.5
150818-2	100	4.16	0.140	4.14	0.5

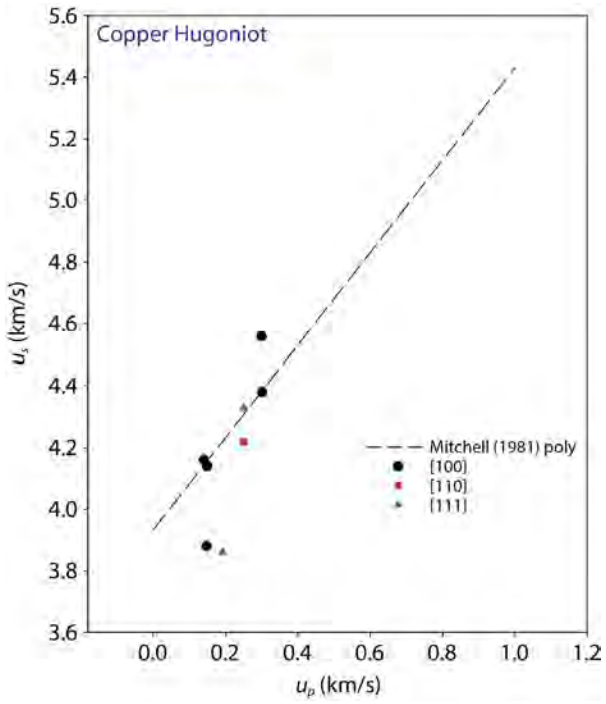

Figure 12. Single-crystal Hugoniot results compared to the Mitchell (1981) polycrystalline data

We may be able to conclude that we are looking at experimental scatter, not systematic differences, but this remains to be verified. We are working on another experimental series that uses a different experimental technique to further explore this issue.

Tin Temperature Measurements

Measurements of both the β to BCT (body centered tetragonal) phase change and melt of shocked tin over a broad range of shock conditions were made by Mabire (2000) by shocking tin with aluminum or copper impactors and observing the velocities of the sample-window (lithium fluoride [LiF]) interfaces. By interpreting structure in the velocity during shock release, they were able to determine the stresses at the times of the phase changes and, using a theoretical equation of state (EOS) to estimate temperatures, calculate a temperature versus pressure phase diagram. Given our recent advances in dynamic temperature measurement techniques, we set out to validate their calculated phase diagram.

To measure the dynamic temperature of a shocked metal accurately enough to impact the EOS, it is necessary to determine more than just the radiance. By adding an emissivity[1] measurement, our group has made state-of-the-art dynamic temperature measurements of ±2% for tin shocked by explosives (La Lone 2013); this uncertainty is much lower than any believable previous measurements of shock temperatures for a metal. However, to obtain a flatter shock wave and to achieve adequate changes in the shock stress

[1] Note that for metals, where the transmittance is 0, the emissivity = 1 – reflectance. We actually measure the dynamic reflectance relative to the (also measured) ambient reflectance.

to study the temperature throughout the phase transition region requires the use of a flat impactor, such as from a gun. Therefore, we began collaboration with the California Institute of Technology (Caltech), where we had access to a gun capable of copper impactor speeds that will melt a tin sample on release. We designed and built a suitable integrating sphere and a pyrometer to field on the gun. With this we began to define the tin melt curve. The skills and experience we gain will enable similar measurements on other metals.

The schematic diagram in Figure 13 illustrates the sample and impactor for the experiments, and Figure 14 is a schematic of the emissivity diagnostic. Radiance measurements were performed using a similar setup but with only two detectors and without an integrating sphere. By choosing the impactor, sample, and appropriate window thicknesses, we can achieve a shock release for which the stress changes slowly enough to enable a measurement of temperature versus stress through a large fraction of the release. After impact the shock travels back through the impactor, releases into a low-impedance material (syntactic foam) separating the impactor from the sabot, and returns to the sample as a rarefaction. As the rarefaction travels, its front spreads out. After sufficient travel distance the front rises slowly (relative to the diagnostic time resolution) at the window interface, causing the stress to release slowly enough to resolve with time. This permits a measurement of emissivity and radiance across a stress range from its peak on the window's Hugoniot at the start of release until either the temperature is too low to measure or the initial shock reaches the back of the window.

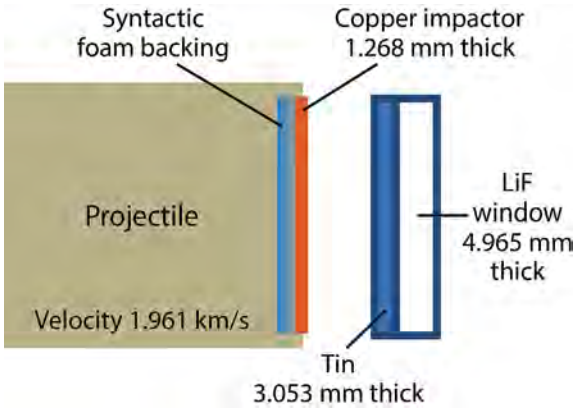

Figure 13. Schematic of the Caltech tin shots showing the flyer and sample just before impact

In FY 2015, we designed experiments to measure the reflectance and radiance of tin as it releases from a shock stress of ~28 GPa, and we fielded a first pair of experiments. Diagnostics include a pyrometer to determine the radiance on the first shot, an integrating sphere (on a separate shot at the same shock conditions as the pyrometer shot) to measure the reflectance, and a PDV velocimeter on both shots to determine the shock stress. The radiance is measured at two wavelengths with fairly wide passbands, 1300 ±175 and 1600 ±100 nm. The radiance is quite

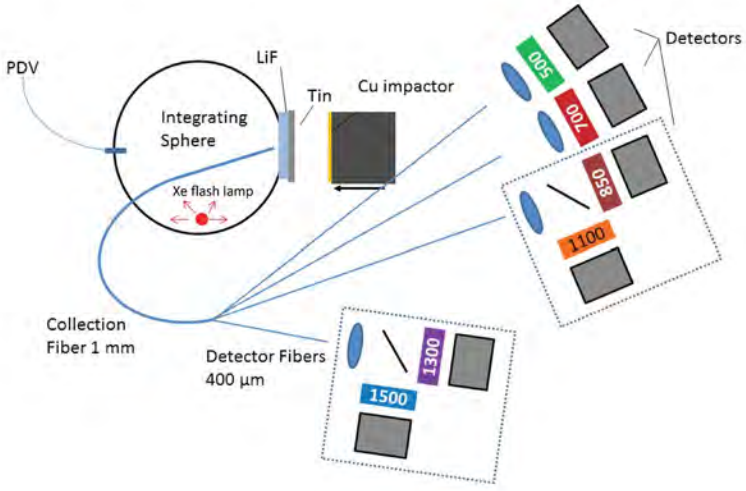

Figure 14. Schematic of the emissivity diagnostic. Light from the xenon flash lamp reflects from the sphere and illuminates the shocked surface prior to, during, and after the phase transition. Light reflected from the tin is collected by a 1 mm fiber and sent to six spectrally filtered photo receivers. The flash lamp is shielded from illuminating the sample directly, so the incident flux is nearly uniform at all angles. The PDV probe is for measuring the velocity of the LiF-sample interface.

low for these temperatures, so the wider bands are used to obtain adequate flux for the temperature determination. The reflectance is measured at six wavelengths with narrower filters (<50 nm wide passbands) to obtain a more detailed spectral emissivity curve at high pressure; the flash lamp provides ample light in all six channels.

Figure 15 shows the ratio of the shocked sample reflectance to the measured ambient value along with the stress derived from the PDV measurement. At shock time the tin transforms almost immediately into the BCT phase, and the emissivity increases 10%–20%, consistent with our prior HE experiments (La Lone 2013). There is a drop in reflectance at around 244.3 μs when the shock release reaches the point where it is thought that the tin melts, about 13 GPa.

From the radiance shot we generated a curve showing the radiance versus time for the two IR wavelengths. Using the *time-averaged* emissivity (1 – reflectance) of Figure 15, we determined the measured temperatures for each wavelength. These results are given in Figure 16. There is very good agreement between the two curves.

Next we combined the two temperature curves, thereby reducing the total temperature uncertainty.

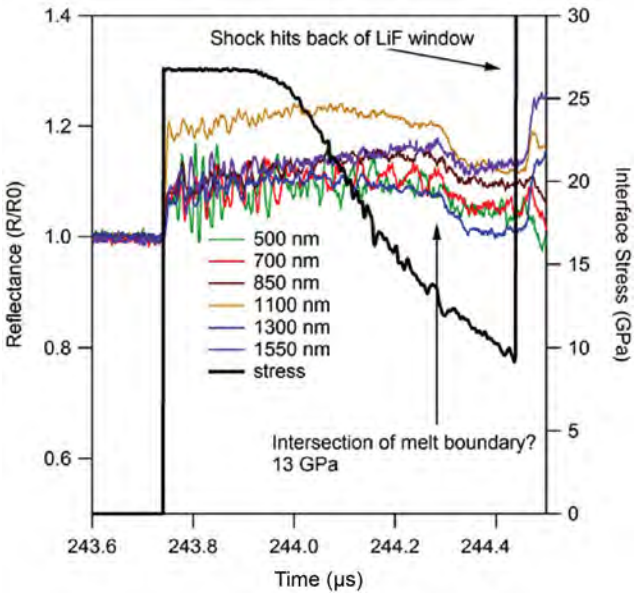

Figure 15. Shock stress (black) and reflectance divided by ambient reflectance (colored curves) measured at the Caltech gun

We plotted this temperature curve versus the experimental shock stress (black curve in Figure 16). We also plotted temperatures that were calculated using the time-dependent emissivity. Those results appear in Figure 17, which also shows Mabire's phase diagram (2000) and the Mabire curve drawn through the Hugoniot as well as the phase change signatures in the

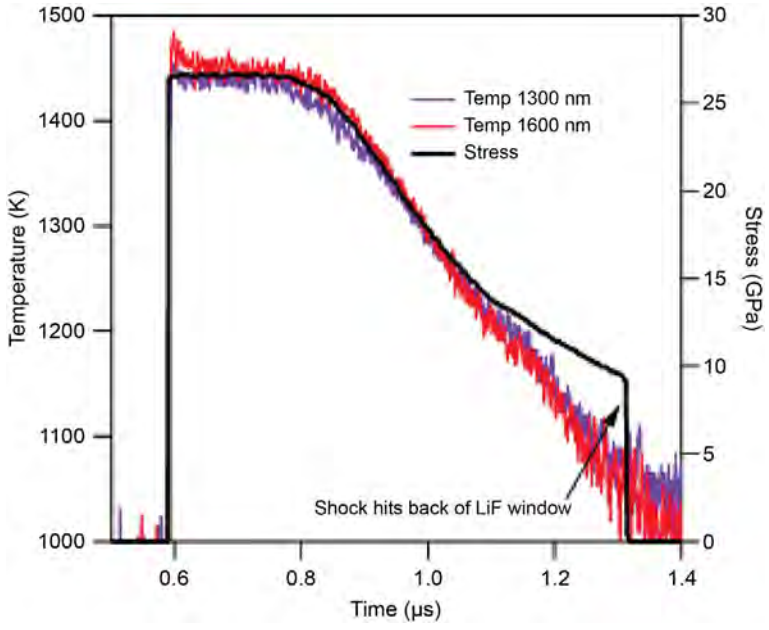

Figure 16. Temperature and shock stress versus time for the first radiance-emissivity shock pair fielded on the Caltech gun. These curves were calculated using a time-averaged emissivity of the dynamic data.

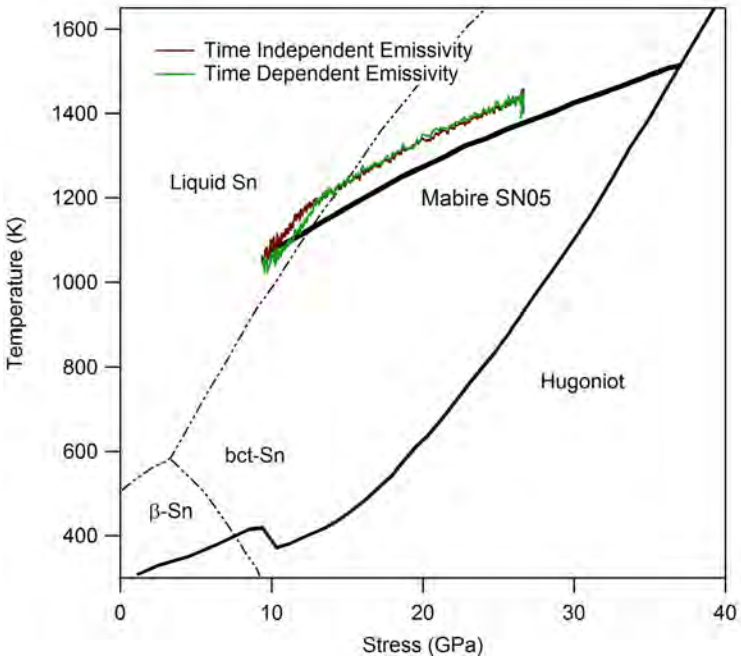

Figure 17. Measured temperatures versus stress for the first Caltech radiance-emissivity pair of tin experiments. The brown curve was calculated using the time-independent emissivity (average dynamic data); the green curve used the measured time-dependent emissivity. The dot-dash lines show the theoretical phase boundaries estimated by Mabire (2000), and the solid black curves are the Hugoniot and a release curve from the same reference. In her work Mabire (2000) did not measure the temperatures, but instead determined the Hugoniot and phase change stresses from their velocimetry data and a theoretical EOS for their temperature data.

velocity measurements of their shot SN05. Our temperatures in Figure 17, which assume a constant value for the emissivity, show a change in slope at 13 GPa, the same stress at which the emissivity suddenly dropped. When we use the time-dependent emissivity curves instead of the constant emissivity, the 13 GPa slope change is even more pronounced.

Below 13 GPa our data follow the shape of the Mabire melt boundary nicely, although they are a little above the Mabire curve. Note that the data points in Mabire (2000) are also a little higher than their melt curve and are more consistent with our data than their calculated phase diagram. In next year's research we will do experiments at a variety of stress and temperature states to determine the shape of the melt curve over a larger stress range. In future radiance measurements we will also use a thicker window to allow us to track the release to a lower stress state.

Gallium Phase Change Studies

Gallium metal can be melted at a relatively low shock pressure, about 200 kbar, and it also is predicted to have two solid-solid phase changes in this region. The EOS has been calculated at LANL (Crockett 2009). It is complicated, but its complexity makes Ga useful for measuring phase kinetics of metals. Figure 18 shows the calculated phase diagram and Hugoniot curves for shocks beginning with solid and liquid metal.

In FY 2015 we obtained the tabular EOS (Crockett 2009) from LANL and converted it into a form that can be read by the hydrodynamics modeling code CTH (McGlaun 1990). Although for the Ga phase change model we do not now have the inherent multi-phase capability (called PTRAN) in CTH, the code should handle the phase information in the Ga EOS table. We have begun to run CTH to try to understand how we can make measurements to verify the EOS. Figure 19 shows the calculated interface velocity for a simulated shot using a copper impactor moving at 400 m/s to shock a solid Ga sample backed by a LiF window to ~5 GPa. Inspection of the phase diagram in Figure 18 indicates that at 5 GPa the Hugoniot curve is on the boundary between phases Ga II and Ga III. Assuming the release is roughly along the Hugoniot, the phase would appear to change to Ga I around 1.5 GPa. With more impact speed we should be able to melt the Ga.

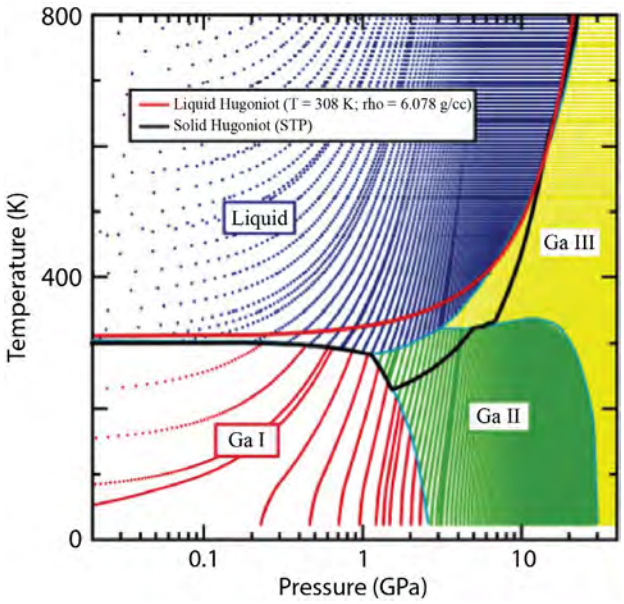

Figure 18. Calculated gallium phase diagram from Crockett (2009). Superimposed are the liquid (red) and solid (black) shock Hugoniot curves.

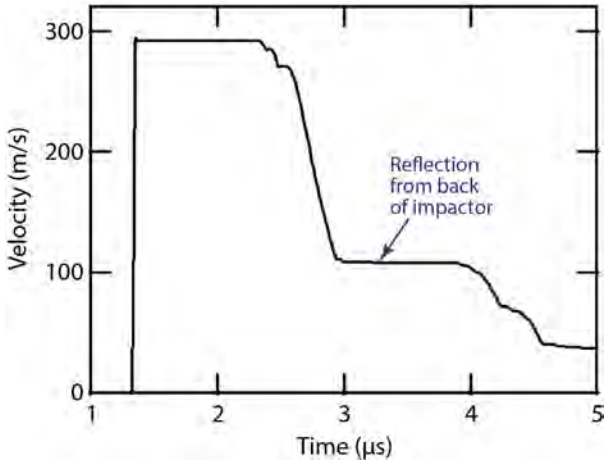

Figure 19. Calculated Ga-LiF interface velocity for a 4 mm thick Ga sample with a LiF window shocked by a 3 mm copper flyer moving at 400 m/s. At 2.5 μs a release wave (rarefaction) from the back of the copper reaches this interface. Note that the release in the Ga is not complete at this time because part of the rarefaction is reflected as a shock at the copper-Ga interface.

Conclusion

Work has progressed well on the acquisition of a new propellant launcher; we expect it to be delivered and installed in 2016.

Initial results on the dynamic properties of single-crystal copper have been obtained on both the 13 mm bore launcher and the 38 mm launcher at STL. Good wave profile and shock speed data were obtained for an initial experiment series using new diagnostic systems and techniques. As usual, some questions have come up in the analysis of results, and experiments need to be checked for reproducibility. Measured spall signatures agree well with those of Minich (2004), and all shots in the [100] orientation show the unusual spall pullback signature that was also seen by Minich (2004). Wave speed results may be suffering from relatively large scatter in some of the experiments, and these results need to be checked for reproducibility. New experimental techniques will also be developed to try to increase accuracy. Our initial results show no discernable trends with orientation.

We also note that work is ongoing to improve dimensional tolerances for targets and impactors to improve metrology and better characterize materials tested. For copper we need to develop a way to anneal samples, to measure grain structure and size for polycrystalline samples, and to double check orientational accuracy of single-crystal samples. Although we can check the overall orientation by using ultrasonic sound speed techniques, this method will not help characterize small deviations.

We have obtained very good temperature (from 1000 K to 1400 K) data on tin that agrees well with the center of the Mabire (2000) phase diagram with temperatures; stresses measure from about 9 to 27 GPa. We plan to continue this work in FY 2016 to map out more of this calculated EOS. The resulting techniques will enable similar temperature measurements in the phase change regime for other metals.

We have begun to design a series of gallium shots with the goal of eventually learning to study very complex metals.

References

Chau, R., J. Stölken, P. Asoka-Kumar, M. Kumar, N. C. Holmes, "Shock Hugoniot of single crystal copper," *J. Appl. Phys.* **107** (2010) 023506-1–023506-6.

Crockett, S. D., C. W. Greeff, "A gallium multiphase equation of state," *AIP Conf. Proc.* **1195** (2009) 1191–1194.

Hixson, R. S., private communication, 2015.

Johnson, J. N., "Wave velocities in shock-compressed cubic and hexagonal single crystals above the elastic limit," *J. Phys. Chem. Solids* **35**, 5 (1974) 609–616.

Jones, O. E., J. D. Mote, "Shock-induced dynamic yielding in copper single crystals," *J. Appl. Phys.* **40** (1969) 4920–4928.

Kanel, G. I., S. V. Rasorenov, V. E. Fortov, "The dynamic strength of copper single crystals," in *Shock-Wave and High-Strain-Rate Phenomena in Materials*, M. A. Meyers., L. E. Muir, K. P. Staudhammer, eds., Marcel Dekker, New York, 1992, 775–782.

La Lone, B. M., G. D. Stevens, W. D. Turley, D. B. Holtkamp, A. J. Iverson, R. S. Hixson, L. R. Veeser, "Release path temperatures of shock-compressed tin from dynamic reflectance and radiance measurements," *J. Appl. Phys.* **114** (2013) 063506-1–063506-14.

Mabire, C., P. L. Héreil, "Shock induced polymorphic transition and melting of tin up to 53 GPa," *J. Phys. IV France* **10** (2000) 749–754.

McGlaun, J. M., S. L. Thompson, M. G. Elrick, "CTH: A three-dimensional shock wave physics code," *Int. J. Impact Eng.* **10** (1990) 351–360.

Minich, R. W., J. U. Cazamias, M. Kumar, A. J. Schwartz, "Effect of microstructural length scales on spall behavior of copper," *Metallurgical and Materials Transactions A* **35**, 9 (2004) 2663–2673.

Mitchell, A. C., W. J. Nellis, "Shock compression of aluminum, copper, and tantalum," *J. Appl. Phys.* **52** (1981) 3363.

Schwartz, A. J., J. U. Cazamias, P. S. Fiske, R. W. Minich, "Grain size and pressure effects on spall strength in copper," *AIP Conf. Proc.* **620**, 1 (2002) 491.

This page left blank intentionally

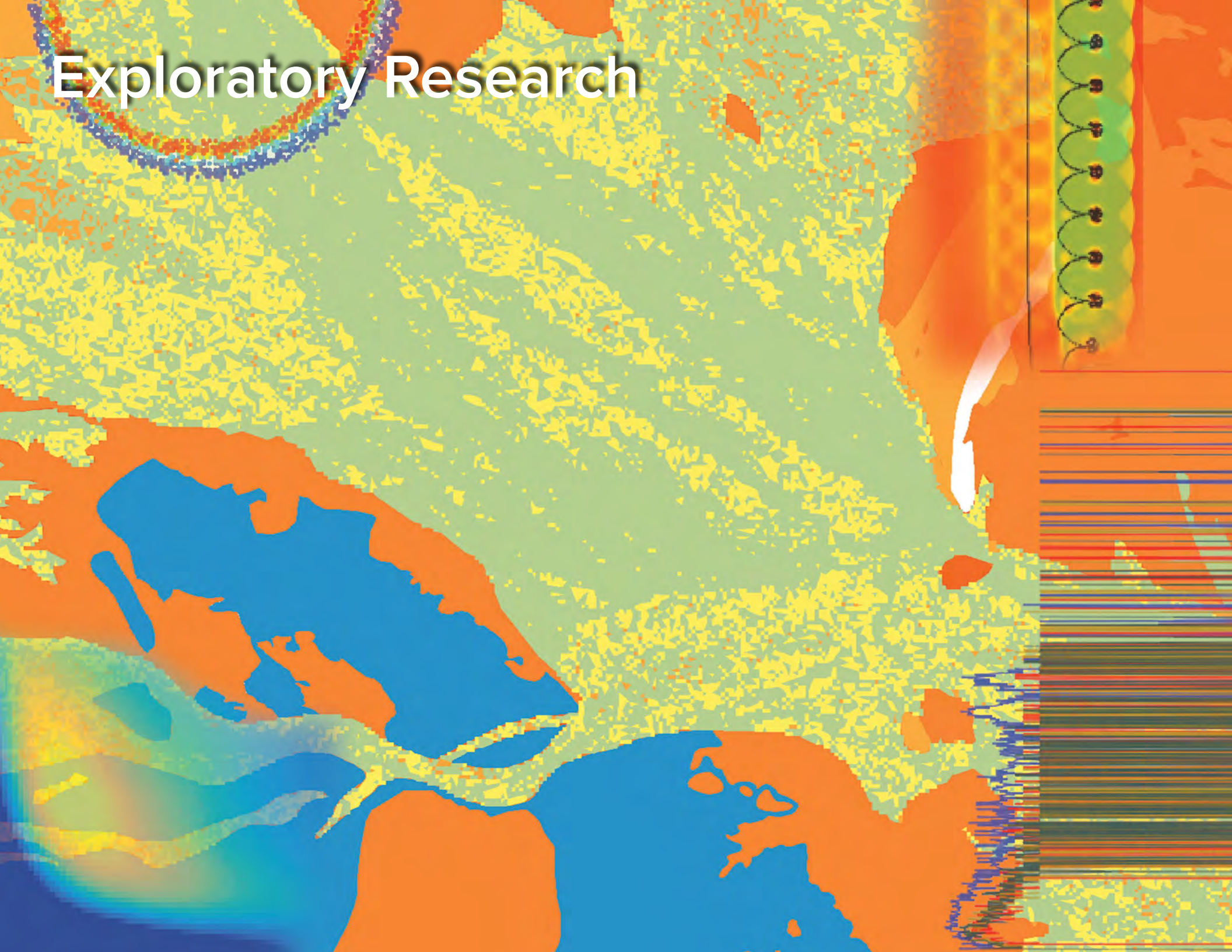
Exploratory Research

Grain-Selective MPDV Experiments

NLV-08-14 | Continued from FY 2014 | Year 2 of 2

Edward Daykin,[1,a] Mike Grover,[b] Robert S. Hixson,[c] Brandon La Lone,[b] Carlos Perez,[a] Gerald D. Stevens,[b] O. Ted Strand,[c] and Dale Turley[b]

Experimental investigations of 2-D spall structure in single-crystal copper and a copper-lead mixture were conducted using multiplexed photonic Doppler velocimetry to quantify dynamic response. We conducted planar impact experiments on single-crystal copper in the [100] orientation to further investigate recently observed shockwave behavior. These experiments confirmed a spall signature unique to the [100] orientation of copper and demonstrated consistent dynamic material response across a 2-D sample area. Explosively driven "spall-recompression" experiments were also conducted on samples of a 1% lead-doped copper metallic mixture. Velocimetry measurements reveal notably different spall behavior for these samples as compared to pure, polycrystalline copper. Velocimetric techniques developed during the first year of this project (Daykin 2015) were leveraged and further expanded during these experiments to include use of two-fiber optical probes and a fiber-optic "pin" to simultaneously measure impactor time of arrival and velocity on gas gun experiments. Experimental methods and results from these investigations are presented in this report.

[1] daykinep@nv.doe.gov, 702-295-0681
[a] North Las Vegas; [b] Special Technologies Laboratory; [c] New Mexico Operations–Los Alamos

Background

The study of shock wave behavior on polycrystalline materials that originated in FY 2014 was expanded in FY 2015 to include investigations of spall in single-crystal copper as well as spall and recompression in a metal alloy of 1% lead-doped copper (Cu:Pb). We built upon the research done in FY 2014 (Daykin 2015) by moving toward a 2-D investigation of the spall process in metals while varying the metal microstructure. Measurement of surface velocities across a 2-D area of a given material under test was made using the Gen-1 multiplexed photonic Doppler velocimetry (MPDV) system. We chose copper as our sample material because it has a relatively high degree of anisotropy and single crystals of it are available in several orientations. The NSTec Special Technologies Laboratory (STL) gas gun and Boom Box experimental facilities were employed to shock compress these samples and measure spall behavior.

In addition to the investigation of shock wave behavior in metals, further development of MPDV diagnostic techniques was accomplished during the course of this project. We extended the utility of multiplexing to gas gun platforms with specialized requirements. For example, these experiments typically require fewer than a dozen data channels of optical velocimetry. However, gas gun experiments include diagnostic requirements to measure impactor velocity, impactor tilt, and relative time of arrival necessary to calculate shock speed. Samples may also be polished to a specular surface finish—all of which is a challenge for PDV. This SDRD project served to develop diagnostic methods that address these challenges and also provided a strategic benefit by collaborating with other SDRD efforts, including "Enhanced Dynamic Materials Research" (Hixson 2016) and "Dynamic

Recompression of Damaged Materials" (Turley 2015), as well as making contributions to improved NSTec experimental capabilities.

Project

Two experimental campaigns accomplished in FY 2015 are summarized in Table 1. Experiment Campaign #1 contrasted spall and recompression in (pure) polycrystalline copper to the spall behavior of Cu:Pb. These experiments employed a high-explosive drive along with MPDV diagnostics methods we developed last year (Daykin 2015) to quantify spall behavior. The lead-doped copper experiments uncovered a distinct difference in material strength and spall signature as compared to polycrystalline copper. Experiment campaign #2 sought repeatability and 2-D heterogeneity in single-crystal [100] copper spall using plate impact experiments. We chose the [100] grain orientation due to a previously reported (Minich 2004, Chau 2010) spall signature—a spike following release—that differed from that of other copper grain orientations but had yet to be repeated or investigated in 2-D.

Experiments on pure polycrystalline copper and 1% lead-doped copper were conducted using Detasheet high-explosive drive to generate spall. Single-crystal copper spall experiments were conducted via planar impact using a 1.5" diameter gas gun. Both experiment campaigns were executed at NSTec STL facilities.

Lead-Doped Copper (Cu:Pb) Boom Box Experiments Compared to Pure Copper

We conducted exploratory investigations to quantify the 2-D spall processes in shocked metals using MPDV diagnostic techniques developed in FY 2014 (Daykin 2015). These experiments were conducted to further investigate phenomena discovered during a previous SDRD project (Turley 2015), which employed an explosive (Taylor wave) drive and soft recovery experimental method to investigate the hypothesized occurrence of spall-recompression in metals (Turley 2016). In this campaign we conducted several experiments with a 1% lead-doped copper mixture with softened grain boundaries acquired from Los Alamos National Laboratory (LANL) (R. Gray). We wished to test the effects of the lead dopant on metal strength and evaluate heterogeneity of the spall process.

Experiments on polycrystalline copper and Cu:Pb had a range of sample thicknesses (Table 1) to generate conditions from complete spall scab separation to full spall recompression. The Gen-1 MPDV system provided a 2-D measurement grid across the sample. High-speed radiography provided corroborating evidence of spall behavior. Velocimetry traces demonstrating formation of the spall layer followed by recompression in pure polycrystalline copper are shown in Figure 1 along with representative 2-D maps of the MPDV measurement points and spall recompression times. This analysis

Table 1. Summary of FY 2015 experiments

Experiment Campaign #1 HE Drive of Polycrystalline Copper vs. 1% Lead-Doped Copper		Experiment Campaign #2 Plate Impact of Single-Crystal [100] Copper	
Sample Material	Sample Thickness (mm)	Impactor Velocity (m/s)	Sample/Impactor Thickness (mm)
Pure copper	0.5	297	2.037/1.0
Pure copper	1.0	601	3.949/2.0
Pure copper	1.9	600	2.048/1.0
Pure copper	3.0	299	3.939/2.0
Pure copper	4.3	281	3.957/2.0
1% lead-doped copper	2.0	--	--
1% lead-doped copper	4.0	--	--

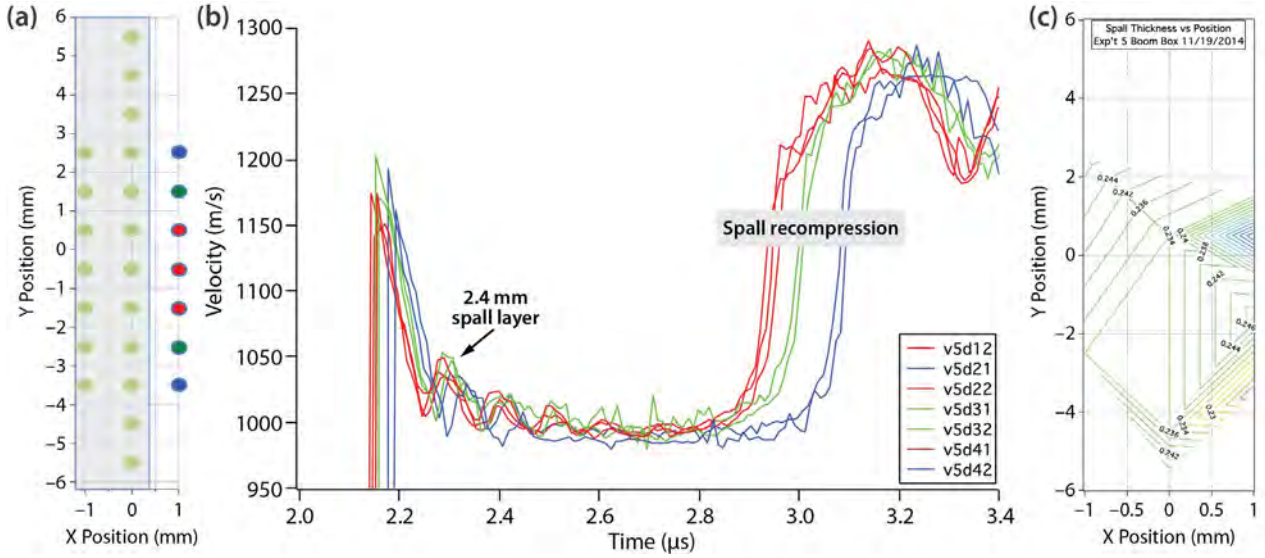

Figure 1. Spall and recompression in 1 mm thick polycrystalline copper measured in 2-D. (a) MPDV target locations on the face of the sample. (b) Several velocimetry traces demonstrating spatial dependence of spall and recollection times. (c) 2-D map of spall layer thickness as a function of position on the sample.

methodology allows for the quantification of material heterogeneities and/or non-uniformities in explosive drive.

Comparison of the spall signatures in pure copper and Cu:Pb are shown in Figure 1, and Figure 2 shows radiographs from three of the experiments. Velocimetry data indicate the spall strength is reduced in the Cu:Pb. It is worth noting that the clearly evident oscillatory ringing that follows release in pure copper is marginally (or not at all) evident in the lead-doped copper. The data suggest a jagged spall plane and/or fragmented spall layer, which is further supported by the radiograph of the 4 mm Cu:Pb sample.

Single-Crystal Copper Symmetric Impact Gas Gun Experiments

Material response to a uniaxial shock wave may exhibit a directional dependence on grain orientation for highly anisotropic material such as copper (Hixson 2016). Recent investigations to measure shock

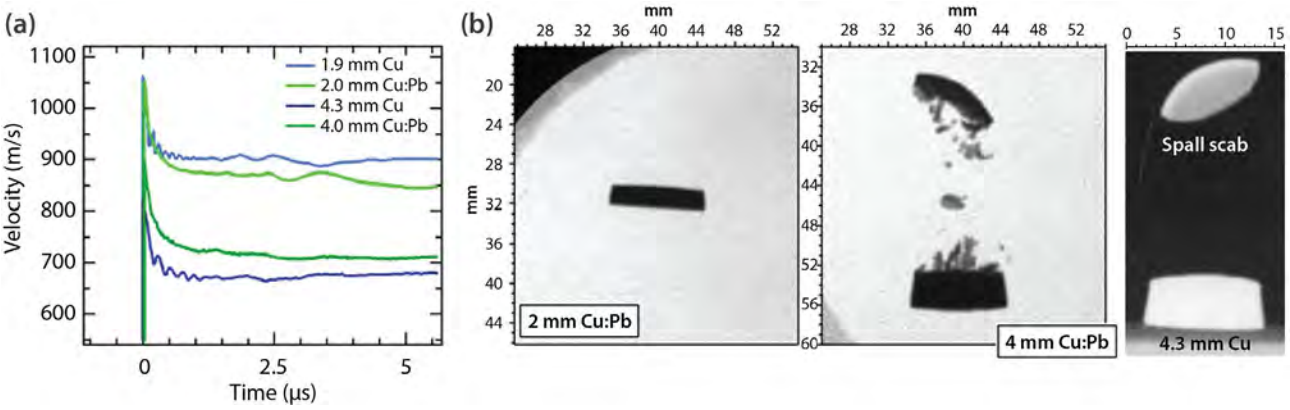

Figure 2. (a) Comparison of spall behavior of pure polycrystalline copper vs. 1% lead-doped copper. Reduced spall strength and damped ringing in Cu:Pb is evident from velocimetry. (b) Radiographs demonstrate no spall separation in 2 mm Cu:Pb, significant fragmentation between the sample and spall plane in 4 mm Cu:Pb, and a "clean" spall plane in pure copper.

Hugoniot and spall behavior in single-crystal copper have resulted in the observation of interesting spall behavior—a spike following the initial pullback. We conducted experiments to confirm the presence of this signature at several shock stresses and across a 2-D cross section of the sample.

Samples of 1" diameter, single-crystal copper in the [100] orientation were procured from MTI Corporation for these experiments. Symmetric impact gas gun experiments were conducted using a like-oriented single-crystal copper impactor and sample. Copper samples were polished to a specular surface finish, measured to be flat and parallel to better than 0.1% of the sample thickness, and verified to be in the [100] orientation by ultrasonic sound speed measurement. Free surface velocimetry was measured using the MPDV system configured to provide seven measurements of surface velocity; one probe was located at the center of the copper disk and the other six distributed in 60° increments at a radius of 5 mm. We also measured impactor velocity during each experiment via a stand-alone probe located on the outside edge of the copper sample and aimed down the gun barrel at the 1.5" diameter impactor.

Representative velocimetry profiles and analysis from each of the five single-crystal experiments are shown in Figure 3. The velocity spike following release may be seen on each of these measurements. Another topic of interest is the spall strength, which is proportional to the pullback velocity Δu_{fs} (difference in free surface velocity between the first plateau and the first trough) as plotted in Figure 3b as a function of stress. The spike following the release trough in the velocimetry data is unique to the [100] orientation and proved repeatable in each experiment as well as across a 2-D area of the sample. Implications and further analysis of this data will be undertaken within the "Enhanced Dynamic Materials Research" on page 15.

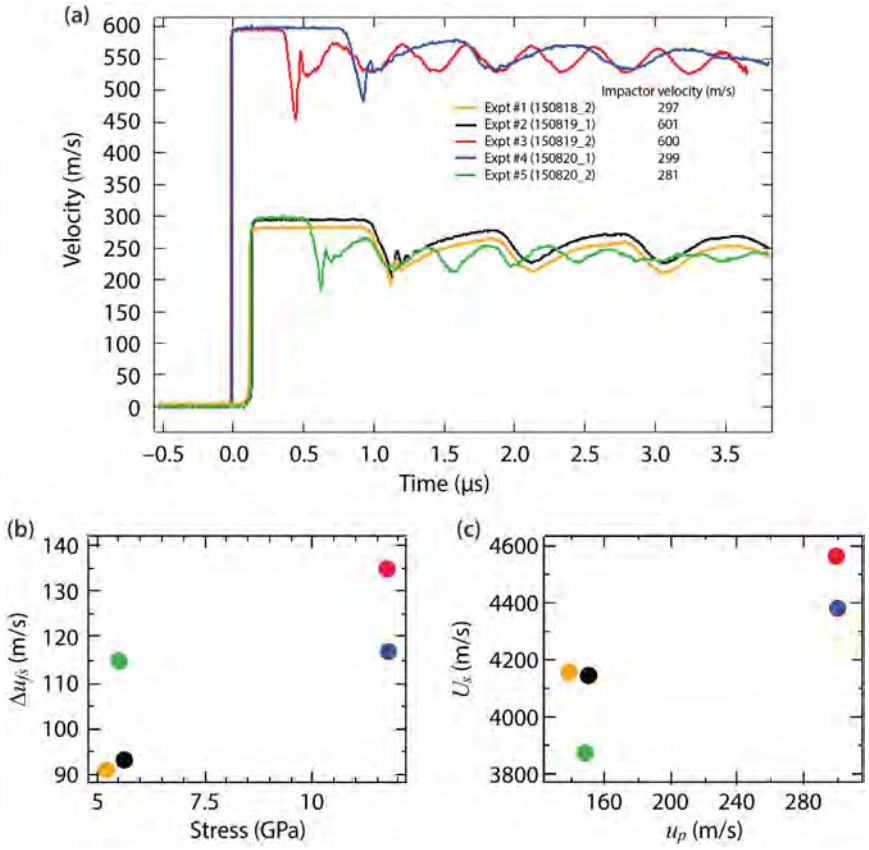

Figure 3. Data from single-crystal [100] copper gas gun experiments. (a) Typical velocimetry time histories from each of the five experiments. (b) Spall strength is proportional to the pullback velocity Δu_{fs}. (c) The Hugoniot is plotted as U_s-u_p.

Diagnostic Development of Velocimetric Techniques for Gas Gun Experiments

For precise determination of shock wave properties during a gas gun experiment, we require in situ measurements of impactor velocity, impactor tilt, and time of impact relative to the free surface measurements. The impactor velocity is often measured by a dedicated PDV probe located radially outside of the sample and viewing down the gun barrel. The conventional method to measure impactor tilt is by electrical shorting pins (Dynasen CS2-50-300). The electrical shorting pins are glued into clearance holes that are located on the perimeter of the sample at regular angular intervals (90° in our case). The shot package—consisting of the copper sample and electrical pins—is then polished to create a flat impact surface. The electrical shorting pins and the velocimetry system are cross-timed such that pin-to-pin and pin-to-velocimetry data may be reconciled to a common time base. Shot data are then analyzed to provide impactor tilt (from the variation in pin shorting times) and time of impact (from their average times).

Using the many PDV channels provided by our MPDV system, we evaluated the performance of a new diagnostic technique: the ability to simultaneously measure both impactor tilt and velocity using a fiber-optic "pin" in place of an electrical shorting pin and the stand-alone PDV probe. The fiber pin consisted of an un-lensed, flat-polished fiber inserted into a clearance hole in the copper sample in place of the electrical pin. This fiber pin was connected to an MPDV channel to measure both impactor velocity (just prior to impact) as well as precise time of impact on the same recording system that measures free surface velocities, thus providing convenient and precise cross-timing. A diagnostic challenge to this measurement is the ~4% optical reflection generated at the flat polished fiber end-face. Laser illumination reflected from this surface acts as a dominant PDV reference source, which not only makes heterodyne (frequency) shifting difficult but can also saturate the photodetector. We accomplished this measurement by dedicating one of the MPDV multiplexed time windows to collecting this data and operating that MPDV channel in a homodyne mode (without frequency multiplexing).

The spectrogram and raw digitizer data from a fiber-optic pin measurement are shown in Figure 4, demonstrating the ability to simultaneously measure impactor velocity and high-precision (sub-nanosecond) time of arrival.

We also desired to measure the elastic precursor shocks with improved precision. Measurement of an elastic precursor is a challenge for any PDV system due to the relatively small changes in velocity over a short time. These measurements may be further degraded due to the biasing effect of the nearby frequency content in an extended baseline. Elimination of the extended baseline from the spectrogram allows

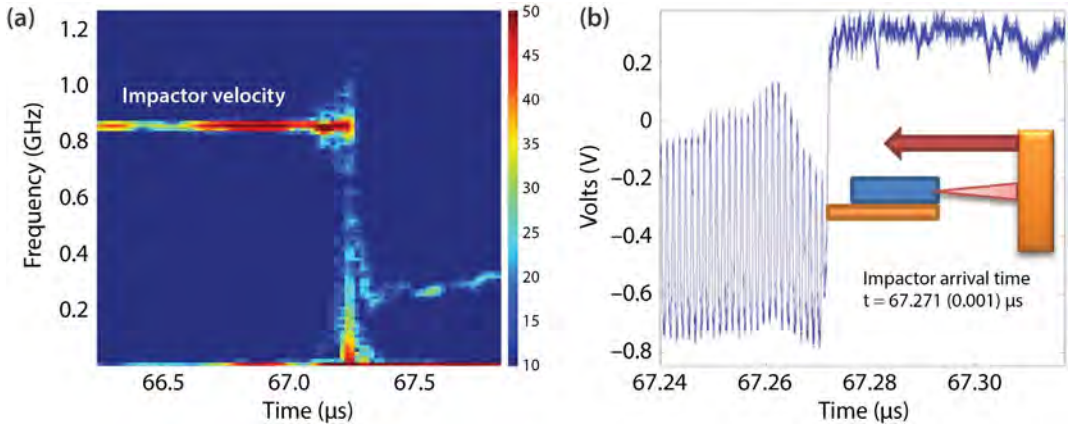

Figure 4. Diagnostic development of MPDV demonstrates simultaneous measurement of (a) gas gun impactor velocity and (b) time of arrival using a single PDV fiber pin

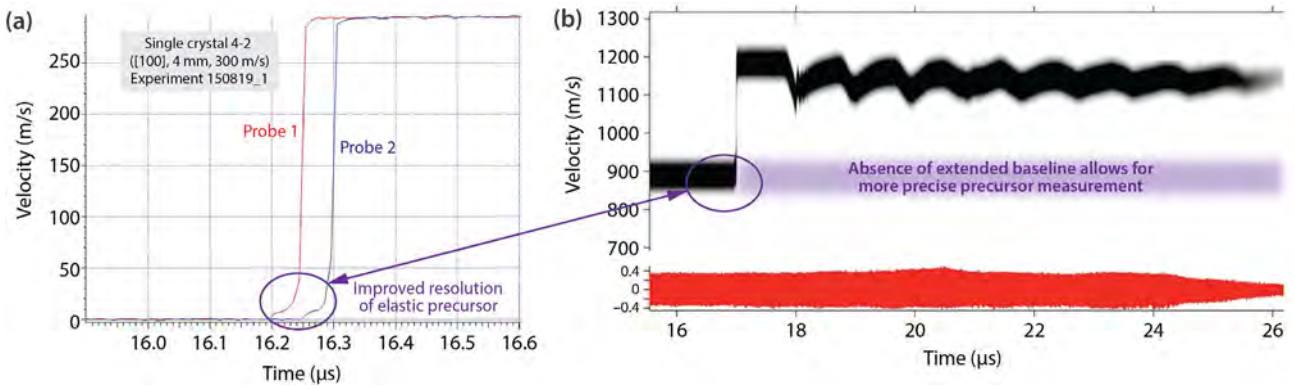

Figure 5. (a) Velocity record and (b) spectrogram demonstrate improved data fidelity of elastic precursor measurement by using separate input and collection fibers to prevent occurrence of an extended baseline in the spectrogram

for improved precision of this measurement. The extended baseline occurs when sources of laser illumination "leak" into the signal path, usually due to probe back-reflections or component leakage. Also, for these experiments the copper samples were polished to a specular finish during initial preparation; however, we did not then roughen the surface finish as is typically done. This polishing method provides a strong signal return helpful to data fidelity, but the combination of a specular surface and single-fiber probes is cumbersome and challenging as it requires the probe's optical vector remain precisely orthogonal to the target surface after shock breakout. We employed two-fiber probes without lensing—target illumination in one and reflected light collection, based on overlap of fiber-optic numerical aperture, in the other—as a simple and inexpensive method to mitigate probe pointing issues and further ensure extinction of the extended baseline. Figure 5 demonstrates a spectrogram free from extended baseline, allowing improved resolution of the elastic precursor. This approach does, however, limit the user to surface motion measurements of only a few millimeters before the spot overlap is gone, and it either reduces the MPDV channel count by 2x or requires an additional laser configuration. Nevertheless, this is a useful technique for a large number of shock wave investigations on gas guns.

Conclusion

We successfully executed experiments to investigate 2-D spall processes on copper while increasing the complexity of the microstructure from single crystals to polycrystals to metallic alloys. Planar impact experiments were conducted on [100] single-crystal copper using the 1.5" NSTec/STL gas gun. This experimental campaign demonstrated repeatability of the spall signature for the [100] grain orientation and confirmed previous measurements of grain-dependent spall behavior. A consistent material response to planar impact across a 2-D cross section of the single-crystal copper samples was observed on each of these experiments. Explosively driven experiments demonstrated reduced spall strength and damped spall ringing in a 1% lead-doped copper alloy as compared to pure polycrystalline copper. Radiographs reinforce this behavior; fragmentation was seen between the sample and spall plane in this copper alloy. To the best of our knowledge, this is the first report of dynamic response to an explosive triangular drive for such an alloy. To support these investigations, MPDV was used and diagnostic techniques were further developed to improve data fidelity through elimination of the extended baseline. The use of MPDV also allowed simultaneous measurement of impactor velocity and time of arrival on gas gun experiments. This project

also provided collaborative contributions to concurrent SDRD projects (Turley 2015, Hixson 2016) and assisted in further development of NSTec shock wave experimental capabilities.

Acknowledgment

We would like to thank Rusty Gray of Los Alamos National Laboratory for his contributions to this work.

References

Chau, R., J. Stölken, P. Asoka-Kumar, M. Kumar, N. Holmes, "Shock Hugoniot of single crystal copper," *J. Appl. Phys.* **107** (2010) 023506-1–023506-6.

Daykin, E., M. Grover, R. S. Hixson, B. La Lone, C. Perez, G. Stevens, O. T. Strand, D. Turley, "Grain-selective MPDV experiments," in *Site-Directed Research and Development*, FY 2014, National Security Technologies, LLC, Las Vegas, Nevada, 2015, 1–9.

Hixson, R. S., B. La Lone, G. D. Stevens, D. Turley, L. Veeser, "Enhanced dynamic materials research," in *Site-Directed Research and Development*, FY 2015, National Security Technologies, LLC, Las Vegas, Nevada, 2016, 15–29.

Minich, R. W., J. U. Cazamias, M. Kumar, A. J. Schwartz, "Effect of microstructural length scales on spall behavior of copper," *Metallurgical and Materials Transactions A* **35**, 9 (2004) 2663–2673.

Turley, W. D., et al., "Dynamic recompression of damaged materials," in *Site-Directed Research and Development*, FY 2014, National Security Technologies, LLC, Las Vegas, Nevada, 2015, 45–58.

Turley, W. D., G. D. Stevens, E. P. Daykin, R. S. Hixson, B. M. La Lone, C. Perez, P. A. Rigg, L. R. Veeser, "Recompression of high-explosive induced shock damage in copper," to be published.

This page left blank intentionally

Characterization of Shock Propagation and Failure Mechanisms in Composite and Additive Manufactured Materials

NLV-16-15 | Year 1 of 1

Thomas Graves,[1,a] Robert S. Hixson,[a] Edward Daykin,[b] Cameron Hawkins,[b] Zach Fussell,[b] Austin Daykin,[b] Michael Heika,[b] Brendan O'Toole,[c] Mohamed Trabia,[c] Shawoon Roy,[c] Richard Jennings,[c] Melissa Matthes,[c] Eric Bodenchak,[c] and Matthew Boswell[c]

The unique contribution of this research is the introduction of experimental and simulation techniques for understanding the behavior of additive manufactured (AM) titanium under shock loading. This is achieved by conducting a series of ballistic impact experiments with a two-stage light gas gun on titanium targets using photonic Doppler velocimetry diagnostics to measure free surface velocity on the back of each target. The experimental measurements are used to validate computational simulations that describe the behavior of these advanced materials under shock. This approach has been used to successfully verify the material models and equations of state used in computational simulations of ballistic experiments with homogeneous target materials (Wang 2013). This work specifically focused on AM titanium and single and multilayered stacks of forged titanium. It was determined that all three materials produce similar velocity profiles during the early stage of impact, with the AM targets exhibiting spall at lower velocities and the multilayered stacks exhibiting vibrations between plates.

[1] graveste@nv.doe.gov, 505-663-2009
[a] New Mexico Operations–Los Alamos; [b] North Las Vegas; [c] University of Nevada, Las Vegas

Background

There is considerable excitement regarding additive manufactured (AM) metals and alloys; however, significant differences between conventional and AM-processed materials have been found. For example, their microstructural morphology and quasi-static mechanical response are significantly different (Needler 2012, Phelps 2013) from non-AM materials. These materials are of particular interest to NNSA, but many outstanding materials science questions still exist regarding them. Additionally, composites are of interest in light of past experiments that explored failure mechanisms of single and double layers of the same material, with the total thickness remaining constant (Becker 2014, Peña 2015).

NSTec and the University of Nevada, Las Vegas (UNLV) partnered to characterize the shock propagation and failure mechanisms in composite (layered titanium) and AM titanium materials. Fully dense AM-processed parts exhibit high levels of residual stresses, as fabricated, and this influences their yielding behavior. Also, their microstructural morphology influences the damage and fracture behavior, potentially making AM parts more brittle and susceptible to the early onset of damage. For better understanding, AM parts need to be observed and studied under dynamic loading conditions.

The AM material of interest in this research was electron beam additive manufactured (EBAM) titanium (Ti). The AM process builds up a part layer by layer, which provides opportunities to tailor geometry and optimize structural performance in addition to minimizing the amount of material waste for oddly

shaped parts, thereby reducing cost. A quasi-static analysis of the mechanical properties of AM materials used in industry shows only 3% to 5% lower properties than a forged counterpart (Becker 2014, Peña 2015). Our study focused on the material properties and failure mechanisms of AM Ti under high dynamic loading conditions. The team used a two-stage light gas gun at UNLV for performing photonic Doppler velocimetry (PDV) experiments to measure target back surface velocities. The experimental data were used to verify and validate high-fidelity computational simulations of shock behavior that were modeled in CTH and LS-DYNA (O'Toole 2015, Roy 2015). This approach has been used to successfully verify the material models and properties used in computational simulations of ballistic experiments with homogeneous target materials. These advanced materials hold great promise for revolutionizing design, fabrication, and assembly of engineered components and could be used for many NNSA-specific applications including armoring, complex elements of nuclear weapons, and customized diagnostic components in subcritical experiments. It is important to continue the basic science study of how these materials behave dynamically so they can be applied to current needs.

Project

Starting with similar ballistic experiments and simulation methods from previous SDRD work (Becker 2014, Peña 2015), this team ventured into a new area and studied the behavior of more complex materials. The first material system of interest included targets made from single-layer and multilayered stacks of a well-characterized material. The challenge was to identify a material that had been well characterized when fabricated with traditional methods that was also available from an additive manufacturing process. The forged material chosen was titanium 6AL-4V, also known as titanium 6-4 (Ti-6-4) or titanium grade 5.

We also studied AM targets. As shown by Figure 1, six preforms were attached to a flat substrate of titanium 6, grade 4MS 4911, onto which the AM material, an extra low–interstitial grade of titanium 6, AMS-4956, was deposited. The six preforms were heat treated and produced using varying deposition parameters, producing three coupons with two deposits each, as follows:

- Type A: high speed, raster on; layer height of 0.125"–0.135"
- Type B: high speed, raster off; layer height of 0.125"–0.135"
- Type C: low speed, raster on; layer height of 0.140"–0.145"

It is noted that the rate of deposition may affect the surface smoothness (i.e., a slow deposition rate will allow the material to cool before more material is layered on top). Preforms were built with three beads of material being deposited per layer. Each bead overlapped slightly with the bead next to it. The centerlines of the beads were spaced 0.36" apart and were approximately from 0.49" to 0.50" wide, creating an overlap of about 0.14". The material may have voids that are 0.020" in diameter.

The advantage of using EBAM vs. a powder-sintered method is a quicker build time and larger parts. Overhangs are difficult using EBAM, but some can be created based on the geometry and reorientation of the part. The face of the part can be surfaced with a mill afterwards to create a smooth surface finish. The cost of the material in wire form (needed to use EBAM) is higher, but the overall cost is lower because less material is being milled off.

Two-Stage Gas Gun Experiments

A series of hypervelocity impact experiments were conducted at UNLV using a two-stage light gas gun, which uses a powder breech to fire a plastic piston into a pump tube that is filled with hydrogen. The gas is compressed as the piston moves through the pump tube and a petal valve that separates the pressurized gas for the launch tube ruptures, causing the projectile to accelerate down the launch tube and into the experimental tank. The projectile, a 0.22" diameter

Figure 1. Electron beam additive manufactured (EBAM) titanium

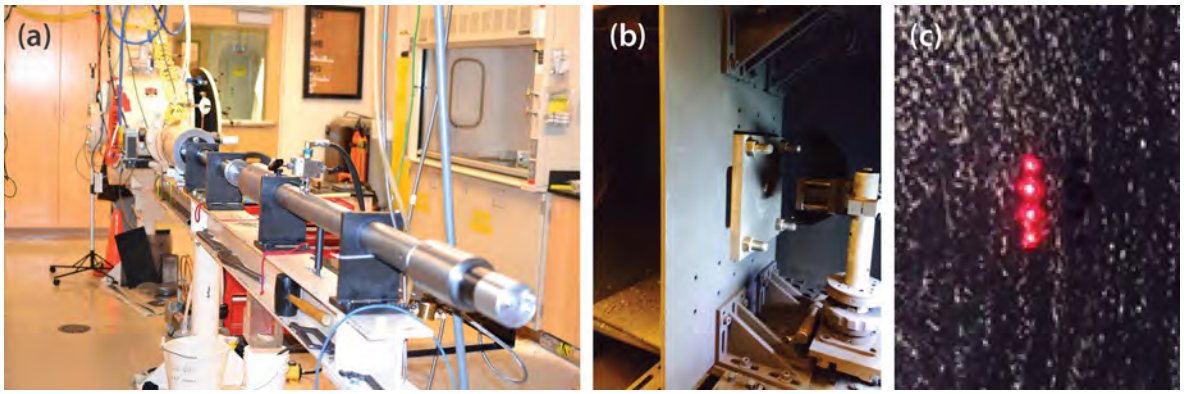

Figure 2. (a) Two-stage light gas gun at UNLV, (b) target chamber assembly, and (c) typical four-channel PDV probe arrangement in target chamber

Lexan cylinder (8.61 mm long) with a mass varying between 0.24 and 0.25 grams, impacts a target plate that is bolted to a mounting plate (Figure 2).

The samples were tested under a wide range of velocities ranging from 4.838 to 6.899 km/s. Initial experiments were performed at lower velocities to ensure that samples were below full penetration and then increased in impact velocity until incipient penetration was achieved. Table 1 shows the description of targets as well as the velocity range for all target types. Figure 3 shows the standard setup in the experimental chamber with the different target types.

Optical velocimetry data were recorded at the back surface of the target plates with a four-channel PDV system. A 2" × 12" linear mechanical transfer (MT) array was mounted in the containment tank with a distance of approximately 52 mm between the array and the back of each test plate. Four out of the total 24 available fibers in the array were used, resulting in four data collection points corresponding to the four-channel PDV system. A four-channel PDV was used to collect experiment data. The spacing between data collection points was manipulated from shot to shot to provide better coverage of the impact zone of the target plates and to achieve the best readings from the bulge on the back of the target plate: 1 mm, 1 mm, 1 mm; 2 mm, 1 mm, 3 mm; and 2 mm, 2 mm, 4 mm.

The light emitted by the MT array was produced by a 1550 nm wavelength RIO ITU 33 base laser. To focus

Table 1. Target descriptions and velocity ranges

Target Size	Sample Qty Tested	Target Type	Target Thickness	Velocity (km/s)
3″ × 3″ and 6″ × 6″	4 and 3	Forged titanium	0.5″	4.838 to 6.610
6″ × 6″	4	Forged titanium	0.25″ (2 ea. stacked)	5.552 to 6.899
6″ × 6″	4	Forged titanium	0.125″ (4 ea. stacked)	5.395 to 6.773
3″ × 3″	3	AM titanium Type A	0.5″	5.175 to 5.976
3″ × 3″	3	AM titanium Type B	0.5″	5.255 to 6.080
3″ × 3″	3	AM titanium Type C	0.5″	5.140 to 5.907

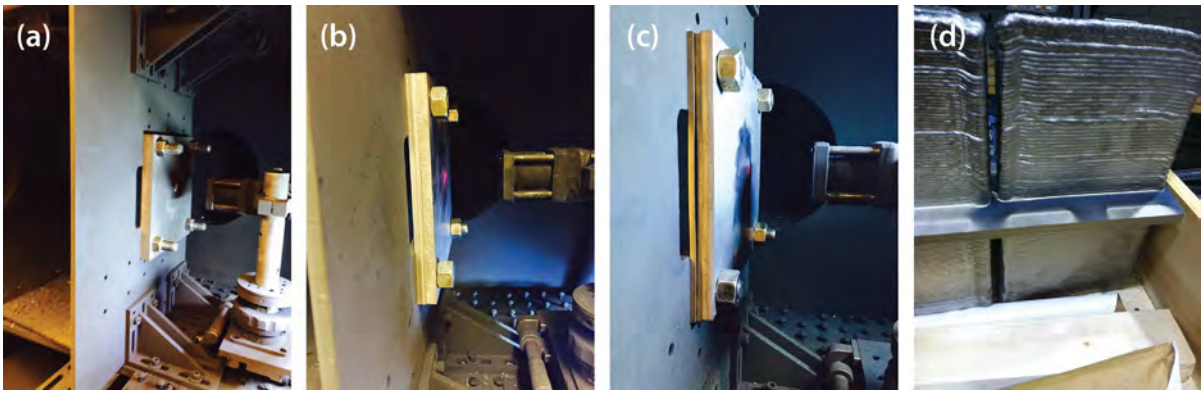

Figure 3. Experimental targets: (a) one 0.5″ thick plate, (b) two 0.25″ thick stacked plates, (c) four 0.125″ thick stacked plates, and (d) AM preform

the light emitted from the array at a desirable working distance of 52 mm, a simple telescope was constructed using two 30 mm acromatic doublet (Thor Labs) lenses. To ensure the light emitted from the array was normal to the surface of the test plate, visible light was sent through the array and projected along a surface that was known to be normal to the test plate. Light normal to the surface of the test plate ensured efficient light return values, thus resulting in a strong signal that could be analyzed by the PDV system.

The PDV recorded surface velocities during the deformation process. The optical system incorporates a base laser that is amplified, split four ways, and then sent to the target through each PDV channel (PDV 1, 2, 3, and 4). The light returning from the target is recombined with the local oscillator (1550 nm laser) and sent to a series of four photodiodes. The signals received by the photodiodes are recorded on the oscilloscope.

An optical beam along the path of the projectile is triggered when broken by the projectile. The projectile is a 0.22″ diameter Lexan cylinder with a mass varying between 0.24 and 0.25 grams. The trigger simultaneously sends a signal to an intervalometer and the delay box (DG535). The signal sent by the DG535 then triggers the start time on the oscilloscope. A proper delay is crucial to the oscilloscope's relatively short operating window for capturing the rapid deformation process.

The density of the forged targets was compared to the density of each type of AM target, with results shown in Table 2. The AM targets exhibit lower density than the forged targets, with AM Type C having the lowest density. As mentioned, the AM material may have voids that are 0.020″ in diameter. These results indicate some level of porosity, which leads to reduced strength and different dynamic behavior.

Table 2. Density of forged vs. AM targets

	Forged Ti	AM Type A	AM Type B	AM Type C
Density (g/cc)	4.368	4.363	4.318	4.178
Percentage Difference (%)	--	0.124	1.16	4.36

The depth of penetration and the shape of the plastically deformed regions were quantified by measuring the crater diameter, bulge, and penetration depth. These physical measurements followed an increasing trend as velocity increased for all target types. The only exception was the crater diameter for the four plates of 0.125", which did not follow any specific trend among the various velocities. This was perhaps due to the first plate undergoing complete penetration. Figures 4 and 5 show the cross sections of some selected forged 0.5" Ti and AM Type A targets, respectively, which particularly illustrate the differences between these two target types. All targets exhibited a small crater on the front face of the target with a bulge on the back surface of the target plate. Both are created as a result of the Lexan sabot impacting the target. As dynamic tensile loads increase, internal fracturing occurs, which leads to spalling at higher impact velocities. This spalling effect is particularly evident in Figure 5c (Type A) and Figure 6d (Type C) for the AM samples, where spalling occurs at a lower velocity than spalling of a forged 0.5" target. Figure 6 also shows the back side of the 0.125" (4 ea.) and 0.25" (2 ea.) forged Ti targets that do not exhibit the same amount of spalling as the forged 0.5" target, which may indicate that a composite structure is more resistant to spall than a single plate of the same overall thickness.

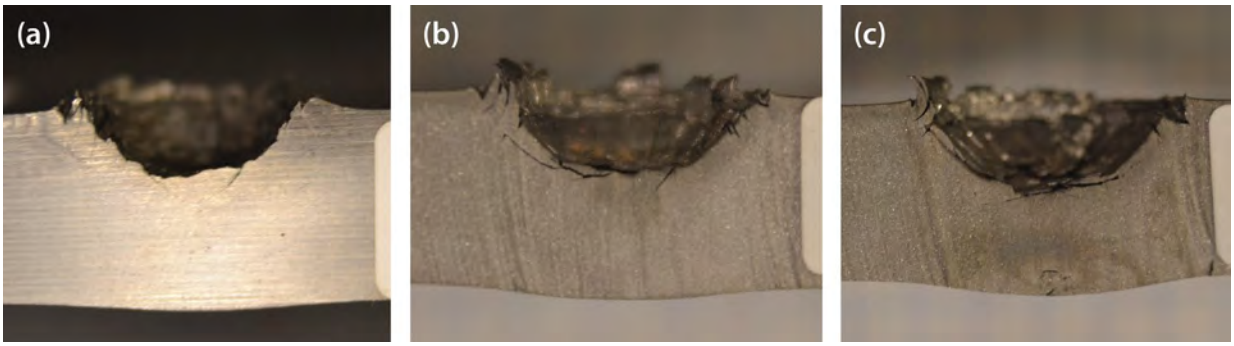

Figure 4. Deformation vs. impact velocity for 0.5" forged Ti plate at velocities of (a) 4.838 km/s, (b) 5.655 km/s, and (c) 6.145 km/s

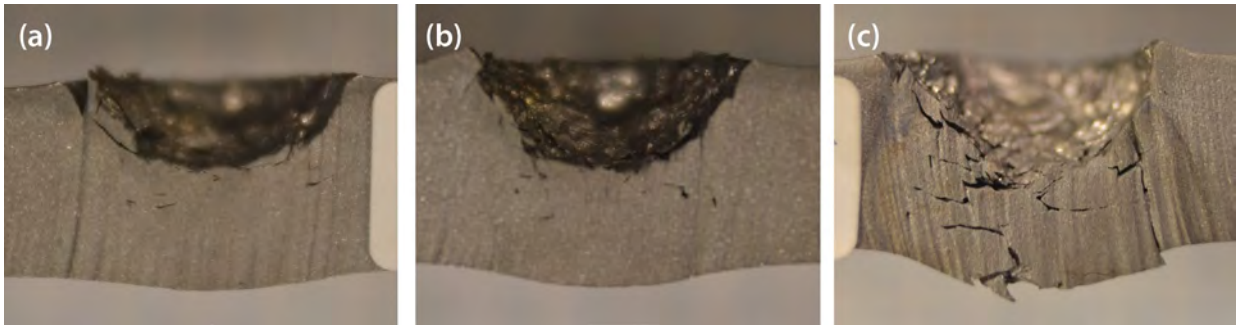

Figure 5. Deformation vs. impact velocity for 0.5" AM Type A plate at velocities of (a) 5.175 km/s, (b) 5.552 km/s, and (c) 5.976 km/s

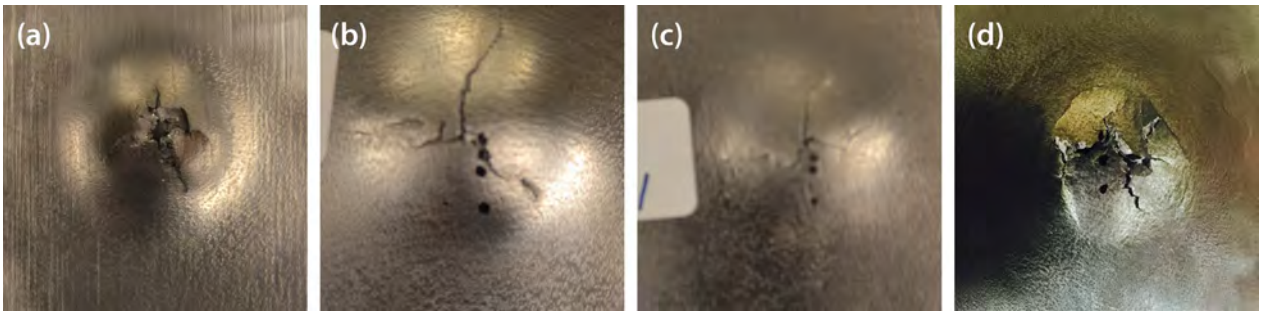

Figure 6. Spall on back side of forged Ti plates (a–c) and an AM plate (d). Shown are (a) 0.5" plate at a velocity of 6.612 km/s, (b) 0.125" (4 ea.) at 6.773 km/s, (c) 0.25" at 6.899 km/s, and (d) AM Type C at 5.907 km/s.

We used QuickView (Diaz 2013), a fast Fourier transform program developed by NSTec, to convert the PDV data into velocity traces of the target surface; these traces were used to compare the forged, stacked, and AM titanium targets. In general, the first 5 ms contain the most important features related to the dynamic properties of the materials. Figure 7 shows velocity traces of some selected tests. Typically, the probe closest to the impact center receives a velocity signal first and will show the maximum velocity profile. All of the velocity traces shown are from one channel, representative of the maximum velocity profile of that specific target.

Experimental data show that size effects are negligible. Figure 7a shows velocity profiles for the six types of targets tested. At a velocity of 5.608 ±0.035 km/s, the 0.5" forged and AM target profiles are similar, and both show no or little spall. The stacked targets vibrate more, especially the four stacked plates, as shown by

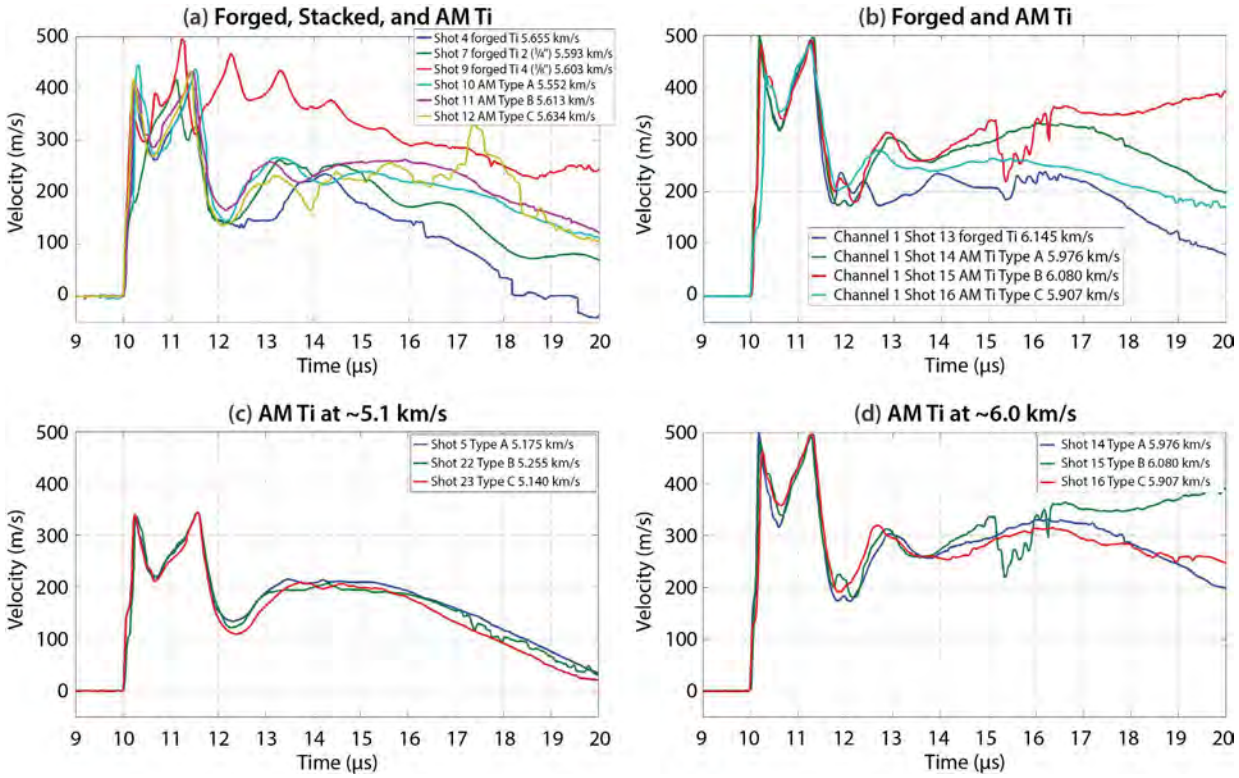

Figure 7. Velocity traces of (a) forged, stacked, and AM Ti at ~5.5 km/s; (b) forged and AM Ti at ~6 km/s; (c) AM Ti at ~5.1 km/s; and (d) AM Ti at ~6.0 km/s

Shot 9 (red), which has a significantly different profile. Figure 7b compares the 0.5" forged and AM targets at a velocity of 6.027 ±0.106 km/s. The four profiles are similar, especially during early impact; however, as the impact continues, the AM targets begin to spall, but the forged targets do not.

Shown in Figures 7c and 7d are the velocity profiles of AM targets at two different velocities, 5.190 ±0.059 km/s and 5.990 ±0.087 km/s, respectively. Also tested, but not shown, was a velocity of 5.600 ±0.043 km/s for all AM targets. The velocity profiles are similar for all types of AM targets at these three velocities. Spalling occurred for all AM types at the 5.990 km/s velocity, with Type C spalling more than the others, possibly due to its lower density.

Simulations Using CTH and LS-DYNA

Computational simulations of the 0.5" thick targets being impacted by a 0.22" Lexan projectile were performed using two finite element methods to simulate the projectile-target interaction. Smoothed-particle hydrodynamics (SPH) in LS-DYNA and the Eulerian hydrocode in CTH were used to verify and validate modeling methods, material models, and material properties. Because the velocity wave did not reach the plate boundaries within the time span of concern, 2-D axisymmetric models were created for projectiles and targets in both software packages, and no boundary conditions were applied using this approach. Johnson-Cook material models with Mie Grüneisen equations of state (EOS) were utilized (Wang 2013).

Experimental data were compared with simulations to assess the accuracy of the proposed simulation approaches. In both cases, a single forged Ti-6-4 plate was impacted with a Lexan projectile. The CTH model used a 0.05 mm zone size for creating the projectile and target plate, while the SPH model in LS-DYNA was constructed with a particle spacing of 0.10 mm for the projectile and target plate. Impact velocities were 5.5 km/s and 6.145 km/s for the CTH and LS-DYNA simulations, respectively. Results shown in Figure 8 indicate that both approaches simulate the impact crater diameter and depth as well as the back surface deformation accurately when compared with the results of the experiment.

As shown in Figure 8b, the simulated back surface velocity profile captures the first peak with a 6.5% difference in magnitude and the second peak with a 2% difference in magnitude. Further adjustment of the material model and EOS parameters is needed to perfectly match the simulation with the experimental data.

An initial simulation was conducted for experiments with two 0.25" thick forged Ti plates. The model was constructed using SPH in LS-DYNA with particle spacing of 0.10 mm for the target plate and projectile. The two

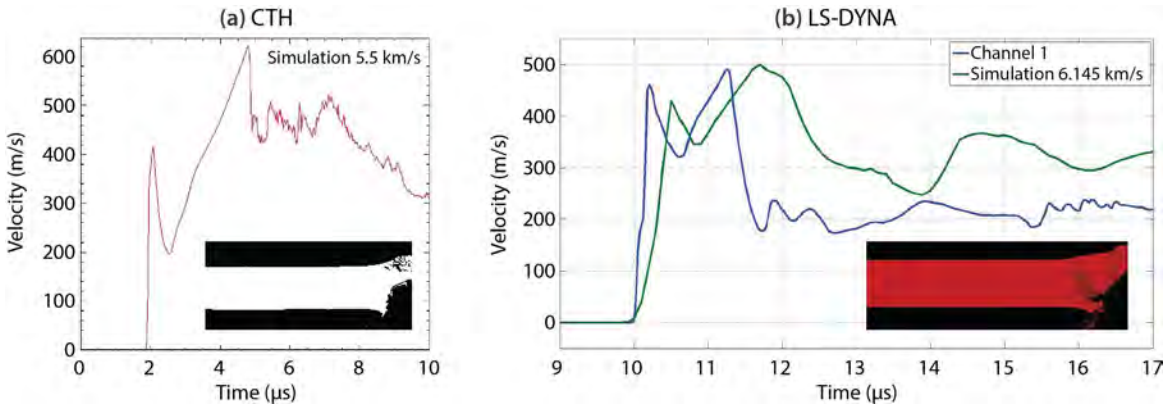

Figure 8. Computational simulations showing back surface velocity vs. time from (a) CTH and (b) LS-DYNA. The inserts show the final deformed shape of a cross section cut through the center of the target.

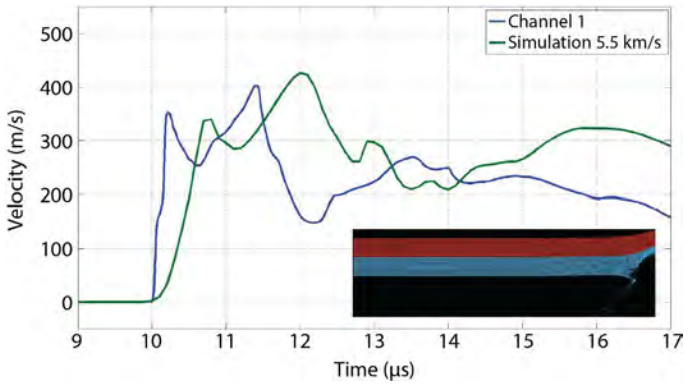

Figure 9. Computational simulation of back surface velocity vs. time from LS-DYNA for two 0.25" plates. The insert shows the predicted final deformed shape of the target plates.

plates were impacted with the Lexan projectile at a velocity of 5.5 km/s, and the velocity profile is shown overlaid with an experimental test at the same velocity in Figure 9. The simulated back surface velocity has an initial peak magnitude difference of 3.4% and a second peak magnitude difference of 5.3%. Again, the velocity profiles cannot be directly compared to time step variations in experimental and simulated data.

Conclusion

During this project, we completed collection of unique experimental data (velocity and deformation) from ballistic experiments with new complex materials in addition to verifying and validating simulations to the experiments using different approaches.

The four-channel PDV experiments were successfully completed. We explored the dynamic properties of forged titanium, stacked forged titanium, and EBAM titanium target plates of different deposition rates. The effect of target size and impact velocity on deformation of forged Ti plates were evaluated, and it was determined that size effects are negligible for 6" × 6" targets vs. 3" × 3" targets. Differences in deformation and failure of six different types of titanium were documented for three different impact velocities. We recommend that additional microscopy analysis of target materials be performed to further understand differences in failure modes.

Due to software limitations, computational models were developed to simulate projectile-target interaction for the forged titanium plates only. Simulation of stacked plate targets should be possible in the future, as a contact algorithm for SPH modeling in LS-DYNA just became available. The EBAM targets are extremely challenging to model because of microstructure, porosity, and property differences (3% to 5% drop in static mechanical properties documented). Approaches should be explored in the future to improve the accuracy of the computational models.

Acknowledgment

This effort was a collaboration between NSTec and UNLV. We would like to acknowledge that UNLV provided the facilities and platform to perform the experiments. The teamwork between NSTec personnel and UNLV personnel was exceptional, and the effort could not have succeeded without a successful collaboration.

During this project multiple students and employees gained knowledge of gas gun operations, PDV setup, data analysis, and computational simulations. It allowed many UNLV students and NSTec employees to train in the diagnostic analysis of dynamic experiments.

References

Becker, S., et al., "Plastic deformation study using a light gas gun," in *Site-Directed Research and Development*, FY 2013, National Security Technologies, LLC, Las Vegas, Nevada, 2014, 37–49.

Diaz, A., "QuickView Software User's Manual, Version 4.2.2," National Security Technologies, LLC, Las Vegas, Nevada, October 2013.

Needler, S., "WDJ1.1: F-35 direct manufacturing: Material qualification results," AeroMat Conference and Exposition 2012, Charlotte, North Carolina, June 18–21, 2012, https://asm.confex.com/asm/aero12/webprogram/Paper30786.html, accessed October 6, 2015.

O'Toole, B., M. Trabia, R. Hixson, S. K. Roy, M. Peña, S. Becker, E. Daykin, E. Machorro, R. Jennings, M. Matthes, "Modeling plastic deformation of steel plates in hypervelocity impact experiments," *Procedia Engineering* **103** (2015) 458–465.

Peña, M., et al., "Plastic deformation study using a light gas gun," in *Site-Directed Research and Development*, FY 2014, National Security Technologies, LLC, Las Vegas, Nevada, 2015, 23–35.

Phelps, H., "Electron beam direct manufacturing (EBDM) on the F-35 Lightning II," NC State Advanced Manufacturing & Logistics Symposium, Raleigh, North Carolina, October 17, 2013, http://camal.ncsu.edu/wp-content/uploads/2013/10/Hank-Phelps-EBDM-Presentation-to-NC-State-Final-RevA.pdf, accessed October 6, 2015.

Roy, S. K., et al., "Study of hypervelocity projectile impact on thick metal plates," *Shock and Vibration* **2016** (2015), http://www.hindawi.com/journals/sv/2016/4313480/, accessed November 23, 2015.

Wang, X., Shi, J., "Validation of Johnson-Cook plasticity and damage model using impact experiment," *Int. J. Impact Eng.* **60** (2013) 67–75.

This page left blank intentionally

Grooved Graded Density Impactor for Simplified Isentropic Compression Experiments

STL-05-15 | Year 1 of 1

Brandon La Lone,[1,a] Gerald D. Stevens,[a] Ruben J. Valencia,[a] Bruce Marshall,[a] and Rachel M. Posner[a]

Graded density impactors (GDIs) are used in gas gun experiments to generate ramped compression waves instead of shock waves. GDIs are frequently constructed from a multilayer stack of materials with different initial densities. These GDIs are very expensive to manufacture, are not very reproducible, and do not generate a smooth (shockless) ramp wave. Here, we investigated a new type of GDI made by machining grooves into the impacting surface. Tapered grooves naturally have a graded areal density that increases smoothly from the tips to the troughs. The groove shape was optimized using 2-D computer simulations of several groove geometries impacting targets. Grooved impactors were then purchased from a wire electrical discharge machining service and tested on gas gun experiments. The shape of the ramped compression wave was measured using either two-point photonic Doppler velocimetry or a line-imaging VISAR. Preliminary results indicate that the technique produces smooth ramp compression waves, but we have not assessed the planarity of the waves.

[1] lalonebm@nv.doe.gov, 805-681-2046
[a] Special Technologies Laboratory

Background

Ramp wave compression of condensed matter enables the determination of a continuous sound speed-pressure-volume path in a single experiment. This loading path is nearly isentropic, as little entropy is generated and the path is reversible, meaning the material will return to near ambient temperature when the pressure is released. In the absence of heat flow, the isentrope is the coldest temperature path that can be accessed under compression. This contrasts with shock wave loading where generally only one pressure state can be investigated in an experiment. This state is on the shock wave Hugoniot, which has higher entropy and therefore is at a higher temperature than the isentrope. Shock wave loading is irreversible, so the material will return to an elevated temperature when the pressure is released. Because ramp wave loading accesses a different region of a material's phase space than shock wave loading, it improves the accuracy of a material's equation of state, which in turn improves hydrodynamic simulations. For these reasons, ramp wave compression experiments are frequently conducted.

Several methods exist for generating ramp waves in the laboratory. Ramp compression experiments are routinely fielded at pulsed power facilities such as the Sandia Z machine (Hall 2001) and the Los Alamos High Explosive Pulsed Power Facility (Tasker 2006). Laser-driven ramp compression has been achieved at the Omega laser (Laboratory for Laser Energetics) (Edwards 2004) and at the National Ignition Facility (Wang 2013). At gun facilities, graded density impactors (GDIs) are used to generate ramp compression waves.

GDIs were originally invented by Barker and fielded on experiments at Sandia (Barker 1984). These impactors

were made using a sedimentation process to set up a density gradient. Modern GDIs are made from a multilayer (up to 100) stack of thin sheets of various materials, each layer having a greater density than the previous layer, setting up a density (or acoustic impedance) gradient. In either case, the acoustic impedance increases with distance from the impacting surface, which is what creates a ramped compression wave upon impact with a target. Researchers at Lawrence Livermore National Laboratory have been making GDIs using this layered concept and have been fielding them at the California Institute of Technology, High Explosives Application Facility, and the Joint Actinide Shock Physics Experimental Research gun facilities. Yep (2013) illustrates the complexity of constructing and characterizing these layered GDIs; major issues with these impactors have been their cost of production and reproducibility. In 2013, researchers at the Atomic Weapons Establishment tested a novel type of GDI, termed the "bed-of-nails" concept (Winter 2014). Using 3-D printing, they manufactured a structured impactor that resembled a bed of nails where each "nail" was a tapered spike that was narrow at the top and wide at the bottom. On average, this creates an areal density gradient that increases with distance from the impacting surface. Therefore, in a similar manner to other GDIs, the bed-of-nails impactors generate a ramped compression wave upon impact with a target. The preliminary results of the bed-of-nails GDI were encouraging, but the 3-D computer simulations were difficult to run and were poorly reproduced in the experiments. Additionally, 3-D printing technology does not yet have the precision to make finely detailed structures from metals commonly used as impactors, such as copper or tantalum.

In this project, we used an approach similar to the bed-of-nails concept, but instead of building a 3-D nail-like structure to create the impactors, we machined a 2-D grooved structure into the face of the impactor. This simplified the hydrodynamic simulations, which then needed only two dimensions instead of three. Additionally, machining techniques are more precise than additive manufacturing techniques, and machined impactors can be made from more common metals.

Project

Determining Groove Shape Using Hydrodynamic Simulations

For the grooved GDI to be useful in a dynamic compression experiment, the drive must be planar when propagating through the target sample so that a condition of uniaxial strain is maintained. For a structured impactor, the pressure profile at the impacting interface will be

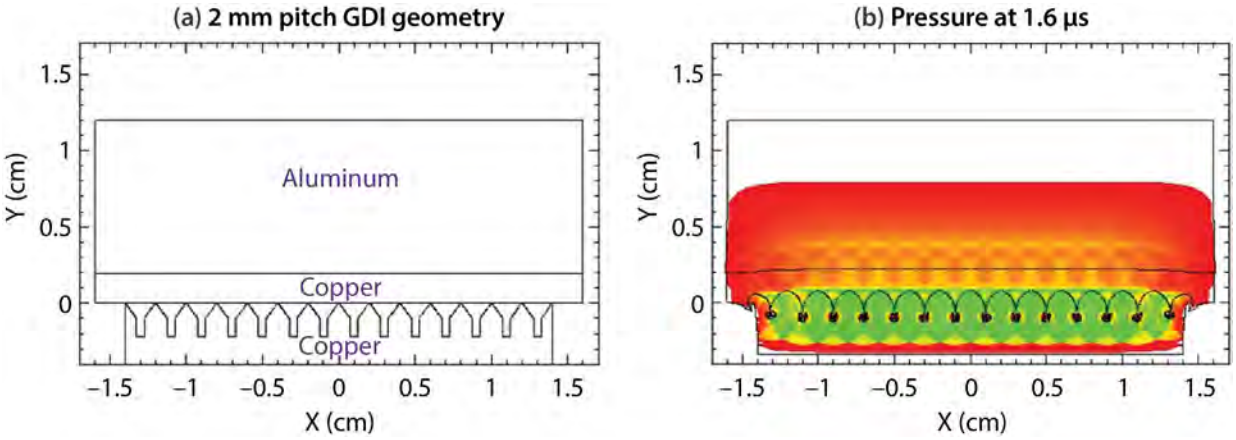

Figure 1. (a) Geometry of one of the CTH simulations of a 2 mm pitch grooved GDI impacting a copper buffer backed by an aluminum target. The impactor moves from bottom to top in this simulation. (b) Colored map of the pressure in the simulation 1.6 µs after impact. The highest pressures are green and the lowest pressures are red.

heterogeneous. The hypothesis was that the initially heterogeneous pressure at the impacting surface would drive a compression wave that smooths out as it propagates through a buffer layer before entering the sample material. Figure 1 illustrates a notional drawing of a grooved GDI impacting a buffer layer backed by a sample material. Therefore, the primary goal of the dynamic simulations was to determine, for a given groove pitch, how thick the buffer layer must be for the ramped compression wave to be planar when it propagates through the sample. We also considered the shape of the compression wave and real-world issues such as the minimum inside radius that can be machined into the sample. All simulations were performed in 2-D using Sandia National Laboratories' CTH code (McGlaun 1990).

Figure 1 shows the geometry of the model before impact and the pressure profile 1.6 µs after impact. The groove shape we settled on resembled a "picket fence"—triangular-shaped grooves with slots between them. The triangular-shaped grooves set up a linear areal density gradient. The slots were added to delay the creation of a shock that forms when the waves reflect from the bottom of the grooves. The grooved GDI and buffer layer were modeled, and an impactor was machined from oxygen-free high thermal conductivity copper. In the simulations, the triangular portions of the grooves were 1 mm deep, and the slot depth was an additional 1.1 mm deep. The groove pitch was varied, and the width of the slot was always 25% of the groove spacing. The copper buffer layer was 2 mm thick, and an aluminum target backed the copper buffer. Velocity tracers were placed at the copper/aluminum interface and 2 mm into the aluminum to assess the planarity of the drive in the simulations.

Simulated velocity histories at the buffer/aluminum interface and 2 mm into the aluminum are shown in Figure 2a. Using the velocity histories, we performed a Lagrangian wave speed analysis (see Fowles [1970] for the case of simple isentropic flow) to obtain a sound speed vs. particle velocity curve from each simulation. If the waves are 1-D, the sound speed curves calculated from the simulation should match the aluminum

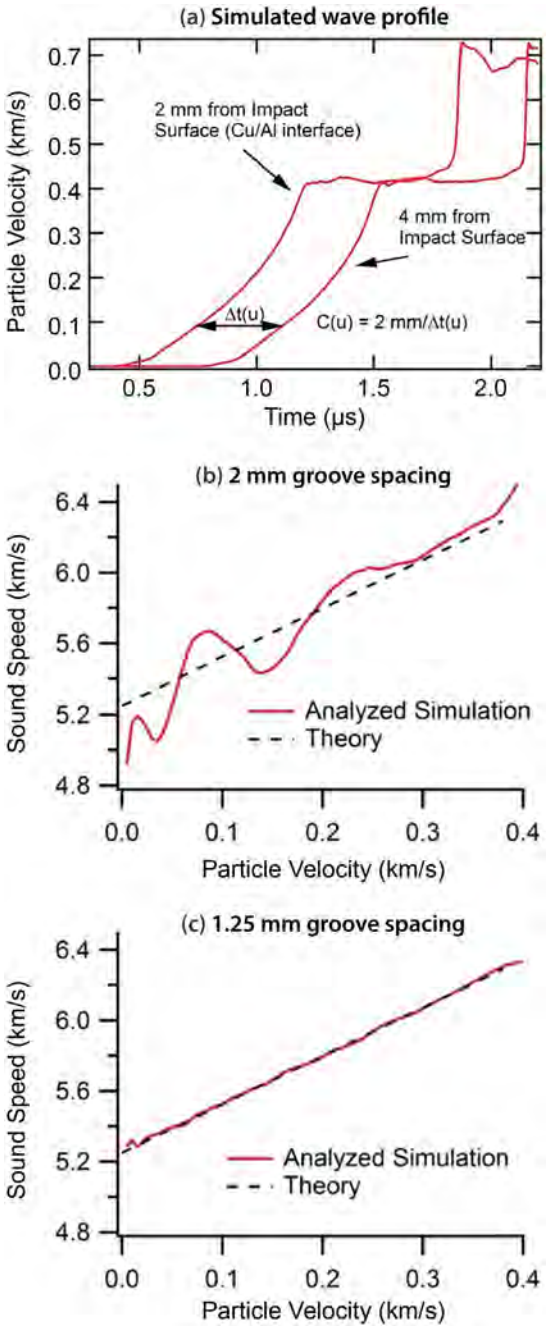

Figure 2. (a) Simulated wave profiles of the grooved GDI experiments. (b) Sound speed vs. particle velocity curve in aluminum resulting from Lagrangian analysis of wave profiles from grooved GDI with 2 mm groove spacing. The dashed black line is the theoretical sound speed. (c) Sound speed vs. particle velocity curve in aluminum resulting from Lagrangian analysis of wave profiles from impactor with 1.25 mm groove spacing.

model that was used in the simulation. Two of these sound speed curves are shown in Figures 2b and 2c, for the case of 2 mm groove spacing and 1.25 mm groove spacing. For the case of the 2 mm groove spacing, the sound speed curve obtained from analyzing the simulated wave profiles was a poor match to the theory. For the 1.25 mm spacing simulation, the sound speed curve was an excellent match. From a series of such simulations, we concluded that the buffer thickness should be at least 1.3x groove spacing to have a quasi–1-D wave propagating in the target.

Gas Gun Experiments with Grooved Impactors on 0.5" Bore

Impactors machined using wire-electrical-discharge-machining were purchased from Santa Barbara Tool and Die. These initial impactors (Figure 3) were made for our 0.5" bore light gas gun; they had the same geometry as the simulated impactors with a 1 mm groove spacing and a 0.25 mm wide slot. The height of all grooves were the same to within ~10 µm.

Figure 4 shows a schematic of the 0.5" bore gun experiments. A 1.8 mm copper buffer was used to smooth out the ramp wave profile before it entered into a z-cut quartz target. Single crystals of z-cut quartz were chosen as the target material as we had previously performed ramp compression experiments on this material (Jaglinksi 2009) using a pulsed power machine, and the elastic sound speed curve is known very accurately. The velocity history of the wave was measured where it entered the quartz and at a depth of 2 mm using two photonic Doppler velocimetry (PDV) probes. Each PDV probe was of the two-fiber

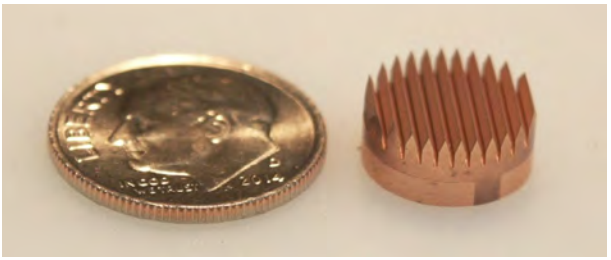

Figure 3. Photograph of 0.5" bore gun grooved GDI next to a dime for scale

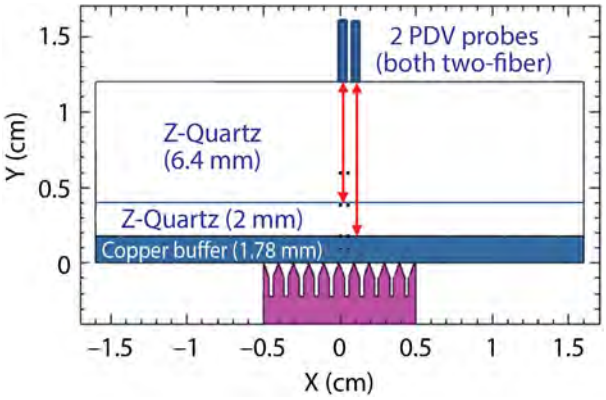

Figure 4. Schematic diagram of the grooved GDI experiments on z-cut quartz

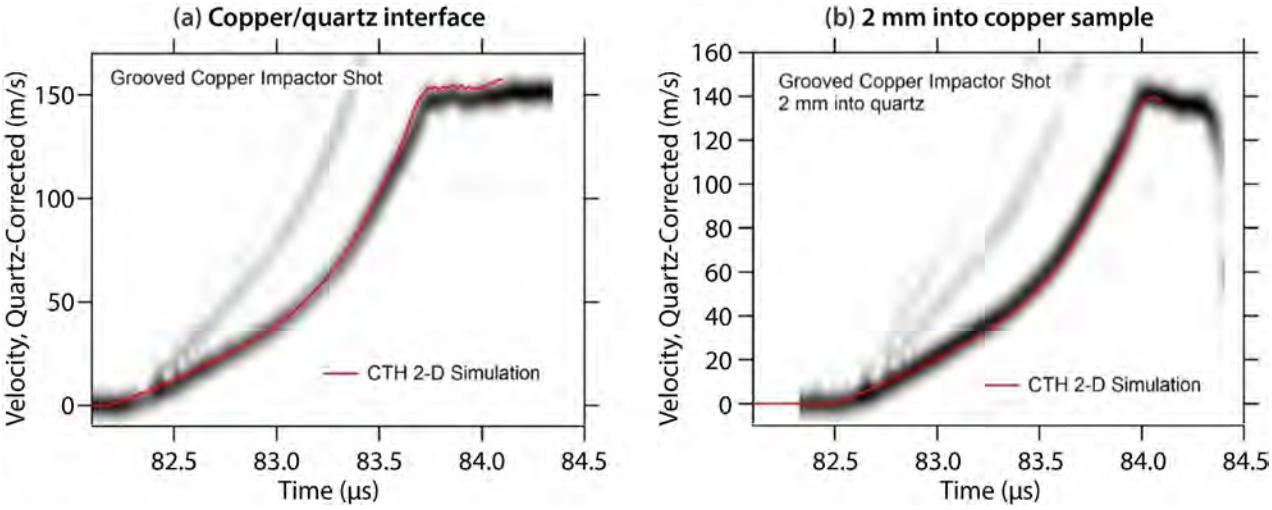

Figure 5. Measured velocity histories at (a) the copper/quartz interface and (b) 2 mm into the copper sample both show good agreement with CTH simulations

frequency-upshifted variety to eliminate the extended baseline in the measured spectrograms. This helped resolve the low-velocity portions of the ramp waves.

Velocity spectrograms, at the two depths, from one of the experiments are shown in Figure 5 along with CTH simulations of the experiment. The velocity traces are smooth, shockless, ramp waves and are in excellent agreement with the CTH simulations. Unfortunately, because of the small diameter of the impactor, edge release waves polluted the experiment so that an accurate Lagrangian sound speed curve could not be obtained from the velocity measurements (Figure 6). This was also apparent from analyzed simulated profiles that also do not match the theoretical sound speed curve for quartz.

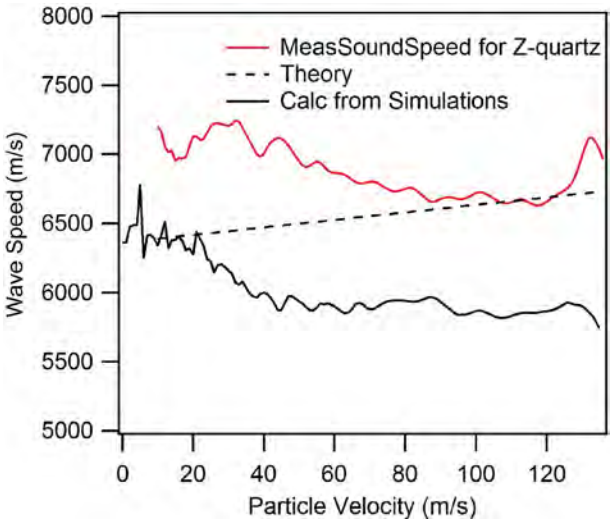

Figure 6. Lagrangian sound speed analysis of the measured wave profiles in quartz and the simulated wave profiles from CTH compared with theory. The poor match to the theory is likely a result of edge release waves that contaminated the experiment.

Gas Gun Experiments with Grooved Impactors on 1.5" Bore

The Special Technologies Laboratory 1.5" diameter bore light gas gun was installed midyear in this project. Using the 1.5" bore gun, we performed additional experiments with larger-diameter grooved impactors. The larger-diameter impactors eliminated the contamination due to edge release waves. We also used a newly constructed line-imaging VISAR, built to support Sandia National Laboratories, to assess the drive planarity. The line-VISAR uses a 60-fiber linear array to relay a line image on the target to the interferometer cavity and records quadrature signals on a streak camera. For these experiments, the fiber spacing on the target was 136 µm, for a total line length of 8.05 mm. The velocity per fringe constant of the line-VISAR was 125 m/s/fringe.

A schematic diagram of the target assembly is shown in Figure 7. The grooved GDI, traveling at ~600 m/s, impacts either a 4 or 6 mm thick copper buffer backed by a 2 mm thick z-cut quartz target followed by a 6.4 mm thick z-cut quartz window. Half of the line image from the VISAR tracked the velocity of the copper/quartz interface; the other half of the line tracked the velocity of the quartz target/window interface.

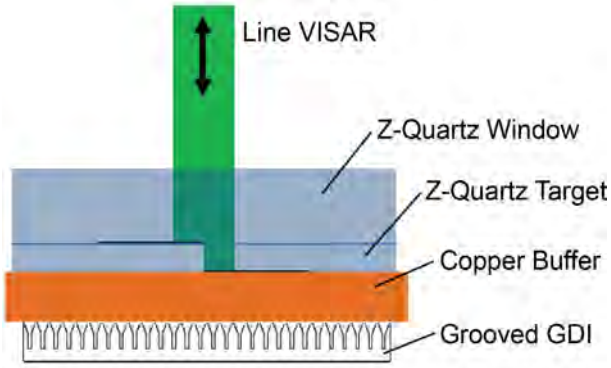

Figure 7. Schematic diagram of 1.5" bore gun grooved GDI experiment with a copper buffer with a z-axis quartz target and window. A line-VISAR was used to record the velocity of the copper/quartz interface and of the quartz target/window interface.

The streak camera image of the four VISAR quadrature signals for the shot with the 6 mm buffer is shown in Figure 8. Time moves from the bottom to the top in the image. Inspection of the image shows that the ramp was smooth and shockless, and extends to a peak pressure of around 2 GPa, but without a complete analysis it is difficult to tell if it is homogeneous. A complete analysis will be performed at a later date.

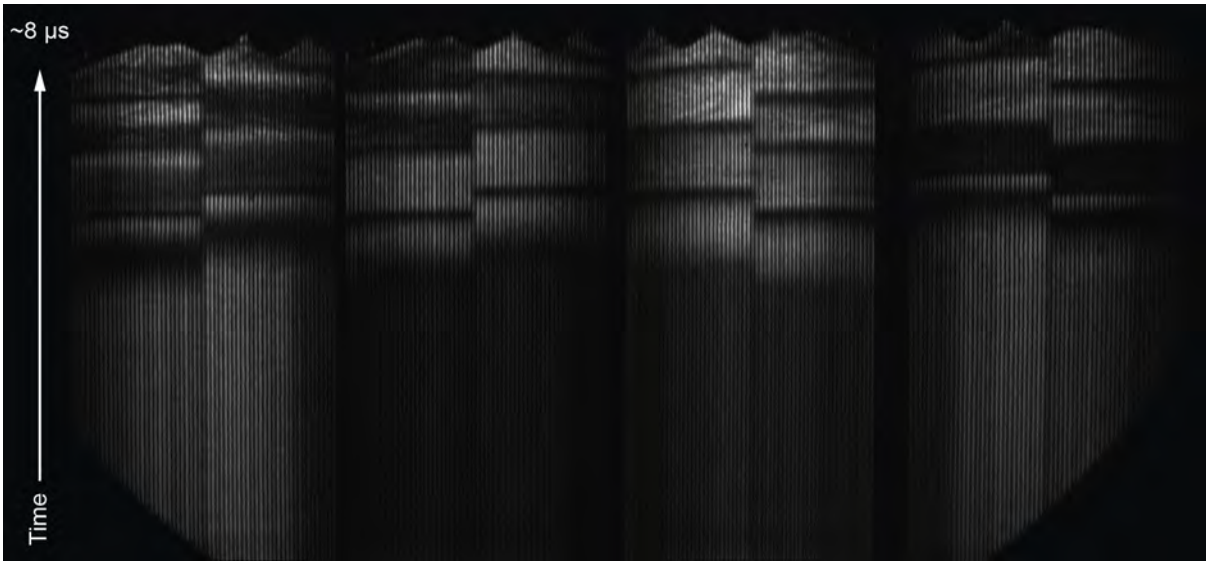

Figure 8. Streak camera image of line-VISAR quadrature signals from a grooved GDI experiment on quartz for a period of ~8 µs

The grooved impactors appear to give a peak ramp stress that is less than half of the peak stress that would be obtained from a solid impactor in a shock wave experiment. For example, a planar copper impactor hitting a quartz target at 600 m/s would generate a peak stress of about 5 GPa, compared with just 2 GPa for the grooved impactor.

Conclusion

For performing ramp wave compression experiments, we tested GDIs made by machining grooves into the impacting surface. We performed a series of experiments using both point-PDV and line-imaging VISAR to assess the planarity of the drive. The impactors do produce smooth and shockless ramps, but further analysis of the experimental data is needed to determine if the impactors are capable of producing planar (1-D) ramp waves.

References

Barker, L. M., "High-pressure quasi-isentropic impact experiments," *Shock Waves in Condensed Matter* (1984) 217–224.

Edwards, J., et al. "Laser-driven plasma loader for shockless compression and acceleration of samples in the solid state," *Phys. Rev. Lett.* **92**, 7 (2004) 075002.

Fowles, R., R. F. Williams, "Plane stress wave propagation in solids," *J. Appl. Phys.* **41** (1970) 360–363.

Hall, C. A., J. R. Asay, M. D. Knudson, W. A. Stygar, R. B. Spielman, T. D. Pointon, D. B. Reisman, A. Toor, R. C. Cauble "Experimental configuration for isentropic compression of solids using pulsed magnetic loading," *Rev. Sci. Instrum.* **72** (2001) 3587–3595.

Jaglinksi, T., B. M. La Lone, C. J. Bakeman, Y. M. Gupta, "Shockless compression of z-cut quartz to 7 GPa," *J. Appl. Phys.* **105** (2009) 083528.

McGlaun, J. M., S. L. Thompson, M. G. Elrick, "CTH: A three-dimensional shock wave physics code," *Int. J. Impact Eng.* **10** (1990) 351–360.

Tasker, D., "Megabar isentropic compression experiments (ICE) using high explosive pulsed power (HEPP)," *Department of Electronic and Electrical Engineering*, Loughborough University, Loughborough, UK, 2006, 406.

Wang, J., R. F. Smith, J. H. Eggert, D. G. Braun, T. R. Boehly, J. R. Patterson, P. M. Celliers, R. Jeanloz, G. W. Collins, T. S. Duffy, "Ramp compression of iron to 273 GPa," *J. Appl. Phys.* **114** (2013) 023513.

Winter, R. E., M. Cotton, E. J. Harris, D. J. Chapman, D. Eakins, "A novel graded density impactor," *Journal of Physics: Conference Series* **500** (2014) 142034, http://iopscience.iop.org/article/10.1088/1742-6596/500/14/142034/pdf, accessed November 24, 2015.

Yep, S. J., J. L. Belof, D. A. Orlikowski, J. H. Nguyen, "Fabrication and application of high impedance graded density impactors in light gas gun experiments," *Rev. Sci. Instrum.* **84**, 10 (2013) 103909.

This page left blank intentionally

Optical Ranging for Shocked Surfaces

STL-04-15 | Year 1 of 1

Bruce Marshall[1,a] and Brandon La Lone[a]

We have developed a high-speed optical ranging system to measure the position and velocity of rapidly moving surfaces in nonplanar explosive experiments. In nonplanar experiments, the distance from the target to the sensing probe cannot usually be determined from the time integral of the measured velocity. The position measurement—based on the technique described by Xia and Zhang (2010), which can determine the target location independent of the target speed at sampling rates up to 100 MHz—is insensitive to Doppler shift and is ideally suited for dynamic applications. In developing the broadband laser ranging (BLR) system, we have extended the full range of the diagnostic to >12 cm with <10 µm position accuracy at a reduced sampling rate of 12.5 MHz. We have multiplexed the range diagnostic with a photonic Doppler velocimetry system so that position and velocity can be tracked simultaneously using a single fiber-optic probe. The BLR was used on a number of explosive and gas gun experiments where surface ejecta and fragments were identified in both the position and velocity signals. The position measurement complements the velocity data and facilitates unambiguous interpretation of the data. A description of the BLR system and our experimental results were published in *Review of Scientific Instruments* (La Lone 2015). This report presents the current status of the diagnostic and future goals.

[1] marshabr@nv.doe.gov, 805-681-2266
[a] Special Technologies Laboratory

Background

Optical velocimetry measurements are central to nearly all dynamic experiments, from wave profile measurements in simple 1-D plate impact experiments to assessing the drive shape for imploding capsules at the National Ignition Facility. In many nonplanar experiments, time-resolved surface position is also desired for comparison with hydrodynamic models and other diagnostics, such as radiography, but the position cannot always be obtained from the velocity data. In general, the surface distance cannot be found from the time integral of the measured surface velocity because velocimetry techniques such as VISAR (Barker 1972) or photonic Doppler velocimetry (PDV) (Strand 2006) measure only one component (parallel to the probe axis) of the surface velocity, and the direction of motion can be unknown or changing.

An interferometric optical ranging technique was developed earlier by Xia and Zhang (2009, 2010). A wide-spectrum, mode-locked fiber laser was used as the light source, and the interference spectrum was converted into the time domain with a dispersive element so that the entire spectrum could be recorded on a single photoreceiver and oscilloscope channel. Their ranging technique is insensitive to the Doppler shift, is sampled every 20 ns, and was demonstrated in quasi-static applications with a measurement precision of 1.5 µm.

In this work, we adapted the Xia and Zhang technique to dynamic experiments by extending the full range to several centimeters and added a PDV system to obtain a simultaneous velocity measurement along a single probe's optical axis.

Project

Our goals in this project were to identify the technical obstacles to be overcome and to determine a basic broadband laser ranging (BLR) design suitable for the applications in the stockpile community. The basic design and operation of our initial single-channel system and its use in explosive experiments are discussed in our published article (La Lone 2015). In this report, we briefly discuss our main accomplishments of this project and the concept of the BLR system. The focus of this report is on the design of a future system configuration, and we discuss the design choices and their relation to the experimental requirements. BLR measurements are inherently more complex than PDV measurements, so we discuss important system considerations aimed at aiding future researchers in the construction and deployment of BLR systems.

Main Accomplishments

We made progress on many different aspects of this project in an effort to design and understand a BLR system that is suitable for stockpile research. This section briefly summarizes our accomplishments throughout this project. Some of the topics in this summary will be elaborated on in later sections.

By adding more dispersion and optical amplification, we extended the full tracking range by more than a factor of two over our prior version of the BLR system, and demonstrated 150 mm of range in explosive tests. During these tests, we also investigated different interferometer configurations with respect to fieldability and practicality. We found it simpler to field a fiber Michelson interferometer, with the beam splitter less than a few meters away from the target, rather than a Mach-Zehnder interferometer with beam splitters at a greater distance from the target of around 30 meters.

For the extended range experiments, we had to reduce the laser repetition rate from 100 MHz to 12.5 MHz to prevent the pulses from overlapping on the photoreceiver. This was accomplished with a Mach-Zehnder modulator driven by an electronic circuit (pulse picker) that was designed and built for this project. We later ordered a laser that operates at 12.5 MHz, negating the need for the pulse picker in the future. This laser is also designed to compress the pulse to the transform-limited point (zero chirp and minimum width in time) only after it travels through 80 meters of fiber-optic cable. This will help us to manage the pulse length in future experiments.

Calibration of the BLR system is central to making accurate measurements for dynamic experiments. We developed calibration techniques and acquired a traceable stabilized helium-neon laser system that measures the calibration positions to an accuracy of ~100 nm.

Because the laser pulses are sub-picosecond in length, the maximum average power that can be delivered fiber optically is limited by nonlinear effects because the peak powers can be quite high. The dominant nonlinear effect in our system is self-phase modulation. We investigated the upper limits of optical power (or pulse energy) for system operation before self-phase modulation degrades the measurement.

BLR System Concept

The BLR is based on the interference of time-delayed femtosecond laser pulses. The interference spectra are converted to the time domain using dispersion for serial recording on an oscilloscope. A PDV system is wavelength-multiplexed onto the shared probe to provide simultaneous velocity measurements.

Figure 1 shows the conversion of the optical interference pattern from the optical frequency domain to the time domain. The time delay between the two pulses is preserved at each optical frequency in the dispersion process. Interference of the dispersed pulses produces a beat frequency proportional to the time delay. Each reflection contributes a corresponding beat frequency

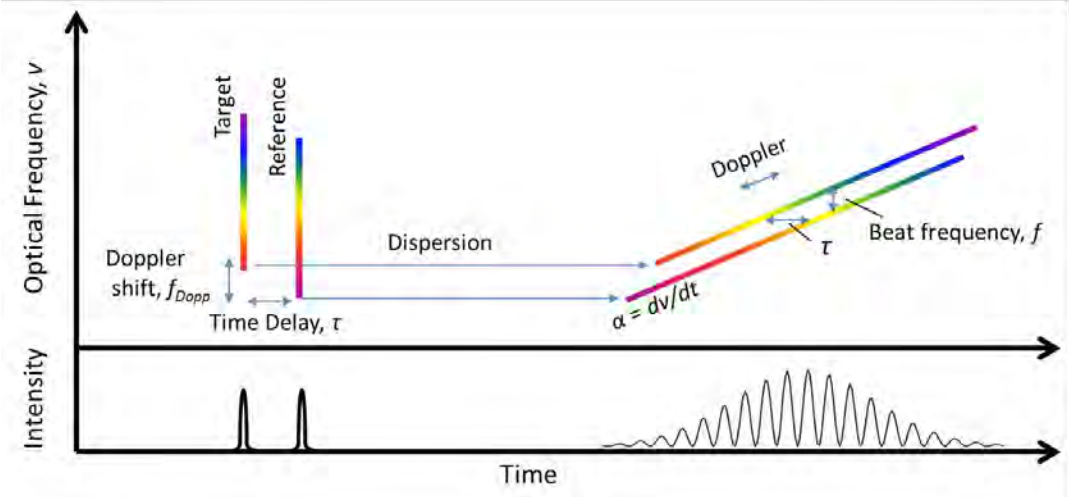

Figure 1. Optical frequency (ν) and pulse intensity versus time diagram shows the concept of the BLR system. Doppler shift (f_{Dopp}), time delay (τ), pulse chirp ($\alpha = d\nu/dt$), and beat frequency (f) are noted in the figure. The pulses are short in time and spectrally broad when a target pulse interferes with a reference pulse early in time. After dispersion, the pulses are chirped and the spectral interference is now observable in the intensity-time plot. Doppler shift due to target motion shifts the target spectrum to higher frequencies, but this only shifts the pulse along the chirped curve and does not affect the measured beat frequency.

to the spectrum, allowing the detection of multiple scattering points in the field of view. A Fourier transform of the pulse gives the locations of all reflections present. If the pulse is not dispersed at the target but is transform-limited, the Doppler shift merely shifts the dispersed pulse along the dispersion curve but does not affect the beat frequency. The relationships between the time delay and the measured beat frequency, and between the target position and the time delay, are given by

$$\tau = \frac{f}{\alpha} \text{ and } z = \frac{c\tau}{2}, \quad (1)$$

where τ = time delay, f = beat frequency, α = dispersion ($d\nu/dt$ where ν is the optical frequency), and z = target distance from the balance point of the interferometer.

Future System Parameters and Options

We have designed a new-generation BLR/PDV system; a diagram of the system design is shown in Figure 2. The instrument is a four-channel system that would suffice for many applications. A single, pre-chirped femtosecond laser serves as the optical source for the range system. A 4×4 splitter distributes the pulses to four probes. PDV and a timing fiducial are injected via the extra inputs on the 4×4 splitter. In each channel, a circulator directs light to and from a Michelson interferometer located near the target to minimize fiber lengths in the interferometer cavity. After returning to the circulator, the PDV signal is split off via an add/drop filter and directed to the receiver and digitizer through an optical switch. If the record length is less than the range signal propagation delay through the dispersing compensating fiber (DCF), the PDV can be recorded before the range signal arrives. Otherwise, the PDV signal can be delayed and recorded after the range signal is recorded, or simply recorded on a different receiver/digitizer channel. The range signal passes through a high-dispersion fiber to convert the optical interference signal to the time domain. Optical gain may be achieved either by distributed Raman amplification in the dispersion fiber or by a discreet erbium-doped fiber amplifier.

Important System Considerations

The use of femtosecond pulses and broadband light in BLR raises a number of issues that are not present in PDV. Some constraints on the system are

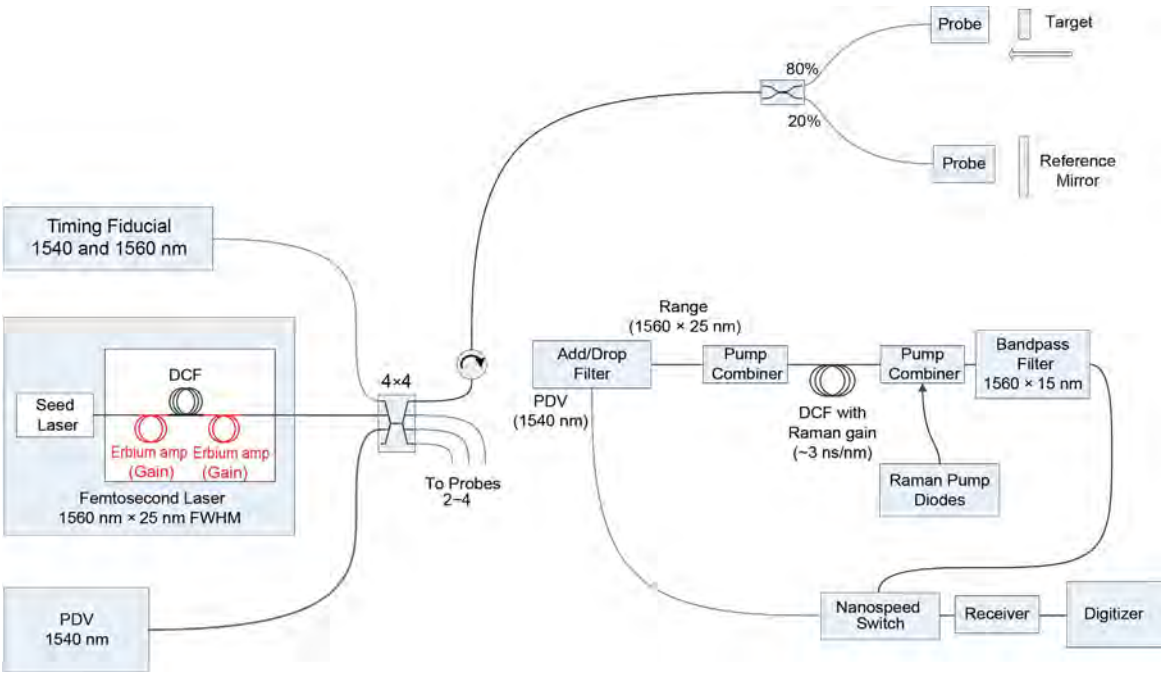

Figure 2. The 4-channel BLR/PDV system diagram with time multiplexing. The PDV signal is recorded while the range signal is propagating through the dispersing compensating fiber (DCF).

as follows: The pulse must be of minimal length and undispersed at the target to avoid a contribution due to the Doppler shift. Dispersion as well as path length must be matched in the legs of the interferometer, and polarization dispersion must be minimized and matched in both paths. Birefringence should also be minimized in the interferometer paths. Optical power must be kept low enough to avoid distortion by nonlinear optical effects; practically this limit is around 0.2 nJ per pulse but depends on many factors such as spectral width, shape, and the pulse width in time. The frequency-to-time dispersion should match the pulse width to the pulse period to make efficient use of the digitizer. We try to fill at least 80% of the time base with signal pulses. Some parameters must be chosen based on the availability of components. Other parameters are more application specific, such as distance the target will be tracked, spatial resolution, sampling rate, length of the probe downleads, and compatibility with other diagnostics such as PDV. These issues are discussed in detail below.

Interferometer Configurations

The Michelson configuration in Figure 2 is designed to minimize the fibers and components in the interferometer cavity for several reasons. Due to variation in fiber properties and layout, it may not be possible to match the dispersion and polarization in the interferometer across the entire range of wavelengths. Shorter fibers are less susceptible to environmental influences. Depending on their proximity to the explosive, the splitter and reference path components may be consumed during an experiment. A Mach-Zehnder configuration, which was used by Xia and Zhang (2009, 2010), could similarly be placed near the target but would require additional components.

Center Wavelength

In selecting the operating wavelength, one must reconcile the operating wavelengths of available components with the need for compatibility with other diagnostics, primarily PDV or MPDV. We initially tried to operate the BLR in the L-band, leaving the C-band available for MPDV. However, we found that the BLR works

better in the neighborhood of 1560 nm, primarily due to the characteristics of erbium fiber femtosecond lasers. Erbium amplifier gain drops considerably at longer wavelengths, resulting in a higher noise figure and additional slope across the band. We used Raman amplification to flatten the gain spectrum, but components such as Raman pump diodes are also more difficult to obtain for longer wavelengths.

Given the complexity of the BLR system, we believe that the best performance will be achieved with the BLR band centered about 1560 nm, near the peak of the erbium gain curve, and the PDV moved to accommodate it. In simple systems where only a few PDV channels are needed, it is much easier to move the PDV to somewhat shorter wavelengths than to move the BLR to longer wavelengths. For MPDV, we only need to ensure that those PDV channels that share probes with the BLR are at compatible wavelengths. However, this may not be practical if the MPDV is highly multiplexed or if a large number of BLR channels are needed. At that point, it may be necessary to consider moving the BLR or the PDV to the L-band.

Optical Bandwidth and Spatial Resolution

The optical bandwidth determines the limiting spatial resolution of the BLR. The spectral frequency of the interferogram fringes is proportional to the optical path difference between the reference path and the probe path, and the resolution of the FFT is determined by the spectral width of the band. The minimum separation between resolvable points Δz_{res} can be estimated from the time domain FWHM of a transform-limited Gaussian pulse:

$$\Delta t \Delta v = 0.44. \quad \textbf{(2)}$$

In terms of wavelength,

$$\Delta z_{res} = \frac{0.44\,\lambda_0^{\,2}}{2\Delta\lambda} = \frac{0.535}{\Delta\lambda}\mu\text{m}, \quad \textbf{(3)}$$

where λ_0 is the center wavelength of 1.56 µm and $\Delta\lambda$ is the FWHM of the laser. A larger value may be more realistic for the non-Gaussian spectra used in the system.

Increasing the number of bins in the spectrogram by, for example, increasing the digitizer sampling rate or the pulse dispersion allows us to detect higher frequencies that correspond to larger distances but does not improve the spatial resolution. Note that this resolution limit refers to the ability to resolve two closely spaced surfaces, not the ability to determine the location of a single surface. If we assume there is only one surface present, we can use the centroid of the FFT peak to determine its location more precisely, analogous to the situation in PDV if a single surface is assumed. The ability to determine the centroid of the peak will depend on the digitizer sampling rate and the signal-to-noise ratio in addition to the spectral width of the laser (Dolan 2010). For most signals, the uncertainty in the peak position can be an order of magnitude better than the resolution given by Δz_{res}; the precise value of the position uncertainty is an ongoing area of research.

Most of our data were acquired with the spectrum defined by a coarse wavelength division multiplexing (CWDM) filter that has a 17 nm rectangular bandpass. The advantages of using a relatively narrow spectrum are that it is easier to obtain a relatively flat, smooth laser spectrum; dispersion can be better compensated; and components generally perform better over moderate spectral ranges.

Doppler Effect, Optical Power, and Chirp

One of the challenges in the BLR system is to deliver sufficient optical power to the surface in a short pulse while avoiding nonlinear optical effects in the fiber. The optical power required depends on the probe efficiency, surface scattering properties, optical loss in the system, and recording system response. However, the maximum acceptable pulse width at the target is limited by the need to avoid sensitivity to Doppler shift. Figure 3 illustrates the effect the Doppler shift has on a slightly chirped pulse at the target. For a pulse at the target with chirp α_{Target}, a Doppler shift of f_{Dopp} produces an equivalent time shift τ_{Dopp} and a corresponding range offset z_{Dopp}.

$$\tau_{Dopp} = \frac{f_{Dopp}}{\alpha_{Target}}. \quad \textbf{(4)}$$

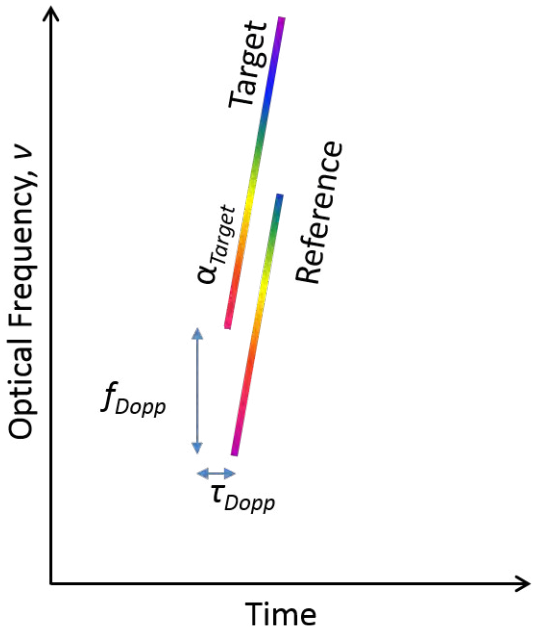

Figure 3. If the pulse is chirped at the target, a Doppler shift f_{Dopp} will produce an apparent time offset τ_{Dopp}, which may be incorrectly interpreted as a target position shift in the BLR data

If the chirp is produced by a length L_{smf} of single-mode fiber with dispersion D_{smf} (ps/nm-km) acting on an initially transform-limited pulse, the chirp α_{Target} can be expressed as

$$\alpha_{Target} = -\frac{c}{\lambda_0^2 L_{smf} D_{smf}} \quad (5)$$

and

$$z_{Dopp} = \frac{c\tau_{Dopp}}{2} = -\frac{f_{Dopp}\lambda_0^2 L_{smf} D_{smf}}{2}. \quad (6)$$

For example, dispersing a transform-limited pulse with 30 m of SMF-28 (D = 17.6 ps/nm-km at 1560 nm) will produce an offset of about 0.64 µm per GHz of Doppler shift, or 0.82 µm per km/s of velocity.

The Doppler range offset, z_{Dopp}, will either add to or subtract from the range signal z depending on the sign of the pulse chirp, the sign of the dispersion, and on which side of the balance position the interferometer is. For an anomalous dispersion fiber, such as an SMF-28 fiber, and with the target moving toward the probe, the apparent shift will be in the direction of larger time delay. Larger time delay is increased distance if the target is on the far side of the balanced interferometer position. The sign of the apparent shift will change when the target crosses the balanced interferometer position, or if a DCF is used, which has the opposite dispersion of an SMF-28 fiber.

It is relatively easy to achieve good signal levels on low-velocity measurements because the small Doppler shift allows for more chirp at the target and therefore higher pulse energy in the fiber near the target. High-velocity measurements are more demanding: the pulse must be more compressed to avoid Doppler response, limiting the energy that can be delivered to the target. The limit on optical power may be compensated to some extent by incorporating optical amplification in the dispersion path. If a simultaneous PDV measurement exists, it may also be possible to correct for the Doppler offset in the range signal if the chirp at the target is known.

The nonlinear effect of self-phase modulation, which we believe to be the most problematic in this system, can be reduced by using a Gaussian spectral distribution and avoiding sharp spectral edges in the part of the system where high optical power is needed. This is because self-phase modulation is created when there is a high rate of change of the optical power. If rectangular bandpass filters are used, they should be placed where the peak power is low, for example, at the detectors or in conjunction with optical amplifiers near the dispersion modules.

Laser

Most of our applications can be addressed with repetition rates between 10 and 100 MHz. Femtosecond fiber lasers are typically available with repetition rates up to 100 MHz, but low repetition rates associated with long travel may be difficult due to instability in the mode-locking mechanism. We initially chose to use a 100 MHz Menlo T-Light laser and built a Mach-Zehnder–based pulse picker to select the repetition rate. The laser has been reliable, but the pulse picker introduces additional loss, cost, and complexity. We subsequently purchased a laser from Kphotonics

that uses an unusual mode-locking technique based on carbon nanotubes, which is stable at low frequencies. We believe that the cost effectiveness and reliability of a laser operating at the correct frequency outweigh the flexibility offered by a high-repetition-rate laser with pulse picker.

Resolution, Repetition Rate, and Digitizer Bandwidth

The spatial resolution, optical bandwidth, repetition rate, dispersion, and recording system bandwidth are interrelated. The optical bandwidth determines the minimum distance between two resolvable points. The pulse period and the recording system bandwidth determine the number of resolvable points. The dispersion is selected to match the stretched pulse width to the pulse period.

Group Delay Balancing of the Fiber Interferometer

To analyze the experimental data, the target distance (z) from the balance point of the interferometer is determined from the interference fringe spacing (obtained via FFT of the pulse) in the optical frequency spectrum. However, the fringe spacing is constant only if the difference in group delay between the two legs of the interferometer is equal at every optical wavelength, where the group delay difference is given by

$$\Delta\tau_g(\lambda) = 1/c\cdot(n_{g1}(\lambda)\cdot L_1 - n_{g2}(\lambda)\cdot L_2), \quad \textbf{(7)}$$

where c is the speed of light, $n_{g1}(\lambda)$ is the wavelength-dependent group refractive index of leg 1, L_1 is the fiber length in leg 1, $n_{g2}(\lambda)$ is the group refractive index of leg 2, and L_2 is the fiber length of leg 2. To accomplish this matching requires that the product of group velocity dispersion (D) and fiber length (L) in both legs of the interferometer is matched, and only a free space gap (dispersion free distance) exists between them. A mismatch will cause the fringe spacing to change across the spectrum, decreasing the accuracy and resolution of the measurement and complicating the analysis. Practically, the match only needs to be better than the distance resolution in order for it to be negligible. Assuming that the dispersion characteristics of all fibers are equal, the fiber length requirement is

$$(L_1 - L_2) < 2\cdot \Delta z_{res}/(c\cdot D\cdot(\lambda_{max} - \lambda_{min})). \quad \textbf{(8)}$$

For 10 µm resolution, a spectral bandwidth of 20 nm, and group velocity dispersion of the fiber of D ~20 ps/nm-km, the fiber lengths (considering that they are double passed) need to be matched to better than ~1.25×10^{-4} km, or about 10 cm. It is important to emphasize that a group delay dispersion mismatch cannot be compensated for with a free space delay, only with a dispersive element.

When the interferometer contains long lengths of fiber, differences in the dispersion characteristics of the fibers in the reference and delay paths may become significant, making group delay matching at all wavelengths impractical. This was one of the reasons for choosing a Michelson configuration with the interferometer located at the target end of the downleads. Components such as filters and circulators are another source of mismatch dispersion in the interferometer. Reflective coatings can have significant dispersion. The best solution is to include only the essential components in the cavity. To provide an accurate match, it may be necessary to duplicate a component such as the add/drop filter, which multiplexes the PDV in the delay path, in the reference path.

Polarization

Polarization and polarization dispersion can result in signal fading and artifacts in the BLR system. As in any interferometric system, polarization must be matched in the separate paths in order to have interference. However, the BLR system requires polarization matching across a broad spectrum rather than at a single laser wavelength. A simple polarization mismatch will result in reduced fringe contrast, but usable data can still be obtained with significant mismatch. Unbalanced birefringence in the interferometer may be more detrimental as it could result in a spectral modulation in the interference signal. This could be falsely interpreted as two closely spaced target positions; we have not yet observed this effect.

Timing

A fiducial is needed to cross-time the BLR and PDV recording systems to the target surface. Due to the large dispersion used in the BLR, the propagation time in the dispersion spool depends significantly on temperature (currently about 1 ns/°C). One solution is to generate simultaneous pulses at the center BLR wavelength and at the PDV wavelength and inject them via the unused inputs to the splitter that distributes the range laser to multiple channels (Figure 2). Because the laser operates asynchronously, it is also necessary to link the wavelength of the fiducial to the corresponding wavelength in the BLR pulse. This can be accomplished by marking the start and end wavelengths in the pulse by the use of steep edges on the bandpass filter.

Calibration and Data Analysis

The system response depends on the dispersion of all of the components. Strict control over fiber lengths would improve our ability to predict the response function, but variations between batches of fiber will still be a problem. Therefore, at present it is best to calibrate the system after it is fully assembled just prior to the experiment.

Calibration consists of a series of range measurements of a substitute target placed at known distances from the probe. A Renishaw XL-80 laser interferometer provided a traceable measure of calibration target displacements.

The BLR signals are a sequence of pulses, each consisting of a spectral interferogram that has been converted to the time domain by dispersion. Data analysis requires locating each pulse, correcting for time stretch nonlinearity due to nonlinear dispersion, and Fourier-transforming it to obtain the spatial distribution of reflections from the surface. Sharp edges or structure in the dispersed laser pulse are useful for locating the pulses but contribute to artifacts in the spectrum. One approach is to use a low-pass filter to remove the interference fringes and fit the pulse envelope to a reference generated from pulses that occurred before shock arrival, then subtract the pulse envelope from all of the signals.

Integration with PDV and MPDV

In Figure 2, the PDV laser is inserted via the splitter that distributes light to each of the channels, and the PDV return is separated via an add/drop filter that follows the circulator. This arrangement avoids the need to place an add/drop filter inside the interferometer cavity but requires the PDV to use the BLR reference mirror. If a filter must be inserted in the signal path in the cavity, a duplicate filter must be inserted into the reference path to balance the dispersion. A duplicate CWDM filter must then be inserted into the reference path to compensate for the dispersion. It has been proposed that the reference mirror could be designed to reflect only the BLR signal and not the PDV signal; however, that would likely cause mismatched dispersion in the cavity and add cost if the cavity is consumed during the experiment.

Conclusion

We have demonstrated a high-speed optical range measurement system for explosive experiments. A number of successful measurements have been made with the system on explosively driven surfaces. Results of our experiments are discussed in our publication in *Review of Scientific Instruments* (La Lone 2015). A practical system design for future systems has been presented along with a discussion of the logic behind the design choices and how they relate to the application requirements. Broadband laser ranging has the potential to provide orders of magnitude more distance measurements than was possible with traditional impact pins. Therefore, we anticipate this system to be one of the main diagnostics on upcoming large-scale experiments. Planning is currently underway to build and field future systems at U1a (NNSS), Site 300 (LLNL), DARHT (LANL), and Z (Sandia).

Acknowledgments

We appreciate our collaboration with Corey Bennett of Lawrence Livermore National Laboratory, who has contributed expertise in several areas, particularly with regard to optical amplification and nonlinear optical effects. Other useful discussions with researchers at Los Alamos and Sandia National Laboratories to improve the BLR system are also gratefully acknowledged.

References

Barker, L. M., R. E. Hollenbach, "Laser interferometer for measuring high velocities of any reflecting surface," *J. Appl. Phys.* **43** (1972) 4669.

Dolan, D. H., "Accuracy and precision in photonic Doppler velocimetry," *Rev. Sci. Instrum.* **81** (2010) 053905, http://www.sandia.gov/pulsedpower/prog_cap/pub_papers/RevSciInstrum_81_053905Dolan.pdf, accessed October 17, 2015.

La Lone, B. M., B. R. Marshall, E. K. Miller, G. D. Stevens, W. D. Turley, L. R. Veeser, "Simultaneous broadband laser ranging and photonic Doppler velocimetry for dynamic compression experiments," *Rev. Sci. Instrum.* **86**, 2 (2015) 023112-1–023112-7.

Strand, O. T., D. R. Goosman, C. Martinez, T. L. Whitworth, W. W. Kuhlow, "Compact system for high-speed velocimetry using heterodyne techniques," *Rev. Sci. Instrum.* **77** (2006) 083108.

Xia, H., C. Zhang, "Ultrafast ranging lidar based on real-time Fourier transformation," *Opt. Lett.* **34**, 14 (2009) 2108–2110.

Xia, H., C. Zhang, "Ultrafast and Doppler-free femtosecond optical ranging based on dispersive frequency-modulated interferometry," *Opt. Express* **18**, 5 (2010) 4118–4129.

This page left blank intentionally

Time-Resolved Phase Transition Kinetics

STL-03-15 | Year 1 of 1

Gerald D. Stevens,[1,a] Brandon La Lone,[a] Dale Turley,[a] and Lynn R. Veeser[a]

Shock compression experiments were performed to measure the dynamic reflectance of light from the surface of tin samples shocked through the β to BCT (body centered tetragonal) solid-solid polymorphic phase transition near 9 GPa. At near-infrared wavelengths, the reflectance shows pronounced changes that indicate the transition. A technique was developed that extrapolates the low- and high-pressure behavior of reflectance through the mixed phase, allowing us to infer the value of the mixed-phase fraction. This parameter is found in most multiphase equations of state and can be used to observe the kinetics of a phase transition.

[1] stevengd@nv.doe.gov, 805-681-2219
[a] Special Technologies Laboratory

Background

For experiments that shock metal samples, prompt diagnostics often have less than a microsecond to make a measurement. Many modern shock wave diagnostics exist with nanosecond or even faster resolution. However, there remain diagnostic requirements for which the available technology is not yet fast enough (e.g., low-temperature optical pyrometry). Reflectance (or emissivity) and radiance measurements for temperature determinations are just now attaining the necessary time resolution; for shock temperatures low enough to require very sensitive long-wavelength IR receivers, the technology is not yet adequate. Among the most difficult dynamic experiments, however, a high time–resolution measurement of the material phase during a shock experiment stands out as particularly challenging.

Velocimetry has historically been the key diagnostic used to indicate shock-induced phase transitions. As a material changes phase, stress is relaxed due to the (typical) reduction in density of the high-pressure material phase. In addition, there may be a change in electronic structure, thermal conductivity, dielectric constants, optical reflectance, or other quantities. Many of these characteristics are difficult to observe directly or dynamically. Surface reflectance is one of the accessible properties of a metal in a shock experiment. We have previously seen indications of correlation between reflectance and material phase (Stevens 2010). In a series of more recent publications (Seifter 2011, Turley 2011, La Lone 2013), our group developed integrating sphere (IS) reflectance techniques to determine the emissivity and temperature of shocked tin in a region up to about 30 GPa, well above the tin β to BCT (body centered tetragonal) phase transition near 9 GPa (Mabire 2000). The Taylor wave release from our explosive drive allowed us to obtain estimates of the temperature versus stress (La Lone 2013), and the dynamic reflectance measured in those experiments showed pronounced changes while reverting phase.

The high explosive (HE) drive used for our published reflectance and temperature experiments was initiated on its axis, causing a little curvature in the shock wave; this curvature causes some variation in shock stress with radial position. The shock wave curvature increased when we reduced the HE thickness to try to lower the shock stress or decrease its release

time. Edge release from the outer diameter of the HE also quickly relieved the stress at the interface under observation, requiring us to estimate pressure with 2-D hydrodynamic calculations. Because of difficulties in accurately centering the velocimetry probe, it was difficult to precisely know the stress in the area where our reflectance measurement was taking place, and we were unable to obtain publishable data for lower shock stress values (crossing the β to BCT phase boundary). To remedy this, we performed experiments using a small gas gun to provide a flat shock over a range of shock stress values.

Project

Our gas gun has a 12.7 mm diameter barrel and uses pressurized helium as the propellant. The maximum flyer velocity of the gun is about 900 m/s. Impactors were 11.4 mm in diameter with either a 21 mm thick aluminum (the sabot) or a 2 mm thick copper impactor. A schematic of the experimental setup is shown in Figure 1. The tin samples were high-purity (99.9%) fine-grain tin purchased from Vulcan Resources, Inc., in Phoenix, Arizona. The samples were 2 mm thick by 25 mm diameter with a 4 mm thick sapphire window glued to the back by a thin (<10 µm) layer of Loctite 326 glue. The higher shock impedance of the sapphire window causes the material to be reshocked to a stress higher than that of the initial shock. This drives the phase transition at the window interface where we are observing reflectance. For shocked tin in this stress regime, the β to BCT transition occurs relatively gradually. Separate waves, commonly referred to as P1 and P2, carry the material first to the transition stress and then to the full shock stress. Conversely, when a window, such as lithium fluoride (with lower impedance than the tin sample) is used, the release of the P1 wave at the window can reduce the stress there sufficiently to prevent the sample from ever reaching the full shock stress near the window (Stevens 2010). In some such cases, therefore, the phase transition may occur in much of the bulk sample material but not at the window, where it can be detected. Our sapphire window anvil eliminates this problem.

IS reflectometry is described in detail in Seifter (2011), and reflectometry for a sample with a window is described in Turley (2011). Our latest IS design uses a custom-manufactured Labsphere Spectralon integrating sphere with an internal xenon flash lamp. Light from this lamp scatters in the IS many times and provides nearly 2π illumination of the sample. Light from the sphere wall reflects from the center of the sample into a 1 mm diameter collection fiber. A pair of fiber-optic beam interrupts separated by 30 mm and 70 mm from the end of the barrel measure the impactor velocity and provide an early (30–60 µs) pre-trigger for the flash lamp.

A small (~1 mm) hole opposite the window along the normal to the sample holds a collimated photonic Doppler velocimetry (PDV) probe. A second hole is placed ~10 degrees from the PDV probe, and contains a 1 mm diameter silica collection fiber. Light from

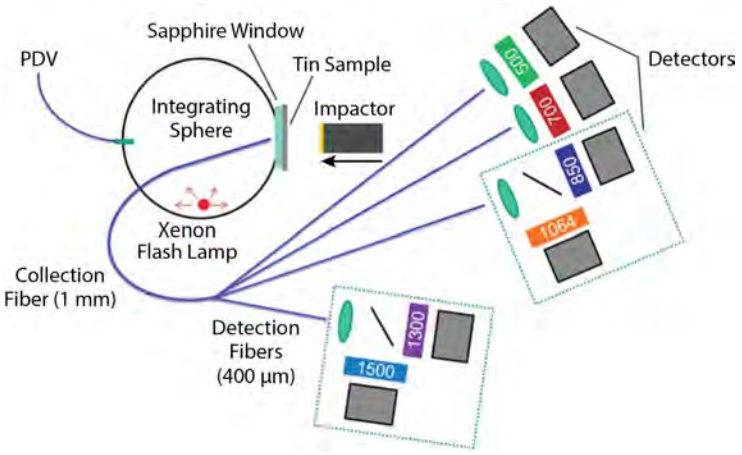

Figure 1. Schematic of experimental apparatus. A copper or aluminum impactor strikes the tin target, driving a high-pressure phase transition in the tin at the sapphire window interface. Light from the xenon flash lamp illuminates the shocked surface prior to, during, and after the phase transition occurs. Light reflected from the tin is collected by a 1 mm fiber, and split to six spectrally filtered photo receivers (details in text).

this fiber is split (by butt-coupling) into four 400 µm silica optical fibers. Between five and six reflectance detectors were used (the sixth 1064 nm channel was added for some later experiments). The basic filter scheme setup is shown in Figure 1. For the two longest wavelengths, the collimated light was split with a Thorlabs DMLP1500 dichroic filter, with the appropriate output going to each detector. The two center wavelength channels, 850 and 1064 nm, were handled similarly but were split with a DMLP950. The filter center wavelengths and pass-bands (in parentheses) were 500 (80), 700 (80), 850 (100), 1064 (10), 1300 (30), and 1550 (40) nm. The indium gallium arsenide (InGaAs) detectors for the IR wavelengths were made by replacing the photodetector on a Terahertz Technologies, Inc., TIA-950 with a larger 300 µm diameter InGaAs PIN diode from Fermionics Opto-Technology to allow use of the same detectors and filters for pyrometry, where higher sensitivity is needed. We verified that the laser light does not contribute a significant signal into the detectors. To determine the ambient reflectance, we compare the static reflectance of the glued sample to a reference standard just before the experiment is fielded. This measurement is made with a Cary 5000 spectrometer. The signals from all the optical receivers are recorded with high-speed (1 GHz) digital oscilloscopes.

Measurement Results

Figure 2a shows the normalized reflectance versus time for tin shocked to 10.6 GPa, ~1 GPa above the phase transition. Figure 2b shows reflectance data for all seven experiments. These include one experiment far below the phase transition, one far above, one near its start, and one slightly above the phase change. The reflectance curves show the (normalized) ratio of the dynamic signal to the pre-shot ambient value for each detector. The dynamic reflectance rises quickly and remains nearly constant for a period of about 300 ns after the shock enters the window. After 300 ns the stress in the sample is relieved because a rarefaction wave arrives from the back of the window. For the two shots below the phase transition, the reflectance decreases with increasing pressure at shorter wavelengths. Above the transition the reflectance increases under shock stress for all wavelengths. Once the transition is complete, the reflectance in the BCT phase decreases with stress. We are planning future experiments to observe the reflectance behavior of tin released across the melt boundary.

Near the transition there is often a small reflectance decrease before the fast rise to a constant level. This suggests that the tin is partially in its β state during the phase-transformation process.

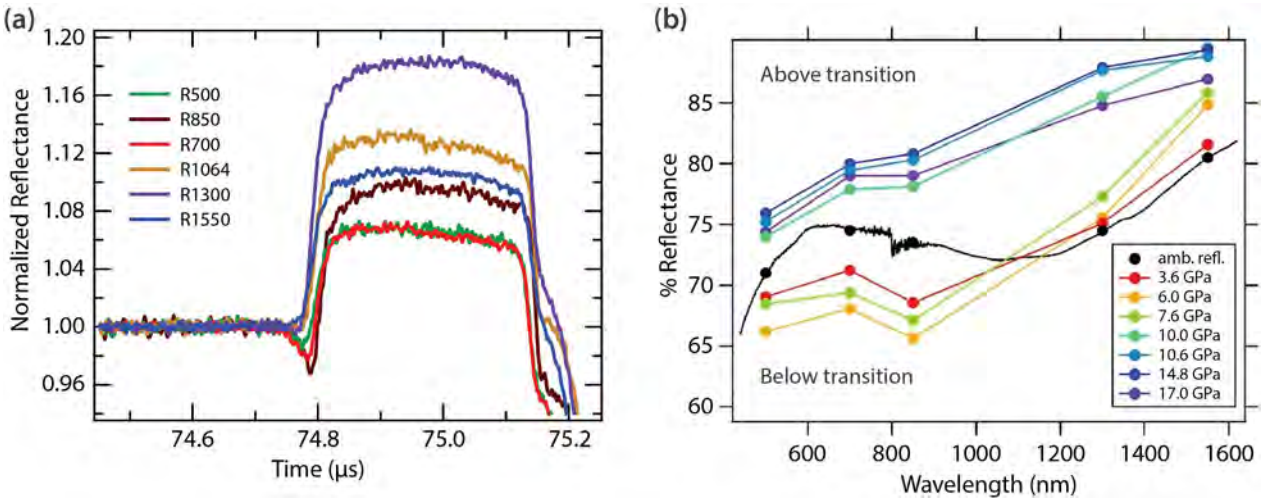

Figure 2. (a) Normalized reflectance (six spectral channels) versus time for tin shocked to 10.6 GPa. (b) Tin reflectance versus wavelength (static, and at pressure, for seven experiments). The low-pressure behavior of the short wavelength channels is a strong indicator of the phase of the material.

The dynamic reflectance changes, ΔR, for all seven experiments are shown in Figure 3. The low-pressure dependence of the β phase may be described for each wavelength by a linear fit (dashed lines). Likewise, the high-pressure behavior of the BCT phase for the two highest pressure experiments was fit by a line. At intermediate stresses near the phase transition, the tin is likely in a mixed phase, so that some fraction (α) of it is in the BCT phase and the remainder in the β phase. We created a reflectance change function, $R(\lambda,P,\alpha)$, from the extrapolated low- and high-pressure linear response and minimized its distance (i.e., $(\Sigma_\lambda (R(\lambda,P,\alpha) - R_{meas}(\lambda,P))^2)^{1/2}$) from our measured reflectance data ($R_{meas}(\lambda,P)$) in order to estimate the phase fraction α from our measurements. The results are shown in Figure 4a, with a sigmoid fit to guide the eye (the sigmoid is a special case of a logistic function used to describe processes that grow exponentially then slow as saturation occurs and growth stops). The gradual onset and completion of the phase transition with stress are highlighted in Figure 4. This phase fraction versus peak stress curve would be nearly impossible to determine from velocity wave profile measurements alone. It is important to notice that the fit fractions for the two points at 3.6 and 14.9 GPa are not 0 and 1. These points were used to define and extrapolate the low- and high-pressure behavior, and should give phase fractions of 0 and 1; the differences from these values could be considered to be approximate error bars.

Our technique to infer phase fraction may also be applied to the time-dependent reflectivity data, using stress determined from the velocity record in order to determine the phase fraction as a function of time, elucidating the kinetics of the underlying transition. The extracted phase fraction as a function of time is shown in Figure 4b: at low stresses the transition takes ~100 ns to progress, while at the highest stress (17.3 GPa), it takes on the order of 20 ns to progress. Our PDV data quality was poor; thus, the extraction of α at early times is uncertain. Early sample motion was also detected, perhaps due to a misaligned barrel extension. Note that the traces in Figure 4b were cropped after shock arrival, where the PDV signal-to-noise ratio was adequate.

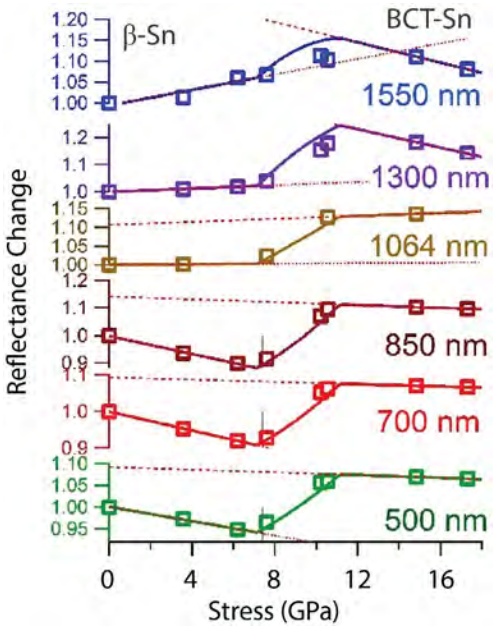

Figure 3. Reflectance changes versus stress for all experiments. Red dashed lines are linear fits to the low- and high-pressure behaviors at each wavelength.

Phase-Transition Modeling

We used two hydrodynamic codes to model the phase transformation and estimate the fractions of material in each phase at a given time during the transformation. One is the 1-D Lagrangian wave propagation code, WONDY (Kipp 1982), with a non-equilibrium, three-phase mixture model developed by Hayes (1975). Phase-transition model parameters (entropy and specific energy) were determined by matching the wave-profile data of Mabire (2000) using the equation of state (EOS) parameters from Mabire (Hayes 2005). The model calculates the phase transformation by equating the temperature and Gibbs free energy of the two phases in the mixture. With WONDY we found that the calculations, which fit the Mabire data well, did not match the data of Anderson (2000) without changing some of the parameters. Because the parameter changes were largely empirical, this process was somewhat disappointing and left us in some doubt as to the validity of the calculated phase fractions. One problem is that our version of the code does not include material strength for the tin.

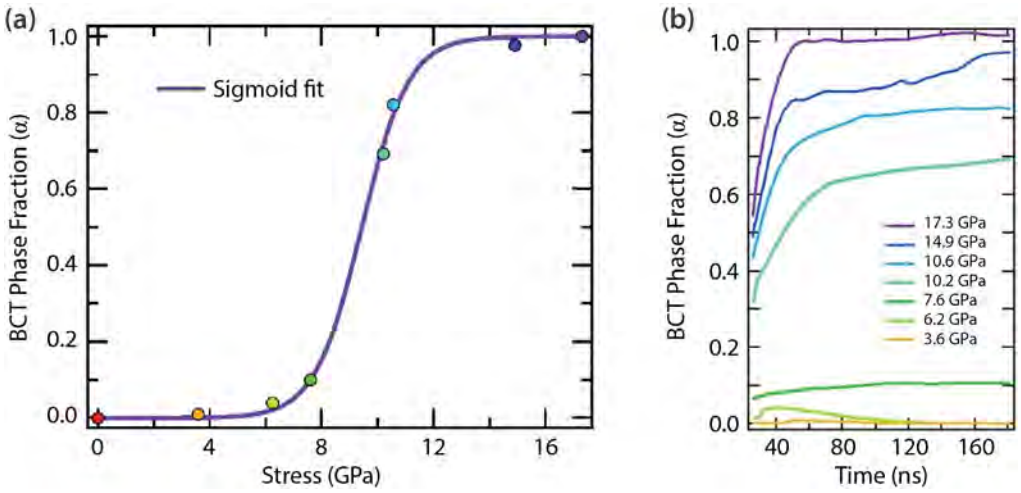

Figure 4. (a) Inferred phase fraction versus stress from our experiments. (b) Phase fraction versus time for seven different peak stresses.

To understand the edge releases and calculate the phase transformation in another way, we carried out 2-D simulations using CTH, a multidimensional Eulerian shock physics code (McGlaun 1990). For tin, we used an elastic-plastic strength model of Steinberg and a Mie-Grüneisen EOS. For the β to BCT phase transition, we used the CTH two-phase EOS model PTRAN (phase transition) with BCT parameters taken, as far as possible, from Anderson (2000). The phase transition is modeled by specifying the pressure at the phase boundary as a function of density and temperature of the mixture, ρ and T, and the fraction of material that has transformed, α.

$$P(\rho,T,\alpha) = P_T + B_T(1 - \rho_T/\rho) + A_T(T - T_0) + A_\alpha\,\alpha. \quad (1)$$

Here P_T and ρ_T are the transition pressure and density of the β phase at ambient temperature, B_T is the bulk modulus in the transition region, A_T is the derivative of the phase boundary with respect to temperature, and A_α is the derivative of the phase boundary with respect to α. From Mabire (2000), P_T = 9.0 GPa and A_T = −0.017 GPa/K. Time dependence of the transformation was modeled by setting the derivative of the transition pressure with respect to the fraction of material remaining untransformed (CTH parameter AX) to 0.8 GPa. Using CTH we again found it necessary to change input parameters to obtain relative agreement with the Anderson data. To match our data, we found it necessary to modify the β-phase density at the transition.

The two codes calculate roughly the same phase fractions. In general they show a considerably sharper transition from β to BCT as a function of stress than that indicated by our measurements, as described above. In light of the difficulties we encountered in matching the free surface velocities, it is difficult to trust either code. Until there is a very accurate EOS for β tin, extensive work on the calculations may be hard to justify. Our results are, however, already pushing us to consider methods to refine the multiphase EOS models within several hydro-codes.

Imaging and Reverse Ballistic Impact Experiments

In addition to the flash lamp integrating sphere reflectance (FISR) experiments, we performed one explosively driven imaging FISR experiment, and nine reverse ballistic impact gas gun experiments. A schematic of our imaging experiment is shown in Figure 5a. A nine-frame framing camera with a 700 × 80 nm filter and a gated mid-wave IR camera (with a 3–5 μm bandpass filter) were placed outside of the IS and explosive vessel, sharing a line of sight via a large calcium fluoride dichroic beam splitter (not shown) with a custom coating that is reflective in

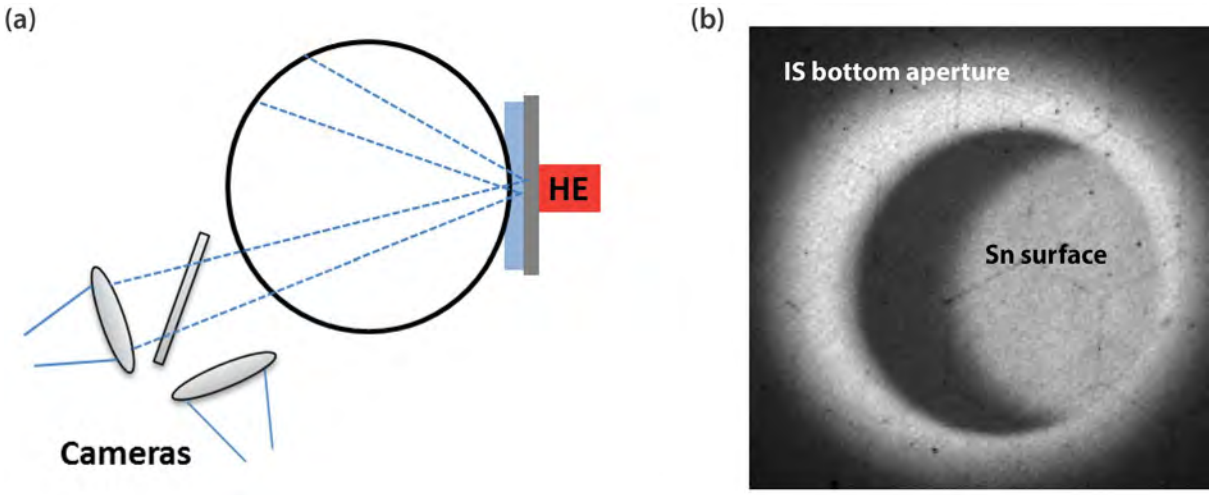

Figure 5. (a) Schematic showing our imaging FISR experiment. Two layers of Detasheet explosives drive the tin to a mixed phase, while we observe light reflected from the surface with two fast cameras. (b) Image of the shocked tin surface showing the uniformity of the light reflected by the mixed-phase tin (dust and a fiber faceplate "chicken-wire" pattern are also visible).

the visible spectrum and transparent at wavelengths longer than 3 microns. The flash lamp was located off to the side of the line of sight so as not to be directly visible or obstruct the view. The images are centered on the bottom aperture of the IS and show a reflection off of the shocked surface as well as a dark crescent-shaped shadow, which is the back side of the sphere reflected off of the surface. The nine visible frames were 166 ns wide, spaced by 300 ns each. Three of the images occurred during the Taylor release of the experiment, while the other frames were prior to motion and after the window shattered.

The third of the nine images, recorded near the peak stress (10 GPa) of the experiment, is shown in Figure 5b. This stress shocks the tin into the mixed phase with a long time constant for the transition. The image shows uniformity across the shocked region (the hexagonal pattern is due to the fiber faceplate of the camera), and the light level recorded for this and the next two frames gave reflectances consistent with 700 nm band values we observed in our gas gun experiments. The IR image was similarly uniform in thermal radiance (it is blind to the flash lamp). This experiment suggests that the β to BCT transition proceeds in a homogeneous manner for the fine-grained tin we used. This is a significant result that supports our fiber-coupled reflectance measurements and extractions of the phase fraction; our inference model assumes that the total reflectance is a mixture of the individual reflectances for the two phases (i.e., that we are not observing individual heterogeneous regions of one phase or the other).

Jensen (2009) demonstrated that the reverse ballistic impact shot configuration gives clear indications of the kinetics of the α to ε phase transition in iron. We performed four tin and five iron reverse ballistic–impact experiments, impacting sapphire targets. Five of the nine experiments implemented the FISR technique, while four only recorded velocimetry. Unfortunately, a gas-shock flash of light made interpretation of the FISR experiments uncertain, and a similar precursor wave (either barrel, or due to the gas shock) made it difficult to observe the overshoot and relaxation into the high-pressure phase. Despite these difficulties, the benefits of this configuration make it worth pursuing in the future, and we intend to continue this line of experiments next fiscal year.

Conclusion

We have developed a methodology to obtain the dynamic phase fraction of shocked materials using

optical reflectance. Our method extrapolates the low- and high-pressure behavior of two isomorphic phases, and minimizes the residuals of the measured reflectance from the extrapolated reflectances across six spectral channels. For tin, we see the β to BCT transition begin at 6 GPa and complete at 12 GPa. The time it takes for the shocked material to come to equilibrium in a final mixed phase varies with stress—from tens to hundreds of nanoseconds. Because our technique requires knowledge of the dynamic stress at the interface as an input parameter, accurate velocimetry will help increase the fidelity of the kinetics behavior observations. The technique works well for tin; future experiments will look for the melt boundary in tin and begin investigating zirconium.

Acknowledgments

The authors would like to thank Roy Abbott, Ben Valencia, Rick Allison, and Mike Grover for technical assistance with experiments.

References

Anderson, W. W., F. Cverna, R. S. Hixson, J. Vorthman, M. D. Wilke, G. T. Gray III, K. L. Brown, "Phase transition and spall behavior in β-Tin," *AIP Conf. Proc.* **505** (2000) 443.

Hayes, D. B., "Wave propagation in a condensed medium with *N* transforming phases: Application to solid-I-solid-II-liquid bismuth," *J. Appl. Phys.* **46**, 8 (1975) 3438.

Hayes, D. B., private communication, 2005.

Jensen, B. J., G. T. Gray III, R. S. Hixson, "Direct measurements of the *α-ε* transition stress and kinetics for shocked iron," *J. Appl. Phys.* **105**, 10 (2009) 103502-1–103502-7.

Kipp, M. E., R. J. Lawrence, "WONDY V: A one-dimensional finite-difference wave-propagation code," SAND81-0930, Sandia National Laboratories, Albuquerque, New Mexico, 1982.

La Lone, B. M., G. D. Stevens, W. D. Turley, D. B. Holtkamp, A. J. Iverson, R. S. Hixson, L. R. Veeser, "Release path temperatures of shock-compressed tin from dynamic reflectance and radiance measurements," *J. Appl. Phys.* **114** (2013) 063506-1–063506-14.

Mabire, C., P. L. Héreil, "Shock induced polymorphic transition and melting of tin," *AIP Conf. Proc.* **505** (2000) 93–96.

McGlaun, J. M., S. L. Thompson, M. G. Elrick, "CTH: A three-dimensional shock wave physics code," *Int. J. Impact Eng.* **10**, 1–4 (1990) 351–360.

Seifter, A., M. Grover, D. B. Holtkamp, A. J. Iverson, G. D. Stevens, W. D. Turley, L. R. Veeser, M. D. Wilke, J. A. Young, "Emissivity measurements of shocked tin using a multi-wavelength integrating sphere," *J. Appl. Phys.* **110**, 9 (2011) 093508.

Stevens, G. D., W. D. Turley, L. R. Veeser, B. J. Jensen, P. A. Rigg, "Reflectance changes during shock-induced phase transformations in metals," *Rev. Sci. Instrum.* **81**, 6 (2010) 065101.

Turley, W. D., D. B. Holtkamp, L. R. Veeser, G. D. Stevens, B. R. Marshall, A. Seifter, R. B. Corrow, J. B. Stone, J. A. Young, M. Grover, "Infrared emissivity of tin upon release of a 25 GPa shock into a lithium fluoride window," *J. Appl. Phys.* **110**, 10 (2011) 103510-1–103510-8.

This page left blank intentionally

Development of Fluorescent Technetium Compounds as a Radioactive Distributed Source

RSLN-25-14 | Continued from FY 2014 | Continuing in FY 2016 | Year 2 of 3

Wendy Chernesky,[1,a] Matthew Ackerman,[b] Kiah Mayo,[b] Eunja Kim,[b] Frederic Poineau,[b] Trevor Low,[b] Julie Bertoia,[b] and Ken Czerwinski[c]

Many types of radioactive sources are used for training at the NNSS. The metastable isotope technetium-99 (^{99m}Tc), due to its relative short half-life, gamma emission, and availability from commercial generators, is an attractive radionuclide for training and evaluation. However, the ground state ^{99}Tc has low specific activity. The ability to detect the host material containing Tc would provide a means to ensure the fate and transport of the element conforms to expectations. Incorporating the ^{99m}Tc into a chemical form that fluoresces in the visible from UV stimulation provides a means to track the Tc. Natural fluorescent minerals based on silicate species can provide a robust host matrix for Tc that is stable and benign in the environment. Two goals of this 3-year project are to prepare a number of fluorescent silicates with technetium incorporated into the matrix and to evaluate the resulting compound stability for each silicate compound. Last year, we prepared fluorescent compounds. Materials and synthetic routes were identified for fresnoite ($Ba_2TiSi_3O_8$), calcium tungstate or powellite ($CaWO_4$), and calcium molybdate or scheelite ($CaMoO_4$) compounds, identifying $CaWO_4$ and $CaMoO_4$ as the fluorescent compounds of interest (Chernesky 2015). This year we modeled Tc incorporation into $CaWO_4$ and $CaMoO_4$, thereby establishing the coordination chemistry of Tc into the candidate materials. Fluorescence and stability of powellite and scheelite were examined in the laboratory through optical spectroscopy studies, synthesis of compounds with Tc, and examination of Tc release in aqueous conditions. Our results demonstrated the ability to produce powellite and scheelite particles with Tc. The fluorescence behavior provided quantitative data for selecting and establishing practices we can employ in the field. The aqueous solubility studies demonstrated that these materials maintain incorporation of Tc. The modeling studies support the selection of both materials, with expected enhanced stability due to interstitial coordination of Tc. When this project continues in FY 2016, we will finalize and prepare the compounds, ultimately using them in training exercises at the NNSS.

[1] chernewj@nv.doe.gov, 702-295-8625
[a] Remote Sensing Laboratory–Nellis; [b] University of Nevada, Las Vegas; [c] North Las Vegas

Background

The focus of this 3-year project is the incorporation of the metastable isotope technetium-99 (^{99m}Tc) into a robust, fluorescent material for operational radiation detection training. The low-energy gamma decay of ^{99m}Tc (142 keV, $t_{1/2}$ = 6.01 hours) allows for small amounts of the nuclide to be added to a host phase and dispersed. Following its decay to ^{99}Tc, which is a pure β-emitter (214 keV, $t_{1/2}$ = 210,000 years) (Schwochau 2000), a dramatic decrease of activity in the material occurs, and detection by standard

techniques becomes operationally challenging for field responders. However, if the technetium is incorporated into a fluorescent mineral, training can be extended to longer periods because dispersed samples can then be easily identified under UV black light.

Ideal characteristics of the fluorescing material include resistance to chemical and environmental degradation, resistance to UV damage from the sun, and optimal synthetic parameters (i.e., one-pot synthesis, absence of atmospheric oxygen in reaction system, short reaction time, synthetic temperatures below 1000°C, cost and availability of starting products) required for generation of the material. Initial investigations on the incorporation of Tc into the minerals were performed in FY 2014 (Chernesky 2015). In FY 2015 we modeled technetium incorporation into calcium tungstate, or powellite ($CaWO_4$), and calcium molybdate, or scheelite ($CaMoO_4$). We then evaluated the resulting amount incorporated and the structural phases present within these materials.

Project

Scheelite and Powellite Synthesis and Characterization

Scheelite and powellite can both be synthesized from the solid-state reaction of MO_3 (M = Mo, W) and calcium oxide (CaO) at elevated temperatures (Abdel-Rehim 2001). Scheelite emits as a blue phosphor, whereas the powellite is yellow. In this year's work, the scheelite and powellite samples were prepared by treating powders of MO_3 CaO at a 1:1.25 mol stoichiometry based on FY 2014 results. These samples were reacted under argon atmospheric conditions in a furnace at 860°C for 2 hours.

Samples with Tc were prepared from 2 grams of precursor. A stock solution in water of $KTcO_4$ at 14.7 mg Tc/mL was added to the precursor at a 1:1.25 mol ratio of MO_3 (M = Mo, W) and CaO. The Tc concentration was varied from 0.1 mol % to 10.0 mol %, which corresponds to 8 µL to 800 µL of TcO_4^- stock solution. After the addition and mixing of the Tc stock, the resulting mixture was treated with methanol in a ratio of 1 gram of oxides to 100 µL of methanol. The powder from small agglomerations, which when heated to 860°C for 2 hours produced fluorescent particles approximately 2 mm in diameter (Figure 1).

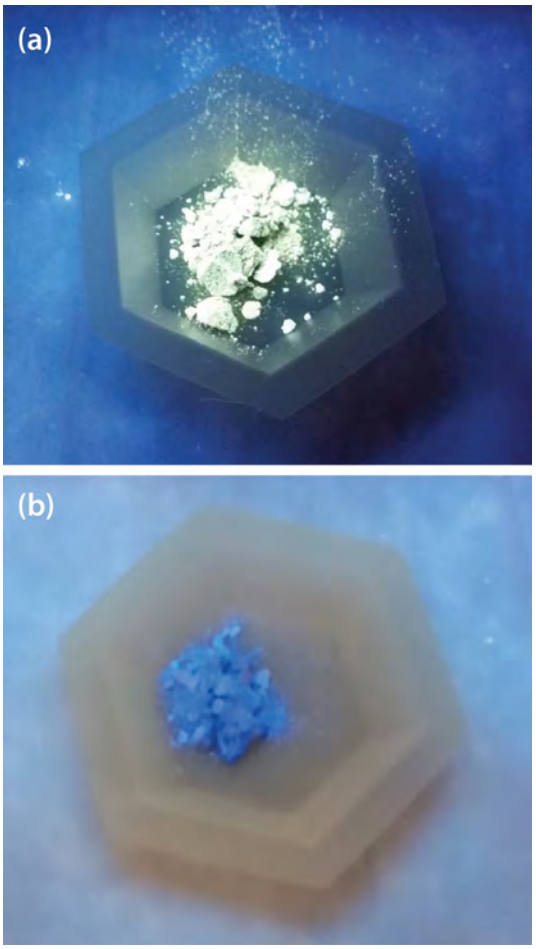

Figure 1. (a) Scheelite ($CaMoO_4$) and (b) powellite ($CaWO_4$) with 1 mol % Tc

The samples in Figure 1 fluoresce under a standard, handheld UV lamp. To provide the optimal conditions for fluorescence observation, the optimal excitation and emission properties of the materials were quantified. The samples were examined with a Fluorolog-3 Spectrofluorometer for both emission and excitation from 200 to 800 nm. Samples of $CaMoO_4$ and $CaWO_4$ with 0 mol % to 1 mol % Tc were placed in reduced volume fluorescence cuvettes and sealed with a screw cap. The optimal excitation condition was evaluated by

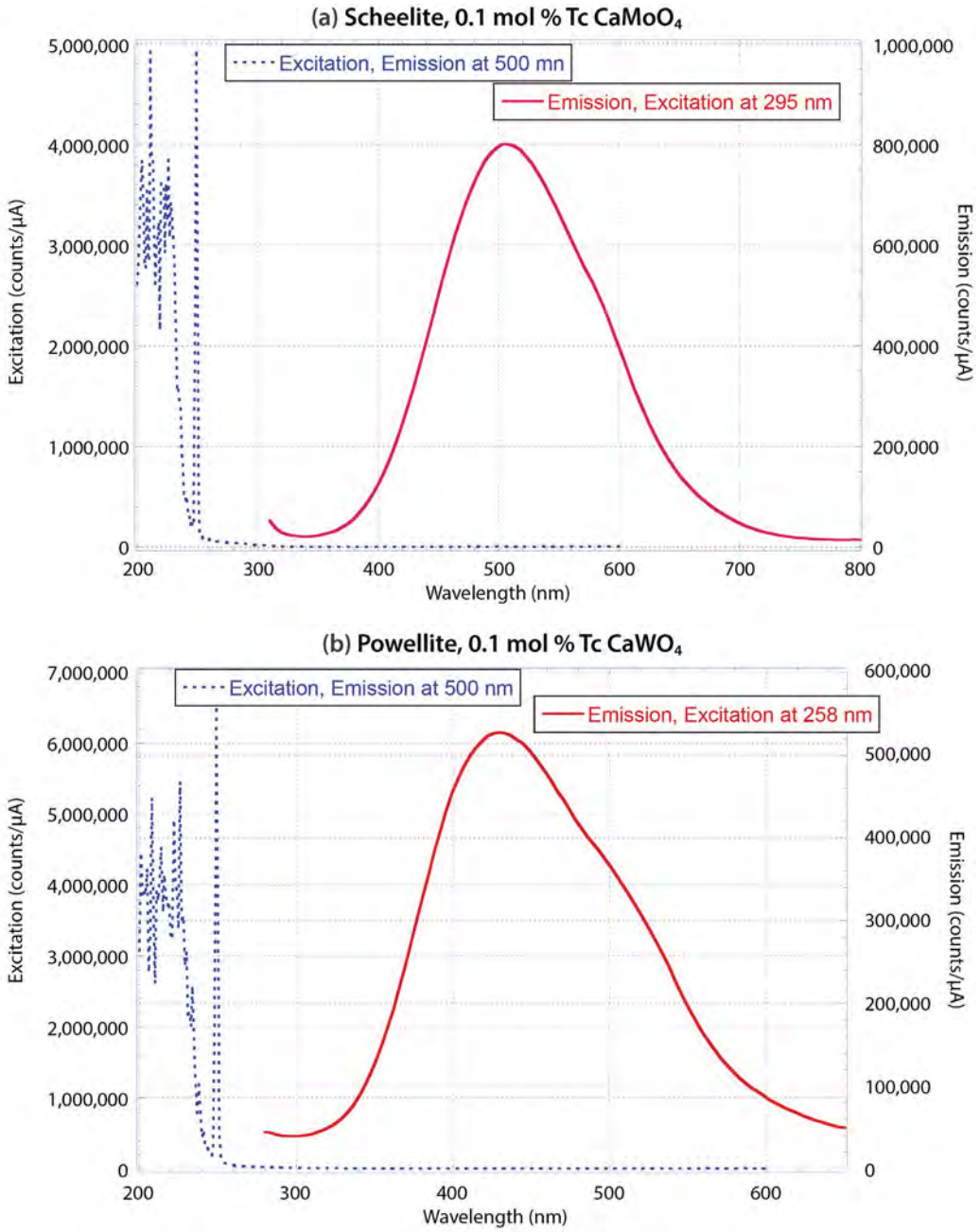

Figure 2. Excitation and emission spectra for (a) scheelite ($CaMoO_4$) and (b) powellite ($CaWO_4$) with 0.1 mol % Tc; changes in the bonds of the silicate from the incorporation of Tc into the matrix may be causing changes in the emission peak for powellite

measuring emission at 500 nm for each sample. These results determined the excitation wavelength, which was, in turn, used to evaluate the sample emission spectra (Figure 2). The data were fairly consistent for the examined samples (Table 1). Variations were observed between the excitation and emission peaks for the materials, indicating a route for discrimination between these matrices. Some change in the emission peak for powellite was observed with increased Tc concentration, which may be due to changes in the bonds of the silicate from the incorporation of Tc into the matrix (Tc coordination).

Table 1. Emission and excitation data for scheelite and powellite with varied Tc concentration. FWHM is the full width half maximum of the emission peak.

Sample	mol % Tc	Excitation Wavelength (nm)	Emission Peak (nm)	FWHM (nm)
Scheelite	0	295	505	149
Scheelite	0.1	295	505	160
Scheelite	1.0	295	508	211
Powellite	0	257	421	113
Powellite	0.1	258	430	161
Powellite	1.0	257	466	166

The solubility of Tc of the prepared samples in water was investigated. The samples had Tc concentrations from 0.1 mol % to 10 mol % Tc. The solubility was examined from 100 mg of material, similar to Figure 1, in 10 mL of water. The solution was mixed; 100 µL was periodically removed for scintillation counting to determine Tc solution concentration. Both materials exhibited an initial rapid release followed by a constant Tc concentration (Figure 3). Higher Tc release was observed for powellite, with a maximum Tc concentration of 1×10^{-7} M in solution. For all systems examined, the released Tc represented less than 0.01% of the total inventory. This release mechanism is consistent with rapid surface desorption for a minor fraction of surface sites.

Computational Studies

The Tc-doping mechanisms in scheelite based on an atomistic approach were investigated using density functional theory (DFT) and compared with experimentally reported results. Technetium incorporation into scheelite was also systematically investigated. The defect formation energies were calculated and used to determine the most energetically stable sites for Tc in scheelite.

First-principles total energy calculations were performed using the spin-polarized DFT, as implemented in the Vienna *ab initio* simulation package (VASP) (Kresse 1996). The exchange-correlation energy was calculated using the generalized gradient approximation

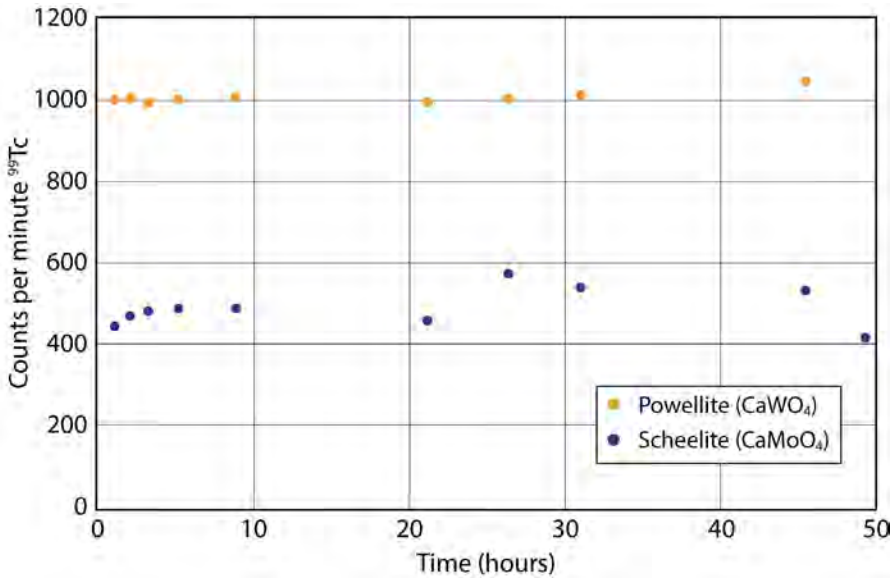

Figure 3. Release of ^{99}Tc from scheelite and powellite with 10 mol % Tc over time in water

with the parametrization of Perdew and Wang (1992). The convergency test was performed by varying the plane-wave cutoff energy for the electronic wave functions from 300 to 500 eV. Structural optimizations and properties calculations were carried out using the Monkhorst-Pack special k-point scheme (Monkhorst 1976). The (4×4×4) k-point meshes were used for integrations in the Brillouin zone of bulk systems. The periodic boundary conditions were employed to mimic the bulk system. The total energy and cell volumes of powellite were used to derive an equation of state for powellite from the following expression:

$$P = -\frac{\partial E}{\partial V}. \quad (1)$$

Calculations were also performed to determine the compression behavior, the bulk modulus (K), for $CaWO_4$.

$$K = V_0 \frac{\partial^2 E}{\partial V^2} \quad (2)$$

A single technetium atom was included at predicted sites among the powellite lattice, and the total energy was calculated. In the case of the Tc-doped species of powellite studied here, the inclusion energy, E_I, was calculated using the following expression:

$$E_I = \sum E_{products} - \sum E_{reactants}. \quad (3)$$

The calculated lattice constants, bulk modulus, and volume compression data of $CaWO_4$ are in excellent agreement with experimental data. Defect formation energies have been calculated for several possible sites of Tc in scheelite. The calculated vacancy formation energies of W and Ca are 11–18 eV, ruling out direct inclusion of Tc in scheelite. It is found that both I(O_h) and S(W) are energetically compatible for Tc doping (Figure 4). The diffraction patterns of each Tc defect were predicted from the optimized structures calculated from DFT, and that may help interpret complex x-ray diffraction patterns experimentally. The results also indicate that Tc incorporated into powellite will minimize energy.

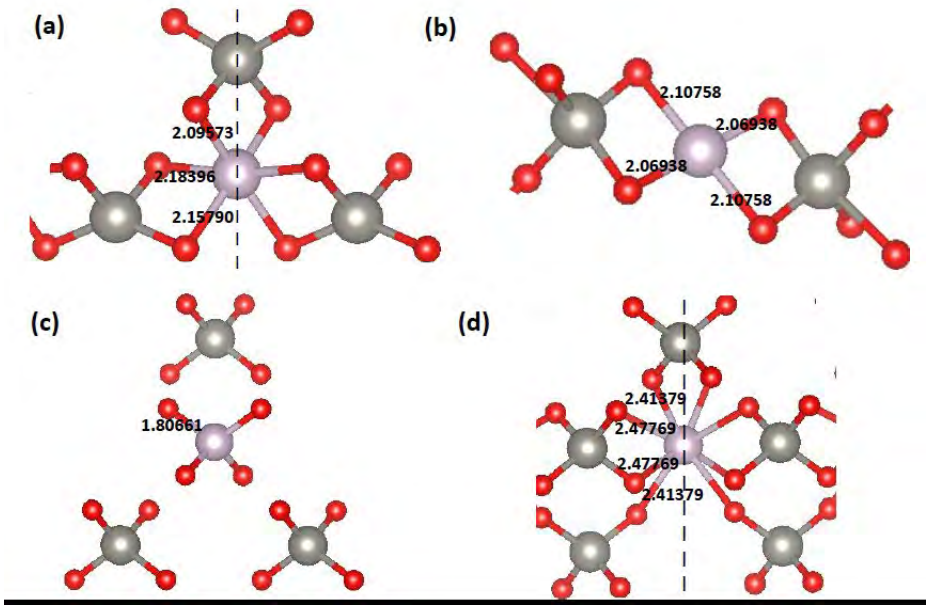

Figure 4. Tc-O bonds and bond distances for (a) $CaWO_4$:Tc; I(O_h), (b) $CaWO_4$:Tc; I(C), (c) $CaWO_4$:Tc; S(W), and (d) $CaWO_4$:Tc; S(Ca). Where appropriate, symmetry in the bond lengths has been indicated by dashed lines. The bond distances are in angstroms (Å).

Conclusion

This was the second year of a proposed 3-year project. The fluorescence and Tc stability of scheelite and powellite were established. Technetium was successfully incorporated into both matrices as 1 cm monoliths and 2 mm particles. The fluorescence behavior provided quantitative data for selecting and establishing techniques for field observation. The aqueous solubility studies demonstrated the ability of powellite and scheelite to maintain incorporation of Tc. The modeling studies support the selection of both materials, with expected enhanced stability due to interstitial coordination of Tc.

Efforts in FY 2016 will develop methods to provide a scheelite or powellite product with ^{99m}Tc for use in the field. The product will be prepared materials to permit application to a test area at the NNSS that is approximately 90 m^2. Based on NNSS test requirements, we expect the activity will need to be 20–40 mCi ^{99m}Tc at the time of application. We also expect to produce ~1000 particles with a diameter of 2 to 5 mm and disperse a concentration of 11.1 particles/m^2 in the test area.

References

Abdel-Rehim, A. M., "Thermal analysis and x-ray diffraction of synthesis of scheelite," *Journal of Thermal Analysis and Calorimetry* **64** (2001) 1283–1296.

Chernesky, W., E. Johnstone, R. Borjas, W. Kerlin, M. Ackerman, K. Mayo, E. Kim, F. Poineau, K. Czerwinski, "Development of technetium into fluorescent materials for training in radiation detection," in *Site-Directed Research and Development*, FY 2014, National Security Technologies, LLC, Las Vegas, Nevada, 2015, 59–69.

Kresse, G., J. Furthmüller, "Efficient iterative schemes for *ab initio* total-energy calculations using a plane-wave basis set," *Phys. Rev. B* **54** (1996) 11169–11186.

Monkhorst, H. J., J. D. Pack, "Special points for Brillouin-zone integrations," *Phys. Rev. B* **13** (1976) 5188–5192.

Perdew, J. P., Y. Wang, "Accurate and simple analytic representation of the electron-gas correlation energy," *Phys. Rev. B* **45** (1992) 13244–13249.

Schwochau, K., *Technetium: Chemistry and Radiopharmaceutical Applications*, Wiley-VCH, Weinheim, Germany, 2000, 3.

Transition Edge Sensor Using High-Temperature Superconductivity Operating at High Critical Temperature Tc

RSLN-21-15 | Year 1 of 1

Paul Guss,[1,a] Michael Rabin,[b] Mark Croce,[b] Nathan Hoteling,[c] and Sanjoy Mukhopadhyay[c]

We demonstrate very high–resolution photon spectroscopy with a microwave-multiplexed 4-pixel transition edge sensor array. The readout circuit consists of superconducting microwave resonators coupled to radio frequency superconducting-quantum-interference devices and transduces changes in input current to changes in phase of a microwave signal. We used a flux-ramp modulation to linearize the response and avoid low-frequency noise. This demonstration establishes a path for the readout of cryogenic x-ray and gamma ray sensor arrays with more elements and spectral resolving powers.

[1] gusspp@nv.doe.gov, 702-295-1552
[a] Remote Sensing Laboratory–Nellis; [b] Los Alamos National Laboratory, [c] Remote Sensing Laboratory–Andrews

Background

A transition edge sensor (TES) is a thermal sensor that measures an energy deposition by the increase of resistance of a superconducting film biased within the superconducting-to-normal transition. Small arrays of TESs have been demonstrated, and kilopixel arrays are under development (Irwin 2005, Figueroa 2014). A TES is essentially a calorimeter made up of two components, a bulk absorber that stops the incident gamma rays and a thermometer made from a thin film electrically biased in the superconducting-to-normal phase transition (Horansky 2007).

This work has three long-term goals. Our first is to perform modern x-ray absorption spectroscopy (XAS) without a synchrotron. Currently, using a 160-pixel microcalorimeter array and a relatively weaker x-ray source, without a synchrotron, it takes about one day to complete XAS. However, actinide extended x-ray absorption fine structure (EXAFS) and x-ray absorption near edge structure (XANES) can lead to a factor up to ten times faster in planned systems for weapons materials measurements supporting stockpile stewardship and environmental legacy work. The second goal is to break the 1% barrier for gamma photopeak energy resolution for special nuclear material (SNM) nondestructive assay (NDA). A 256-pixel microcalorimeter array holds promise to do this with a strong immunity to a large class of systematic errors. This immunity transfers to improvement over high-purity germanium (HPGe) measurements for worldwide nuclear safeguards and emergency response. Our third goal is to perform microchemical analysis in electron microscopy. Just a 16-pixel microcalorimeter array can measure x-ray chemical shifts, measuring oxidation states, elemental ratios, and organic bonding (C, N, O) with 10–100 nm resolution for nuclear forensics. Figure 1 graphically depicts the potential of each goal.

This project addresses two major barriers to reaching the goals outlined above: (1) Practical analytical instruments will need thousands of pixels, each tens of times faster than current microcalorimeters, at a factor hundreds higher data throughput. (2) We can fabricate and cool high-resolution sensor arrays, but

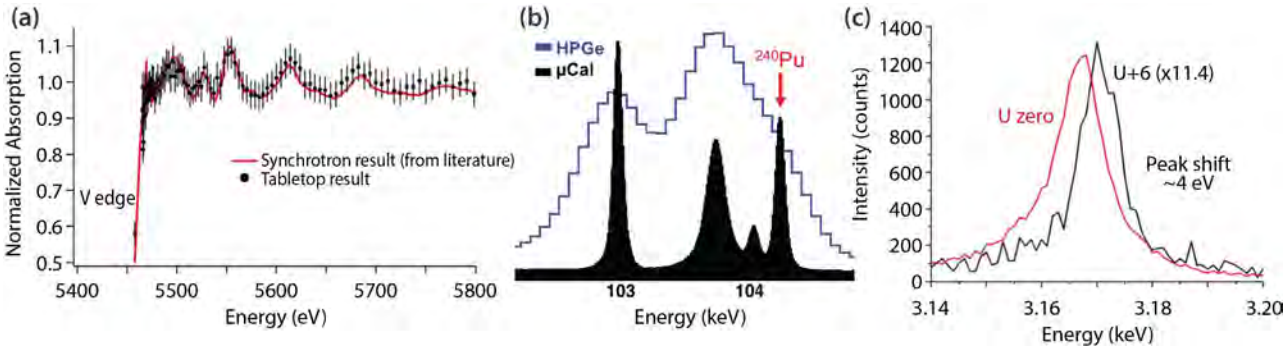

Figure 1. Impact of TES technology shown for (a) XAS, (b) SNM NDA, and (c) microchemical electron microscopy

we cannot read them out due to heat load, cryogenic complexity, and cost. A scalable readout technology is required.

In approaching this work, we sought to leverage several key science ideas related to low-temperature detectors. To begin, very low temperatures translate into low noise; this is now much more easily achieved (10 mK < T < 10 K with no liquid helium and no liquid nitrogen). We also sought to exploit the low noise aspect for unparalleled measurement performance of signal-to-noise ratio (for magnetic or electric field response, absorbed power or energy, and response time). Superconductors allow us to do things impossible with conventional materials, one example being their very low band gap (meV) compared to that of semiconductors or scintillators (eV). Ultimately, our successful development of this technology would benefit quantitative nuclear materials characterization, including x-ray, gamma ray, alpha particle, and nuclear reaction energy spectroscopy. The technology could be useful in the areas of actinide chemistry, nuclear forensics, treaty verification, and safeguards.

TESs, superconducting single-photon detectors, have been useful thermal detectors since the 1990s (Figure 2). When an x-ray is absorbed in a detector, its energy is converted into heat; the TES measures the temperature change in the following manner. A very small current is run through a thin superconducting film whose temperature is kept just inside the transition region between its normal and superconducting states (Figure 3). The transition is not a step function, and it occurs over a narrow range in temperature. In that narrow temperature range, the TES acts as a very sensitive thermometer. We exploit this effect to make a very precise measurement of the energy of incoming x-rays. TESs not only have high resolution, but also are high-efficiency detectors. Their characteristics make them superb x-ray spectrometers. Being able to do high-resolution spectroscopy allows us to analyze a large number of measurements relevant to DOE core missions (Morgan 2015).

A TES is a thermometer made from a superconducting film operated near its transition temperature Tc. The low temperature is needed because the energy resolution of these devices scales with temperature,

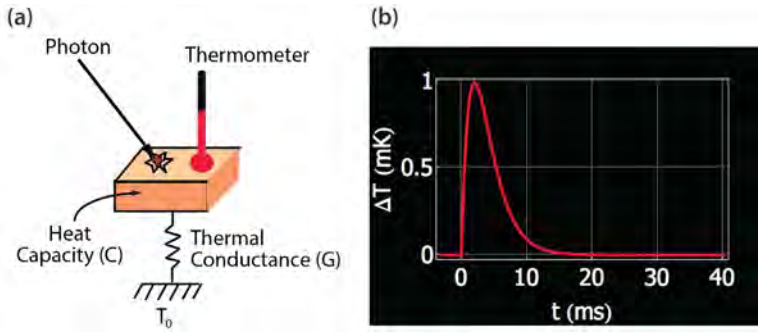

Figure 2. (a) A superconducting TES works on the principle that photon absorption in a membrane is converted to heat, which in turn creates a change in electrical resistance; (b) thermal relaxation times may be long (i.e., milliseconds) (Rabin 2013)

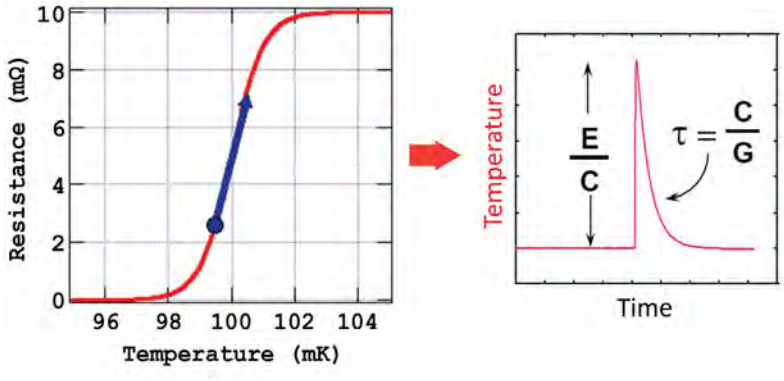

Figure 3. A TES is a thermometer made from a superconducting film operated near its transition temperature Tc, during which, in its transition from superconductor to normal metal, a small change in temperature causes a large change in resistance (figure based on Figueroa 2014)

so cryogenic temperatures are needed for high-energy resolution. While in its transition from a superconductor to normal metal, a very small change in temperature causes a large change in resistance. Transition widths are typically on the order of a millikelvin. The figure of merit for microcalorimeter resistive thermometers is a parameter called α, defined as

$$\alpha = (d\ \ln R / d\ \ln T)V = \text{constant}, \quad \textbf{(1)}$$

where T is the temperature and R is the resistance of the TES. The energy resolution of a TES can be approximated by (Figueroa 2014)

$$\Delta E_{FWHM} = 2.355\ [4\ k_B\ T^2\ C\ [n/2]^{0.5} / (\alpha)]^{0.5}, \quad \textbf{(2)}$$

where k_B is Boltzmann's constant, T is the TES temperature, C is the microcalorimeter's heat capacity, n is a number whose value depends on the dominant thermal impedance between the substrate and the electrons in the superconducting film, α is as defined in Equation 1, and the factor of 2.355 converts the standard deviation into FWHM. For good energy resolution, one wants to have a low heat capacity C, a high α, and operate the devices as cold as is achievable. An important limitation is that the TES operates well as a thermometer only in its transition. When it goes normal, resistance will no longer change with temperature as much, and $\alpha \rightarrow 0$. This implies a maximum temperature change in the TES, which in turn implies a maximum energy of the incoming photons (Figueroa 2014),

$$E_{MAX} = C\ \Delta T_{MAX} \sim C\ T/\alpha. \quad \textbf{(3)}$$

The parameters C and α are tied by the desired energy bandpass of the microcalorimeter. The theoretical energy resolution of a microcalorimeter in a simple formula that only depends on the temperature of operation and the bandpass of the device (Irwin 1995a, Figueroa 2014), is

$$\Delta E_{FWHM} = \frac{2.355\ [4\ k_B\ T\ E_{MAX}\ [n/2]^{0.5}]^{0.5}}{[(\alpha)]^{0.5}}. \quad \textbf{(4)}$$

Groups both at NASA and NIST have demonstrated TESs with resolving powers of over 1000, or from 1 to 2 eV resolution at 1 keV, and TESs have been successfully used at the longer wavelengths, such as the sub-millimeter wavelength on ground-based telescopes and balloons. In this context they are no longer single-photon detectors, as they are measuring the average power of the incoming light. In this case, the TES acts as a bolometer, which is a microcalorimeter, as opposed to a single-photon detector. Bolometers have been successfully deployed in a number of scientific instruments; for example, they have a long history of use on x-ray sounding rockets. As single-photon detectors, TESs are at a low technical readiness level and not far along in the laboratory (Morgan 2015).

Project

The motivation of this work is to explore operating TESs at relatively higher temperatures associated with the Tc of high-temperature superconductors (HTSs). However, near Tc the capacitance of the membrane $C \sim T^3$. From Equation 2, this presents the challenge

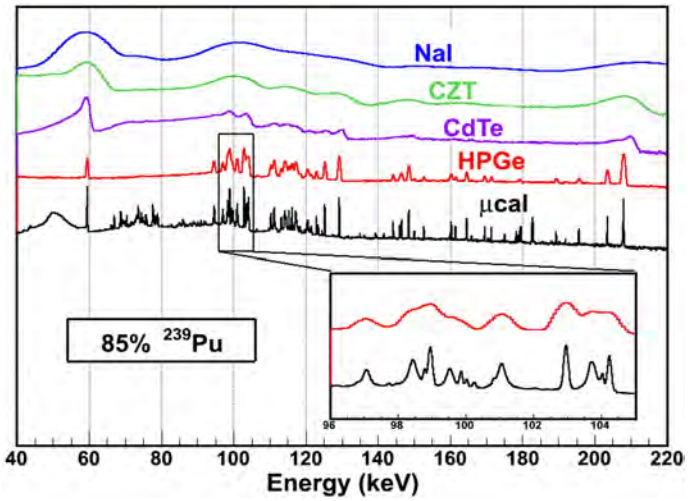

Figure 4. Progression of spectra with increasing spectral resolution from top to bottom. Each step reveals greater detail. The inset shows the improvement of microcalorimeter (μCal) detectors over HPGe in the congested 100 keV region for plutonium isotopic analysis (Rabin 2010).

that the energy resolution ΔE_{FWHM} is proportional to $T^{5/2}$, yielding useful energy resolutions with TES only for single-digit kelvin operating temperatures. To this end, we focused on the idea of improved microwave resonator readout concepts and improved detector efficiency. These concepts would apply directly to other theoretical work, looking most promising for warmer-temperature HTS thermal kinetic inductance devices with extremely high energy resolution. Figure 4 demonstrates that nuclear fingerprints with extremely high energy resolutions are vital for both material identification and quantitative materials analysis (e.g., isotopic composition).

The TES concept was used as early as the 1940s, when an apparatus for measuring infrared radiation had been constructed by Andrews (1942) using fine tantalum wire, operated at a temperature of 3.22–3.23 K in the transition zone between superconduction and normal conduction (Andrews 1942). More recently, superconducting quantum interference devices (SQUIDs) provided for a stable readout of TESs. The TES itself acts as a sensitive thermometer (Figure 2) (Irwin 1995b, Saab 2006).

The high energy resolution (Figure 4) is derived from operation at temperatures below 100 mK, a temperature range now accessible without liquid helium. As

Table 1. Radiation measurement resolutions and resolving powers achievable with a TES (Rabin 2010)

Radiation Measured	Energy (E)	Resolution (ΔE_{FWHM})	Resolving Power (E/ΔE)
X-ray	1.0 keV	0.7 to 1.0 eV	1000
X-ray	5.9 keV	1.6 to 2.5 eV	>2300
X-ray or gamma ray	100.0 keV	22 eV 50 to 80 eV array	4500 >1250
Alpha particle	5.0 MeV	0.7 to 0.8 keV	>6000
Q (for alpha decay)	5.6 MeV	1 keV	5600
Electron capture	6.5 keV	~8 eV	800
Beta particle	20.0 keV	TBD	TBD

HPGe detectors have a ten-fold improvement over single-crystal scintillators (NaI:Tl), a microcalorimeter has a five- to ten-fold improvement over an HPGe detector. See Figure 4 and Table 1 (Rabin 2010).

Scalable Readouts for Very Large Arrays

Microwave frequency domain readout is a viable technique to read out a large array of low-temperature detectors, such as TESs (Noroozian 2013, Bennett 2014, Ferri 2015). We used a readout technique (Figure 5) based on microwave transmission and reflection. A microwave tone signal probes the state of the sensor elements coupled to simple microwave resonant circuits (Figure 6). The major challenge is synthesizing and demodulating the carrier tones. It is possible to fabricate thousands to millions of resonators, each with a unique, identifying resonant frequency, using standard lithography tools. This approach is compatible with frequency-domain multiplexing, thus allowing a large array of sensors to be probed using only two coaxial signal lines (Ullom 2013). The use of microwave techniques simplifies the packaging and interconnections required for large or distributed sensor arrays. However, this approach transfers the complexity to room-temperature electronics that must synthesize a microwave tone for each sensor and determine the amplitude or relative phase of the reflected or transmitted microwave power at each frequency as this information encodes the state of the sensors. This type of multichannel signal processing is similar to the digital techniques used in modern cellular communication, and, consequently, powerful commercial electronics are becoming available to perform exactly this task. Using commercial electronics as a starting point, the University of Colorado, Boulder (CU) developed software, firmware, and hardware that enabled the use of microwave readout techniques in measurement problems relevant to DOE's mission (Ullom 2013).

The readout circuit consists of superconducting microwave resonators coupled to radio frequency–SQUIDs (RF-SQUIDs) that transduce changes in input current to changes in phase of a microwave signal. A flux-ramp

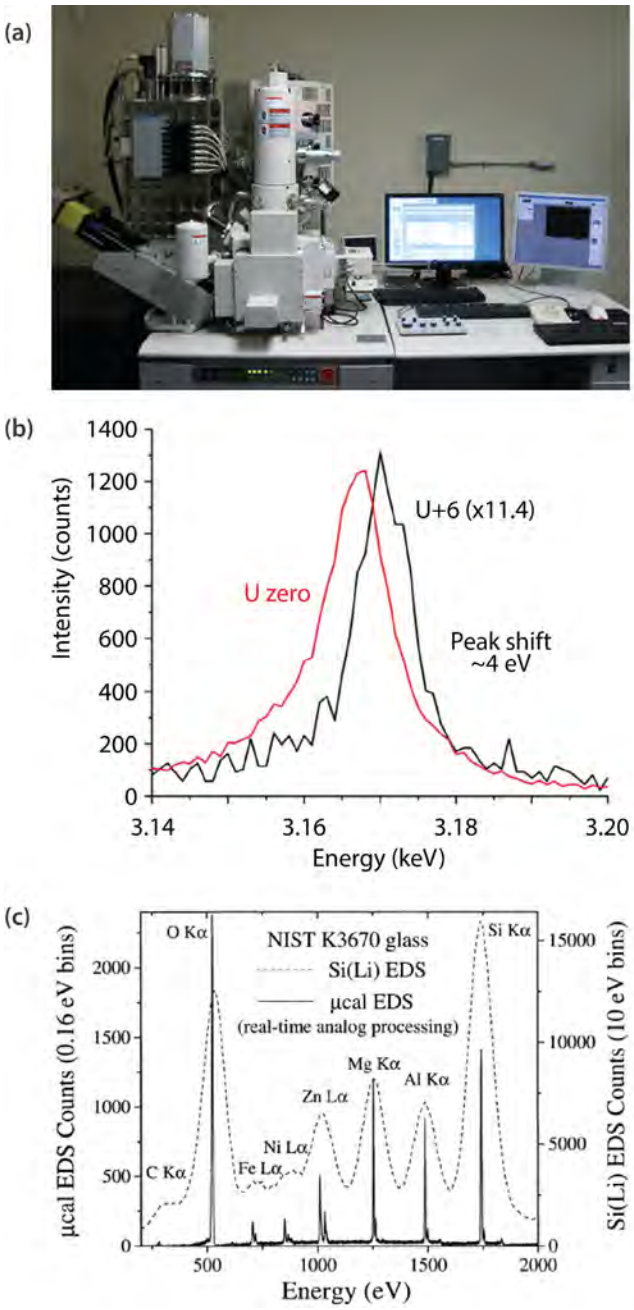

Figure 5. (a) Adiabatic cooler for TES; (b) TES data acquired with this setup for microchemical analysis, with fidelity to indicate oxidation states; and (c) TES data acquired for energy-dispersive x-ray spectroscopy (EDS), allowing for better trace element analysis than achievable with Si:Li detectors

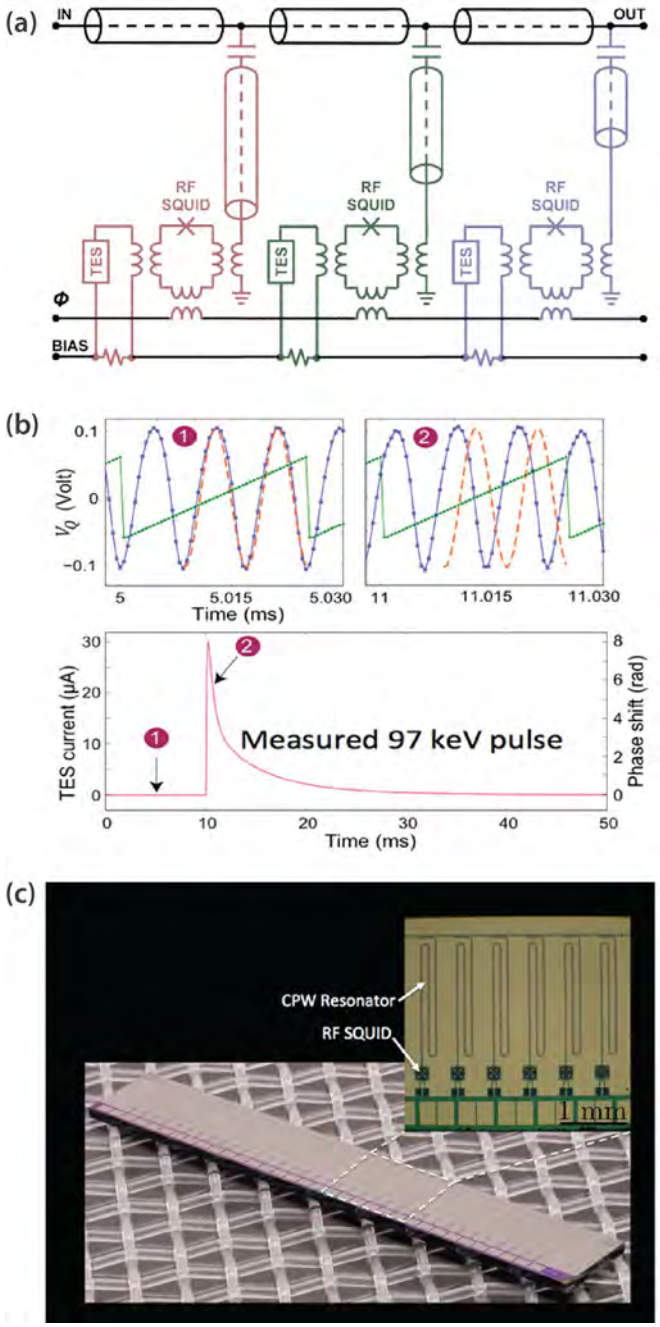

Figure 6. Microwave SQUID multiplexing employs flux-ramp modulation, which eliminates the need for a flux-locked loop.

(a) Circuit schematic for multiplexed gamma ray spectroscopy. Resonator circuitry is shown in black, RF-SQUID components, TES components, flux ramp components (Φ), and bias circuit are shown in different colors for each TES. These circuit components constitute the cold stage of the adiabatic demagnetization refrigerator (ADR). Microwave attenuators at various stages have been omitted for clarity (Noroozian 2013).

(b) The measured quadrature-phase component V_{Q2} (blue circles) of the microwave signal, the flux-ramp modulation sawtooth signal V_{fr} (green triangles), and a pure sinusoidal waveform (orange dashed) over a 32 μs window sometime before (1) and during (2) a 97 keV gamma ray pulse in TES 1. The bottom panel shows the corresponding TES current (left axis) and resonance phase shift (right axis) pulse after demodulation (Noroozian 2013).

(c) The transmission lines for the feedline and resonators are coplanar waveguides (CPW) of niobium on high-purity silicon. A CPW consists of a center conductor with ground plane on both sides separated by a gap. The NIST time-division multiplexer with an identical layout of bond pads can be easily coupled to any detector chip that was designed for readout with the NIST time-division multiplexer. To fit the roughly 5 mm long resonators on the 3 mm wide chip, the resonators are routed like trombones, changing the slider length by 3 μm between adjacent resonators so that Δl = 6 μm, and the frequency spacing is close to 6 MHz. The CPWs shown here have 10 μm center strips and 6 μm gaps (Mates 2011).

modulation linearizes the response and evades low-frequency noise. Flux-ramp modulation has the added benefit that the signal is up-converted to frequencies above the low-frequency two-level system noise that is intrinsic to the resonator (Noroozian 2013) (Figure 7). CU and the Los Alamos National Laboratory have demonstrated that readout noise from an RF-SQUID is negligible (Mates 2011). They demonstrated one path for the readout of cryogenic x-ray and gamma ray sensor arrays with many elements and spectral resolving powers $R = \lambda/d\lambda > 10^3$ (Noroozian 2013). Employing microwave techniques, only two coaxial cables and existing commercial electronics are sufficient to poll thousands of resonators. The telecommunications industry already employs a similar functionality. This architecture may benefit from steady

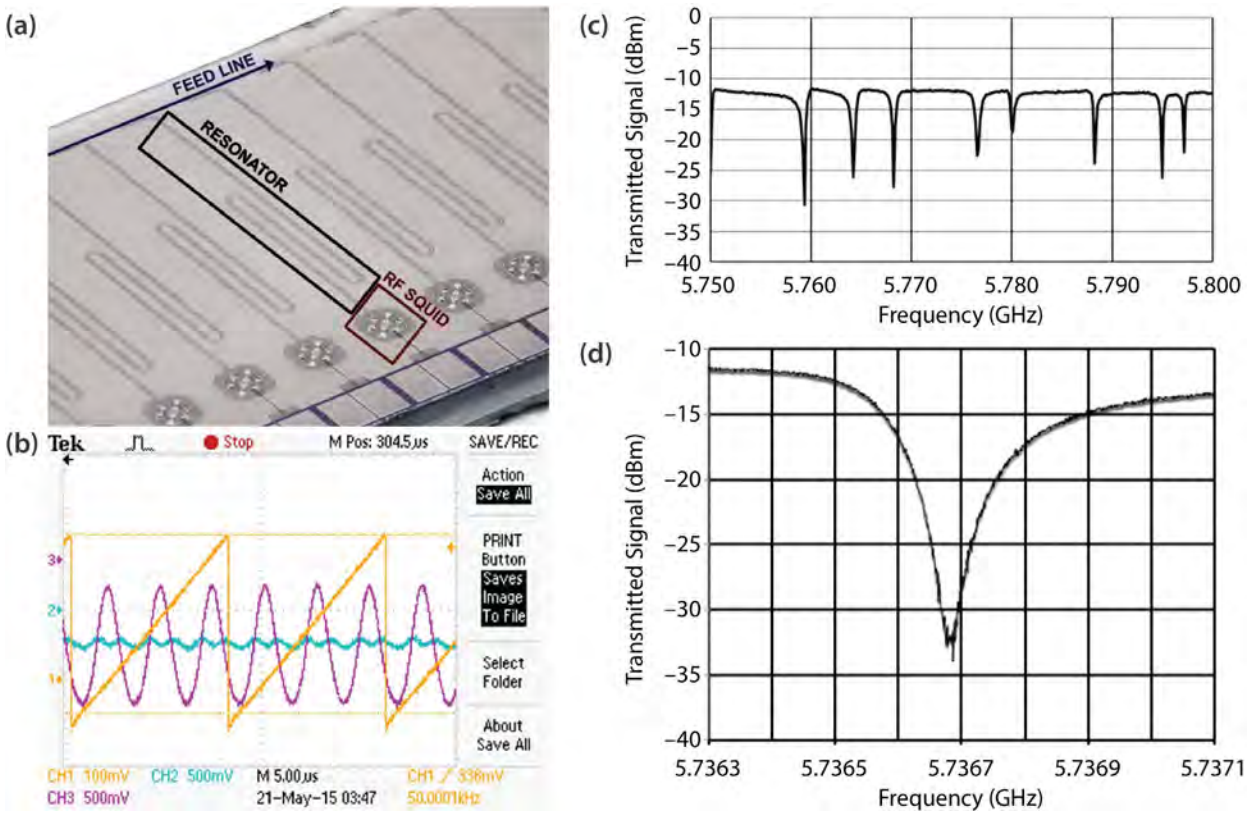

Figure 7. Resonator, RF-SQUID, and sensor testing are demonstrated by (a) multiple superconducting microwave resonators on a chip, (b) a periodic ramp that sweeps through multiple flux quanta in the RF-SQUIDs with a slew rate of this ramp that greatly exceeds that of any expected input signal, (c) microwave resonances shifted with the magnetic flux in their respective SQUIDs, and (d) magnification of one resonance that can be described by the peak in reflected power or dip in transmitted power with a recognizable Lorentzian line shape. We can place multiple RF-SQUIDs at the current anti-node and separate their signals by coupling them to the flux ramp with different mutual inductances so that they modulate at different frequencies. Their input signals then appear in different sidebands of the microwave carrier (Mates 2011).

improvement in field-programmable gate arrays (FPGAs), analog-to-digital converters (ADCs), and data acquisition systems (DACs) (Figure 8).

Spectrometers based on arrays of microcalorimeter detectors with thousands of pixels have the potential for high efficiency, high speed (>10^5 cps), and ultra-high resolution (1–3 eV at 6 keV; 20–80 eV at 100 keV). The technology exists today to fabricate and cool such arrays. However, we cannot read out such large sensor arrays due to the cryogenic complexity, excessive heat load, high wire count, and cost of current methods. Radical innovation is required for scalable electronic readout. Developing a scalable sensor readout will lead to tabletop spectrometers suitable for almost any laboratory, supporting major long-term DOE goals.

Figure 9 shows the energy spectrum of a gadolinium-153 (^{153}Gd) source measured using our 4-pixel TES array and the RF-SQUID multiplexer. We measured a ^{153}Gd photon source with an achieved energy resolution of 70 eV, a FWHM of 100 keV, and an equivalent readout system noise of 90 pA/pHz at the TES. We sequentially shifted horizontally and vertically the spectra acquired from each TES pixel.

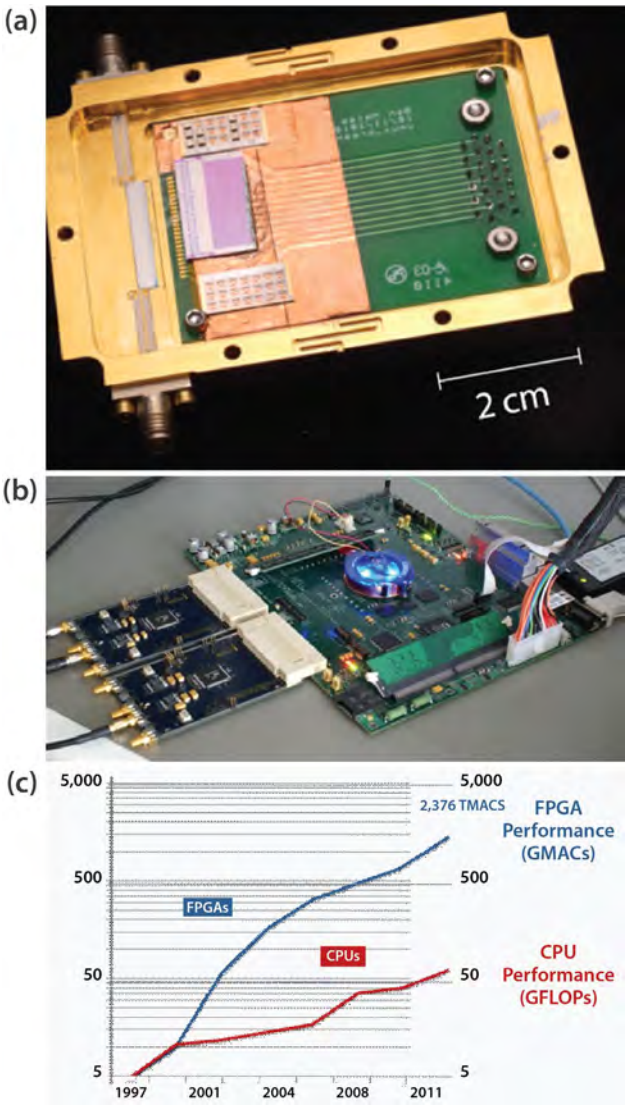

Figure 8. Microwave techniques enable thousands of resonators.

(a) A full device box with two microwave SMA connectors (Noroozian 2013).

(b) The multiplexing demonstrations by CU used two microwave signal generators to generate the tones for simultaneous readout of 2 pixels. In the future, tens, hundreds, or thousands of pixels may be read out, but clearly not at the cost associated with thousands of $10,000 signal generators. Instead, we explored software-defined radio (SDR), used by microwave kinetic inductance detector (MKID) groups, capable of digitally generating and demultiplexing hundreds of tones. For our SDRD, we explored a new generation of open-source electronics for SDR and commissioned it to demonstrate 4-pixel multiplexing of TESs (Mates 2011).

(c) Although 4 pixels are not qualitatively different from 2 pixels, a successful demonstration does increase confidence in the scalability of the microwave SQUID multiplexer and ability to take advantage of ever-increasing CPU performance as a function of time. For instance, today's FPGAs are capable of many tera multiply-accumulate operations (TMACs) and today's CPUs are capable of hundreds of giga floating-point operations per second (GFLOPs). Scalability will only increase in the future.

Software-Defined Radio

Software-defined radio (SDR) leverages industry investments in ADCs and FPGAs (Figure 8). SDR generates frequency combs and can up-convert to frequencies of interest. SDR can amplify signals. One may down-convert and digitize the signal with SDR or channelize signals into a powerful FPGA. SDR can process pulses or output a simple time stream (sub-millimeter) (Mazin 2012). Figure 9 displays data we acquired in the first simultaneous combination of all key innovations in a 4-pixel demonstration, including microcalorimetry, microwave multiplexing, RF-SQUIDs, and SDR.

Conclusion

We believe this project has improved capabilities and substantively advanced the science useful for missions such as nuclear forensics, emergency response, and treaty verification through the explored TES developments. These TES developments combined key DOE NNSA nuclear capabilities and investments, such as chemistry, isotopic analysis, sensor, and innovative engineering sciences. The result is very high–resolution photon spectroscopy with a microwave-multiplexed 4-pixel transition edge sensor array. We performed and validated a small-scale demonstration and test of all the components of our concept

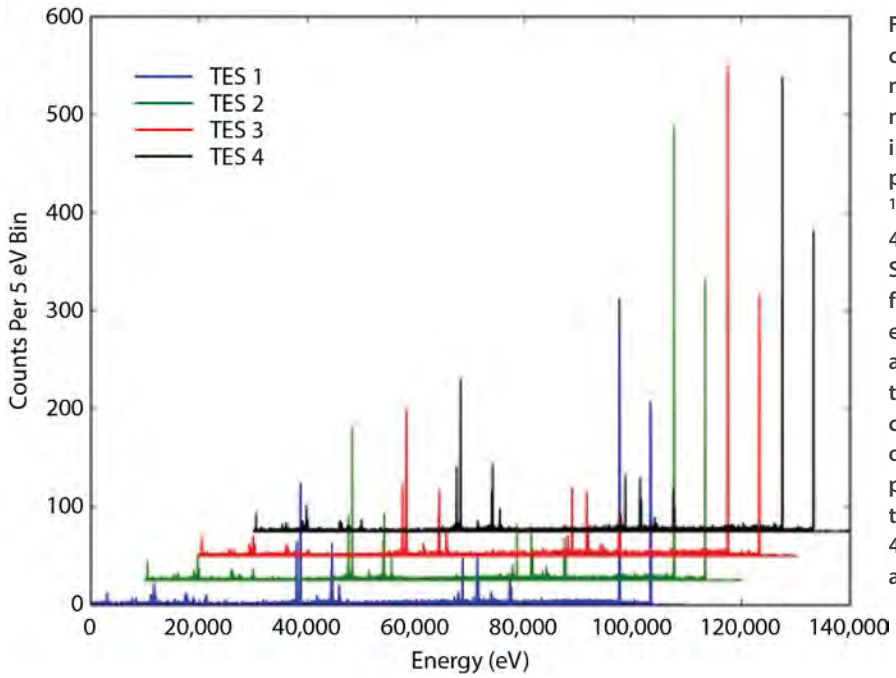

Figure 9. First simultaneous combination of all key innovations: microcalorimeters, microwave multiplexing, RF-SQUIDs, and SDR in a 4-pixel demonstration. Figure presents the energy spectrum of a ^{153}Gd source measured using our 4-pixel TES array and the microwave SQUID multiplexer. The spectra from TES 2, 3, and 4 pixels have each been successively horizontally and vertically shifted relative to the spectrum from TES 1 pixel for clarity. For each pixel, one can observe the two 97.4 and 103.2 keV photopeaks. In addition, each of the four spectra has photopeaks at 40–49 keV where the europium K_α and K_β complexes can be seen.

system, which encompassed microcalorimetry, microwave multiplexing, RF-SQUIDs, and software-defined radio. The University of California, Santa Barbara has performed SDR readout with thousands of low-resolution sensors (Mazin 2012) and CU has implemented two high-resolution sensors with RF-SQUIDs but without SDR (Noroozian 2013). However, no one has combined all these concepts together at scale until now. Further experiments simultaneously combining all key innovations are continuing under SDRD.

Acknowledgments

We would like to thank Kristina Brown, Amanda Klingensmith, and Alexander Plionis for their contributions to this work.

References

Andrews, D. H., W. F. Brucksch Jr., W. T. Ziegler, E. R. Blanchard, "Attenuated superconductors I. For measuring infra-red radiation," *Rev. Sci. Instrum.* **13** (1942) 281.

Bennett, D. A., J. A. B. Mates, J. D. Gard, A. S. Hoover, M. W. Rabin, C. D. Reintsema, D. R. Schmidt, L. R. Vale, J. N. Ullom, "Integration of TES microcalorimeters with microwave SQUID multiplexed readout," *IEEE Trans. Appl. Supercond.* **25**, 3 (2014) 2101405.

Ferri, E., et al., "Microwave multiplex read out for superconducting sensors," Frontier Detectors for Frontier Physics, 13th Pisa Meeting on Advanced Detectors, La Biodola, Isola d'Elba, Italy, May 24–30, 2015, https://agenda.infn.it/getFile.y/s?contribId=310&sessionId=14&resId=0&materialId=poster&confId=8397, accessed September 30, 2015.

Figueroa Group, Massachusetts Institute of Technology, "Transition edge sensors (TES)," 2014, http://web.mit.edu/figueroagroup/ucal/ucal_tes/, accessed September 30, 2015.

Horansky, R. D., et al., "Superconducting absorbers for use in ultra-high resolution gamma-ray spectrometers based on low temperature microcalorimeter arrays," *Nucl. Instrum. Methods Phys. Res. A* **579**, 1 (2007) 169–172.

Irwin, K. D., "An application of electrothermal feedback for high resolution cryogenic particle detection," *Appl. Phys. Lett.* **66** (1995a) 1998.

Irwin, K. D., "Phonon-mediated particle detection using superconducting tungsten transition-edge sensors," Ph.D. Dissertation, Stanford University, Stanford, California (1995b), http://cdms.berkeley.edu/Dissertations/irwin.pdf, accessed September 30, 2015.

Irwin K. D., G. C. Hilton, "Transition-edge sensors," *Topics Appl. Phys.* **99** (2005) 63–150.

Mates, J. A. B., "The microwave SQUID multiplexer," University of Colorado, Boulder, Colorado, Ph.D. Thesis (2011), http://www.asiaa.sinica.edu.tw/~ctli/tp/Mates_microwave_squids.pdf, accessed September 30, 2015.

Mazin, B., "MKIDs for coronagraphic direct detection," Mazin Laboratory, University of California, Santa Barbara, CA, 2012, http://exep.jpl.nasa.gov/files/exep/ExoPAG5/10_Mazin-MKID.pdf, accessed September 30, 2015.

Morgan, K., "Developing transition-edge sensors for new space-based applications," NASA Early Stage Technology Workshop: Astrophysics & Heliophysics, Crystal City, Virginia, March 27, 2015, https://www.youtube.com/watch?v=vGHB80tqD5w, accessed September 30, 2015.

Noroozian, O., et al., "High-resolution gamma-ray spectroscopy with a microwave-multiplexed transition-edge sensor array," *Appl. Phys. Lett.* **103**, 20 (2013), 202602, http://arxiv.org/pdf/1310.7287.pdf, accessed September 30, 2015.

Rabin, M. W., et al., "Cryogenic sensors for high-precision safeguards measurements," Symposium on International Safeguards, Preparing for Future Verification Challenges, Vienna, Austria, November 1–5, 2010, https://www.iaea.org/safeguards/symposium/2010/Documents/PapersRepository/194.pdf, accessed March 26, 2014.

Rabin, M. W., et al., "Cryogenic detectors and neutrino mass measurement," Los Alamos National Laboratory (July 26, 2013), http://public.lanl.gov/friedland/info13/info13talks/Rabin-INFO13.pdf, accessed January 11, 2016.

Saab, T., S. R. Bandler, K. Boyce, J. A. Chervenak, E. Figueroa-Feliciano, N. Iyomoto, R. L. Kelley, C. A. Kilbourne, F. S. Porter, J. E. Sadleir, "Optimizing transition edge sensors for high-resolution x-ray spectroscopy," *AIP Conference Proceedings* **850** (2006) 1605–1608, http://www.phys.ufl.edu/~tsaab/Useful_Papers/files/Saab_lt24_LT2178.pdf, accessed September 30, 2015.

Ullom, J., K. Irwin, D. Schmidt, J. Brevik, M. Rabin, "Microwave readout techniques for very large arrays of nuclear sensors," U.S. Department of Energy Fuel Cycle Research and Development Division FC-3, F C R&D Materials Controls & Instrumentation, Nuclear Energy University Programs (NEUP), November 25, 2013, https://neup.inl.gov/SiteAssets/FY%202013%20Abstracts/NEUP/18-U%20Colorado%20Boulder.pdf, accessed June 1, 2015.

Enhanced Radiation Detection through Spatial-Spectral Data Convergence

RSLN-09-15 | Year 1 of 1

Michael Howard,[1,a] Heather Howard,[a] Aaron Luttman,[b] Chris Joines,[a] and Marylesa Howard[b]

This research aims to improve the accuracy of radiation detection results by exploiting coincident spectral image data from the visible through infrared portion of the electromagnetic spectrum. Spectral, spatial, and temporal aspects were considered to determine the optimum specifications of an electro-optical spectral imager that would complement the radiation search system flown on the helicopter platform. Research was conducted to determine the spectral regions most capable of distinguishing and mapping terrestrial materials that are relevant to the radiation environment. A compact hyperspectral imager with 535 co-registered visible, near infrared, and shortwave infrared channels was selected to best integrate with the radiation helicopter mission while covering the spectral bands most suited for identification and mapping of the natural and man-made landscape.

[1] howardme@nv.doe.gov, 702-295-8751
[a] Remote Sensing Laboratory–Nellis; [b] North Las Vegas

Background

Due to the non-directional nature of radiation emission and inverse correlation with distance of radiation energy, two primary challenges in airborne radiation detection are recognizing the existence of an anomalous signal and characterizing and/or identifying the nature or source of the anomaly as benign or hazardous. Given the current state of radiation detection and electro-optical (EO) imaging sensors, it is possible to detect radiological anomalies and to characterize source and background materials with the respective technologies; however, these two capabilities do not exist as a single system taking advantage of multiple sensing modalities simultaneously. This project sought to define the optimal sensor configurations and develop the computational methods for fusing current radiation detector signals with simultaneously acquired multi- or hyperspectral image data. This convergence of orthogonal data would drive the next generation in radiological search and source discrimination technology, resulting in a unified system to recognize and suppress background radiological sources while enhancing relevant target source signals.

Fusing optical and radiological spectral modes to discern natural versus man-made background elements is relevant for NSTec aerial crisis response and consequence management missions. NSTec's primary approach to airborne radiation detection is to use a sensor that measures the gamma radiation in each of a large number of energy bins at a 1-second interval. Various analysis algorithms are applied to the airborne radiation data to map the distribution of elevated gamma gross counts, variations in the isotopic concentrations from background, or the distribution of a specific isotope of interest. While detailed analysis of the gamma spectrum can readily distinguish between natural and man-made radiation sources, the interpretation of the spatial distribution can be obscured for several natural, physical, and operational reasons.

For example, the radiation signal may be elevated due to changes in predominant rock or soil composition, abrupt changes in vegetative cover, inappropriate selection of background/reference spectrum for the local geology or urban environment, or the presence of a highly radioactive source that is far away from the aircraft nadir position (Hendricks 1999). A precision map of ground material classes within the target area measured at the same time as the radiation signal would readily rule out benign origins of radiation anomalies and reduce the time it takes to interpret an airborne radiation dataset. The exploitation of the reflected and thermal portion of the electromagnetic spectrum for material classification and identification is an advanced technology, as is the precise geospatial rectification of image data acquired from mobile airborne platforms. Therefore, naturally, a convergence of these data modalities acquired concurrently would significantly enhance source detection and characterization. In turn, improved detection and characterization accuracy of radiation anomalies allows for more efficient response actions and direction of resources to a radiological incident by reducing the risk of misdirecting resources to adjudicate false-positive detections.

Project

This project aims to employ a multi-modal concept to exploit multiple relevant portions of the electromagnetic spectrum (i.e., visible, near infrared [NIR], shortwave infrared [SWIR], longwave infrared [LWIR], gamma) rather than just any one alone. While both EO remote sensing and radiation detection are independently mature technologies, they have never been temporally and spatially analyzed together to take advantage of the combined spectral-spatial information for detecting radiological sources. The overall objective of this work is to develop the computational methods for fusing current radiation detector signals with simultaneously acquired multispectral and hyperspectral image data to produce the next-generation radiological search system. The initial part of this research and development effort was determining the optimum spectral-spatial resolution and spectral ranges of a multi-modal sensor for radiological applications, as well as acquiring an electro-optical imaging system that would optimize the spatial-spectral information while conforming to the operational limitations of the radiation detection system.

In defining optimized sensor specifications, the scope of the search was limited by the operational requirement for the combined system to be mounted on the Bell 412 helicopter platform. The helicopter platform is utilized to increase the sensitivity of the radiation detection system. While improving the spatial resolution of the radiation data, the low acquisition altitude also increases the sensitivity to changes in ground surface materials. Therefore, it is the helicopter mission that will benefit most from the detailed surface material mapping provided by the EO imaging sensor and is the mission targeted for this research. The rotary wing environment and the mount location under the nose place rigid restrictions on size, weight, and ruggedness; this constraint pushes the envelope of EO imaging technology, requiring that we consider several spectral-spatial trade-offs.

After an initial survey of existing assets and immediately available technologies, the path forward to a satisfactory EO portion of this system was narrowed down to four options: (1) employ one of the two existing Daedalus multispectral systems, (2) purchase a SWIR hyperspectral imager, (3) purchase a hyperspectral imager with visible through SWIR capability, or (4) rent a hyperspectral imager for the term of this research.

In addition to technical objectives and in order to gain a business perspective for future research and development opportunities, the project team consulted with SDRD program management regarding the best option. It was determined that the highest value for the current research and future developments would be achieved through the ownership of a visible through SWIR hyperspectral imager. The following is a discussion of the three parameter domains (i.e., spectral, spatial, and temporal) that were considered in selecting the Headwall Photonics Hyperspec VNIR-SWIR

Spectral Modes	VNIR (400-1000 nm); SWIR (950-2500 nm)
Spectral Bands	535 (VNIR – 369; SWIR – 166)
Spatial Pixels	333 co-registered
Total FOV	25.45°
IFOV	1.36 milliradians
Spectral Resolution	<6 nanometers
Maximum Frame Rate	>250 frames per second
Digitization	16-bit

Figure 1. Specifications of the Headwall Photonics Hyperspec VNIR-SWIR Airborne Hyperspectral Imaging Sensor

Airborne Hyperspectral Imaging Sensor as the optimal spectral imager to benefit the helicopter radiological detection mission (Figure 1).

Spectral Considerations

The spectral domain refers to both resolution and wavelength range. Spectral data that span multiple optical modalities are needed to map the wide variety of thematic content of both urban and natural terrain. However, the larger the spectral range measured, generally, the broader the spectral bands must be in order to achieve acceptable signal. The trade-offs between multispectral (tens of spectral bands from visible through thermal) and hyperspectral (hundreds of spectral bands in one or two spectral regions) were considered with regard to the signatures of materials relevant to the radiological detection problem.

Figure 2 shows the visible through LWIR spectra of natural and man-made materials that make up a large portion of rural and urban scenes. Some of these materials may contribute to an elevated radiation background, and others can introduce changes in the radiation signal that are unrelated to the radiological environment, thereby increasing the complexity of interpreting the airborne radiation data. While there are unique features in every spectral range, only a multispectral system would be able to collect data in the full range from visible through LWIR. Figure 3 shows the visible through SWIR spectrum of the same materials after having been convolved with the Daedalus 1268 multispectral scanner (MSS) detector response. With such a system, only major classes of materials, such as rock versus vegetation, could be made with confidence. It would be difficult to distinguish, for example, granite from limestone, grass from

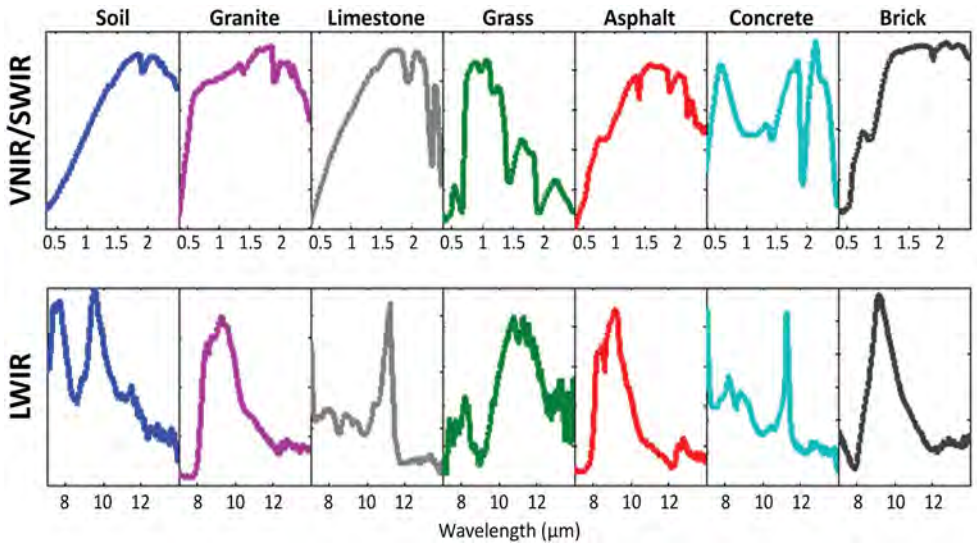

Figure 2. Spectra of natural and man-made materials showing distinguishing features in the VNIR, SWIR, and LWIR regions

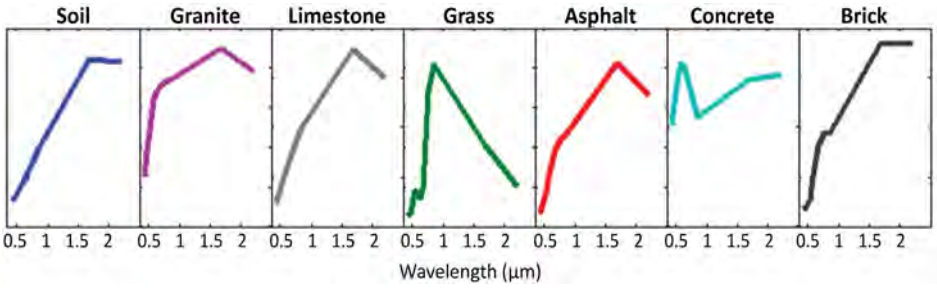

Figure 3. Spectra of natural and man-made materials as measured by the Daedalus 1268 MSS

forest, and rock from asphalt or concrete. As such, it was decided to select a hyperspectral sensor in order to capture fine details of the spectrum that separate common materials.

Furthermore, while hyperspectral thermal imaging is on the forefront of research in the intelligence community, the algorithms for vegetation and geologic mapping are far more advanced for the VNIR/SWIR portion of the spectrum. Recent advancements in optical design and efficiency have led to compact hyperspectral imagers that span the visible, NIR, and SWIR regions that allow the application of advanced spectral analysis algorithms developed for handheld single-pixel spectrometer data. Figure 4 compares the spectral resolution of the Hyperspec imaging sensor with the 10 VNIR/SWIR bands of the Daedalus 1268 MSS. The Hyperspec offers a significant advantage, particularly in the SWIR region where many geologic materials have unique spectral signatures, and will allow for material mapping rather than categorical classification only.

Spatial Considerations

In terms of spatial considerations, the higher the spatial resolution of the image data, the more information and context can be extracted. High spatial resolution facilitates interpretation of morphological characteristics and provides context to the data acquired by the non-imaging radiation detector. In general, high spectral resolution usually requires a trade-off in spatial resolution in order to achieve adequate signal after dividing the incoming energy into hundreds of spectral bands. By limiting the operational environment to a low and slow airborne

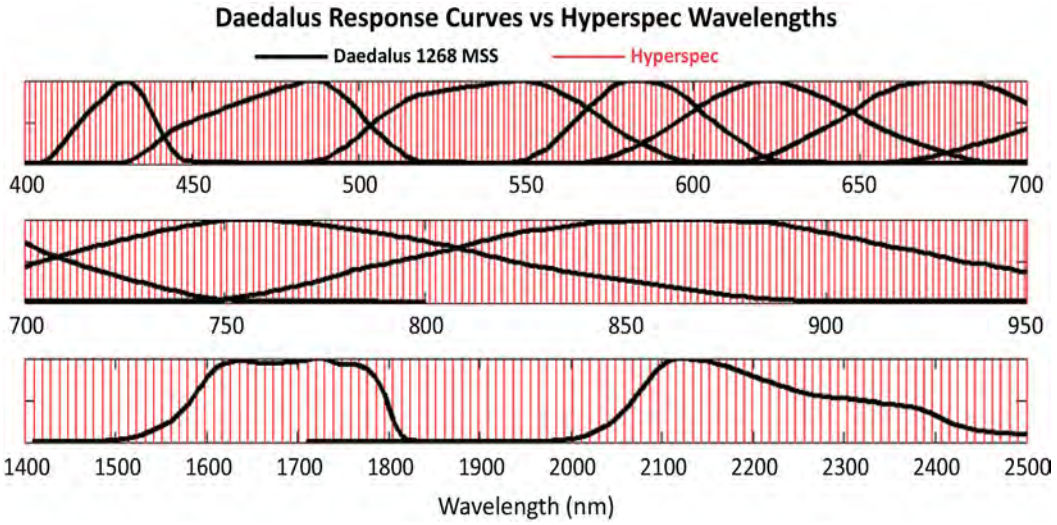

Figure 4. Broad and widely spaced Daedalus 1268 MSS response curves (black) compared with the narrow band spacing of the Hyperspec imaging sensor (red) in the VNIR-SWIR region, showing the improved definition of a material spectral signature provided by a hyperspectral sensor over a multispectral sensor

platform, a hyperspectral pushbroom sensor can achieve high spatial resolution due to the low altitude while maintaining high signal strength due to the slow ground speed, which increases integration time. The Daedalus 1268 MSS is a line scanner that accommodates the very short integration time at 100 Hz scan speed with a very large axe-blade rotating mirror to maximize photons reaching the detectors. However, due to the large mass of the mirror and other mechanical design factors, the sensor head is too large for the helicopter nose mount. While the Daedalus can be mounted externally on the side of the helicopter, extensive research on vibration was conducted and has shown vibration to be detrimental to data.

Figure 5 shows the spectral versus ground sample distance for various commercially available airborne imaging sensors (blue), satellite-based sensors (purple), and the Headwall Hyperspec imaging sensor (red). The area highlighted in yellow indicates the spectral and spatial bounds desired for the combined EO/radiation detection system. The Headwall Hyperspec falls within the preferable upper left quadrant of this region (i.e., large spectral bands and small ground sample distance).

Another aspect of spatial consideration is the total field-of-view (FOV) or swath width. The extent of the optical sensor should match the sensitivity of the radiological sensor in order to ensure measurement of the same temporal and spatial phenomena. For the typical operational altitude of 150 feet above ground level, the radiation sensor has a region of sensitivity of approximately 300 feet. At this altitude, the Hyperspec has a swath of only 70 feet and would therefore require a more narrow spacing between adjacent flight lines. This is a significant trade-off to get high spectral resolution with consequences to flight time and acquisition costs, which are balanced by the order of magnitude increase in information content with the hyperspectral system over the wider FOV Daedalus 1268 MSS. A future modification to the Hyperspec with a wider FOV lens would provide better alignment

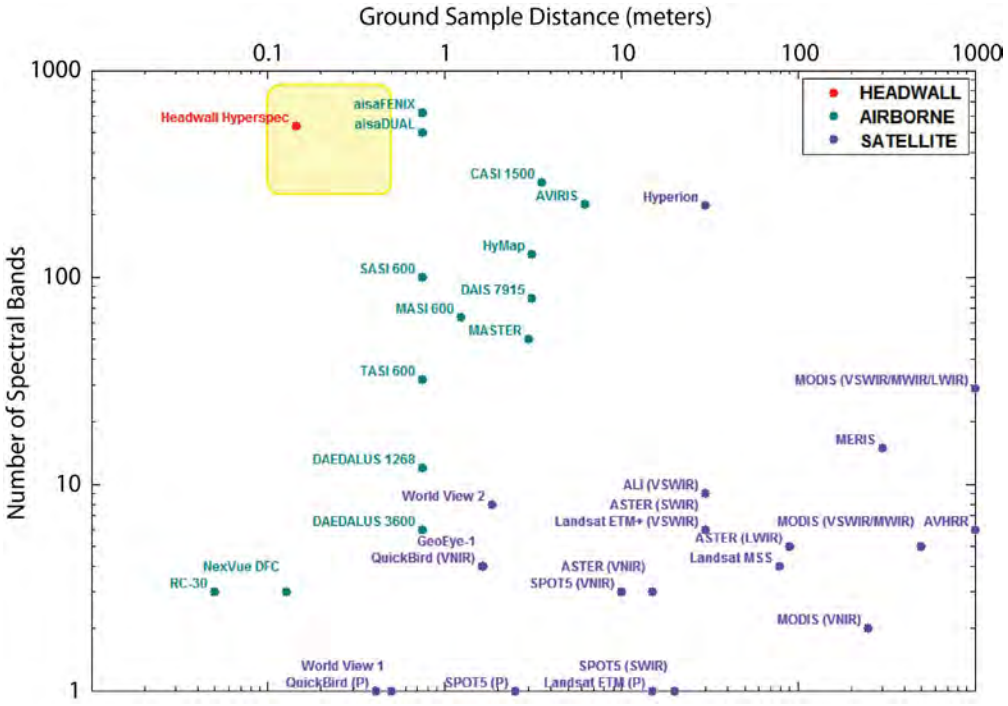

Figure 5. Spectral-spatial comparison of commercially available airborne sensors, satellite-based sensors, and the Hyperspec imaging sensor. The area highlighted in yellow indicates the desired spectral and spatial specifications for the combined EO/radiation detection system. Graphic adapted from Schowengerdt (2007).

with the radiation sensitivity swath, but it would come at the cost of spatial pixel size. This trade-off would need to be evaluated in reference to the data fusion algorithms.

Temporal Considerations

With regards to the temporal domain, targets of interest may be transient; therefore, coincidental data must be collected to avoid inclusions and exclusions between datasets. A routine practice is to refer to satellite imagery for spatial context. However, in addition to not meeting spatial or spectral needs, satellite image data may be days, months, or years old and never coincident with radiation measurements. The objective of this research requires an EO imager that can be installed and operated with the radiation equipment on the same helicopter platform so that the orthogonal datasets are measuring the exact same environment in both time and space. As discussed previously, the Bell 412 with the radiation detectors installed requires the EO sensor to be mounted under the nose. This essentially requires a pushbroom sensor over a line scanner in order to achieve the small physical size required to maintain ground clearance.

In order to exploit the full visible through SWIR spectrum using advanced analysis techniques, the three portions of the electromagnetic spectrum must be very accurately co-registered. Many manufacturers of hyperspectral imagers have separate systems for the VNIR and the SWIR regions. The current state of georegistration methods is not positionally accurate enough to fly multiple sensors for each spectral range. The Hyperspec imaging sensor is one of few commercially available sensors that offers a hyperspectral imager with co-registered visible, NIR, and SWIR bands in a single system. This system will allow for the analysis of the full spectral range for the highest accuracy mapping of surface materials present at the time of radiation data acquisition.

Conclusion

A VNIR/SWIR hyperspectral imaging sensor was selected and acquired based on spectral range, spatial resolution, spectral resolution, and operational limitations required for contemporaneous collection with airborne radiation data. These specifications are optimum for characterization and identification of radiation source and background materials. The sensor meets the requirement to operate on a high-vibration platform without compromising signal-to-noise ratio and meets the size limitations of a mount under the nose of the Bell 412 helicopter.

Continued research in the area might include addressing three aspects of this research and development that remain. An accurate training dataset must be collected from both radiation and EO systems simultaneously by integration of both sensors onto the helicopter platform and synchronizing acquisition parameters. This dataset would be the basis for the development of the sensor models needed to spatially and temporally fuse the information from the orthogonal data sources. Next, research and development of data fusion algorithms that allow for the efficient and quantitative exploitation of the fused data product using bi-directionally coupled synchronization (Brown 2000) should be explored. The completion of this research would, for the first time, establish the basis for the direct comparison and quantitative exploitation of the information provided by these distinct parts of the electromagnetic spectrum that, up until now, have only been exploited independently.

References

Brown, R., L. Kocarev, "A unifying definition of synchronization for dynamical systems," *CHAOS* **10**, 2 (2000) 344–349, http://www.dynamics.unam.edu/Bibliografia/SDC/PorRevisar/PhaseLocking/unifiying.pdf, accessed October 21, 2015.

Hendricks, T. J., S. R. Riedhauser, "An aerial radiological survey of the Nevada Test Site," DOE/NV/11718--324, Bechtel Nevada, Las Vegas, Nevada, 1999, http://www.osti.gov/scitech/servlets/purl/754300, accessed October 21, 2015.

Schowengerdt, R. A., *Remote Sensing: Models and Methods for Image Processing*, Academic Press, 2007.

LIBS as a Complement to Large-Scale Detonations and Means to Characterize Intermediates

STL-05-14 | Continued from FY 2014 | Year 2 of 2

Clare Kimblin,[1,a] Rusty Trainham,[a] Gene Capelle,[a] Xianglei L. Mao,[b] and Rick E. Russo[b]

We have demonstrated that laser-induced breakdown spectroscopy (LIBS) can complement high-explosive field tests and the modeling for such tests. Aluminum data collected using LIBS was compared to both explosive test chamber and field data, and studies involving LIBS of graphite and sparked air—relevant to detonation product species and explosion-shocked air—were performed. We conclude that LIBS produces results consistent with chamber and field results, and offers finer resolution than either chamber or field collects. The cost of the finer resolution is, however, narrowing of the complexity of the materials examined. Further, our initial temperature comparisons of sparked air with and without graphite present have laid the foundation for future studies of this type. As a result of this work, LIBS is being applied to support planning and analysis of customer-directed work at the NNSS.

[1] kimblicw@nv.doe.gov, 805-681-2257
[a] Special Technologies Laboratory; [b] Applied Spectra, Inc.

Background

Large-scale high-explosives (HE) tests are conducted at the NNSS to characterize and provide data for models of optical and RF explosion emissions. Such tests are data rich but expensive and time consuming. It is difficult to collect high temporal and high spatial resolution data in the field and to separate the many variables. Our goal has been to determine whether optical signatures can be generated in the lab that accurately mimic large-scale detonations, using a less labor- and time-intensive benchtop technique. We chose laser-induced breakdown spectroscopy (LIBS) as an optical emission platform that provides high temporal and high spectral resolution data, and determined that LIBS can (1) aid test and evaluation of new diagnostics to be fielded at HE experiments, (2) inform field collection parameters and analysis methods, and (3) provide data of interest to modelers.

LIBS creates a microscopic version of an explosion. With nanosecond LIBS, a ~12 ns laser pulse impacts a tiny target (typically a few hundred microns in diameter) with gigawatts of power, which causes the target to be ablated with such high energy that conditions similar to those created by an explosion are achieved: temperatures over 10,000 K (as high as 50,000 K [Bogaerts 2003]), pressures up to 10^5 atmospheres, and shock waves are produced. These conditions create a plasma, and as the plasma cools, ionic and atomic elemental constituents can be discerned, followed by formation of gaseous molecular products. Laser ablation can be performed at 5–10 Hz repetition rates and the shots integrated for a high signal-to-noise ratio. The technique permits tracking of species spectroscopically in time, extraction of electron density from line profiles, and temperature from intensity ratios and/or molecular band structure.

In the first year of the project, we focused on the collection of LIBS data for aluminum (Al). Al casings were used at the High Explosive Testing (HET) field

campaign in FY 2014, and will be used in follow-on Helios tests in FY 2017. In FY 2015, graphite and sparked air were also studied. Graphite is predicted as a major detonation product (Kuhl 2015), and modelers are interested in understanding the effect of carbon on the temperature of HE tests. Species produced by LIBS-sparked air correlate to some of those expected in the field from shocked air. Using a high-speed camera (with optical filters chosen based on LIBS results) and a UV-Vis spectrometer, NSTec will attempt to identify species that produce RF signatures in the field in the FY 2017 test. Planning for these tests will be guided by LIBS results.

The Special Technologies Laboratory (STL) has a unique lab-to-field (and back) loop. In FY 2014, this project supported the HET field campaign with a successful optical field collect. This led to FY 2016 DOE funding for the follow-on Helios project. To support Helios, the STL LIBS platform will continue to be used to prepare and inform optical diagnostics.

Project

The LIBS data presented in this report were collected and analyzed at STL, unless noted. A schematic of the LIBS and shadowgraphy setup is shown in Figure 1. As in FY 2014, a 1064 nm, 12 ns, Nd:YAG laser was used for ablation of samples or for sparking air. The gas chamber was either under vacuum or back-filled with air or argon. In FY 2015 a second Nd:YAG laser, doubled to 532 nm, was incorporated for shadowgraphy. Shadowgraphy provided images of shock waves, which were used for orientation in graphite and air-spark experiments. The position of the maximum energy density could be controlled by adjusting the height of the ablation laser focusing lens. The position of the optical fiber could also be adjusted to look at different regions of the plasma. Solid targets were in the form of Al or graphite rods that could be rotated or translated in the chamber to arrive at a spot clear of ablation craters. In our experiments, a 35 mJ/pulse (for most Al experiments) to 55 mJ/pulse (for graphite and air spark) laser pulse was focused onto the target (as well as above and into it with graphite). The laser beam was about 8 mm in diameter upon going into the focusing lens (Thor Labs LA1986, focal length of 125 mm at 587.6 nm). A 55 mJ pulse focused onto the surface of an Al rod produced a ~200 µm diameter spot. At the collection end, the optical fiber consisted of 19 close-packed fibers (silica/silica [core/cladding], high hydroxide ion content, 200/220/240 [diameter in microns of core/cladding/buffer]). The fiber collected emission from a ~1.1 mm diameter region of the plasma.

Al LIBS Experiments

To demonstrate the concordance between LIBS and explosions, Al species produced using laser ablation were compared with the detonation of an aluminized explosive (PBXN-113) in an explosive test chamber (Carney 2006) (Figure 2). In both cases, the decay rate of atomic aluminum (Al-I: 394.4 nm, 396.2 nm, $3s^24s\ ^2S \rightarrow 3s^23p\ ^2P^0$ transition, shown in blue in Figure 2) and the growth and decay of aluminum monoxide (AlO: centered at 484 nm, $B\ ^2\Sigma^+ \rightarrow X\ ^2\Sigma^+$ transition, shown in red in Figure 2) are similar. AlO appears about 2 µs after ablation with LIBS, and at 2 µs after first light in the explosive test chamber. And in both experiments, as AlO is formed, neutral Al decays exponentially. One difference between LIBS and the chamber is the faster decay for neutral Al with LIBS. This may result from higher initial LIBS temperatures (emission intensities were not corrected for temperature). Using integrated peak intensities for Al-II (Al^+) lines ($3s4f\ ^3F^0 \rightarrow 3s3d\ ^3D$ transition at 358.7 nm and $3s4p\ ^1P^0 \rightarrow 3p^2\ ^1D$ transition at 466.3 nm), and assuming a Boltzmann distribution, the electron excitation temperature was found to be ~30,000 K at 50 ns.

AlO is formed from gaseous (g) neutral aluminum (Al(g)) as indicated in Equations 1 and 2 below. The reaction is in cooperation or competition with oxygen (O) recombination (Equation 3).

$$Al(g) + O_2 = AlO + O \quad \textbf{(1)}$$

$$Al(g) + O + M = AlO + M \quad \textbf{(2)}$$

$$O + O + M = O_2 + M \quad \textbf{(3)}$$

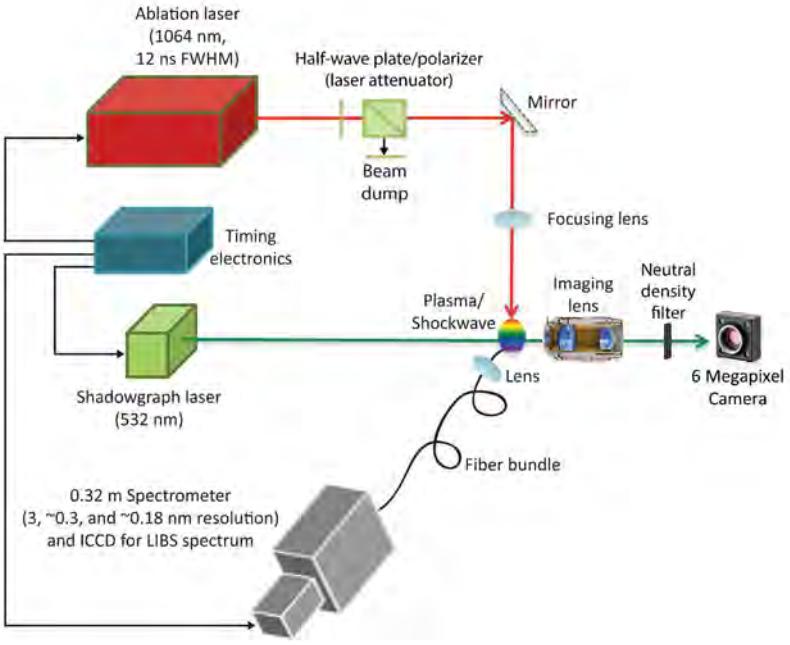

Figure 1. Schematic of LIBS and shadowgraphy setup

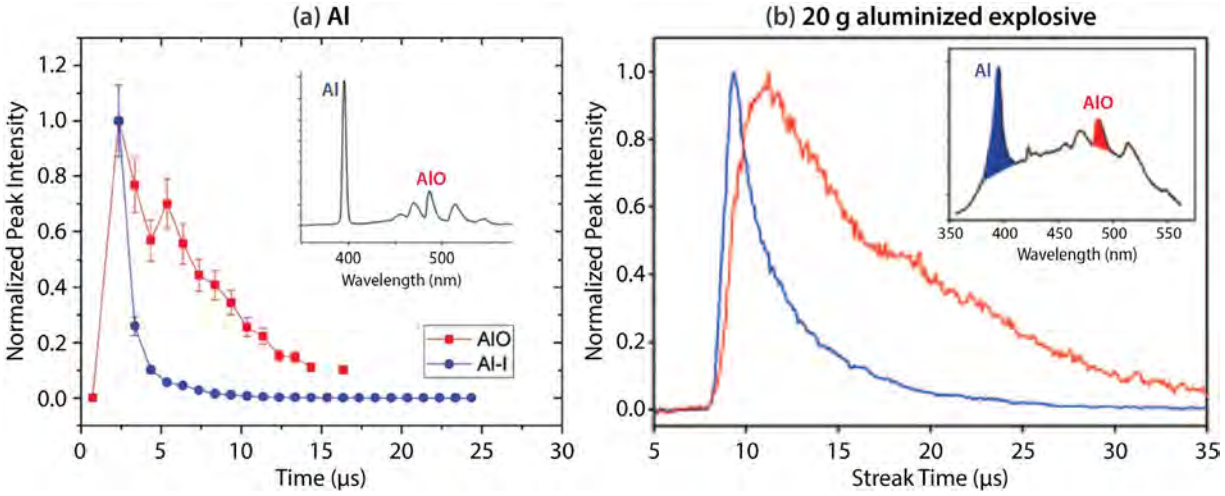

Figure 2. Al-I and AlO optical signatures generated by (a) LIBS of Al are similar to those from (b) a 20 g aluminized explosive in an explosive test chamber

The temperature at which reactions 1 and 2 both favor AlO formation is ~4300 K (Bai 2014). By fitting the $\Delta\upsilon = -1$ AlO band ($B\ ^2\Sigma^+ \rightarrow X\ ^2\Sigma^+$ transition) using a spectral simulation program at Applied Spectra, Inc. (ASI), we determined that this is roughly the temperature at which we started to observe AlO in the lab (Figure 3).

An example of another parameter that can be controlled with LIBS is the availability of O for combustion. We compared the decay of Al-I in vacuum, air, and argon (Figure 4) and observed that the decay of Al-neutral is faster in air than in argon (a comparatively dense but inert gas). In vacuum, the apparent rapid decay of Al-I is due to the lack of plasma confinement. In air, as seen in Figure 2a, the decay of Al-I is accompanied by the appearance of AlO.

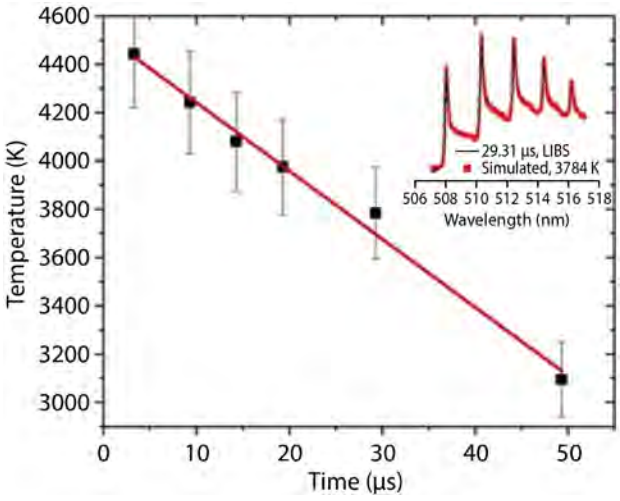

Figure 3. Mixed rotational and vibrational temperature vs. time, determined from AlO B–X, Δυ = –1 band, showing (inset) the lab spectrum (black) and simulated fit (red)

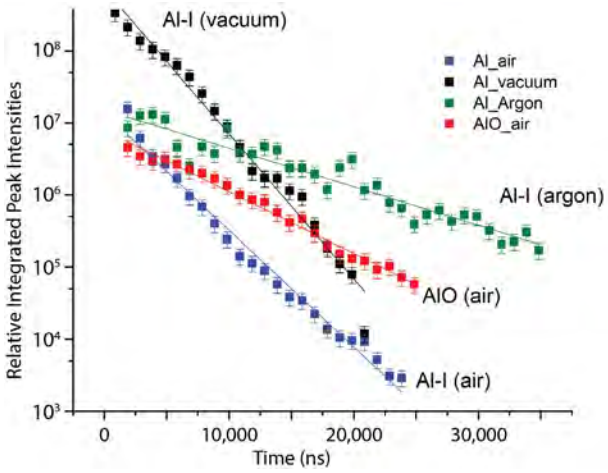

Figure 4. We compared the decay of atomic aluminum in vacuum, air, and argon and observed that the decay rate of neutral Al is faster in air than in argon, a comparatively dense but inert gas. In vacuum, the decay of Al-I is due to the lack of plasma confinement. In air, as shown also in Figure 2a, the decay of Al-I is accompanied by the appearance of AlO.

Time-resolved UV-Vis spectral data collected following detonation of an Al-cased explosion at HET in FY 2014 and time-resolved LIBS data for Al in air are also compared (Figure 5).

As seen in Figure 5, the atomic Al and AlO emission features are similar, but their timing differs. At HET, Al-I and AlO are observed in the millisecond range, whereas in the lab they are seen in the nanosecond-to-microsecond range. There is also significant blackbody emission at HET (presumably coming from smoke and other large particles). In addition to the scales of the experiments (~kg of Al at HET vs. micrograms ablated with Al LIBS), other differences, such as Al particle sizes produced and O throttling at HET (due to depletion during the explosive burst followed by turbulent in-welling), all likely contribute to the differences in timescales.

Additionally, the apparent temperatures of AlO when it is most prominent in the field (~6000 K from 2 to 4 ms after the burst, based on an STL temperature simulation) and of AlO in the lab (~4400 K at ~2 ms) are different. It is not clear why this is the case. We note that in the field there is strong blackbody emission; as well, molecular temperature is very sensitive to the shape of the background, so an accurate flat-field correction is required. We also note that reaction pathways may differ in the field vs. in the lab. At high temperatures, the chemical reaction in Equation 1 is favored over the reaction in Equation 2. If molecular O is more abundant than atomic O in the field vs. in the LIBS experiment, the available reaction pathways and thus temperatures when AlO is first observed may well differ. By 2 ms, turbulent in-welling should be occurring in the field. Using LIBS we did not look to see if more diatomic or atomic oxygen might be available for reacting with Al, but initially we observed a lot of atomic oxygen in sparked-air experiments.

Finally, ionic species were not observed at HET; it is likely that with millisecond gate widths, the hundreds-of-nanoseconds lifetime ionic emissions are buried in the blackbody background. Ionic Al was observed with LIBS on the nanosecond timescale. Al^{2+} (Al-III) could be observed in vacuum and Al^{+} (Al-II) in air, as shown in Figure 6.

The analogies demonstrated indicate that LIBS data can help guide field collects to spectral regions and gate widths that have the greatest impact in terms of extracting relevant parameters from field data. For FY 2017 Helios collects, STL is particularly interested

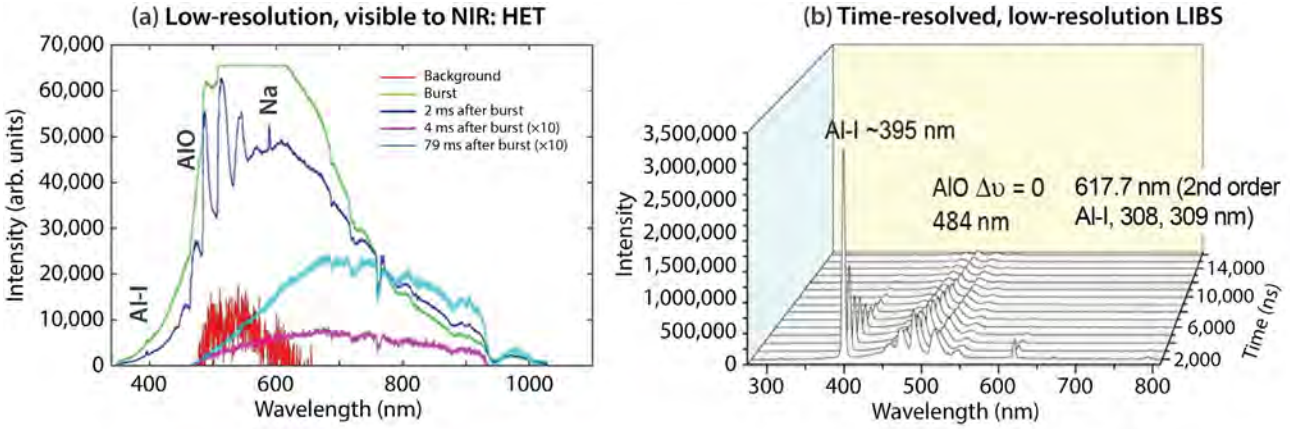

Figure 5. (a) HET vs. (b) Al LIBS. Optical signatures generated by LIBS of Al are similar to those from a HET explosion with an Al shell at 2 ms after the burst, but blackbody emission is strong at HET, and the timescales are very different. Second order Al-I lines seen with LIBS at ~617 nm correspond to Al-I emissions (at 308 and 309 nm) observed 5 ms after the explosive burst using a UV modular spectrometer in the field (UV spectrometer field data not shown here).

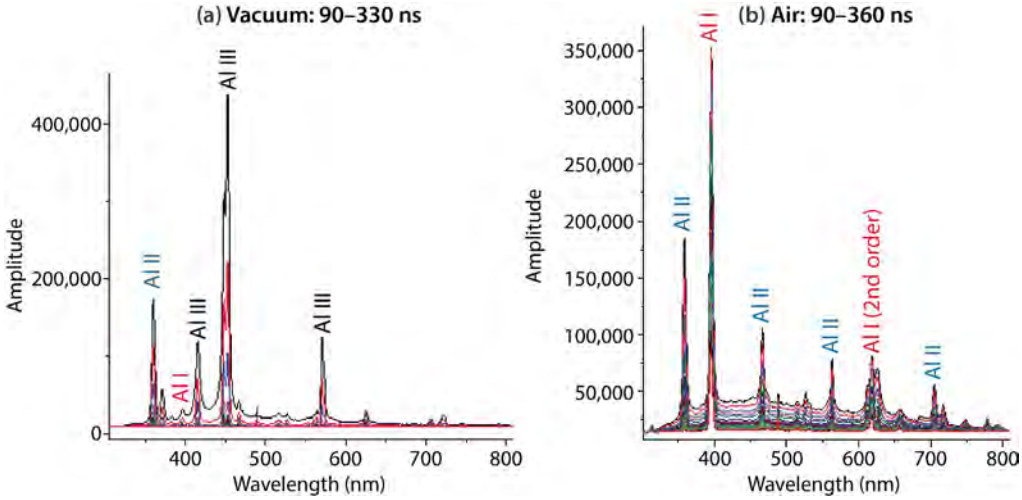

Figure 6. Time-resolved traces at 10 ns intervals, with early time emissions stronger than later time emissions, and highly charged species decaying to lower charged and atomic species at later times. (a) In vacuum, free expansion permits persistence of Al-III (Al^{2+}) species in the 90–330 ns range, whereas (b) in air, Al-II (Al^{+}) is the most highly ionized species observed under our LIBS conditions.

in fielding UV and UV solar-blind diagnostics because blackbody is lower in the UV, and solar emission is not contributing to signal in the solar-blind region (230–290 nm). Based on our work with Al and sparked air (described in the ***Graphite and Air-Spark LIBS Experiments*** section), examples of parameters derived from species observed in the UV with LIBS, which may be observed in the field (if gate widths are sufficiently narrow and spectral resolution is sufficiently high) include the following:

- Electron density vs. time via Stark broadening (e.g., Al-II 3s4s $^1S \rightarrow$ 3s3p $^1P^0$ transition at 281.6 nm [Figure 7])
- Relative local temperature derived from pairs of Al species (Al-I: $3s^23d\ ^2D \rightarrow 3s^23p\ ^2P^0$ transition at 308.2 and $3s^24s\ ^2S \rightarrow 3s^23p\ ^2P^0$ transition at 396.1 nm, and Al-II: 3s5f $^3F^0 \rightarrow$ 3s3d ^3D transitions at 263.8 nm and 3s4s $^1S \rightarrow$ 3s3p $^1P^0$ at 281.6 nm)

- Local temperature derived from molecular emissions (cyano-radical [CN] [violet system between $B^2\Sigma^+$ and $X^2\Sigma^+$ molecular states, ~340–425 nm]; nitrogen [N] monopositive ion N_2^+ [first negative system between $B^2\Sigma^+$ and $X^2\Sigma^+$ molecular states, ~340–480 nm]) (see ***Graphite and Air-Spark LIBS Experiments*** section)
- Species of interest to RF modelers (ionic Al species [Figure 5]) and CN and N_2^+ (first negative B-X transition bands at approximately 350–358 nm and 380–392 nm)

CN and N_2^+ are relevant to RF modelers interested in seeing effects of coronal discharges in the field. The observation of CN and N_2^+ in laser-sparked air (with and without graphite present) is influencing filter selection for a high-speed camera to be fielded at Helios in FY 2017. LIBS studies producing these species are described in more detail next.

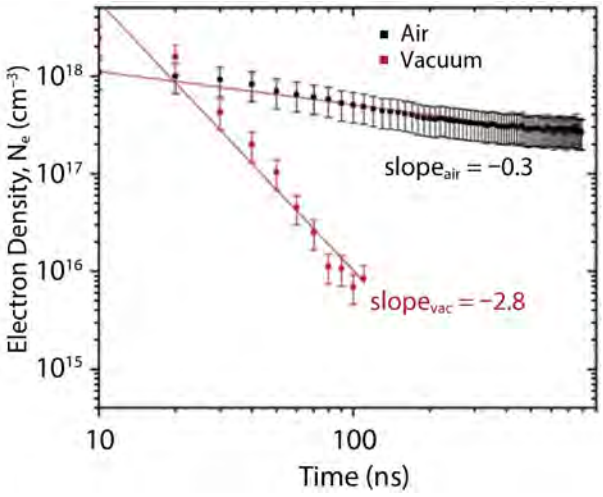

Figure 7. The influence of pressure on electron density, calculated using the line width of the 3s4s $^1S \rightarrow 3s3p\ ^1P^0$ transition of the Al^+ ion at 281.6 nm (Stark-width constant derived from Konjević [2002]). In vacuum, electron density decays with a slope close to –3, indicating free expansion of the plasma. In air, the decreased decay rate (slope –0.3) indicates plasma confinement.

Graphite and Air-Spark LIBS Experiments

According to models, graphite is the most abundant detonation product for a number of explosives, including TNT (Kuhl 2015). Modelers are interested in knowing how carbon affects the temperature of HE tests. Using LIBS, we performed a preliminary study comparing the temperatures of laser-sparked air with and without ablated graphite present. We also looked at the formation of atomic and molecular species as a function of laser focus at, above, and below the surface of a graphite substrate.

To orient ourselves and compare propagation of shock waves in air, with, and without graphite present, we used shadowgraphy. Shock wave images produced at 300 ns from an air spark alone (Figure 8a) and from an air spark generated with the laser focus immediately above a graphite rod (Figure 8b) are shown. Corresponding time-resolved spectra (Figures 8c and 8d) show that atomic O, N, and hydrogen (H) are present from air breakdown in both cases. The intensity of these species decays rapidly. In the absence of graphite, N_2^+ is the predominant molecular species observed in the 300–800 nm spectral region, whereas CN radical is the predominant molecular species observed with graphite present.

To determine temperature with and without graphite present, we focused our attention on the 360–480 nm spectral region (Figures 9a and 9b), where molecular species appear at a 10 µs gate delay. At 10 µs, Stark broadening contributions are minimal, and our results were comparable to that from an air-spark study performed at Pacific Northwest National Laboratory (Harilal 2015). Specair (Spectralfit S.A.S. 2015) software calculates temperature and concentrations of air plasma species from vacuum UV to mid-IR, and was used for temperature simulation and molar ratio determination.

Under our collection conditions (with the optical fiber looking towards the base of the air spark and at the surface of the graphite rod), our preliminary study indicates that the calculated plasma temperature (assuming local thermodynamic equilibrium)

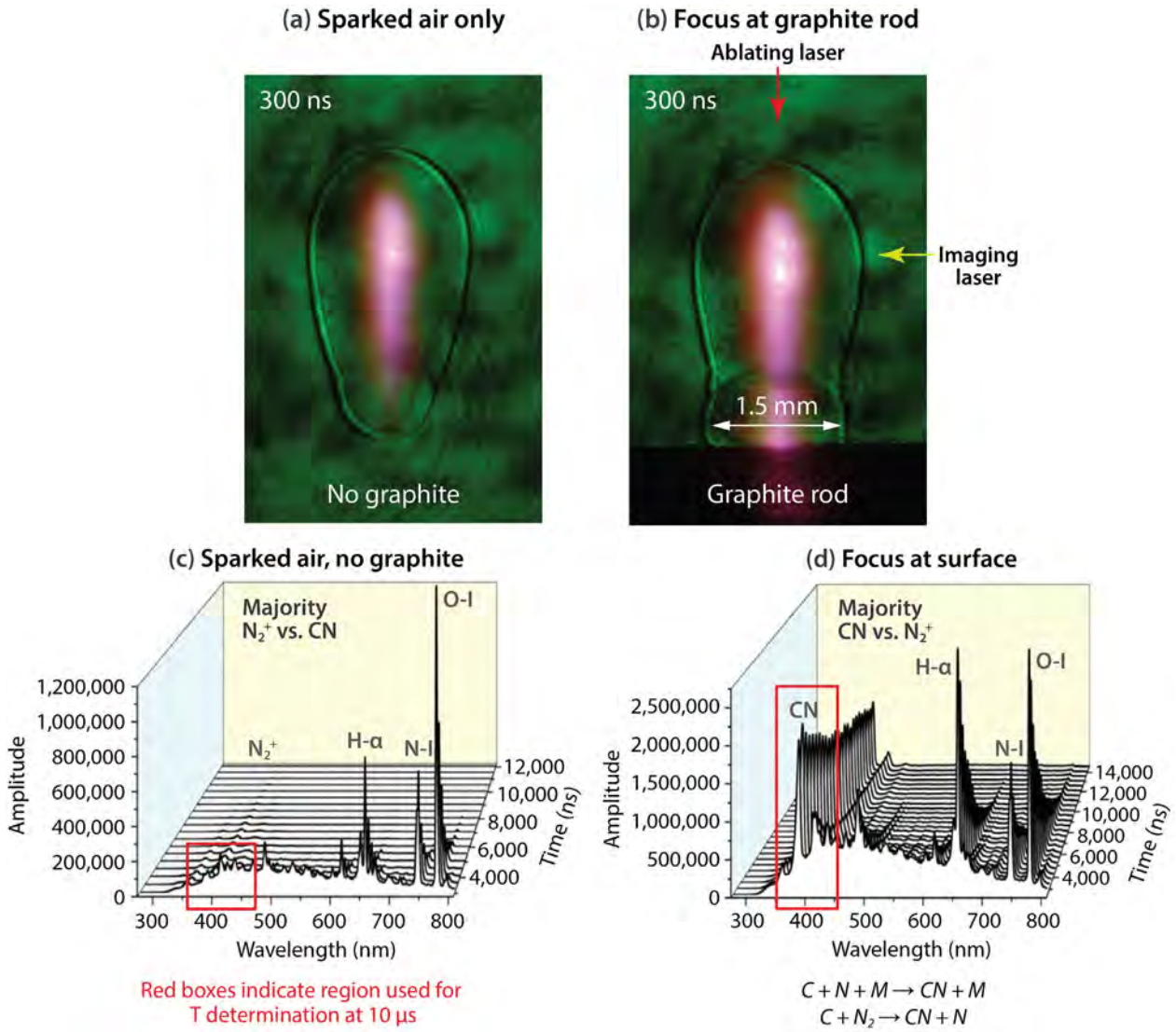

Figure 8. Shock wave images (a) in air and (b) at the surface of a graphite rod at 300 ns. The shock waves were ~1.5 mm laterally at 300 ns. By 10 μs, they had expanded to a ~12 mm diameter sphere (without graphite) and a ~13.5 mm wide hemisphere (with graphite present; not shown), indicating shock wave velocities of ~1 km/s. The pinkish light corresponds to the plasma light emitted over its light-emitting lifetime—not just 300 ns. Also presented are time-resolved LIBS spectra (c) of sparked air with no graphite and (d) with the focus at the surface of a graphite rod.

is about 700 K lower, and the concentration of CN is ~50x higher, with graphite present than without. Two reasons the plasma may be cooler with graphite are (1) the graphite may be acting as a heat sink and (2) incandescent emission may be cooling the plasma. (Delayed firework-like emission—attributed to ejected hot particles or droplets formed by overheating of trapped gases in the layered graphite structure—has been observed by intensified CCD [ICCD] for graphite in vacuum [Harilal 2011]).

We also performed experiments that involved moving the laser focus above a graphite rod. This alters where the maximum energy goes. With the focus both above and at the graphite surface, air is entrained, and

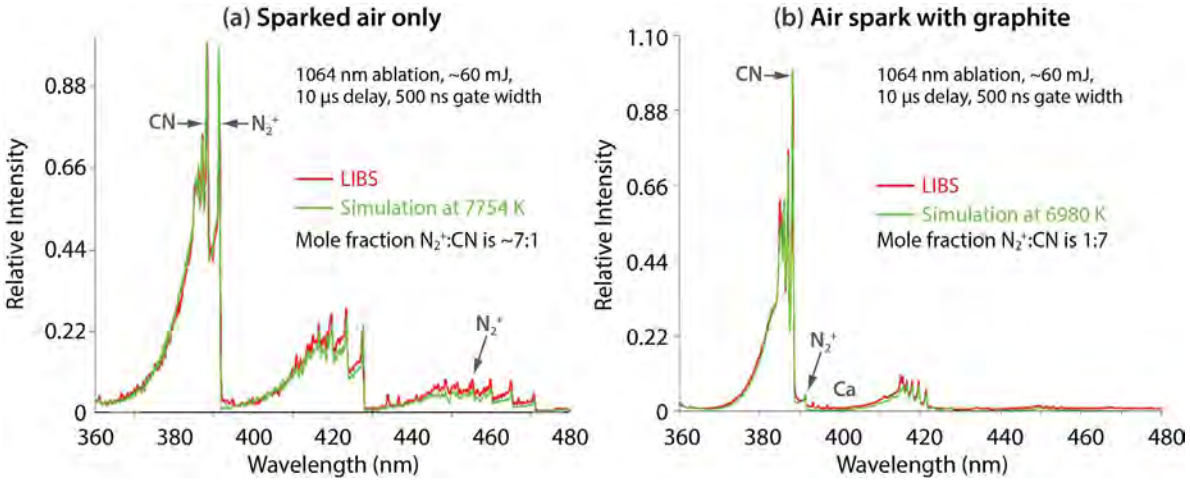

Figure 9. LIBS spectra (red line) overlaid by temperature simulations (green line) with (a) air spark only and (b) air spark with graphite. Calcium (Ca) is an impurity in the graphite.

the time-resolved spectra indicate that the decay of air species and production of CN and N_2^+ appear to be fairly steady in time (Figure 10a and 10b). With the laser focus moved to 2 mm below the graphite surface (Figure 10c), less air appears to be entrained in the plasma (O, N, and H are not prominent in the spectra, and the shock wave is not axially elongated nor indicative of air- and substrate-borne shocks, which fuse together), and emission from CN is less persistent. This decay may be related to the decreased availability of atomic and molecular N and/or more efficient scavenging of the CN radical at or near the surface. Additionally, there is less blackbody contribution, which is consistent with the power density being lower at the surface than it was when the focus was in the air, or at the surface of the substrate. More C_2 is also observed with the focus below the surface. This is also consistent with lower power density. Sánchez-Aké (2009) observed more C_2 at lower flux and attributed it to the layer-by-layer ablation of graphite and production of C_n (n>2) carbon clusters, which dissociate to C_2 after collisions with energetic electrons. At higher fluences, the probability of direct C_n formation is decreased.

Species distributions and decay will also differ *spatially* for a given laser-focus position; this was demonstrated with LIBS of Al in air at ASI in FY 2014, when AlO production was monitored spatially in time. Collection of species emissions onto a fiber array, or directly onto a spectrometer slit, would aid our understanding of the spatial nature of the LIBS air spark and graphite products. In addition, collection of LIBS spectra in the mid-IR would permit a more complete understanding of other molecular species produced by air sparks as well as those with graphite present. These could, in turn, prompt collection of IR and coupled-RF emissions in the field.

In FY 2014, this project also supported a preliminary investigation into Cantera chemical kinetics software (Goodwin 2014) for modeling combustion of Al. It was not possible to perform in-depth kinetic modeling for Al_2O_3 production because the necessary thermodynamic data were unavailable for many of the relevant Al reactions. These constants are more accessible for air and carbon chemistry, however, and could be applied to conditions and air and carbon species observed with LIBS and HE tests.

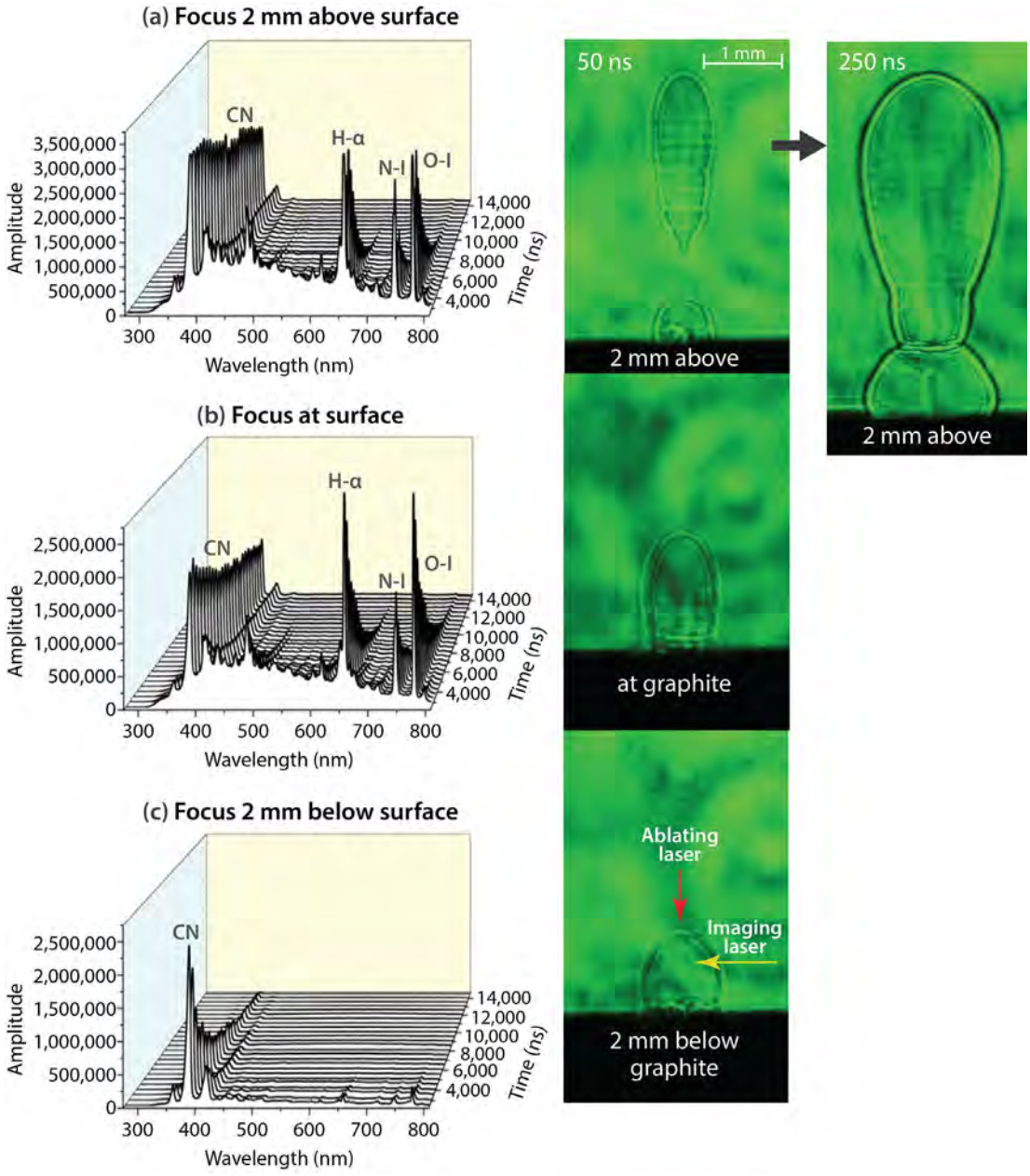

Figure 10. Time-resolved spectra and representative shock wave images at 50 ns with the focus (a) 2 mm above the graphite substrate, (b) at the surface of the substrate, and (c) 2 mm below the graphite substrate. With the focus 2 mm above the graphite, air and graphite shock waves begin to fuse at 250 ns (image at top, far right).

Conclusion

At the beginning of this project, we believed that LIBS could complement explosive test chamber and field characterizations of HE. The results described above have moved NSTec from plausible belief to empirically derived knowledge.

This project has further developed our LIBS capabilities and increased our knowledge regarding collection and analysis techniques for the lab and field. We have used LIBS to create time- and cost-effective, micro-scale high-energy states that provide optical signatures analogous to those from conventional explosions. LIBS

can provide high temporal and spectral resolution that feeds outward to HE tests for field diagnostic calibration and specifications, for field data analysis, and as an investigative tool to support HE modeling.

In addition to permitting comparison to explosive test chamber and large explosive tests, our work with Al allows us to use it as a benchmark for other metals. By comparing relative lifetimes and emission strengths of Al lines to those of other metals and molecular species in the lab, we can infer the likelihood of seeing emissions of other metals and molecular species in the field.

Our initial studies with graphite and air sparks indicate that molecular species produced by LIBS with graphite present are cooler relative to an air spark alone. Diamond is a major detonation product (according to modeling), and corresponding chemistry and temperature studies with diamond are also of interest to modelers. This project has laid the foundation for future studies of this type.

Our LIBS data and the bench-top platform will be used to aid the design of collection diagnostics, and to calibrate a bank of spectrometers and a high-speed camera for fielding. LIBS will be used for spectral intensity and luminosity measurements, to determine dynamic range and thresholds, and as an indicator of exposure times in the field. The LIBS-generated Al and air-spark spectra are being used to help select the best filter to permit high-speed imaging of species likely responsible for generating RF signatures recorded at HE tests. It is likely that a filter that permits observation of N_2^+ (as well as any CN) emission (~345–360 nm or ~380–392 nm) will be chosen.

The work conducted in this SDRD project has led to a solicitation for further Defense Nuclear Nonproliferation R&D–funded work in FY 2016 (the requested proposal has been delivered and is being evaluated). We expect to write a joint proposal for FY 2017 with Sandia National Laboratories (SNL), supported by ASI.

Acknowledgments

We would like to thank Ben Valencia (STL), Rick Allison (STL), and Glen Anthony (formerly STL) for their assistance in preparing samples for the LIBS apparatus this year. We also thank Dominique O'Neill (summer hire) for exploring AlO temperature simulations using the STL code, and Daryl Dagel (SNL) and Olga Spahn (SNL) for helpful discussions.

References

Bai, X., V. Motto-Ros, W. Lei, L. Zheng, J. Yu, "Experimental determination of the temperature range of AlO molecular emission in laser-induced aluminum plasma in air," *Spectrochim. Acta, Part B: Atomic Spectroscopy* **99**, 1 (2014) 193–200.

Bogaerts, A., Z. Chen, R. Gijbels, A. Vertes, "Laser ablation for analytical sampling: What can we learn from modeling?" *Spectrochim. Acta, Part B: Atomic Spectroscopy* **58**, 11 (2003) 1867–1893.

Carney, J. R., J. S. Miller, J. C. Gump, G. I. Pangilinan, "Time-resolved optical measurements of the post-detonation combustion of aluminized explosives," *Rev. Sci. Instrum.* **77**, 6 (2006) 063103-1–063103-6.

Goodwin, D. G., H. K. Moffat, R. L. Speth, "Cantera: An object-oriented software toolkit for chemical kinetics, thermodynamics, and transport processes" (version 2.2.0), http://www.cantera.org/docs/sphinx/html/index.html, accessed September 30, 2014.

Harilal, S. S., A. Hassanein, M. Polek, "Late-time particle emission from laser-produced graphite plasma," *J. Appl. Phys.* **110**, 5 (2011) 053301-1–053301-5.

Harilal, S. S., B. E. Brumfield, M. C. Phillips, "Lifecycle of laser-produced air sparks," *Phys. Plasmas* **22**, 6 (2015) 063301.

Konjević, N., A. Lesage, J. R. Fuhr, W. L. Wiese, "Experimental Stark widths and shifts for spectral lines of neutral and ionized atoms (A critical review of selected data for the period 1989 through 2000)," *J. Phys. Chem. Ref. Data* **31**, 3 (2002) 819–927.

Kuhl, A. L., "On the structure of self-similar detonation waves in TNT charges," *Combustion, Explosion, and Shock Waves* **51**, 1 (2015) 72–79.

Sánchez-Aké, C., M. Bolaños, C. Z. Ramirez, "Emission enhancement using two orthogonal targets in double pulse laser-induced breakdown spectroscopy," *Spectrochim. Acta, Part B: Atomic Spectroscopy* **64**, 9 (2009) 857–862.

Spectralfit S.A.S., Specair Version 3.0.2.0, http://specair-radiation.net/, accessed August 2015.

This page left blank intentionally

Solid-State Neutron Detectors Using Uranium Oxides

LAO-22-13 | Continued from FY 2014 | Year 3 of 3

Craig Kruschwitz,[1,a] David Schwellenbach,[a] Sanjoy Mukhopadhyay,[b] Thomas Meek,[c] and Brandon Shaver[c]

In this project we attempt to develop and test a new type of neutron detector using uranium oxides. It has been known for many years that uranium dioxide (UO_2) and other uranium compounds exhibit semiconducting characteristics with a broad range of electrical properties. We seek to exploit these characteristics to make a UO_2-based direct-conversion semiconductor neutron detector. This year we focused on improving the quality of the samples used to test for neutron sensitivity. In particular, we focused on trying to grow higher-quality crystals and possibly a p-n junction. To achieve this, the University of Tennessee, Knoxville established new crystal growth capabilities but was not able to produce new crystals before the end of the year. We also conducted alpha and neutron sensitivity tests with UO_2 thin films. Results of the tests were inconclusive, as it was impossible to separate interactions in the UO_2 from those occurring in the sapphire substrate upon which the film was deposited.

[1] kruschca@nv.doe.gov, 505-663-2023

[a] New Mexico Operations–Los Alamos; [b] Remote Sensing Laboratory–Andrews; [c] University of Tennessee, Knoxville

Background

High-efficiency neutron detectors are required for a wide variety of applications, such as high-energy physics, nuclear forensics, nonproliferation, oil well logging, and many others. Recent shortages in ^{3}He gas, the standard material for neutron detection for many years, have driven a search for new neutron detector materials. Semiconductor-based devices are one such alternative. These devices have the advantage of being more compact and requiring smaller voltages to operate compared to ^{3}He detectors. Semiconductor neutron detection devices are typically classified as one of two types: indirect-conversion devices and direct-conversion devices.

In an indirect-conversion device, a layer of a neutron-reactive substance (usually ^{10}B or ^{6}Li) is placed in contact with a separate detector material, typically a silicon (Si) diode. A neutron interacting in the reactive layer produces energetic reaction products, some of which deposit energy in the detector material, generating electron-hole pairs and hence a signal. A shortcoming of such devices is that only some of the reaction energy can be deposited in the detecting medium; the rest is either absorbed in the reactive material or moves away from the detecting medium to conserve momentum in the reaction. Therefore, there is a fundamental limit to the efficiency of such a device. Use of etching technologies to create complex indirect-conversion devices with highly optimized geometries have increased these limits (McGregor 2009, Bellinger 2010, Nikolic 2010), but there exists still the desire to improve upon such devices with the discovery of a suitable direct-conversion device material.

In a direct-conversion device, the neutron-reactive material and the detector material are one and the same—virtually all of the reaction energy is available for detection. But materials suitable for direct-conversion devices are relatively rare, and

their properties are often poorly understood. In the past, much research has been conducted into boron-based compounds, such as boron carbide and boron nitride, which both use ^{10}B as the neutron-reactive isotope. More recently, groups at Fisk University, Y-12, and Radiation Monitoring Devices have investigated lithium indium selenide ($LiInSe_2$) (Kargar 2011, Tupitsyn 2012), another promising material that uses ^{6}Li as the neutron-reactive isotope. However, none of these materials have yet truly demonstrated their viability as direct-conversion materials.

This project continues SDRD work started in FY 2013 (Kruschwitz 2014) and FY 2014 (Kruschwitz 2015). The goal was to evaluate the feasibility of using uranium dioxide (UO_2) as a candidate material for a direct-conversion semiconductor neutron detector. UO_2 and other uranium oxides have been overlooked as neutron detector materials, despite being known to have semiconducting properties and to be neutron reactive. In this initial work we use depleted uranium, which consists of approximately 99.7% ^{238}U, with ^{235}U comprising most of the remaining 0.3%. The cross sections for neutron-induced fission as a function of neutron energy for ^{238}U and ^{235}U are plotted with the cross sections for the $^{10}B(n,\alpha)$ reaction and the $^{6}Li(n,\alpha)$ reaction for comparison in Figure 1. The data are from the ENDF/B VII tables (Chadwick 2006). The slow neutron cross section of ^{235}U is comparable to, but somewhat smaller than, those of ^{10}B and ^{6}Li, showing that a detector with a significant amount of ^{235}U could be an effective thermal neutron detector. The fission cross section of ^{238}U for slow neutrons is small, but for >1 MeV energy neutrons, the ^{238}U fission cross section approaches that of ^{235}U. The fast neutron fission cross sections of uranium are much larger than for ^{10}B or ^{6}Li, which suggests that a uranium-based detector is particularly suitable for fast neutron detection.

In addition to its superior sensitivity to fast neutrons, a second potential advantage of using uranium as the neutron-sensitive material is the large amount of energy that is released in the fission of a uranium nucleus. The neutron-induced fission of a ^{238}U or ^{235}U nucleus releases >165 MeV of energy, much greater than the energy released in the $^{10}B(n,\alpha)$ (~2.3 MeV)

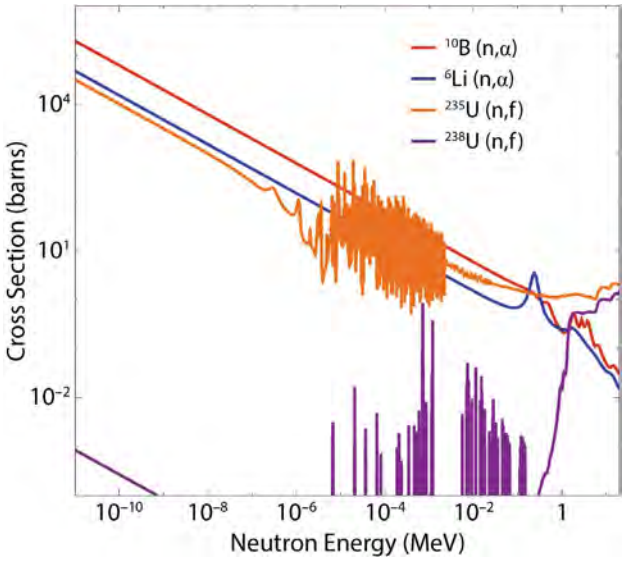

Figure 1. Neutron-induced fission or transduction cross sections versus neutron energy for ^{235}U, ^{238}U, ^{10}B, and ^{6}Li. ^{235}U has a relatively high cross section for thermal and low-energy neutrons, comparable to those of ^{10}B and ^{6}Li. Both ^{238}U and ^{235}U are much more sensitive than ^{10}B or ^{6}Li to neutrons with energies greater than 1 MeV.

or in the $^{6}Li(n,\alpha)$ (~4.8 MeV) reactions. The large amount of energy released as a result of the fission of a uranium nucleus raises the possibility of developing a neutron detector with superb background noise and gamma discrimination. In general, the energy deposited by gamma interactions is likely to be much less than that deposited by fission events. The exception to this would be gamma rays with sufficient energy (>6 MeV) to induce photofission in ^{238}U and ^{235}U. Photofissions from such gammas would produce signals indistinguishable from neutron-induced fissions.

Properties of UO_2

UO_2 has been studied extensively due to its use as a nuclear fuel and consequently has long been known to exhibit semiconducting properties (An 2011). The resistivity of intrinsic UO_2 is about 1.5×10^3 Ω-cm at room temperature, which is similar to Si and GaAs. This value, however, depends sensitively on the stoichiometry of the sample, with hypostoichiometric compositions becoming much more insulating, and hyperstoichiometric compositions becoming more conductive

(Meek 2001). The carrier mobility for UO_2 has not been very precisely determined, with the measured values exhibiting wide variation. Most measurements indicate a low mobility, from 10^{-2} to 10^{-1} $cm^2/(V{\cdot}s)$. Some early measurements yielded a much higher mobility (~10 $cm^2/(V{\cdot}s)$) (Hartmann 1936), but these are generally not considered to be reliable.

Because of the semiconducting properties of UO_2, there has recently been some interest in using it to fabricate semiconductor devices (Meek 2001, 2005, 2008). Meek (2008) and coworkers report successfully fabricating Schottky diodes using UO_2 deposited in thin films, and a simple p-n-p transistor using a single crystal of UO_3 implanted with various dopants. Meek (2005) and coworkers have also studied the effects of various dopants on the electrical properties of UO_2. In a recent review paper, Caruso (2010) suggested that uranium oxides and other compounds might make useful semiconductor neutron detectors, owing to their sensitivity to neutrons and semiconductive properties. Caruso drew particular attention to the large release of energy accompanying the fission of a uranium nucleus, suggesting that because of this, uranium-based semiconductor detectors could exhibit unprecedented background suppression characteristics. This SDRD project represents the first attempt to develop a uranium-based semiconductor neutron detector.

Project

Fabrication of UO_2 and Thin Film Samples

Fabrication and preparation of UO_2 samples was performed by the Meek group from the University of Tennessee, Knoxville (UTK), Materials Science and Engineering Department. Much of the work was performed at the UTK Radiochemistry Center for Excellence. UTK attempted to provide depleted-UO_2 samples fabricated using three different techniques: single crystals of UO_2 grown using both an arc-fusion technique and vapor phase growth, and thin film samples using chemical solution deposition. The single-crystal samples grown using arc-fusion were produced by Professor Meek as part of previous research into UO_2 but were used for this project in FY 2013 and FY 2014 (Kruschwitz 2014, 2015). After the crystal surfaces were sputter cleaned, Au and Ag electrodes were coated onto the crystal surfaces in an attempt to make a Schottky diode with the Au as the rectifying contact and the Ag as the ohmic contact. These attempts proved to be unsuccessful; however, rectifying behavior was often observed initially, but faded rapidly, leaving two ohmic contacts and hence a resistive device rather than a diode. Neutron pulse-counting experiments were attempted using these resistive devices in FY 2013 and FY 2014 (Kruschwitz 2014, 2015). While there were some promising results obtained, for the most part the results showed the need to improve the quality of the samples we were using. Specifically, they demonstrated the need for either very high–resistance samples or for a p-n or Schottky junction. Pulse counting with a reverse-biased p-n or Schottky diode is effective because background currents can be suppressed in such a configuration. This allows the large electronic pulses resulting from a neutron-induced fission to be easily detected. A similar effect can be achieved by using a material with a very high resistivity. Therefore, in FY 2015, we emphasized improving the quality of the single crystals used by establishing a new crystal growth mechanism. We also explored using thin films of UO_2, which exhibit very high resistance, for neutron detection.

In an attempt to produce higher-purity single crystals of UO_2, UTK established an apparatus to grow the crystals using vapor phase deposition. The hope was that with higher-purity crystals, our difficulties making a Schottky diode might be overcome. We also believed that it would be possible to use this technique to make a p-n junction by depositing or growing an n-type material on the UO_2 crystal, which is inherently p-type. The apparatus was completed at the end of June 2015, but safety and radiological procedures were not approved and in place in time for any crystals to be produced by the end of FY 2015. Therefore, we proceeded to use thin film samples for the remainder of our study.

Thin film polycrystalline-depleted UO_2 samples were produced by a chemical solution deposition technique. With this technique uranyl acetate precursors are deposited onto sapphire substrates. The sapphire substrates are first plasma cleaned, and then a 50 nm layer of Au is sputtered onto a third of the surface to be used as a rectifying contact. The solvent is then evaporated and the thin film annealed in an argon atmosphere. Upon cooling, a 50 nm layer of Ag is sputtered onto the top surface to create an ohmic contact. A schematic of the thin film samples is shown in Figure 2.

The maximum film thickness that can comfortably be obtained with this method is approximately 500 nm, which presents some challenges in using the thin films to detect neutrons. The thinness of the films means that there is very little uranium present with which incoming neutrons can interact. Thus, long integrations or extremely active neutron sources are necessary in order to see fission. The thinness also means that much of the energy of the fission products will not be captured in the UO_2. The range of the fission fragments, the energetic charged particles produced in fission, is on the order of 5–10 microns in UO_2. Thus, the fragments will likely escape along with much of their energy. GEANT4 (Agostinelli 2003) was used to simulate the expected pulse height distribution for a 500 nm thick film. The result is shown in Figure 3. Clearly, even though much of the 165 MeV or so of fission fragment energy escapes, a clear peak between 10 and 20 MeV can be expected. This should present a signal that can be unambiguously attributed to fission.

The thin film samples had one compelling advantage over the arc fusion–produced single crystals used previously, however. The resistance of the devices made with the films appeared to be extremely high (tens of MΩ or more), perhaps due to the films being slightly hypostoichiometric. This meant that pulse counting was a real possibility, and thus we attempted some experiments with the films.

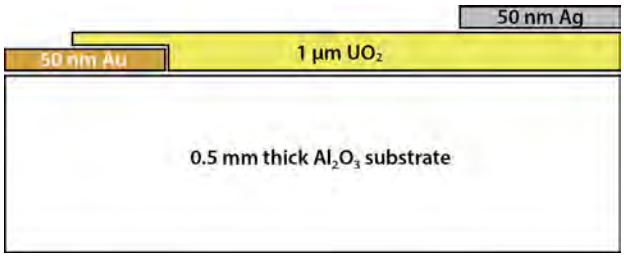

Figure 2. Schematic of a UO_2 thin film sample

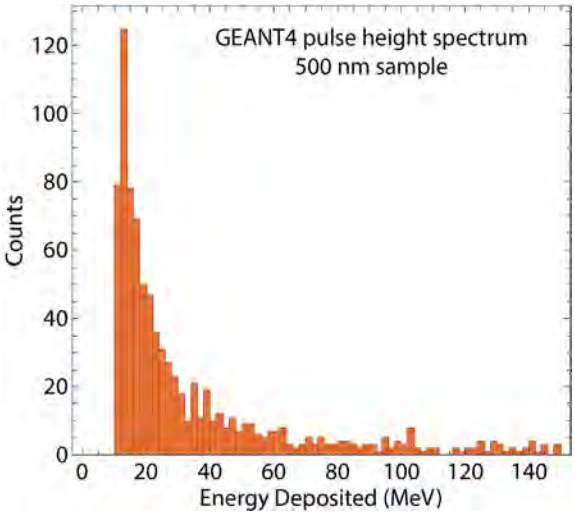

Figure 3. Simulated energy deposition pulse height spectra for 10 MeV neutrons incident on a 500 nm UO_2 sample generated with GEANT4. Most fission fragment energy escapes the sample, but a peak around 10 to 20 MeV is still expected.

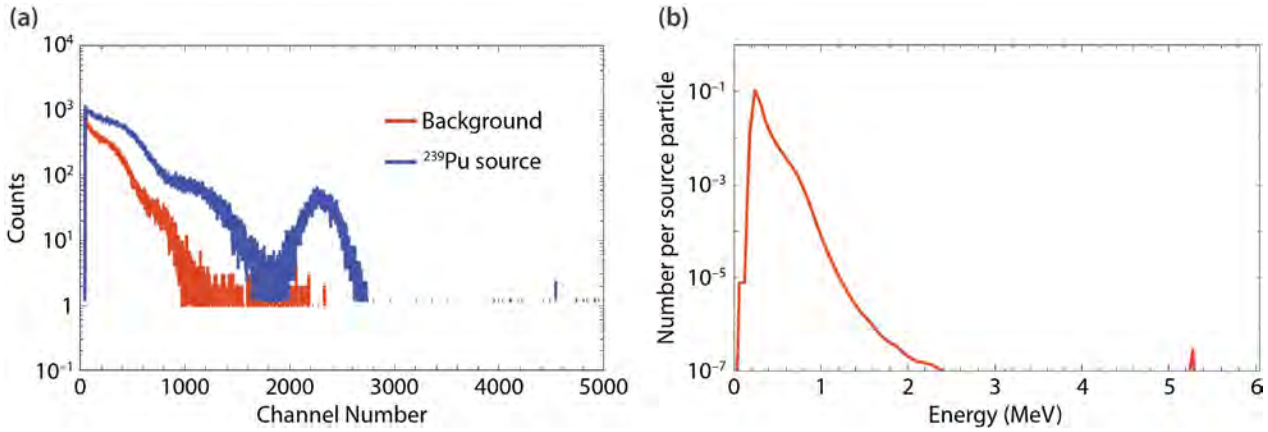

Figure 4. (a) Measured background and ^{239}Pu source pulse height spectra. A clear spectral feature is seen with a peak around channel number 2200. (b) MCNPX simulation of the pulse height spectrum for 5.2 MeV alpha particles in a 500 nm thick UO_2 layer. Very little energy is deposited in the UO_2 layer.

Experimental Tests

Tests of the alpha particle and neutron sensitivity were done on several UO_2 thin films provided by UTK. While we are interested in evaluating the feasibility of UO_2 as a neutron detector material, rather than its sensitivity to alpha particles, an alpha particle source is useful to establish that energetic charged particles can be detected with UO_2. A 1 µCi ^{239}Pu source was used as a source of 5.2 MeV alpha particles. The source was placed so that it was as close as possible to the UO_2 film, and a pulse height spectrum was collected using an 8000-channel multichannel analyzer (MCA). An example of a background and ^{239}Pu source pulse height spectrum is shown in Figure 4a. There is a peak in the ^{239}Pu at around MCA channel 2200 clearly separable from the background. This suggested strongly that the UO_2 is an effective charge particle detector, and further suggests it likely could be used to detect the charged fragments from neutron-induced fission.

A more thorough analysis, however, suggests that the strong peak in the pulse height spectrum is likely due to alpha particle energy deposition in the sapphire substrate rather than the UO_2. An MCNPX simulation of the pulse height spectrum for 5.2 MeV alpha particles into a 500 nm thick layer of UO_2 is shown in Figure 4b. It is clear that very little of the alpha particle energy is deposited in the UO_2 (~100–200 keV). However, we can make a rough estimate of the energy to which the peak must correspond based on the settings of the MCA and other electronics used to collect the spectra. This estimate shows that the peak must correspond approximately to the full alpha particle energy. This suggests that we are collecting a signal not just from the UO_2 layer, but from the sapphire substrate as well, and because the substrate is so much larger than the UO_2, it clearly dominates the overall signal. It is possible that a parallel plate electrode geometry would ameliorate this somewhat by isolating the electric field, and therefore the electrical signal, in the UO_2 layer. Unfortunately, this could not be accomplished with the equipment available.

A neutron sensitivity test was also performed using a 0.1 µCi ^{252}Cf source. Because of the small amount of uranium in the thin film, relative weakness of the source, and limited integration time, no distinct neutron-induced fission spectrum was seen.

Conclusion

In FY 2015, we completed our exploration of UO_2 as a potential direct-conversion semiconductor neutron detector material. The results of the previous 2 years of this project showed the need for samples with either very high resistance or a high-quality Schottky or p-n junction. The focus this year, therefore, was to improve the quality of the UO_2 single-crystal and polycrystalline thin film samples used in our experimental tests, and

to explore techniques for producing a uranium oxide–based p-n junction. UTK established a new crystal growth apparatus at the UTK Radiochemistry Center for Excellence capable of growing UO_2 crystals using a vapor phase deposition technique. In addition to being able to produce crystals of superior quality and purity to the arc fusion–grown crystals used in FY 2013 and 2014, we believed it might be possible to produce a p-n junction by growing an n-type material on a p-type UO_2 substrate. The apparatus was completed, but we were unable to produce any new crystals by the end of FY 2015.

We also performed alpha and neutron sensitivity tests on some UO_2 thin film samples. An initially promising alpha particle pulse height spectrum was obtained with a 1 µCi ^{239}Pu source. A more careful analysis, however, revealed that the pulse height spectrum could not be conclusively attributed to alpha particle energy deposition in the UO_2, but was more likely dominated by the sapphire substrate. A spectrum collected using a 0.1 µCi ^{252}Cf source in an attempt to detect a neutron-induced fission signature was similarly inconclusive.

Because this was the final year of this SDRD project, we sought alternative funding sources to continue to investigate the concept explored here. A proposal to investigate U_3O_8 and UO_3 as candidate detector materials, with Professor Meek of UTK and Professor Anthony Caruso of the University of Missouri, Kansas City as co-principal investigators, was submitted to the Defense Threat Reduction Agency. This proposal was accepted and work on it is expected to start in FY 2016. A second proposal to continue our study of UO_2 as a neutron detector material, with Professor John Auxier of UTK as principal investigator, was submitted to the Defense Advanced Research Projects Agency. A decision on this proposal is forthcoming.

References

Agostinelli, S., et al., "GEANT4—a simulation toolkit," *Nucl. Instrum. Methods Phys. Res. A* **506**, 3 (2003) 250–303.

An, Y. Q., A. J. Taylor, S. D. Conradson, S. A. Trugman, T. Durakiewicz, G. Rodriguez, "Ultrafast hopping dynamics of 5*f* electrons in the Mott insulator UO_2 studied by femtosecond pump-probe spectroscopy," *Phys. Rev. Lett.* **106**, 20 (2011) 207402.

Bellinger, S. L., R. G. Fronk, W. J. McNeil, J. K. Shultis, T. J. Sobering, D. S. McGregor, "Characteristics of the stacked microstructured solid state neutron detector," *Proc. SPIE* **7805** (2010) 78050N.

Caruso, A. N., "The physics of solid-state neutron detector materials and geometries," *J. Physics Cond. Matter* **22** (2010) 443201.

Chadwick, M., et al., "ENDF/B-VII.0: Next generation evaluated nuclear data library for nuclear science and technology," *Nuclear Data Sheets* **107**, 12 (2006) 2931–3060.

Hartmann, W., "Elektrische untersuchungen an oxydischen halbleitern," *Zeitschrift für Physik* **102**, 11–12 (1936) 709–733.

Kargar, A., J. Tower, H. Hong, L. Cirignano, W. Higgins, K. Shah, "Lithium and boron based semiconductors for thermal neutron counting," *Proc. SPIE* **8142** (2011) 81421P.

Kruschwitz, C. A., D. Schwellenbach, S. Mukhopadhyay, T. Meek, J. Auxier, B. Shaver, T. Cunningham, "Solid-state neutron detectors using uranium oxides," in *Site-Directed Research and Development*, FY 2013, National Security Technologies, LLC, Las Vegas, Nevada, 2014, 97–102.

Kruschwitz, C. A., D. Schwellenbach, S. Mukhopadhyay, T. Meek, B. Shaver, "Solid-state neutron detectors using uranium oxides," in *Site-Directed Research and Development*, FY 2014, National Security Technologies, LLC, Las Vegas, Nevada, 2015, 131–137.

McGregor, D. S., W. J. McNeil, S. L. Bellinger, T. C. Unruh, J. K. Shultis, "Microstructured semiconductor neutron detectors," *Nucl. Instrum. Methods Phys. Res. A* **608**, 1 (2009) 125–131.

Meek, T., M. Hu, M. J. Haire, "Semiconductive properties of uranium oxides," *Waste Management Symposium* **10**, 6 (2001), http://www.wmsym.org/archives/2001/14/14-3.pdf, accessed October 1, 2014.

Meek, T., B. von Roedern, P. Clem, R. Hanrahan, Jr., "Some optical properties of intrinsic and doped UO_2 thin films," *Materials Letters* **59**, 8–9 (2005) 1085–1088.

Meek, T. T., B. von Roedern, "Semiconductor devices fabricated from actinide oxides," *Vacuum* **83**, 1 (2008) 226–228.

Nikolic, R. J., et al., "Nine element Si-based pillar structured thermal neutron detector," *Proc. SPIE* **7805** (2010) 78050O.

Tupitsyn, E., P. Bhattacharya, E. Rowe, L. Matei, M. Groza, B. Wiggins, A. Burger, A. Stowe, "Single crystal of $LiInSe_2$ semiconductor for neutron detector," *Appl. Phys. Lett.* **101**, 20 (2012) 202101.

This page left blank intentionally

An Experimental and Theoretical Investigation into the Chemical Properties of Uranium and Thorium Ions

STL-19-13 | Continued from FY 2014 | Year 3 of 3

Manuel J. Manard[1,a]

The development of an instrument that embeds a variable-temperature, high-pressure drift/reaction cell between two quadrupole mass analyzers for the purpose of investigating gas-phase interactions of uranium (U) and thorium (Th) ions with neutral reactant species is discussed. This is the third year of a 3-year collaborative effort involving the Special Technologies Laboratory and the University of California, Santa Barbara. Our overall aim is to probe the interactions of U and Th ions in the gas phase. The primary goals of the final year of the project were to complete the assembly of the instrument and acquire data for gas-phase, ion-neutral reactions. Toward these ends, instrument assembly was completed in FY 2015, and the system was used to generate proof-of-concept data for the interaction of atomic uranium cations with oxygen and water. These data were compared with ab initio calculations, performed as part of an FY 2010 SDRD project (Trainham 2011), which sought to utilize density functional theory to theoretically model the bonding interactions of uranium dioxide ions with water.

[1] manardmj@nv.doe.gov, 805-681-2121
[a] Special Technologies Laboratory

Background

A deeper understanding of the chemical properties of uranium (U) and thorium (Th) compounds could lead to advancements in techniques used to detect these compounds for the purposes of nuclear nonproliferation. Here, a detailed investigation into the fundamental chemical interactions that occur, for example, when these materials are exposed to the atmosphere or are spilled on the ground, could unearth new proliferation signatures or generate new methodologies for remote detection. Additionally, by generating metal or mixed-metal cluster ions in addition to U and Th, the potential of observing reactions that occur when shocked materials are ejected into the surrounding environment exists. These studies could result in new or improved diagnostics for the shock physics community. In all cases, by comparing or contrasting the experimental data collected on species of interest in the gas phase and on surfaces and combining these findings with theoretical calculations using density functional theory (DFT), we expect to further our knowledge about the fundamental chemical properties of these systems.

Studies involving mass-selected ion-neutral interactions have the potential to elucidate some of the complex factors involved with the bonding processes of these species. By experimentally determining the fundamental physical properties of these molecules, such as bond dissociation energies, association entropies, molecular geometries, and reaction energetics (to name a few), a deeper understanding of these processes will be gained, leading to the possibility of manipulating their chemistry for a specific outcome. The results of these studies can also be used as

an experimental point of reference to verify the accuracy of theoretical methods used to predict these properties for more complicated systems.

Project

A schematic representation of the instrument as well as an illustration of the type of data generated by the system are shown in Figure 1. The design details of the components that make up the various regions of the instrument were described in the final report for the first year of the project (Manard 2014), and the details of the mechanical design of the assemblies and subassemblies of the instrument were given in the final report for the second year of the project (Manard 2015). Thus, only a brief discussion of the system design will be provided below. The mechanical design of the system was generated using the SolidWorks software package, and ion trajectory simulations were performed using Simion 8 to determine the optimal configuration of electrodes and electric field strengths to efficiently guide the ion beam through the system.

Instrumentation

The completed instrument is shown in Figure 2. Ions are generated using either electronic impact, DC-discharge, or laser vaporization ion sources that are housed in the ion source chamber. The ionization technique chosen is based on the nature of the analyte being studied. An isolation valve is situated between the source chamber and the rest of the instrument. The valve allows the sample/ion source to be changed without having to vent the entire system. Ions generated are accelerated out of the source and injected into the first quadrupole mass analyzer, which is located in the first quadrupole (Quad 1) chamber. Ions that are mass selected by the first quadrupole are injected into the reaction cell housed in the main chamber.

The reaction cell is the heart of the instrument. Based on the design of Kemper and Bowers (1990), it consists of a cylindrical copper shroud that contains the heating/cooling passages, an end cap that is electrically isolated from the shroud, and eight ring electrodes that provide the uniform drift field through the cell. A precision resistor chain delivers the proper potentials to the individual drift rings. Ions are drawn though the cell under the influence of the electrical field. The field is weak enough so that the thermal energy of the ions is not significantly perturbed. The drift volume is 4 cm in length and 1.5 cm in diameter, with entrance and exit orifices measuring 0.5 mm in diameter. The maximum operating pressure of the cell is 5 Torr. The pressure in the cell is monitored using a capacitance manometer. Separate gas inlet connections are made to the helium (He) buffer gas,

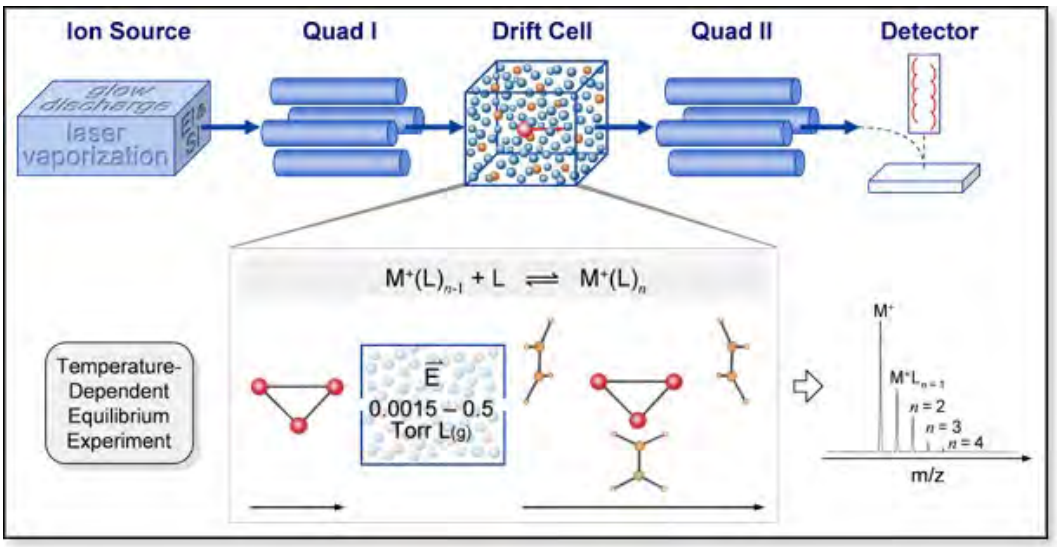

Figure 1. Schematic representation of the quadrupole-cell-quadrupole mass spectrometer

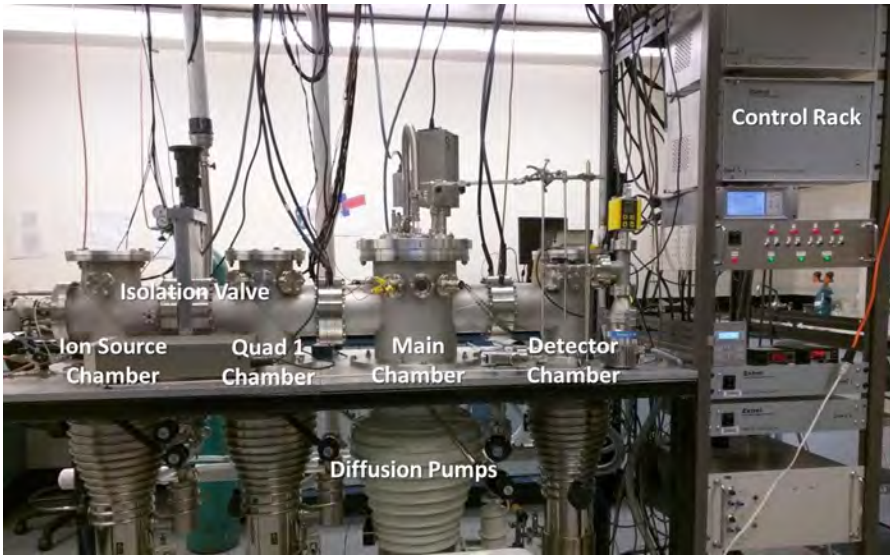

Figure 2. The quadrupole-cell-quadrupole instrument. The chambers shown (left to right) include the ion source chamber, the first quadrupole chamber, the main chamber, and the second quadrupole or detector chamber. The various subassemblies are housed within these vacuum chambers.

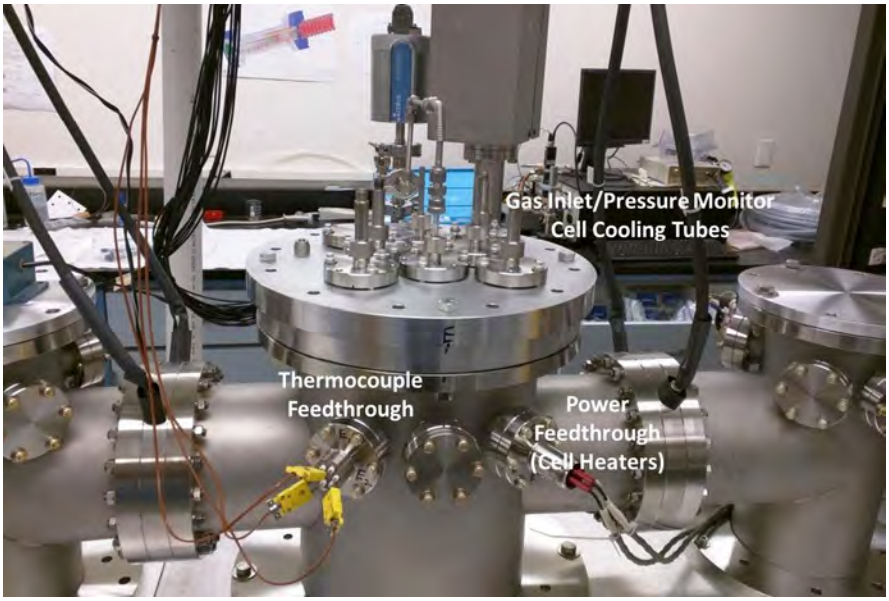

Figure 3. The main chamber of the instrument, showing the reaction cell gas inlet tubs along with the cell heating, cooling, and thermocouple feedthroughs

the reactant gas, and to the pressure monitor. The experimental temperature range of the cell is variable from 80 to 800 K. Temperatures greater than 300 K are achieved by resistive heating of tantalum resistors embedded in the cell body, while temperatures below 300 K are reached by flowing nitrogen gas cooled in liquid nitrogen through channels in the cell body. The temperature is monitored by three thermocouples, placed at various locations on the cell, to determine whether significant temperature gradients exist across the cell and if errors in the temperature reading are present. The main chamber is shown in Figure 3; the inlet and feedthrough connections for the reaction cell can be observed in detail.

Ions exiting the cell are mass selected by the second quadrupole mass analyzer situated between the main chamber and the detector chamber. The second quadrupole is generally scanned so that the relative abundances of product and reactant ion species can be recorded. Ions are detected using a conversion dynode and a Channeltron electron multiplier located

in the detector chamber. The resulting quadrupole mass scans are collected by an Ortec multichannel scaler board having a resolution of 100 ns.

Experimental Methods

Equilibrium Reactions

Equilibria are rapidly established in the cell for successive association reactions of neutral ligands to the core ions (Equation 1).

$$M_m^{+/-}L_{n-1} + L \rightleftarrows M_m^{+/-}L_n \quad (1)$$

Integrated peak areas of the various $M_m^{+/-}L_n$ ions are recorded, and these values, along with the pressure of the ligating gas (P_L) in Torr, are used to determine an equilibrium constant (K_p°) for each reaction, using Equation 2.

$$K_p^\circ = \frac{\left[M_m^{+/-}L_n\right]}{\left[M_m^{+/-}L_{n-1}\right]} * \frac{760}{P_L} \quad (2)$$

The equilibrium constants are then used to calculate the standard Gibbs free energies for the reactions,

$$\Delta G_T^\circ = -RT\,ln\left(K_p^\circ\right), \quad (3)$$

and the values obtained for ΔG_T° plotted versus the temperature, to obtain ΔS_T° and ΔH_T° for each reaction, using Equation 4.

$$\Delta G_T^\circ = \Delta H_T^\circ - T\Delta S_T^\circ \quad (4)$$

The resulting plots are linear over the experimental temperature range. A least-squares fitting procedure is used to obtain slopes and intercepts of each line. The slopes will be used to determine the association entropy (ΔS_T°) for Equation 1, and the intercepts will give the corresponding binding energies (ΔH_T°) values.

Results

Initial Testing

We conducted initial instrument tests to ensure that the ions generated by the source could be efficiently transported through the system. To accomplish this task, the electron impact ionization source was used to generate a beam of argon (Ar^+) ions (m/z = 40). Electron impact ionization is well known for its ability to generate large amounts of ions and, thus, was chosen to characterize the first ion signal generated by the system. Figure 4 shows the first mass spectrum acquired. The data were acquired with the first quadrupole set to mass-select m/z = 40, and the second quadrupole set to scan from m/z = 10 to 65. The reaction cell was filled to approximately 2.5 Torr with He. It is clear from the data in Figure 4 that a peak is present at m/z = 40, which suggests that Ar ions are being transported through the instrument and detected. No attempt to optimize the resolution of either quadrupole was made, which accounts for the asymmetric shape and width of the peak at m/z = 40. This was due to the desire to transmit as many ions as possible in order to generate these early data and to optimize the experimental parameters that result in efficient ion transport through the system.

Ion-Neutral Interaction of U, O_2, and H_2O: Experiment and Theory

As part of an FY 2010 SDRD project (Trainham 2011), DFT was used to calculate the solution properties of uranium dioxide (UO_2) ions with H_2O. The project investigated how H_2O ligands affect the optical properties of the UO_2 ion. The DFT minimum energy structure resulting from a series of H_2O ligand additions to the UO_2 ion is shown in Figure 5. The calculations suggest that the first five H_2O ligands add to the UO_2 ion in the first solvation shell. These five ligands form relatively strong bonds (approximately 2 eV) with UO_2. The following ten H_2O ligands coordinate to the UO_2 ion in the second solvation shell, forming weaker bonds with the UO_2 ion. Although the results of these calculations were clear, no experimental data were available to validate their predictions. The authors concluded that DFT calculations "require a high degree of physical and chemical insight to properly interpret calculations." Experimental data would serve to provide the required insight.

To test the results of these theoretical calculations while simultaneously generating proof-of-concept

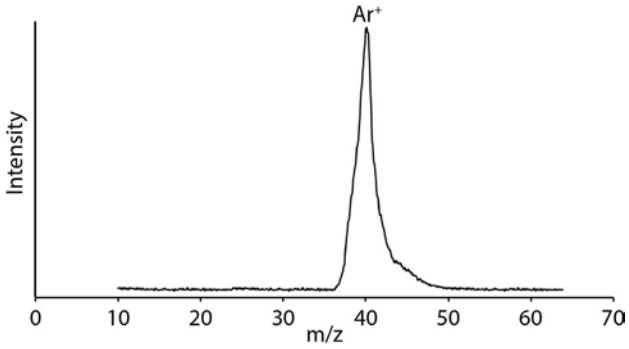

Figure 4. Mass spectrum of Ar^+ acquired with an electron impact ion source

chemical data, a sample of depleted uranium was placed in a DC-discharge ion source and U^+ cations were formed. Additionally, the reaction cell was filled with 2 Torr of He to which 0.005 Torr of O_2 was added. The resulting mass spectrum is shown in Figure 6a. It should be noted that the O_2 gas inlet line was not pumped out prior to adding O_2 to the cell. This was done intentionally to allow a portion of ambient air into the cell with the O_2. The humidity in the ambient air was used to add a partial pressure of H_2O to the cell. Using this method, the pressure of H_2O in the cell is not precisely known. Due to this uncertainty, thermodynamic/kinetic data cannot be measured. However, the data produced can be used to demonstrate the capabilities of the system.

Figure 6a shows that a substantial amount of reaction occurred. The ions generated by the interaction of U^+ with O_2 and H_2O are UO^+, UO_2^+, and $UO_2^+(H_2O)_n$ (n = 1 to 5). Three observations are made from the formation of these species. (1) U^+ is reacting to form UO^+; however, it is not clear if the reaction proceeds via insertion of U^+ into the O–O double bond or by reaction with H_2O to generate neutral H_2. This issue can be resolved by simply studying the interaction of U^+ with either O_2 or H_2O in the reaction cell without the other species present. It is interesting to note that no $U^+(H_2O)$ species are observed in the mass spectrum. This suggests that the reaction with O_2 must occur first (higher exothermicity) before sequential addition of H_2O takes place. This also suggests that formation of UO^+ likely proceeds via reaction with O_2. (2) If the $U^+ + O_2$ reaction results in the breaking of the O_2 bond, the process may be observable on the timescale of the experiment. This would allow the kinetic-rate constants for the reaction to be measured. Additionally, by measuring the reaction rates as a function of temperature, further insight into the details of the mechanism of the reaction could be determined. (3) The sequential addition of H_2O ligands to the UO_2^+ ion is observed. The ratios of these peaks do not change when the drift voltage is varied. The magnitude of the drift voltage determines the amount of time the ions spend in the

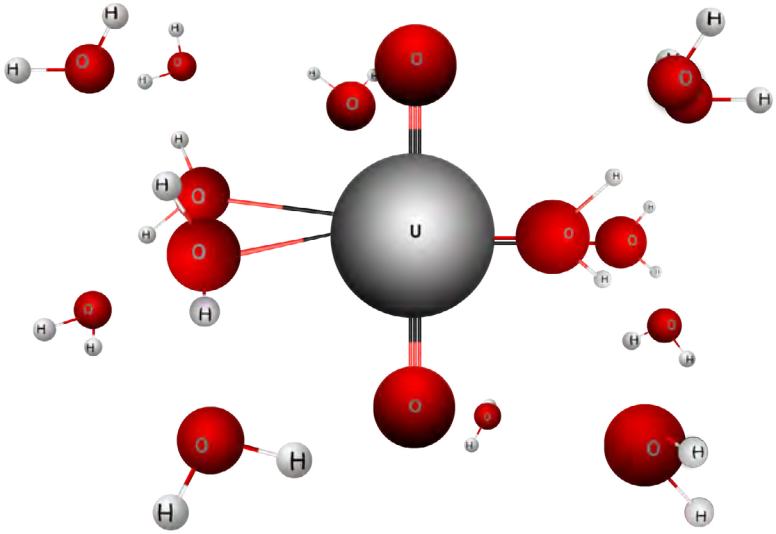

Figure 5. The DFT minimum energy structure of $UO_2^+(H_2O)_{15}$ calculated as part of an FY 2010 SDRD project (Trainham 2011). The calculation suggests that five H_2O ligands bind to UO_2^+ in the first solvation shell, and ten additional ligands bind in the second solvation shell. Note that one ligand in the first solvation shell is hidden behind the uranium ion.

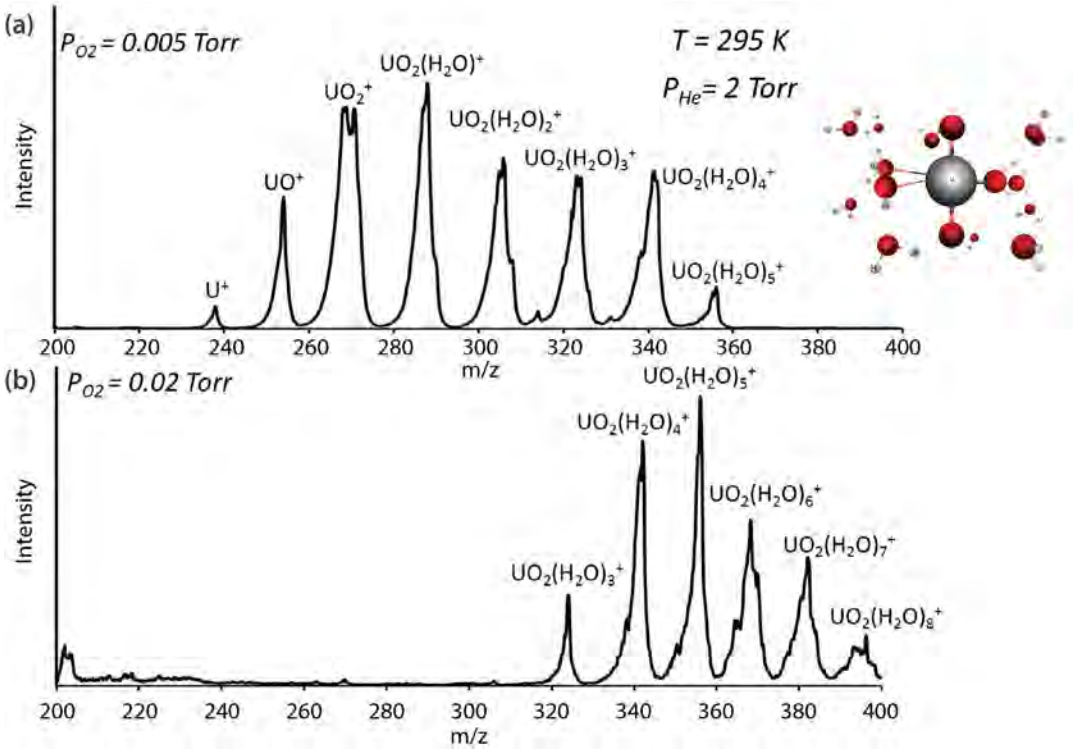

Figure 6. Mass spectra acquired for mass-selected U^+ ions interacting with O_2 and H_2O. (a) Mass spectrum resulting with a partial O_2 pressure of 0.005 Torr. (b) Mass spectrum resulting with a partial O_2 pressure of 0.02 Torr. In all cases, an unknown partial pressure of H_2O is also present in the cell that is directly proportional to the O_2 partial pressure.

reaction cell. If the ratios of the peaks in the spectrum do not change with time, the system has reached equilibrium, and the situation shown in Equation 1 is achieved. This means the equilibrium constant of the reaction can be measured using Equation 2 if the partial pressure of H_2O is known. Accordingly, Equation 3 could then be used to measure ΔG_T for the interaction. Finally, the temperature could be changed and the process repeated to determine ΔH_T and ΔS_T of each ligand addition using Equation 4.

The mass spectrum that results when the partial pressure of O_2 (and H_2O) is increased by a factor of 4 is shown in Figure 6b. The data clearly indicate that the increase in pressure of O_2 and H_2O affects the equilibrium and leads to additional H_2O ligands binding to UO_2^+. The data show that the dominant peak in the spectrum is $UO_2^+(H_2O)_5$, with up to eight H_2O ligands adding to UO_2^+.

The data shown in Figure 6 provide experimental insight into the results of the DFT calculations performed in FY 2010 (Trainham 2011). Figure 6a illustrates that at relatively low reactant gas pressures, five H_2O ligands add to UO_2^+. When the pressure is increased, more ligands are observed to bind to UO_2^+, and $UO_2^+(H_2O)_5$ becomes the largest peak in the spectrum. The data suggest that the first five ligands form similar bonds with the core ion. Additionally, the fifth addition seems to complete this series, with all other ligands binding in a different and likely weaker fashion. These results imply that the predictions of the DFT calculation could be correct, with five ligands binding in the first solvation shell of the ion and additional ligands (up to ten) binding in the second solvation shell. Although more data are required to adequately validate these observations, these preliminary data do demonstrate the ability of the system and support the results previously obtained.

Conclusion

An instrument that embeds a variable temperature, high-pressure reaction cell between two quadrupole mass analyzers for the purpose of studying gas-phase, ion-neutral reactions/interactions was designed, built, and tested. In FY 2013 and FY 2014, the instrument was designed and developed to examine the thermodynamic and kinetic properties of U and Th ions when reacting with ligands of interest in the gas phase. In FY 2015, the assembly was completed, including pumps, plumbing, cooling lines, and data acquisition system. Instrument testing was also completed during FY 2015. The testing included vacuum/leak testing and ion transport efficiency, which was determined by using an Ar^+ ion beam generated by electron impact. Finally, proof-of-concept data for the interaction of atomic uranium cations with oxygen and water were acquired. These data were used to provide some experimental validation for theoretical calculations performed as part of an earlier SDRD project (Trainham 2011). Follow-on funding, made available through the stockpile stewardship community, is expected to be received in FY 2016 to explore the ion-neutral reaction chemistry of cerium with ligands of interest.

References

Kemper, P. R., M. T. Bowers, "A hybrid double-focusing mass spectrometer—High-pressure drift reaction cell to study thermal energy reactions of mass-selected ions," *J. Am. Soc. for Mass Spectrom.* **1**, 3 (1990) 197–207.

Manard, M. J., "An experimental and theoretical investigation into the chemical properties of uranium and thorium ions in the gas-phase and on surfaces," in *Site-Directed Research and Development*, FY 2013, National Security Technologies, LLC, Las Vegas, Nevada, 2014, 103–107.

Manard, M. J., "An experimental and theoretical investigation into the chemical properties of uranium and thorium ions in the gas-phase and on surfaces," in *Site-Directed Research and Development*, FY 2014, National Security Technologies, LLC, Las Vegas, Nevada, 2015, 139–145.

Trainham, R., M. J. Manard, "Density functional theory computations for uranium chemistry," in *Nevada National Security Site–Directed Research and Development*, FY 2010, National Security Technologies, LLC, Las Vegas, Nevada, 2011, 171–176.

This page left blank intentionally

Ionospheric Plasma Coupling to Low-Frequency Electromagnetic Radiation

LAO-04-14 | Continued from FY 2014 | Year 2 of 2

Alfred Meidinger,[1,a] Kelsey Kramer,[a] J. Andrew Green,[b] and Derek Aberle[a]

This 2-year project has leveraged the concept of monitoring for concealed nuclear detonation using the combined Global Navigation Satellite System (GNSS)–ionosphere system as a nuclear detonation detection mechanism. Conceptual work and study in FY 2014 indicated that this system will provide tangible information on concealed detonations by applying appropriate analysis techniques to GNSS carrier signals. The second year of research focused on developing a working model of electromagnetic pulse–ionosphere interactions and, in lieu of applicable seismically decoupled nuclear test data, analysis of earthquake magnetic precursors and their impact on ionospheric total electron content. Although not fully implemented, significant progress was achieved in developing the interaction model. Analysis of the 2008 Wenchuan earthquake strongly suggests a correlation between lithospheric magnetic activity and analogous anomalies in ionospheric total electron content. The Wenchuan results combined with experimental underground pulsed solenoid results by a Los Alamos National Laboratory research group formed the basis for follow-on pulsed solenoid experiments slated for FY 2016.

[1] meidina@nv.doe.gov, 505-663-2018
[a] New Mexico Operations–Los Alamos; [b] Remote Sensing Laboratory–Nellis

Background

When a nuclear device is detonated, two physical processes result: (1) energy is released as heat, acoustic (pressure) waves, and electromagnetic (EM) waves, and (2) physical byproducts are created as both elements and compounds. The released energy interacts with the surrounding materials matrix to generate propagating waves through solid earth, ocean, and atmosphere while the resulting physical byproducts are released into the surrounding medium and, in the case of underground and underwater detonations, possibly leaked into the atmosphere. These physical processes provide unique identifying signatures for nuclear detonations.

The International Monitoring System (IMS) is part of the verification regime of the Comprehensive Test Ban Treaty (CTBT). When completed, the worldwide system will consist of 321 monitoring stations and 16 radionuclide laboratories designed to monitor the subsurface (underground and underwater) and the atmosphere for evidence of nuclear detonations. The verification regime relies on four monitoring technologies: seismic, hydroacoustic, infrasound, and radionuclide (CTBTO 2014). Although very robust, the IMS will not be capable of detecting nuclear weapon detonations below a certain yield. Seismic detection experts postulate 10% detection thresholds of 6 tons for fully seismically coupled events with regional detection (event-station distances less than 1600 km) to 6.2 kilotons for fully seismically decoupled events in salt domes with teleseismic detection (event-station distances greater than 1600 km) (National Research Council 2012).

These detection limits present a challenge to the scientific community: Can we develop a means for detecting detonations below the given thresholds? It is important to note the IMS does not utilize EM signatures in its detection scheme. This fact does not reflect unwillingness to use EM signatures for detection; significant effort was applied in developing this technique as a treaty verification technology (Sweeney 1989). Notably, these efforts, despite producing valuable scientific results, suggested the technique was not viable based on then-existing technologies.

As noted in the FY 2014 SDRD annual report (Meidinger 2015), simulations of electromagnetic pulse (EMP) interactions with the ionosphere as well as earth-borne and space-borne measurements suggest coupling between lightning-induced EMP and hydromagnetic waves that propagate in the spherical-shell ionospheric Alfvén resonator (IAR) as Alfvén waves. There is evidence suggesting Alfvén waves couple to fast magneto-sonic modes, which can propagate several thousand kilometers in the ionospheric waveguide. Lightning strokes emit broadband radiation, ranging from approximately 1 to 10^{20} Hz, with a significant portion of EM energy below 300 MHz.

Also, as noted in the FY 2014 SDRD report, more than two decades of research provide compelling data, indicating a correlation between preseismic lithospheric EM field fluctuations (manifesting as geomagnetic field fluctuations) and fluctuations in the local ionospheric total electron content (TEC). The source of these emissions is called the earthquake preparation zone, which can cover vast areas spanning hundreds of kilometers. Preseismic EM earthquake signals are very low frequencies, typically below 10 Hz, although some authors claim frequencies in the megahertz range (Stanica 2010, Donner 2015). Surface geomagnetic field fluctuations are typically a few nanotesla (nT) in magnitude.

Research results for FY 2014 show that a fully seismically decoupled underground nuclear event (UNE) of 1 kiloton will generate surface magnetic flux densities comparable to those measured for lightning strokes.* Based on this observation, it is safe to assume, with a reasonable degree of confidence, seismically decoupled UNEs will leave a signature in the local TEC. What is not clear is how the ionosphere responds to relevant frequencies; lightning strokes generate pulses with frequency components much higher than UNE surface frequencies, which span the lower-most portion of the lightning spectrum, while earthquake precursors generate signals at frequencies well below those measured for UNEs. The intent of future experiments is to test ionospheric response to recorded UNE frequencies in the range from 0.1 to 10 Hz (Sweeney 1996).

Project

Earthquake Precursors

Without the benefit of nuclear testing, a direct test of the proposed method for detecting seismically decoupled nuclear detonations is not possible. This fact drives the need to investigate alternative sources of EM signals comparable to those experienced during nuclear detonations and to develop surrogate experiments that mimic the EM signature of underground detonations. The need to separate EM signatures from acoustic signatures poses a significant challenge; most available EM sources that resemble the signature of a nuclear detonation, for example, lightning strokes or chemical mine explosions, generate an acoustic signal accompanying the EM signal. The acoustic signal adds to the overall signature of these events, obfuscating the EM signature. Despite this complication, there is evidence of lightning-induced EM coupling with the ionosphere through excitation of the IAR (Bösinger 2008, Schekotov 2011).

One source of purely EM signals, albeit at lower frequencies and larger spatial extent compared to underground nuclear detonations, is the apparent EM signal associated with earthquake precursors. Numerous peer-reviewed publications indicate this

* A lightning strike (cloud-to-ground event) or lightning flash (cloud-to-cloud or inter-cloud event) is typically composed of several individual discharges called strokes.

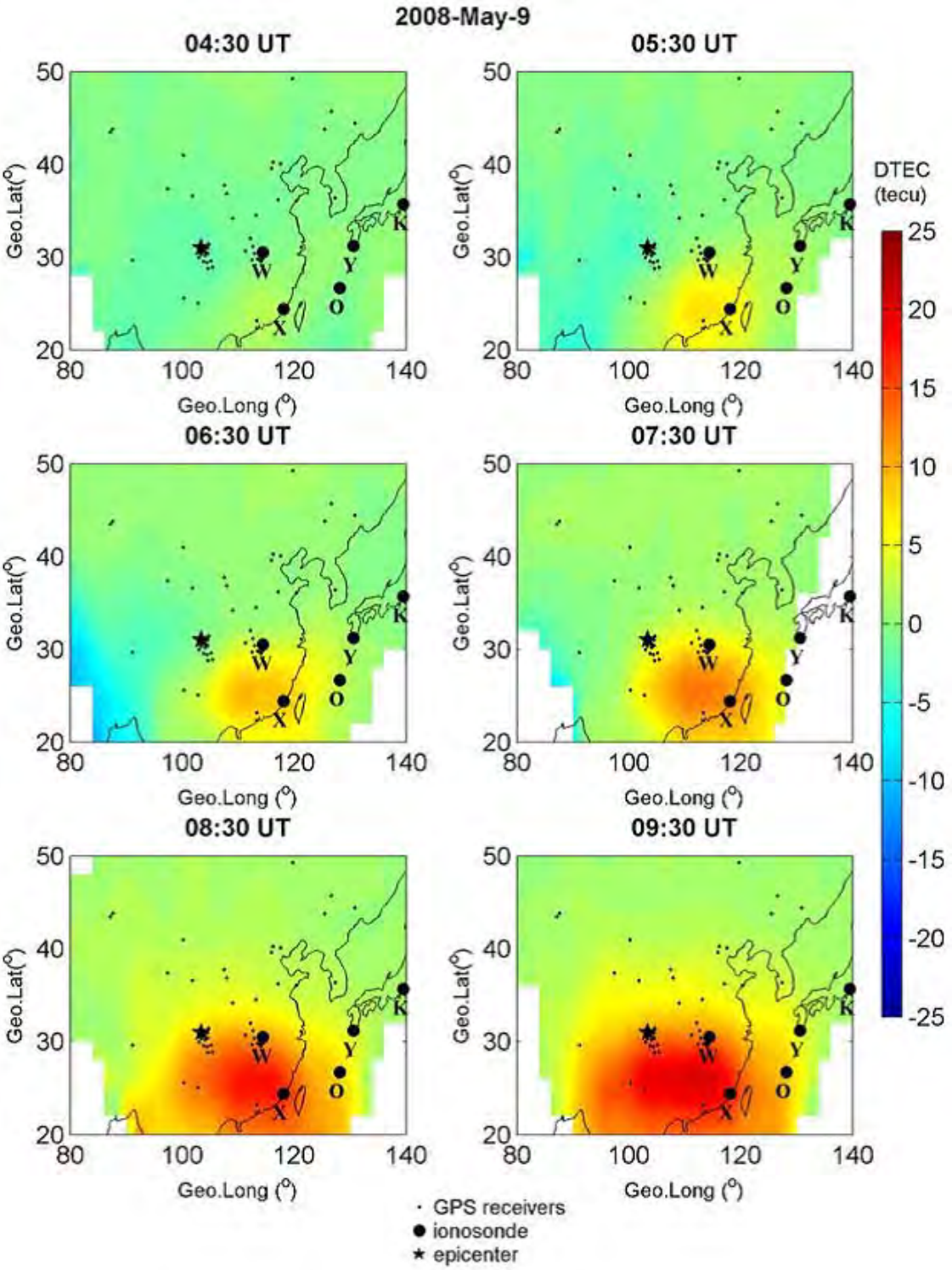

Figure 1. 2-D maps for differential TEC (DTEC) on May 9, 2008, from 04:30:00 to 09:30:00 UT, respectively. The dots and solid circles denote the positions of GPS receivers and ionosondes, respectively. The star represents the epicenter (Zhao 2008).

Figure 2. Location of INTERMAGNET sites LZH, KNY, GZH, and PHU relative to the 2008 Wenchuan earthquake along with GNSS receiver sites SUWN, DAEJ, WUH2, SHAO, and PIMO

phenomenon is real but poorly understood. Although this research approach is controversial, we decided to use existing ionospheric research, along with recorded geomagnetic data having a statistical correlation with recorded earthquake activity, as a means of verifying the coupling. Zhao (2008) provides a reasonable and comprehensive analysis of ionospheric precursors to the 2008 Great Wenchuan earthquake, an earthquake of magnitude M_s = 8.0 that struck Wenchuan County Sichuan Province in southwest People's Republic of China on May 12, 2008. Zhao selected May 9, 2008, as the optimum precursor day for analysis because it was a very quiet day from the geomagnetic perspective, meaning that solar wind activity was low, the interplanetary magnetic field was relatively stable, auroral electrojet activity was stable, and the 3-hour planetary index (K_p, a measure of geomagnetic storm activity) was low. Figure 1 illustrates the May 9, 2008, deviation from the 12-day average for the vertical total electron content (VTEC) prior to the earthquake as presented by Zhao (2008). The data indicate a gradual increase in VTEC beginning at approximately 04:30:00 universal time (UT) (local time = UT + 8 hours) through 09:30:00 UT. Interestingly, the ionospheric anomaly does not occur directly overhead of the earthquake epicenter, but rather approximately 1200 km southeast

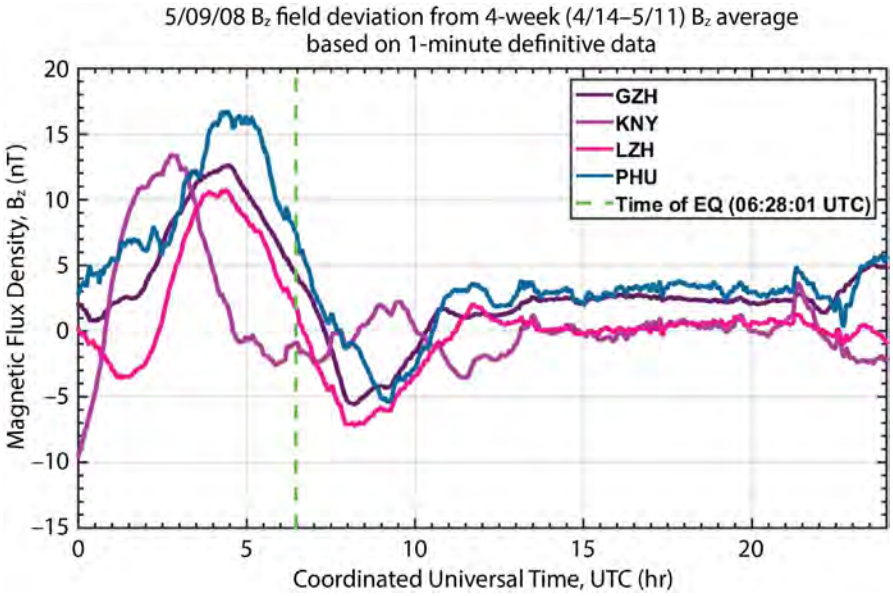

Figure 3. Geomagnetic field deviation from the prior 4-week average for the four INTERMAGNET observatories used in this study. Three of the sites, located on mainland China, accurately track the VTEC deviation characterized by the GNSS receiver site SHAO. The fourth site (KNY), located on mainland Japan, leads the other sites by approximately 2 hours.

near Hong Kong. The southward component is easily explained by the nature of the geomagnetic field; the geomagnetic field inclination in the Wenchuan area is 47.5°. The eastward component can be explained in part by the geomagnetic field declination of –1.7°, but this does not entirely explain the easterly drift distance. A possible explanation is that the equatorial electrojet "drags" the ionosphere disturbance in an eastwardly direction.

Because our goal is to identify EM perturbation in TEC, we sought lithospheric geomagnetic data to correlate with the ionospheric data published by Zhao (2008). Our source for geomagnetic data is INTERMAGNET, a global system of magnetic observatories (INTERMAGNET 2015); Figure 2 shows locations of INTERMAGNET observatories used in this study. INTERMAGNET observatories measure surface magnetic fields, subsequently sending the data to Geomagnetic Information Nodes via satellite link for storage. The magnetic observatories provide measurements to accuracy better than 5 nT. Definitive data, data that are corrected for baseline variations and spike removal, were downloaded and used for analysis. Figure 3 illustrates the May 9, 2008, geomagnetic field deviation from the 4-week average for the four INTERMAGNET observatories used in this study. Notable is the increase in the vertical component of the magnetic flux density (B_z) for the three observatories (LZH, GZH, and PHU), located on the Chinese mainland, which coincides with the VTEC deviation characterized by Zhao (2008). The inflection point for B_z occurs at the same time the VTEC increase begins, at approximately 04:30:00 UT, and reaches minimum value in the 08:30:00 to 09:30:00 UT time frame. The data for the KNY observatory, located on the Japanese mainland, lead the other sites by approximately 2 hours; the reason for this is not clear.

Although inconclusive, the data suggest lithospheric magnetic activity and ionospheric response are coupled via the geomagnetic field. An analysis routine based on Zhao's analysis is under development; additional earthquakes will be analyzed to look for similar phenomena. The magnitude of magnetic field perturbation associated with the earthquake precursor is on the scale of that expected for decoupled

underground nuclear detonations in the kiloton range, while the frequency is several orders of magnitude lower.

EM-Ionosphere Interaction Model

During FY 2014 we investigated a coupling model using off-the-shelf particle-in-cell plasma modeling software. Due to the scale of model parameters combined with strict cell size limitations imposed by the Courant limit, this approach proved intractable using available computing resources. FY 2015 modeling efforts focused on developing modeling and simulation software that will overcome the Courant limit issues by splitting the analysis into two calculations, one retaining the small cell structure required for EM propagation at light speed, the other for plasma wave propagation at speeds well below the speed of light, thus allowing larger cell size and longer time steps between calculations. Although the model was not fully completed, preliminary observations indicate this approach will substantially reduce computational overhead. No definitive results are available since the model is not fully implemented at this time.

Experimental Effort

Conceptual design of experiments and procurement of some necessary GNSS data acquisition software and hardware were completed in FY 2015 in preparation for FY 2016 experiments. Los Alamos National Laboratory (LANL) Intelligence and Space Research (ISR-2) has successfully conducted underground pulsed-solenoid experiments in a LANL tunnel, demonstrating the ability to measure surface geomagnetic fluctuations well in line with those measured for UNEs; we will conduct a follow-on set of similar experiments to monitor ionospheric response to simultaneously measured geomagnetic fluctuations. In addition to GNSS measurements, we are investigating collaboration with the Air Force Research Laboratory (AFRL) Ionospheric Hazards Section (RVBXI). RVBXI possesses portable ionosonde stations that would provide the ability to characterize ionosphere response using bottom-side soundings. Ionosondes are routinely used to characterize ionospheric activity; capturing this information would provide a form of ground truth for any ionospheric response measured using GNSS techniques.

Conclusion

Analysis of surface geomagnetic field fluctuations prior to high-magnitude earthquakes supports the UNE ionospheric perturbation hypothesis; geomagnetic fluctuations associated with earthquake precursors are of the same magnitude as those resulting from UNEs, albeit at lower frequencies and of greater surface extent. This analysis, when combined with FY 2014 results correlating lightning strokes with ionospheric response, provides a sound basis for follow-on experiments in FY 2016. FY 2016 experiments will leverage proven pulsed-solenoid technology to investigate coupling between geomagnetic perturbations and ionospheric response using existing GNSS capabilities along with potential AFRL-sponsored ionosonde measurement support. If coupling is verified, this method will provide a means for monitoring seismically decoupled underground detonations in support of existing nuclear nonproliferation efforts.

Acknowledgment

We would like to thank Timothy Neese for his contributions to this work.

References

Bösinger, T., S. L. Shalimov, "On ULF signatures of lightning discharges," *Space Sci. Rev.* **137** (2008) 521–532.

CTBTO, Preparatory Commission for the Comprehensive Nuclear-Test-Ban Treaty Organization, http://www.ctbto.org, accessed September 3, 2014.

Donner, R. V., S. M. Potirakis, G. Balasis, K. Eftaxias, J. Kurths, "Temporal correlation patterns in pre-seismic electromagnetic emissions reveal complexity profiles prior to major earthquakes," *Phys. Chem. Earth* **85–86** (2015) 44–55.

INTERMAGNET, International Real-time Magnetic Observatory Network, 2015, http://www.intermagnet.org/index-eng.php, accessed May 15, 2015.

Meidinger, A., D. Clayton, D. Aberle, K. Kramer, W. Zimmerman, "Ionospheric plasma coupling to low-frequency electromagnetic radiation," in *Site-Directed Research and Development*, FY 2014, National Security Technologies, LLC, Las Vegas, Nevada, 2015, 147–155.

National Research Council, *The Comprehensive Nuclear Test Ban Treaty—Technical Issues for the United States*, The National Academies Press, Washington, D.C., 2012, 104–117.

Schekotov, A., V. Pilipenko, K. Shiokawa, E. Federov, "ULF impulsive magnetic response at mid-latitude to lightning activity," *Earth Planets and Space* **63** (2011) 119–128.

Stanica, D., D. A. Stanica, "Constraints on correlation between the anomalous behaviour of electromagnetic normalized functions (ENF) and the intermediate depth seismic events occurred in Vrancea Zone (Romania)," *Terr. Atmos. Ocean. Sci.* **21** (2010) 675–683.

Sweeney, J. J., "An investigation of the usefulness of extremely low-frequency electromagnetic measurements for treaty verification," UCRL-53899, Lawrence Livermore National Laboratory, Livermore, California, January 1989.

Sweeney, J. J., "Low-frequency electromagnetic measurements as a zero-time discriminant of nuclear and chemical explosions - OSI research final report," UCRL-ID-126780, Lawrence Livermore National Laboratory, Livermore, California, December 1996, http://www.iaea.org/inis/collection/NCLCollectionStore/_Public/37/073/37073983.pdf, accessed October 1, 2014.

Zhao, B., M. Wang, T. Yu, W. Wan, J. Lei, L. Liu, B. Ning, "Is an unusual large enhancement of ionospheric electron density linked with the 2008 great Wenchuan earthquake?" *J. Geophys. Res.* **113** (2008), http://onlinelibrary.wiley.com/doi/10.1029/2008JA013613/full, accessed November 25, 2015.

This page left blank intentionally

Networked Radiation Detection System for Rapid Tactical Response

RSLA-02-15 | Year 1 of 1

Sanjoy Mukhopadhyay,[1,a] Richard Maurer,[a] Ronald Wolff,[a] Stephen Mitchell,[b] and Paul Guss[c]

This project fulfilled an urgent need to develop a deployable, tactical, networked radiation detection system that is agile, reconfigurable, and capable of rapid threat assessment with certainty for the radiological emergency response community, particularly that of law enforcement. The prototype we developed is a highly sensitive, modular, plug-and-play radiation detection system that uses in situ field data to deliver a GO/NO-GO decision in less than 3 seconds with a high degree of specificity and a very low false-alarm rate. The system is intelligence driven and would be deployed only when other (than radiological) verifiable information on a target exists. A networked, sensor array gamma radiation detection system with directional sensitivity and gamma energy spectral data acquisition capability was developed and tested; our tests focused on the trade-offs between false positive rates, true positive rates, and time to detect one or more radiation sources in a large urban area (~1000 square meters). We performed empirical and simulation analyses of critical system parameters such as number of sensors, sensor placement, and sensor response functions. Using all available data from networked sensors to determine the constantly changing background gamma radiation signature over an urban area, we found the overall sensitivity and detectability of the system increased. Employing multiple sensors, our networked system reduced false-alarm rates by over-determining the presence of the threat sources. Furthermore, not having to use a reach back to a large database or server reduced network-related latency and made the radiation data an actionable intelligence to emergency responders. A theoretical study was performed in collaboration with Arkansas State University, in which the properties of rare earth–doped heavy metal halides were evaluated as potential next-generation, luminescent materials with high efficiency at low cost.

[1] mukhops@nv.doe.gov, 301-817-3319
[a] Remote Sensing Laboratory–Andrews; [b] North Las Vegas; [c] Remote Sensing Laboratory–Nellis

Background

The DOE NNSA Office of Emergency Response (NA-42) and other agencies, such as the Radiological Nuclear Search Group (RNSG) are partnering with law enforcement in resolving and eliminating rapidly changing radiological and nuclear crisis incidents of potentially very grave consequences. Also, the Domestic Nuclear Detection Office (DNDO), nuclear materials security and safeguards programs (NA-22) have been investing in predictive search models (such as those developed in this project) that would exploit the current computational capabilities in palm-held tablets. This project furthers the NA-42 effort to become a better tactical partner to law enforcement and provides more advanced tools for predictive search capabilities.

System Requirements

The requirements of the networked sensor array/detection system and our associated considerations are described below.

The overall architecture of the detection system is intelligence driven and is deployed only when other (than radiological) verifiable information on the target is in hand. The survey area is often limited, so the required detection range is small (yet needs to be quantified for deployed equipment). The requirement is to detect a threat source out to 30 meters.

A threat determination is required within 3 seconds or less. Using the Currie limits of detection, the false positive rate α, or Type I error, may be as high as 1%, but the false negative rate β, or Type II error, must be kept lower than <<1%. A superior receiver operating characteristic (ROC) curve is among the most important requirements for this system. Whenever deployed, the system should be characterized for false-alarm rates (Currie 1968). Threat signatures and system response characterization to threat devices will be incorporated in the decision-making basis. Use of Rad-Detect type software will aid in determining this guidance.

System-specific, smarter algorithms needed for alarm generation will be developed. These algorithms may have to be configuration dependent. The nuisance-rejection spectral comparison ratio anomaly detection (NSCRAD) algorithm and the wavelet-assisted variance reduction anomaly detection (WAVRAD) algorithm together provide an excellent basis on which to build. For rapid response, reduction of dimensionality by principal component analysis will be required. Dimensional reduction techniques will be closely tied to the threat metrics. The alarm threshold has to be carefully studied against realistic sources and background variation to obtain the most effective field-usable value.

The software platform is required to handle multiple forms of data input (multichannel analyzer [MCA] data, transistor-to-transistor logic counting, live video/audio, etc.). The system should be capable of sub-second data acquisition. Sub-second radiation detection time is a necessary property for fast, directional radiation detection. Sensitivity of the system is sufficient to detect ionizing radiation in much less than 0.1 second. Detector elements that can be read out independently and daisy chained simultaneously are preferred. Software will accommodate modes of data acquisition that can be selected for maximum effect on sensitivity, directionality, or imaging.

For the deployment to be flexible, the detection suite needs to be rapidly reconfigurable in terms of size, shape, and outer appearance. This requires a cache of detectors of various sizes and sensitivities to be ready for deployment. The system must be capable of running multiple radiation detection components (viz., two or more sodium iodide [NaI] scintillators running independently, multiple neutron detectors running in stand-alone proportional counting mode) that may be employed to independently "over-determine" the existence of the threat object. Individual detection elements need to be plug-and-play types with an interchangeable power supply and a common data acquisition system. Rapid response, electronic dose rate meters are required components of the equipment suite.

Radiation detection materials should be fast (viz., faster scintillators). High sensitivity is of primary importance. Sensitivity may be tuned by use of a modular system. Data may be independently acquired from modules. The system's modular design and architecture has sensors that can be daisy chained, permitting easy and rapid configuration and reconfiguration in the field to tune sensitivity, directional detection, and imaging attributes.

In mobile search operations it is important to determine the angular position of a radiation source. Gamma ray directional sensitivity has been built into the detection system. Gamma ray counting devices should depend on digitization and rapid pulse shape discrimination to discriminate against neutron sources.

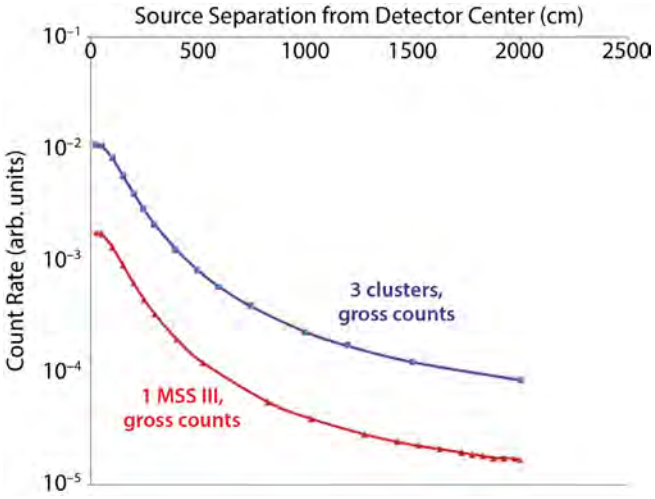

Figure 1. MCNP5 simulated count-rate comparison between the MSS III (current system) and the proposed detector array. Gross count rates between the gamma energy ranges from 30 to 3000 keV are calculated from simulated spectral response. A FWHM energy resolution of 7.5% at 662 keV was assumed.

Project

We employed a multifaceted approach to the project, pursuing three major areas of focus: (1) Monte Carlo simulations of detector sensitivity and angular response, (2) prototype development and testing, and (3) theoretical predictive modeling. These efforts are described below.

Monte Carlo Simulation

The Monte Carlo N-Particle Transport Code MCNP5 (Brown 2015) developed at Los Alamos National Laboratory was used to simulate the sensitivity and angular response of the two mobile systems—the Multispectral Scanner, MSS III, with four gamma logs and the new system with three clusters of four gamma logs. Figure 1 shows the gamma count rates from the two systems: (1) four gamma logs as used in MSS III and (2) 12 gamma logs in three clusters spaced 60 cm apart. The count rates are shown as a function of the central distance between the gamma-emitting source and the detector. The source used is a combination of ^{241}Am, ^{137}Cs, and ^{60}Co (common industrial radioisotopes), each 0.25 mCi, placed at various distances from the detector center with zero vertical offset.

An asymmetry (A_y) of counts was calculated for different angular position (Θ) of the source as

$$A_y(\Theta) = \frac{N_1 - N_4}{N_1 + N_2 + N_3 + N_4}, \quad (1)$$

where N_1 and N_4 are the counts from detectors facing the source (left and right, respectively) and N_2 and N_3 are the counts from detectors in the back (left and right, respectively). This asymmetry function varies linearly with the angle of source position with respect to the center of the detector array. Knowing the instantaneous value of the asymmetry, one can determine the angular position of the source with a high degree of accuracy. Figure 2 shows the linear relationship between the asymmetry function, characteristics of the detector array, and the angular position of the detector arrays. As there were three clusters of detectors available, three different asymmetries were plotted, and they all seem to show the same linear variation. A least squares linear fit of the general variation of asymmetry with angle is obtained as

$$\Theta = 114.77\, A_y(\Theta) + 0.0246. \quad (2)$$

Prototype Development and Testing

We developed and studied networked sensors (three and four in a mesh network at a time) to establish a comprehensive background radiological map using all detection elements, determine confidence level when the radiation anomaly is detected, and study energy spectral data with 25 gamma energy bins with specific radioisotopes in mind.

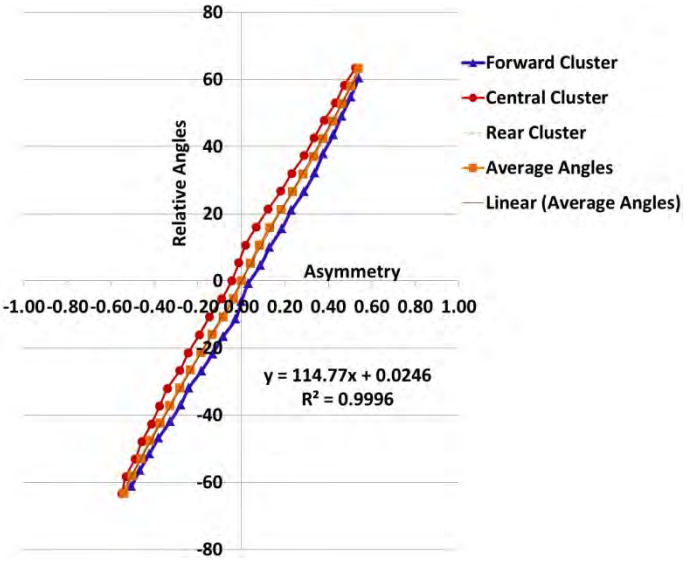

Figure 2. Asymmetry functions for three different clusters are shown as a function of angular position of the source over the range of field of view of ±60°. This method provides a quick way to determine the instantaneous angular position of the source and is independent of background variation. The error in angle measured is less than 3°.

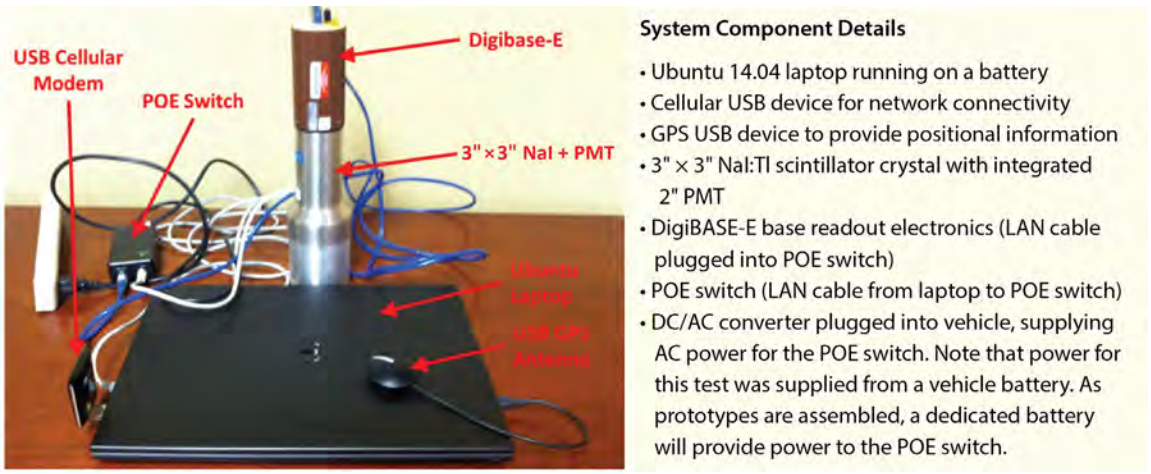

Figure 3. A single prototype unit showing the laptop, NaI detector with readout, and associated support hardware

Four prototype units were built; one is shown in Figure 3. The prototype consists of a 3" × 3" NaI detector with an integrated photomultiplier tube (PMT), DigiBASE-E readout, laptop for data readout and transmission, and GPS adapter for location.

The unit in Figure 3 leverages an existing asset of the Passport System, developed under a separate project, the DigiBASE-E controller software with the base control unit (BCU) architecture from Passport's NetS^2 product line (Passport Systems 2015). The laptop transmits data over the network to a reachback server that is being monitored by a separate BCU running Passport's algorithms. The detectors were characterized for efficiency and resolution for inclusion in the algorithms.

Measurements were performed with 100 µCi ^{137}Cs and ^{60}Co sources. The sources were hidden in a parking lot measuring approximately 120 yards by 40 yards (5000 square yards). The four prototype units "walked" the area to detect, locate, and identify the sources. The three scenarios tested were (1) stationary source, moving detectors; (2) moving source, stationary detectors; and (3) moving source, moving detectors. Results are described below.

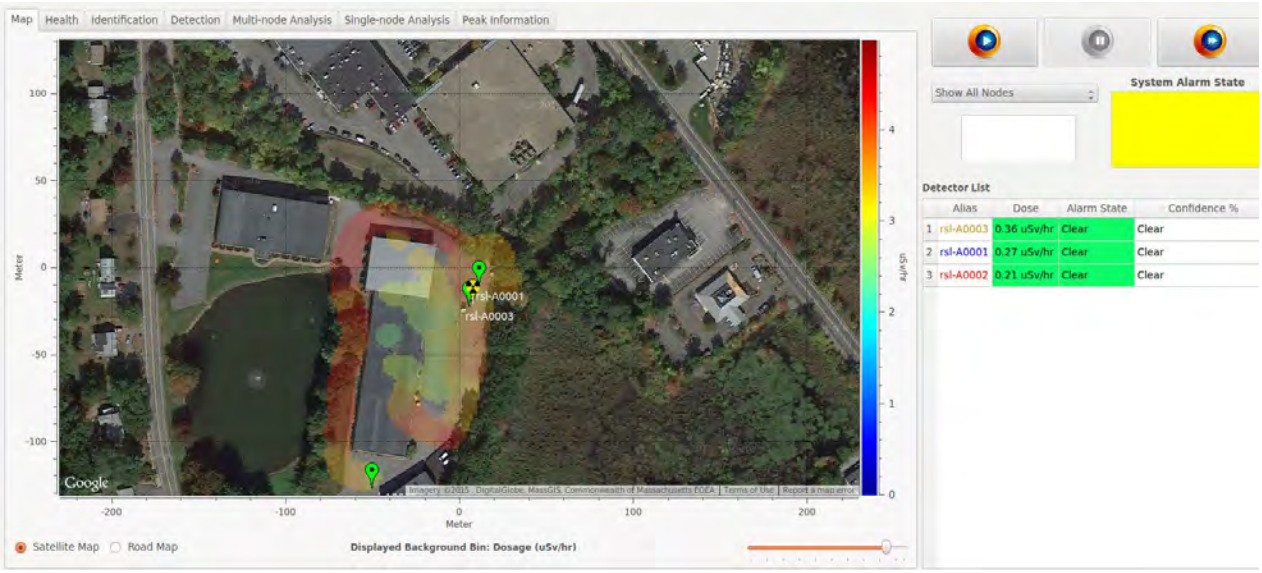

Figure 4. Instantaneous image of the background map, showing the cumulative effect of the three detectors just before the confirmation of first detection

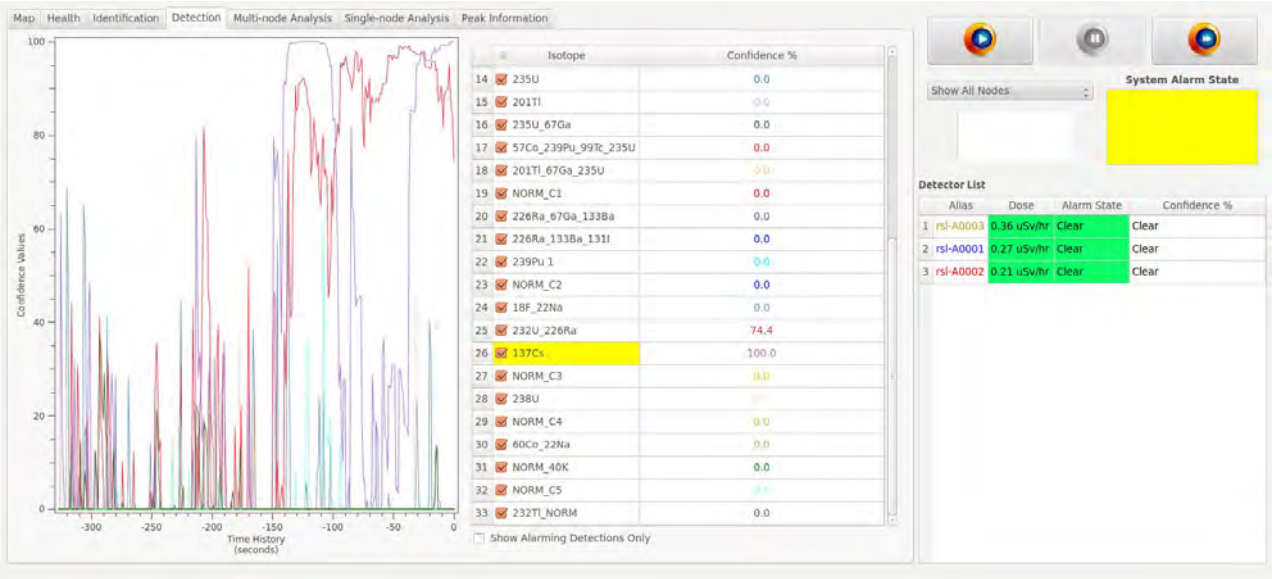

Figure 5. Detection confidence value for the system when the ^{137}Cs is first detected

Scenario 1: Stationary Source, Moving Detectors

For the first scenario, we hid a 100 µCi ^{137}Cs source and used three detector units. The background map just prior to the source being detected is shown in Figure 4. The background intensity (color) in this plot is proportional to the total count rates in the detectors.

The detection algorithms use a particle filter that calculates the probability of a source being present and estimates a location based on data available to the system. The spectra are separated into roughly 25 energy bins corresponding to specific isotope(s) or naturally occurring radioactive material (NORM). The historical confidence values when the system first detects the source are shown in Figure 5. Note that the ^{137}Cs bin has the highest confidence.

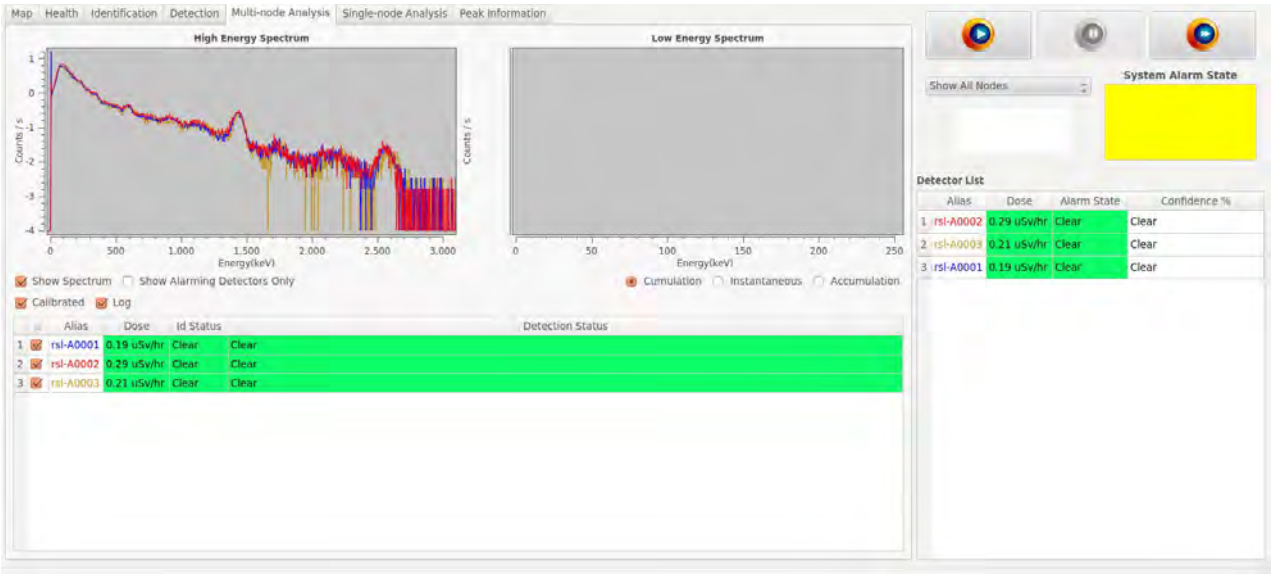

Figure 6. Gamma energy spectra for the three detectors at the time of detection

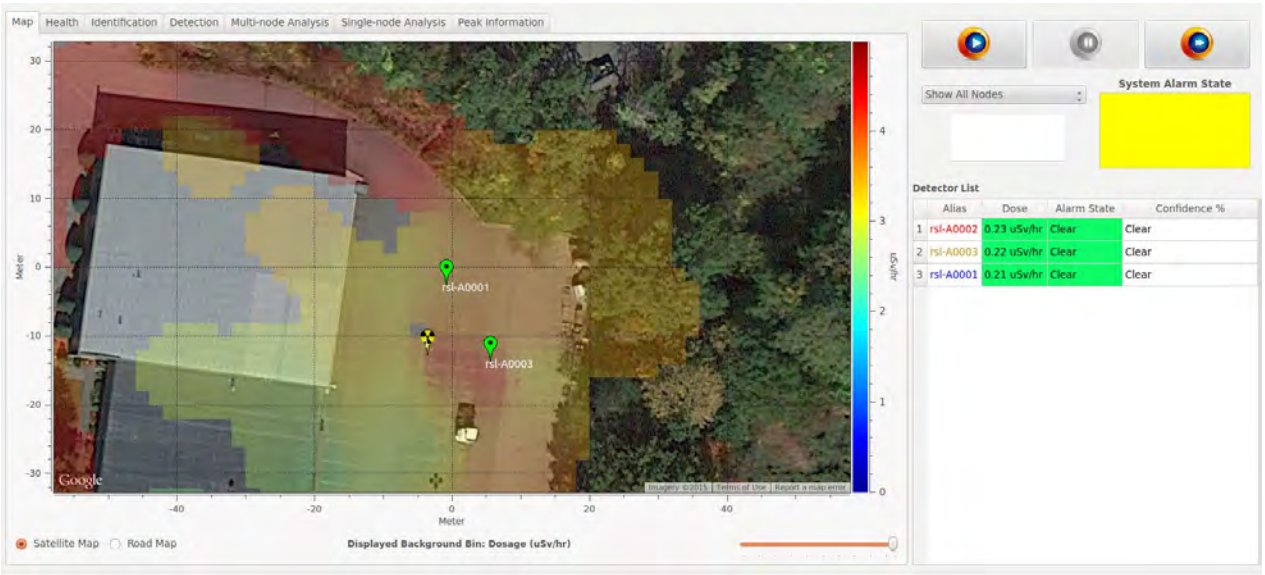

Figure 7. Location estimate when the ^{137}Cs source is first detected

The gamma energy spectra from the three detectors at the time of first detection are shown in Figure 6. Visual inspection of the spectra gives very little indication of anomalies, even though the algorithms have detected the presence of a ^{137}Cs anomaly. This establishes the algorithm's superiority over spectral detection alone.

When the source is first detected, the uncertainty in the location is relatively high. As additional data and statistics are acquired, the uncertainty is reduced and the accuracy improves. The estimated location when the source is first detected is shown in Figure 7. In this case the estimated source location and the real location are off by approximately 4 meters. Note that the GPS error is one of the major causes of positional uncertainty.

As additional statistics are acquired, a specific identification occurs (i.e., a peak of statistical significance). This is shown in the user interface in Figure 8. The identification occurs in detector A0003, which is the detector with the highest dose rate. The spectra are

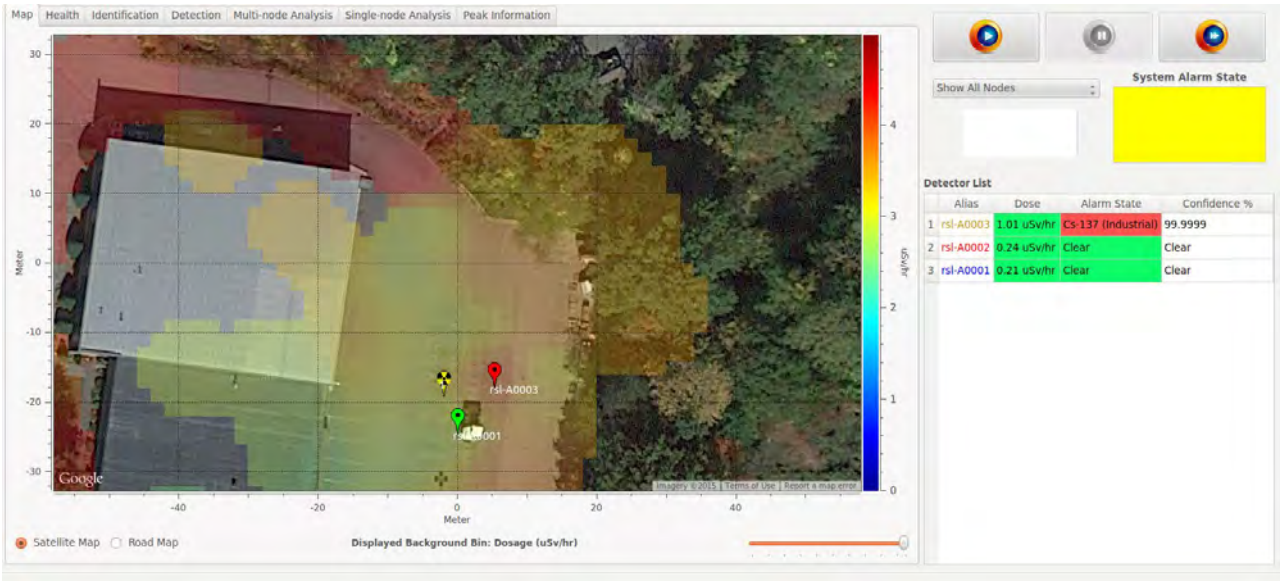

Figure 8. Identification of the source as ^{137}Cs

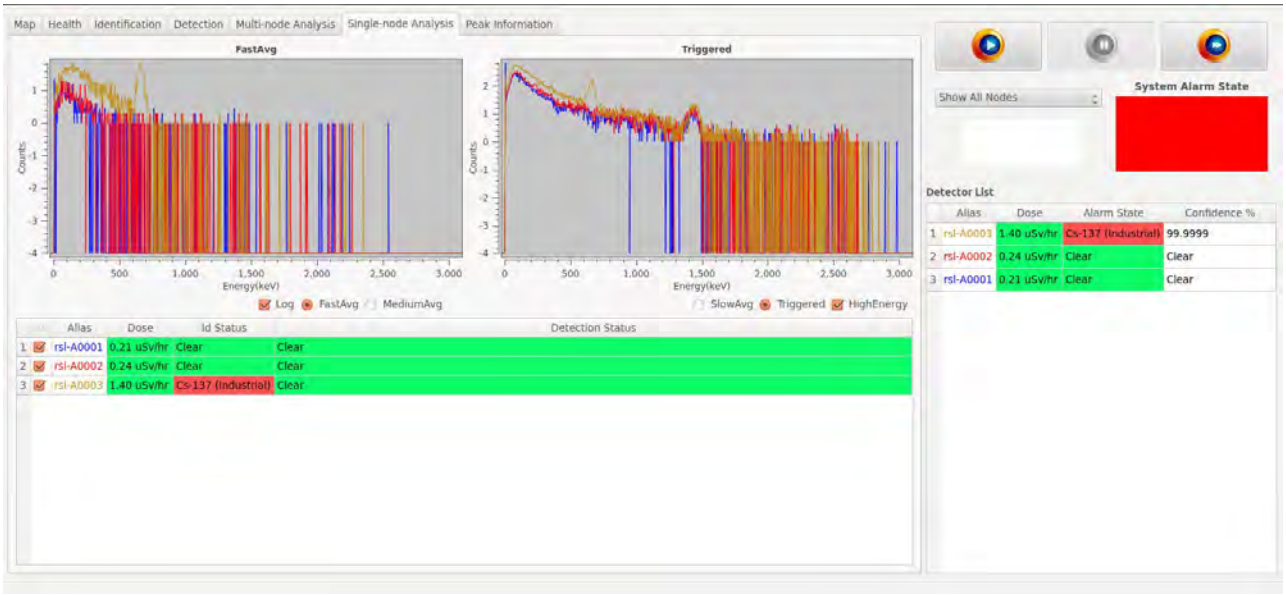

Figure 9. Gamma energy spectra from three sensors when the identification occurs. Two time buffers are displayed: (1) the fast time buffer, which is approximately 4 seconds of data, and (2) the triggered time buffer, which starts after a detection occurs.

shown in Figure 9. The cesium peak is clearly seen in the spectra. Identification by two detectors is shown in Figure 10.

Scenario 2: Moving Source, Stationary Detectors

In the second scenario four detector units were used to detect a hidden, movable 100 µCi ^{60}Co source. The background map just prior to when the source is first detected is shown in Figure 11. Displaying only the ^{60}Co bin indicates a much larger signal-to-noise ratio than the total count/dose rate shown in Figure 12. The localization and identification of the source are shown in Figures 13 and 14, respectively.

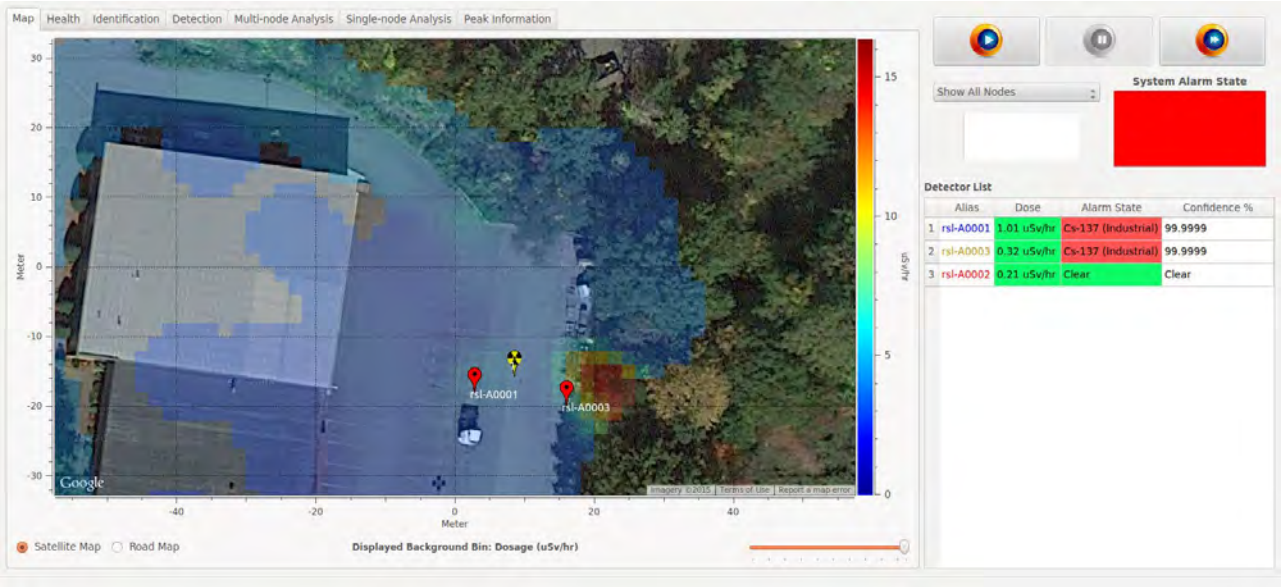

Figure 10. Interface showing identification by two detectors

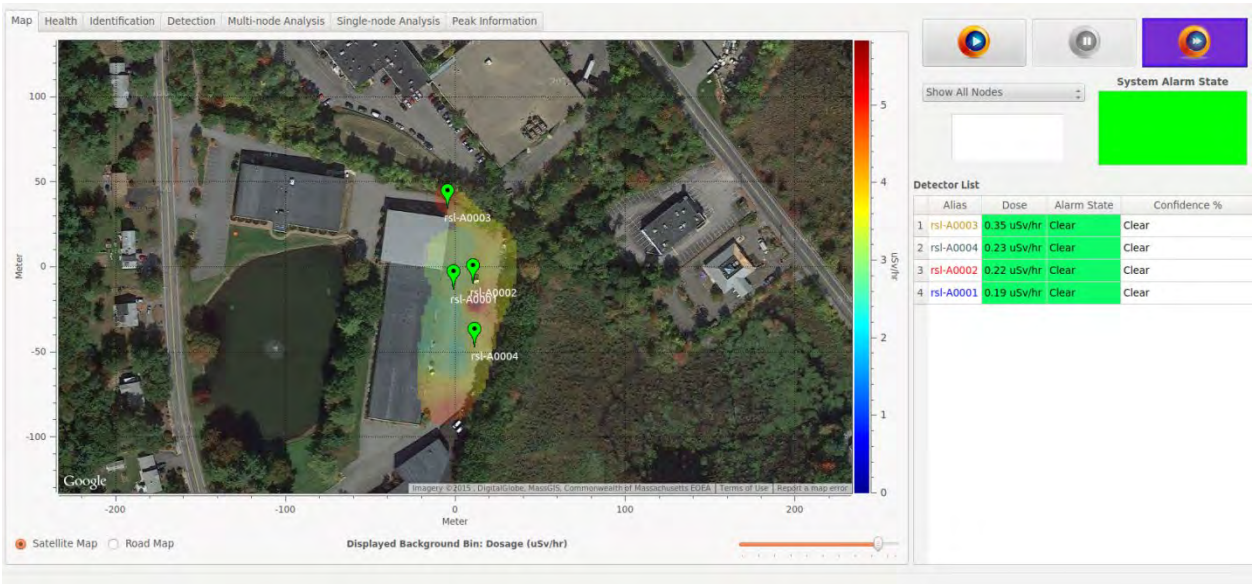

Figure 11. Background gamma radiation map just prior to detection of the ^{60}Co source

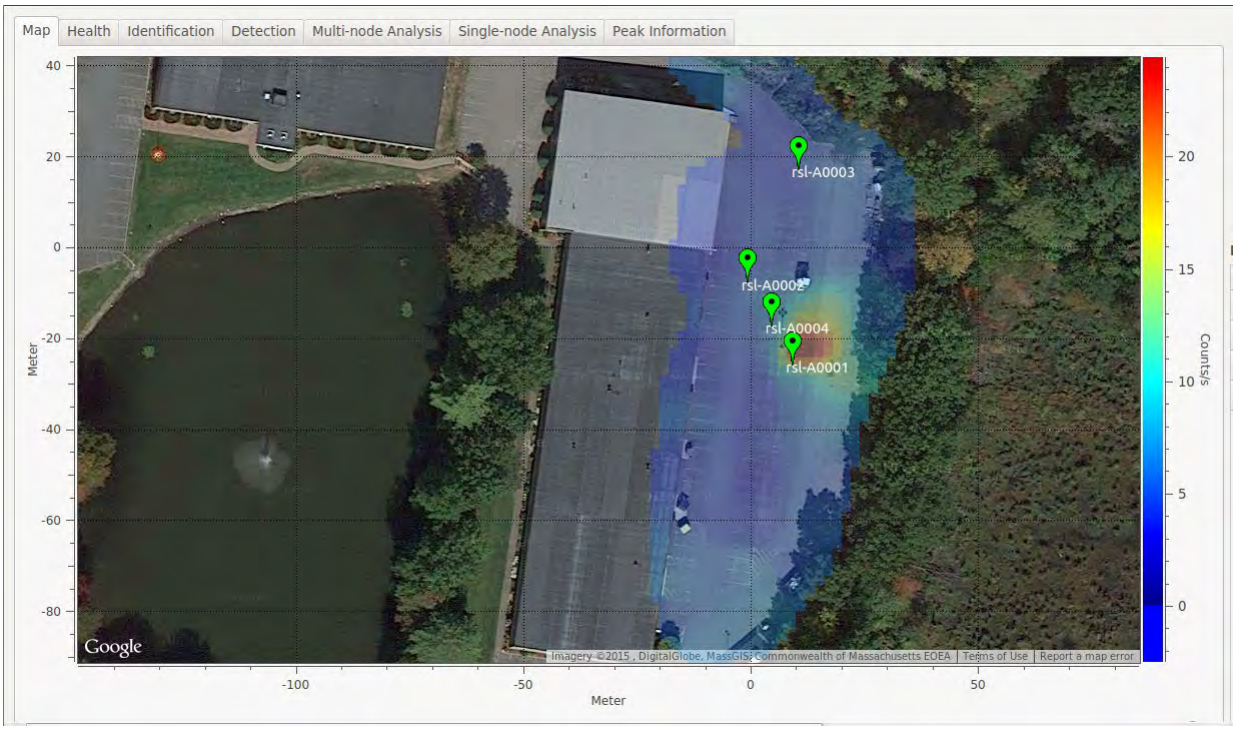

Figure 12. Background map showing only the ^{60}Co energy bin

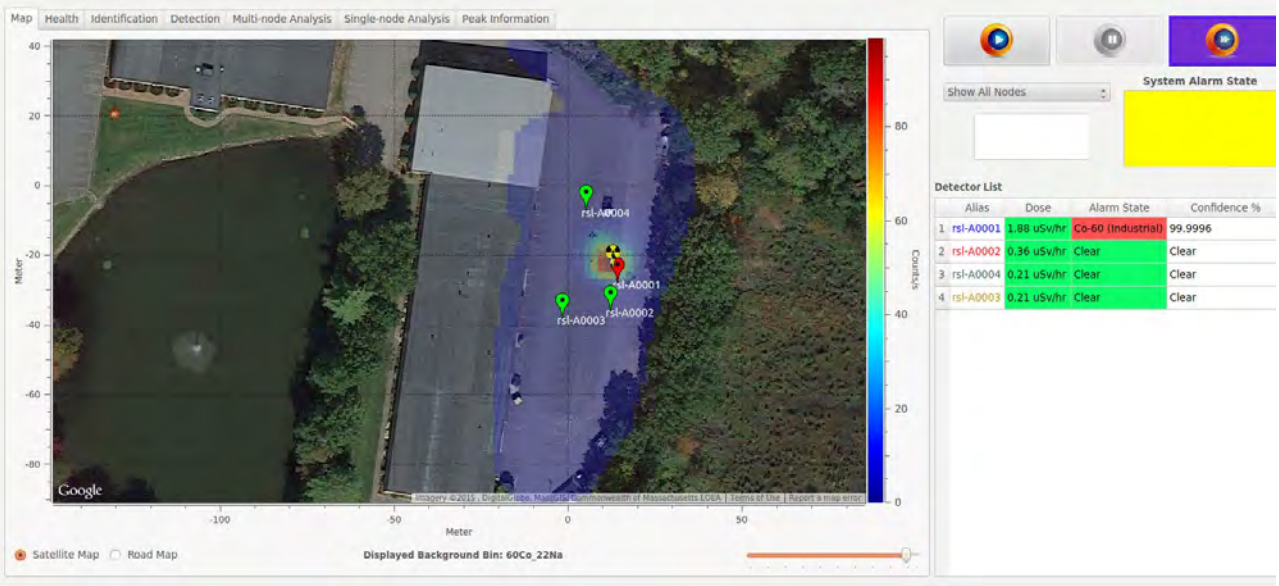

Figure 13. Map showing localization of source

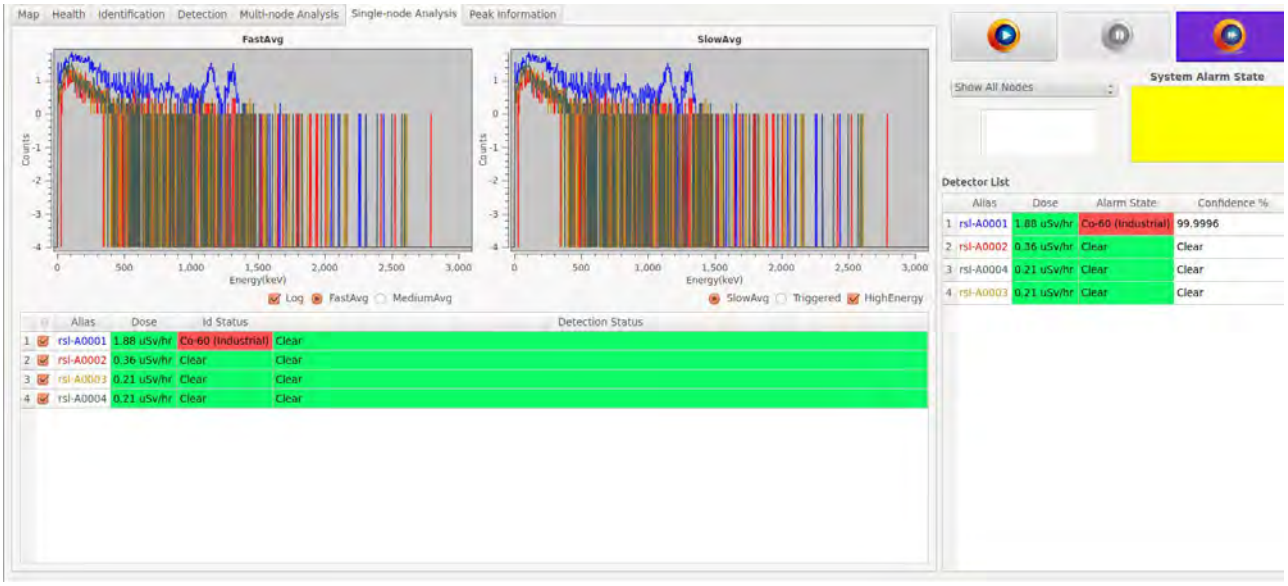

Figure 14. Gamma energy spectra as recorded and identification of the source as ^{60}Co

Scenario 3: Moving Source, Moving Detectors

The third scenario involved a moving 100 µCi ^{137}Cs source and four detector units. Two time periods showing the detection and localization of the source are shown in Figures 15 and 16.

Theoretical Studies of Rare Earth–Doped Complex Alkali Halides—Next-Generation Scintillators

Finally, we performed some theoretical predictive modeling studies utilizing density functional theory (DFT) of the electronic behavior of rare earth–doped alkali halide crystals that have the potential to surpass the sensitivity and specificity of radioisotope identification observed among currently used scintillation materials.

The stable proportionality of the photon yield from these scintillators as the incident gamma ray energy varies makes these alkaline-halide scintillators very attractive. Recently there has been additional progress in Eu-doped alkaline earth–containing materials, including binary and ternary halides (e.g., $CsBa_2I_5:Eu^{2+}$ and $KSr_2I_5:Eu^{2+}$, and $SrI_2:Eu^{2+}$). These halides have improved light yield, favorable decay times, and energy resolution less than 3% at 662 keV, making them prime candidates for a variety of applications (Zhuravleva 2014, Stand 2015).

Since the discovery of the scintillating properties of $CsBa_2I_5:Eu^{2+}$ (light yield reports ranging from 80,000 to 102,000 photons/MeV and energy resolution about 3.9% to 2.3% at 662 keV) (Shirwadkar 2013, Gascón 2014), ternary alkali-alkaline earth iodides (e.g., $AB_2I_5:Eu^{2+}$ [A = Li-Cs, B = Sr, Ba]) have become a subject of interest. $KSr_2I_5:Eu^{2+}$ was also recently found to exhibit advanced scintillation properties. In particular, these crystals are also reported to be less hygroscopic compared to the well-known binary halides, $LaBr_3:Ce^{3+}$ and $SrI_2:Eu^{2+}$ (Bourret-Courchesne 2009). The possibility of growing large crack-free crystals—having no self-activity—at a relatively lower cost makes the $AB_2I_5:Eu^{2+}$ family a potential set of candidates for the next generation of scintillators.

The crystal structure of $CsBa_2I_5$ is monoclinic with space group $P2_1/c$ (two-fold screw axis along c-direction). In the crystal, there are two distinct crystallographic sites for alkaline earth B atoms (referred to here as the eight-coordinated $B1^{(VIII)}$ and seven-coordinated $B2^{(VII)}$) and five different Wyckoff sites for iodine. Figure 17 shows the coordination of the cations in $CsBa_2I_5:Eu^{2+}$, where the Ba occupies a $B1^{(VIII)}$ site and Eu is at a $B2^{(VII)}$ site. The calculated electronic band structure (a) and the total density of states (b) are shown in Figure 18. It has been shown by the current study that within the

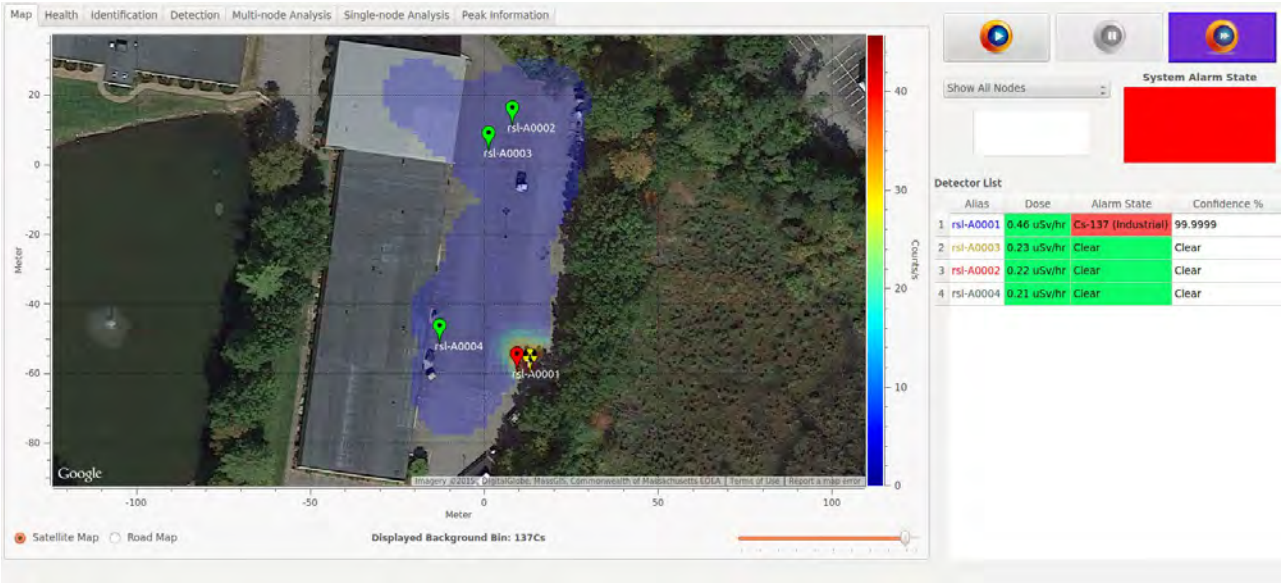

Figure 15. Initial detection and localization of the moving ^{137}Cs source

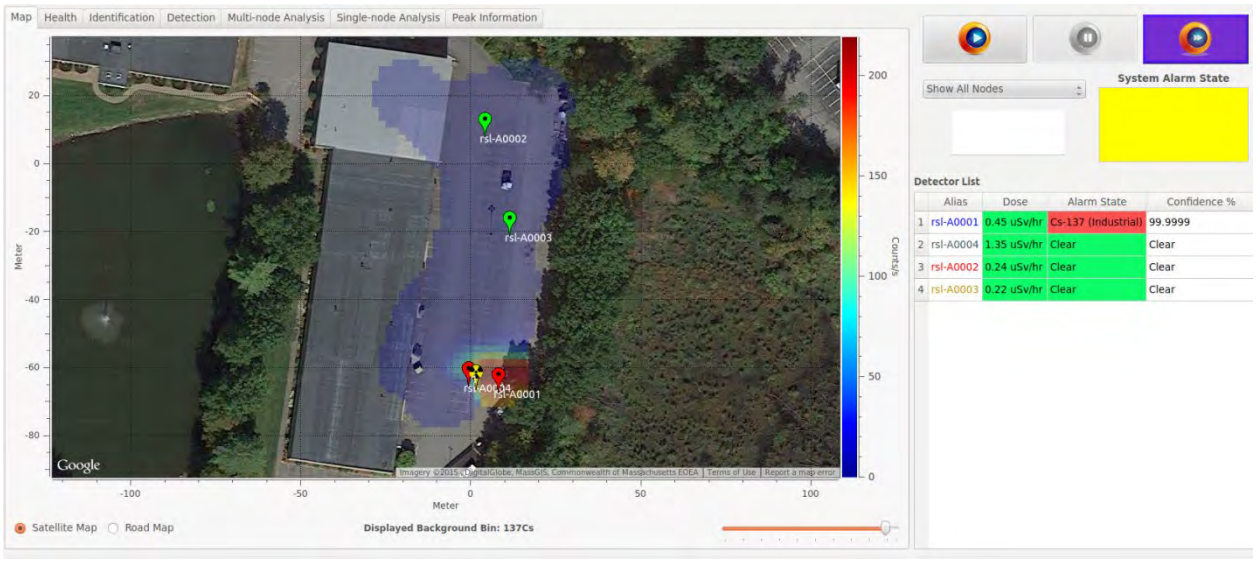

Figure 16. Subsequent localization of a moving ^{137}Cs source with a second detector

$AB_2I_5:Eu^{2+}$ compounds there is a striking difference in Eu distribution between the Sr- and Ba-containing crystals. The Eu ions energetically prefer the $B2^{(VII)}$ over the $B1^{(VIII)}$ sites in the Ba-containing compounds. No such preference is observed in the Sr-containing compounds. The Sr, Ba-mixed quaternary iodides of the type $ABa^{VIII}(Sr_xEu_{1-x})^{VII}I_5$ hold the promise of having enhanced homogeneity and electronic properties for better light yield and decay time, and so merit further investigation.

The first-principles DFT-based study on the Eu occupation in the AB_2I_5 host crystals demonstrated two distinct behaviors of activator distribution. In the Sr-containing crystals, Eu activators occupy both the $B1^{(VIII)}$ and $B2^{(VII)}$ sites. However, in the Ba-containing crystals Eu strongly favors the $B2^{(VII)}$ sites and shows a tendency toward forming Eu-rich domains. These domains may create crystal inhomogeneity and are also associated with 4f-CBM (conduction band minimum)

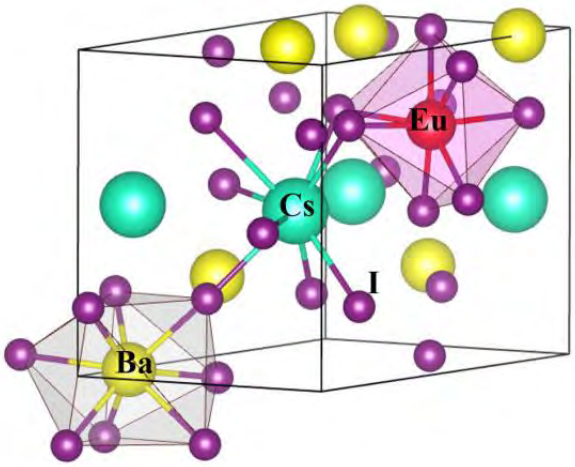

Figure 17. Schematic crystal structure and coordination of metal atoms in $CsBa_2I_5:Eu^{2+}$. Here, Ba occupies a $B1^{(VIII)}$ site and Eu is at a $B2^{(VII)}$ site (Biswas 2015).

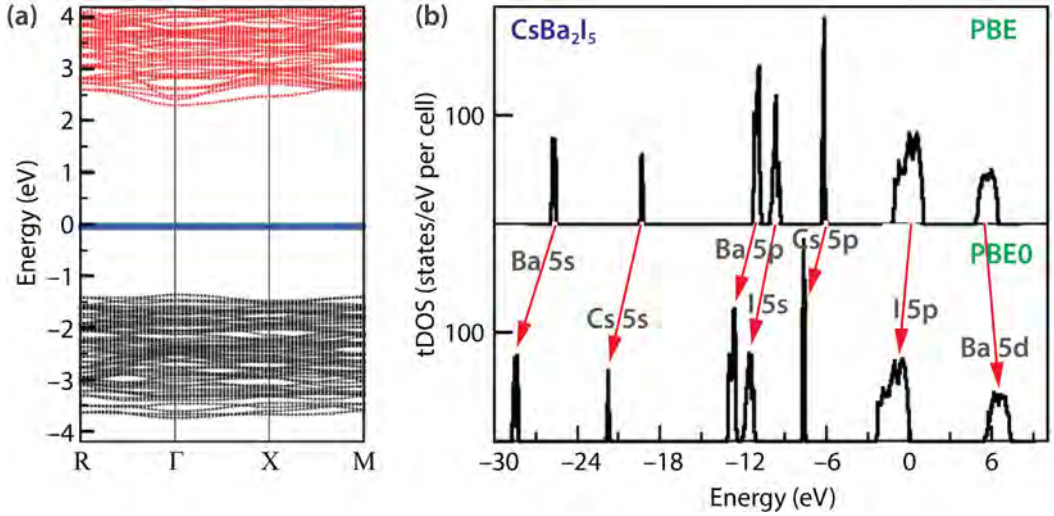

Figure 18. (a) Band structure of $CsBa_2I_5:Eu^{2+}$ and (b) total density of states of $CsBa_2I_5:Eu^{2+}$ are shown as a function binding energy. Observed are semi-core filled levels, narrow 2 to 3 eV valence band, and a conduction band of mainly d-character with a ~5 eV gap. The Eu ion introduces half-filled f-states inside the host band gap (Biswas 2015).

energy gap narrowing, possibly causing the observed luminescence peaks to shift to longer wavelengths while adding a slower component to scintillation time response. Inhomogeneous distribution of the domains may be circumvented by employing a (Sr, Ba):Eu mixed quaternary iodide ($ABa^{VIII}(Sr_xEu_{1-x})^{VII}I_5$), where Sr and Eu both preferentially occupy the $B2^{(VII)}$ sites. This should allow better crystal quality and control over Eu content to improve performance and proportional response of these scintillators.

Conclusion

Even though based on a robust networking system, existing national search equipment works independently when identifying and locating a radiation source. The system we have developed is significantly different in that it uses a small number of sensors that are integrated over the network, constantly exchanging data, and creating a common operating picture based on a probability distribution function determining the location of the radiological source. Current NA-42 detector systems do not exchange data among

themselves; the Search Management Center is more of a reporting, adjudicating, and accounting platform. It doesn't "lead" the search process.

The present networked system directs itself to the source of radiation; like a Bayesian-predictive search system, it actively finds the source. Currently deployed systems depend on CONOPS (thoroughness of search pattern, grids, or prior intelligence) to find a source. We have incorporated sub-second GPS and data acquisition times, which directly improve the quality of collected data, particularly in aerial measurements. By using an ad-hoc mesh networking system, we have cut down the network latency time (data do not have to go through Remote Sensing Laboratory or deployed servers). Our theoretical study shows when a single B-element (Sr or Ba) is used, rare earth–dopant Eu tends to create Eu-rich domains, which gives rise to an additional slower component to scintillation time response and deteriorates the scintillator properties. However, if both Sr and Ba are used to form a quaternary iodide ($ABa^{VIII}(Sr_xEu_{1-x})^{VII}I_5$), Sr and Eu both preferentially occupy the $B2^{(VII)}$ sites.

Acknowledgments

Joshua Jahn (Remote Sensing Laboratory–Andrews [RSL-A]) collected background gamma radiation data over a large section of Washington, D.C., from vehicle-mounted detection systems with NaI:Tl scintillators using the Advanced Visualization and Detection (AVID) system. Jack Meade (RSL-A) provided graphic drawings for publications and presentations. Mikhail Wolff (RSL-A) has been instrumental in developing the sub-second GPS-driven data acquisition system. Ethan Smith from Keystone International, Inc., has incorporated spectral data from multiple high-purity germanium detectors along with the low-resolution spectral data from NaI scintillators. Prof. Koushik Biswas from Arkansas State University has worked on basic theoretical models on electronic band structure properties of ternary alkali-alkaline earth halide scintillators having the general formula $A_iB_jX_k$, where A (alkali metal) = Na, K, Cs; B (alkali earth metal) = Ca, Sr, Ba; and X (halogen) = Cl, Br, I.

References

Biswas, K., C. M. Fang, "Preferential Eu site occupation and its consequences in ternary luminescent halides $AB_2I_5:Eu^{2+}$ (A=Li–Cs; B=Sr, Ba)," 22nd International Symposium on Room-Temperature Semiconductor X-Ray and Gamma-Ray Detectors, San Diego, California, October 31–November 7, 2015 IEEE Nuclear Science Symposium & Medical Imaging Conference, 2015.

Bourret-Courchesne, E. D., G. Bizarri, R. Borade, Z. Yan, S. M. Hanrahan, G. Gundiah, A. Chaudhry, A. Canning, S. E. Derenzo, "Eu^{2+}-doped Ba_2CsI_5, a new high-performance scintillator," *Nucl. Instrum. Methods Phys. Res. A* **612**, 1 (2009) 138–142.

Brown, F., B. Kiedrowski, J. Bull, "MCNP5-1.60 Release Notes," https://laws.lanl.gov/vhosts/mcnp.lanl.gov/pdf_files/la-ur-10-06235.pdf, accessed April 9, 2015.

Currie, L. A., "Limits for qualitative detection and quantitative determination. Application to radiochemistry," *Anal. Chem.* **40**, 3 (1968) 586–593.

Gascón, M., E. C. Samulon, G. Gundiah, Z. Yan, I. V. Khodyuk, S. E. Derenzo, G. A. Bizarri, E. D. Bourret-Courchesne, "Scintillation properties of $CsBa_2I_5$ activated with monovalent ions Tl^+, Na^+ and In^+," *J. Lumin.* **156** (2014) 63–68.

Passport Systems, Inc., "NetS² SmartShield™-Rad Survey and Detection Technology," http://www.passportsystems.com/pg/products/nets2-smartshield, accessed September 30, 2015.

Shirwadkar, U., R. Hawrami, J. Glodo, E. V. D. van Loef, K. S. Shah, "Promising alkaline earth halide scintillators for gamma-ray spectroscopy," *IEEE Trans. Nucl. Sci.* **60**, 2 (2013) 1011–1015.

Stand, L., M. Zhuravleva, A. Lindsey, C. L. Melcher, "Growth and characterization of potassium strontium iodide: A new high light yield scintillator with 2.4% energy resolution," *Nucl. Instrum. Methods Phys. Res. A* **780** (2015) 40–44.

Zhuravleva, M., C. L. Melcher, L. Stand, A. Lindsey, H. Wei, C. Hobbs, M. Koschan, "High energy resolution scintillators for nuclear nonproliferation applications," *Proc. SPIE* **9213** (2014) 921303.

This page left blank intentionally

High-Yield X-Ray Photocathodes for Next-Generation Imaging Detectors

LO-03-15 | Continuing in FY 2016 | Year 1 of 2

Kathy Opachich,[1,a] Andrew MacPhee,[b] Otto Landen,[b] Ning Chen,[c] Ashwini Gopal,[c] Salah Udin,[c] Terry Hilsabeck,[d] Eric Huffman,[d] Jeffrey A. Koch,[a] Jun Feng,[e] Patrick Ross,[a] Dave Bradley,[b] and Sabrina Nagel[b]

In this 2-year project, we are developing a next-generation, high-yield x-ray photocathode for use in the spectral energy range from 1 to 20 keV. In our first year, our goals were to fabricate a silicon photocathode and develop a coating procedure for the gold metal emission layer. This anisotropic, high aspect ratio structure has been produced in silicon using inductively coupled plasma-etching technology. The process is specifically developed with respect to the pattern density and geometry of the photocathode chip to achieve the desired sidewall profile angle. The tapered sidewall profile angle precision has been demonstrated to be within ±2.5° for a ~12° wall angle, with feature sizes that range between 3 to 9 μm in diameter and from 3 to 17 μm deep. Here we discuss the device applications and design, and present the method used to produce a set of geometrically enhanced high-yield x-ray photocathodes in silicon. In FY 2016 we will measure the yield enhancement from the photocathode prototypes in the 4–12 keV range. In addition, a full-scale photocathode will be fabricated and used for testing in an x-ray streak camera in order to evaluate the effect of the structured surface on detector spatial and temporal resolution.

[1] opachiyp@nv.doe.gov, 925-960-2520
[a] Livermore Operations; [b] Lawrence Livermore National Laboratory; [c] NanoShift, LLC; [d] General Atomics;
[e] Lawrence Berkeley National Laboratory

Background

Time-resolved x-ray diagnostics are widely used at the National Ignition Facility (NIF) (Miller 2004). Currently the facility uses streak camera detectors, such as the Diagnostic Insertion Manipulator Imaging Streak Camera (Khan 2012, Opachich 2012) and time dilation imaging tubes (Hilsabeck 2010, Nagel 2012) for imaging in the 5 to 10 keV range. The introduction of the Advanced Radiographic Capability at NIF will provide imaging sources that extend well above the 10 keV limit. However, current detectors rely on photocathode materials to convert photon signals to electrons, which are then dispersed temporally with the use of voltage ramps and magnetic fields. The imager detector efficiency and operational range is somewhat limited to below 10 keV due to a sharp reduction in quantum efficiency (QE) of most photocathode materials (i.e., gold and cesium iodide) (Hara 2000, Khan 2013, Opachich 2014). Geometrically enhanced photocathodes provide a potential solution, and they can be easily integrated into existing detectors without compromising performance.

The electron yield can be improved by better matching the x-ray path length to the very thin top-most emission layer of the photocathode, defined as the electron escape depth. This is accomplished by changing the incidence angle of x-ray photons to a very shallow, near-grazing geometry, as shown in Figure 1.

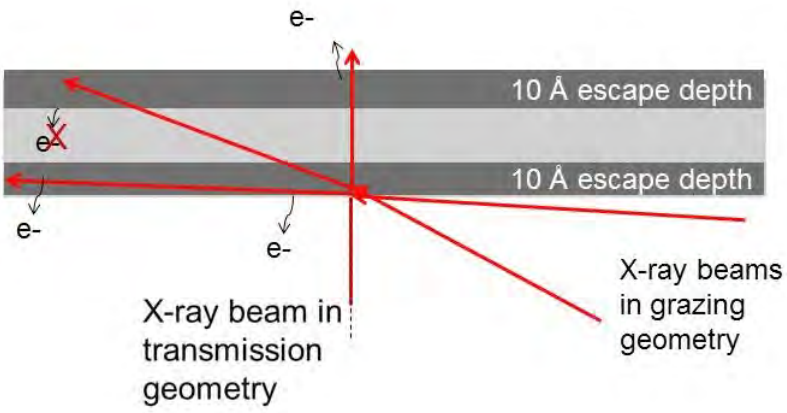

Figure 1. Example of the grazing incidence and transmission geometry. The electron escape depth (not to scale) is shown on both sides of the photocathode. Electrons that are generated within the bulk do not contribute to the measured yield.

The secondary electron escape depth is typically very thin; for example, in gold (Au) it is limited to the top 10 Å and to 250 Å of the photocathode surface (Henke 1981, Fraser 1992). Angles θ below ~20° are needed to provide significant enhancement. Grazing incidence detectors have utilized this geometry and demonstrated improvement in photocathode QE by a factor of 15–20 times in the soft x-ray range (Feng 2010). This effect can also be extended to the 10–20 keV range, as predicted by the semi-empirical model by Fraser (1983a, 1983b).

Changing the incidence angle of current NIF detectors is costly and may not be possible due to engineering design constraints; however, it is fairly simple to change the design of the photocathodes by introducing geometrically enhanced surfaces such as pillars, cones, or recessed cavities. A recent study used CST Studio Suite, an electromagnetic modeling software, to determine a set of structured photocathode designs that would increase the observed yield by up to 3.5 times without changing the spatial and temporal performance of current x-ray detectors (Opachich 2014). Based on this work, we decided to use recessed cone and pyramid designs to develop a set of structured photocathode prototypes. The two designs are shown in Figure 2.

Project

Based on CST Studio Suite modeling work previously done at NSTec Livermore Operations, two structures were chosen: the recessed cone and pyramid (Opachich 2014). The model predicted a yield increase as a function of structure depth. To test this prediction, three depths of 3, 8.4, and 16.8 µm were chosen for each structure type. The design drawings included specifications for two cathode types with three structure depths. Table 1 summarizes the requested structure types, the depth and diameter/width of the structures, and their relative expected yield. These drawings were used along with the fabrication specifications listed in Table 2.

A plasma etch recipe that would satisfy these requirements for devices that had an active region of 8 × 8 mm was developed. The coatings were electron beam sputter–deposited onto the silicon (Si) substrate. The project was split into four phases and accomplished in several development steps in order to minimize risk. In the first phase an initial resist mask was developed, and several methods were evaluated on test wafers. It was decided that the pyramid structures had a better etch quality in comparison with recessed cones, and the pyramid design was chosen as the preferred structure for the remaining work. In phase two the etching process was further tested and developed on prototype wafers. Phase three focused on coating methods and developing an etch recipe for back thinning the devices. During the final phase, the prototype structures were completed.

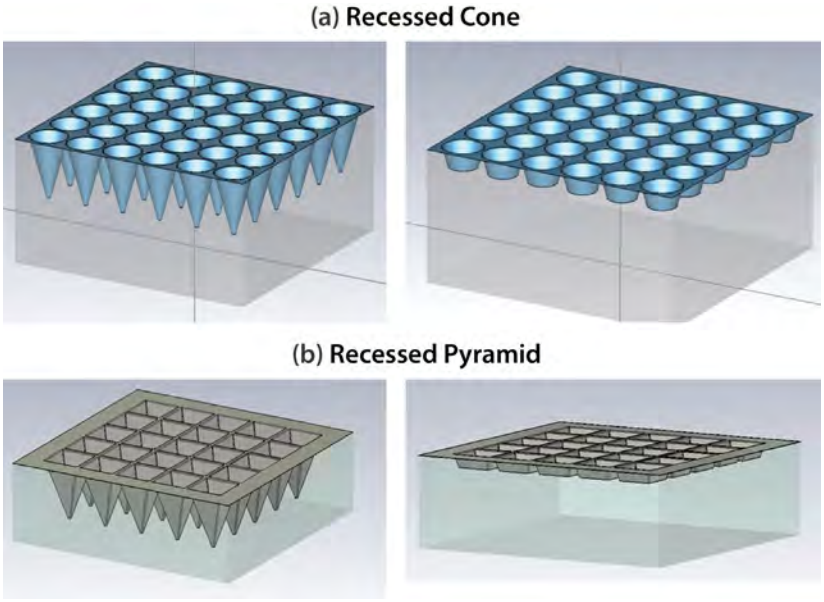

Figure 2. The recessed designs: (a) full-length and shallow cone structures and (b) the full-length and shallow pyramid structures. The substrate material is silicon (Si) with a 700 Å gold coating at the top surface.

Table 1. Cone and pyramid prototype specifications

Recessed Geometry	Incidence Angle	Diameter/Width (µm)	Depth (µm)	Au Yield Relative Increase at 14 keV
Cone	15	9	3	1.60
Cone	15	9	8.4	2.36
Cone	15	9	16.8	2.81
Pyramid	15	9	3	1.75
Pyramid	15	9	8.4	2.73
Pyramid	15	9	16.8	3.31

Table 2. Fabrication requirements

Requirement #	Description	Value	Tolerance
1	Wall Angle	12°	±2.5°
2	Depth	3, 8.4, and 16.8 µm	±2 µm
3	Pitch	2 µm	±0.2 µm
4	Diameter/Width	9 µm	±0.2 µm
5	Coating Thickness	20 Å Ti (wetting layer) and 700 Å Au	±200 Å
6	Coating Roughness	200 Å	--
7	Substrate Thickness	150 µm	±2 µm

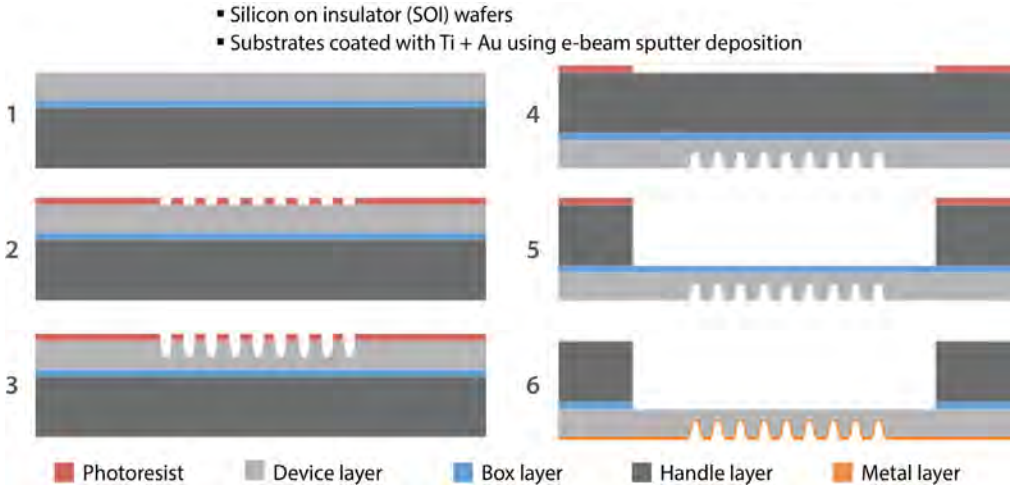

Figure 3. Summary of the six-step process used to fabricate the structured photocathode prototypes

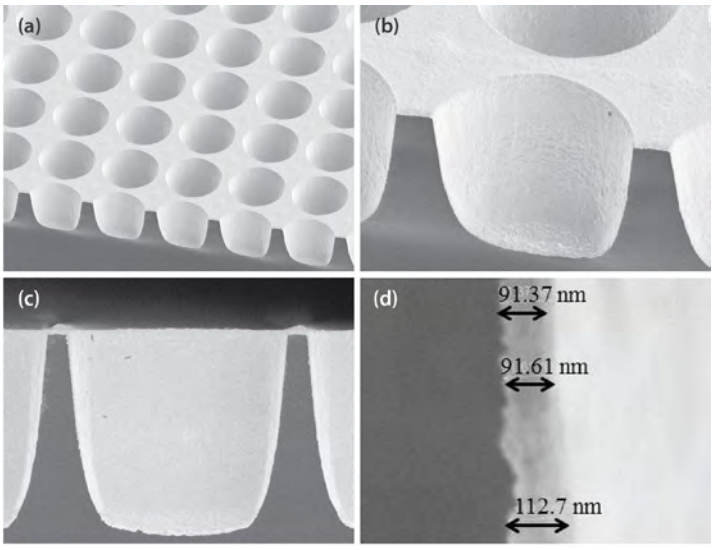

Figure 4. Scanning electron microscope images of a mid-length recessed cone structure. (a) Wide view of the structured photo-cathode. (b) Cross-sectional pan view of the quality of the coating at the edge. (c) Side view of the structures with a recessed cavity wall of ~12°. (d) Image of the sidewall coating.

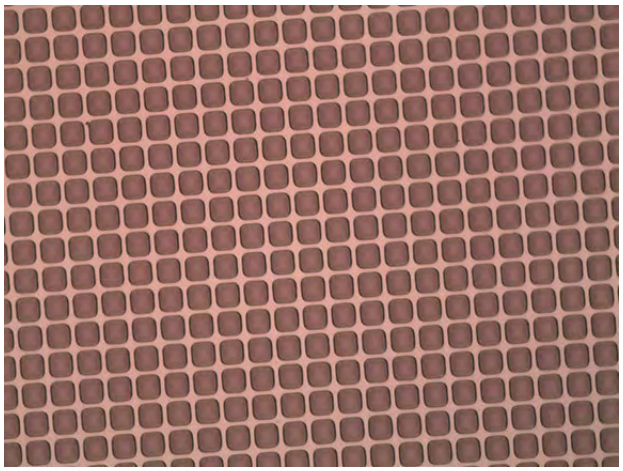

Figure 5. Optical image of the recessed pyramid structures. There is some rounding at the corners due to the plasma-etching process. This will help alleviate field reduction in future detector testing. Because this is an image taken on an optical system, only the top surface is seen due to the depth of focus of the microscope objective.

Figure 3 summarizes the final etching and coating process that was developed. The devices were built from Si on insulator wafers that have an insulating layer that separates the device into two regions, the device layer and the handle. The device layer was masked with photoresist, and the structures were etched out by using a plasma-etching system. After etching, the mask was removed and a photoresist applied to the handle region for back thinning. After back thinning was completed, the total device thickness was 150 µm. The final step involved electron beam–sputtering onto the substrate a thin wetting layer (20 Å) of titanium (Ti) followed by 700 Å of Au.

An example of the recessed-cone photocathode prototypes is shown in Figure 4. The recessed pyramid devices have a similar etch quality. An optical image of the final recessed pyramid structures is shown in Figure 5. Here we see that the structures are 9 µm in diameter or width, with a sidewall angle of ~12°. The coating thickness is from 900 to 1100 Å with a roughness of ~200 Å. This thickness is adequate for higher x-ray energies and satisfies our requirement. The structures are very periodic and show little deviation from the pitch and width requirements.

Conclusion

In the first year of this project, we completed the design and drawings of the prototype structured photocathodes. We were able to quickly place a subcontract with NanoShift, LLC, and begin the development of a fabrication process. This work resulted in a patent application (14-L-20 NSTECH.0038P) between NSTec, Lawrence Livermore National Laboratory, and General Atomics. Two manuscripts were published, one in *Review of Scientific Instruments* (Opachich 2014) and one in *SPIE Proceedings* (Opachich 2015). The work was also presented as a conference poster at the High Temperature Plasma Diagnostics conference in Atlanta, Georgia (Opachich 2014), and as a talk at the SPIE Optics + Photonics conference in San Diego, California (Opachich 2015).

In FY 2016 we will measure yield enhancement from the structured photocathode prototypes in the 4–12 keV range. The work will result in a publication in *Applied Physics Letters*. A full-scale prototype will be fabricated and tested in an x-ray streak camera. We plan to collect and analyze full-scale detector performance data in time for the 2016 High Temperature Plasma Diagnostics conference, where we will present a poster and publish results in *Review of Scientific Instruments*. These two studies will validate our computer simulation and provide a viable solution for current x-ray detectors.

References

Feng, J., K. Engelhorn, B. I. Cho, H. J. Lee, M. Greaves, C. P. Weber, R. W. Falcone, H. A. Padmore, P. A. Heimann, "A grazing incidence x-ray streak camera for ultrafast, single-shot measurements," *Appl. Phys. Lett.* **96**, 13 (2010) 134102.

Fraser, G. W., "The characterisation of soft x-ray photocathodes in the wavelength band 1–300 Å: I. Lead glass, lithium fluoride and magnesium fluoride," *Nucl. Instrum. Methods Phys. Res.* **206**, 1–2 (1983a) 251–263.

Fraser, G. W., "The characterisation of soft x-ray photocathodes in the wavelength band 1–300 Å: II. Caesium iodide and other insulators of high photoelectric yield," *Nucl. Instrum. Methods Phys. Res.* **206**, 1–2 (1983b) 265–279.

Fraser, G. W., M. T. Pain, J. E. Lees, C. R. Binns, J. F. Pearson, P. R. Houghton, "The characterization of gold x-ray photocathodes," *Nucl. Instrum. Methods Phys. Res. A* **321**, 1–2 (1992) 385–391.

Hara, T., Y. Tanaka, H. Kitamura, T. Ishikawa, "Performance of a CsI photocathode in a hard x-ray streak camera," *Rev. Sci. Instrum.* **71**, 10 (2000) 3624–3626.

Henke, B. L., J. P. Knauer, K. Premaratne, "The characterization of x-ray photocathodes in the 0.1–10-keV photon energy region," *J. Appl. Phys.* **52**, 3 (1981) 1509–1520.

Hilsabeck, T. J., et al., "Pulse-dilation enhanced gated optical imager with 5 ps resolution," *Rev. Sci. Instrum.* **81** (2010) 10E317.

Khan, S. F., et al., "Measuring x-ray burn history with the Streaked Polar Instrumentation for Diagnosing Energetic Radiation (SPIDER) at the National Ignition Facility (NIF)," *Proc. SPIE* **8505** (2012) 850505.

Khan, S. F., et al., "Characterization of the x-ray sensitivity of a streak camera used at the National Ignition Facility (NIF)," *Proc. SPIE* **8850** (2013) 88500D.

Miller, G. H., E. I. Moses, C. R. Wuest, "The National Ignition Facility: Enabling fusion ignition for the 21st century," *Nuclear Fusion* **44**, 12 (2004) S228.

Nagel, S. R., et al., "Dilation x-ray imager a new/faster gated x-ray imager for the NIF," *Rev. Sci. Instrum.* **83**, 10 (2012) 10E116.

Opachich, Y. P., et al., "High performance imaging streak camera for the National Ignition Facility," *Rev. Sci. Instrum.* **83**, 12 (2012) 125105.

Opachich, Y. P., P. W. Ross, A. G. MacPhee, T. J. Hilsabeck, S. R. Nagel, E. Huffman, P. M. Bell, D. K. Bradley, J. A. Koch, O. L. Landen, "High quantum efficiency photocathode simulation for the investigation of novel structured designs," *Rev. Sci. Instrum.* **85**, 11 (2014) 11D625.

Opachich, Y. P., et al., "Precision fabrication of large area silicon-based geometrically enhanced x-ray photocathodes using plasma etching," *Proc. SPIE* **9591** (2015) 95910O.

Advanced Spatial and Spectral Data Analysis for Aerial- and Ground-Based Gamma Radiation Detection

RSLA-02-14 | Continued from FY 2014 | Year 2 of 2

Johanna Turk,[1,a] J. Doug Hague,[a] Marylesa Howard,[b] and Michael Mazur[a]

The development of functional data analysis techniques for gamma ray mapping and search with aerial, vehicular, pedestrian, and maritime-based data collection methods is described. The algorithms and techniques are especially suitable for use by emergency response teams. We pursue the following parallel—and interrelated—research tracks for all of the data collection methods: statistically robust data mapping and superior spectral anomaly detection. We demonstrate an ability to perform kriging interpolation in a quick and reliable way in order to exploit the inherent statistical capabilities of the method. We also demonstrate increased accuracy and sensitivity with spectral anomaly detection methods, as compared to the currently used technique.

[1] turkjl@nv.doe.gov, 301-817-3333
[a] Remote Sensing Laboratory–Andrews; [b] North Las Vegas

Background

Decisions for the nation's nuclear emergency response actions are heavily dependent on reliable data analysis and radiation visualization techniques. In the past, radiological emergency response programs, such as the Aerial Measuring System (AMS), the Radiological Assistance Program (RAP), and the Nuclear/Radiological Advisory Team (NRAT), have proven successful in the event of disasters; however, the data analysis methods used have not been advanced to the current, next-generation techniques in the field of mathematics and analysis and fail to extract all usable information from the data. Sodium iodide gamma ray detectors are the most common radiation detection systems for emergency response due to their advantageous properties: they are scalable, highly efficient, non-cryogenic, and inexpensive. Due to the ubiquitous use of this detector medium, likely for decades to come, a fruitful and cost-effective way to advance radiation detection for emergency applications is to improve data handling and analysis. Our desired project goal is to reduce noise and variance at different steps in the data collection and analysis process, in order to detect the presence of non-NORM (naturally occurring radioactive materials) isotopes at low thresholds, while not triggering on natural variations in the NORM background, and perform statistically robust data interpolation to understand the uncertainties in the results.

Project

Spectral Anomaly Detection

The detection of anomalies based on gamma ray spectral information is of central significance for nearly all applications of nuclear and radiological search. The work represented here reflects an effort to both develop new methods of spectral anomaly detection and to quantitatively understand previously established methods. These studies are not intended to fully encompass the full scope of available analytic

techniques but, rather, understand the limitations and applicability of methods readily available to field-deployable scientists.

To this end, we illustrate two new methods, the Wavelet Assisted Variance Reduction for Anomaly Detection (WAVRAD) and Kolmogorov-Smirnov statistic, and compare them to two previously developed methods: the so-called Golf Alarm and the Nuisance Rejection Spectral Comparison Ratio Anomaly Detection (NSCRAD) algorithms (Turk 2015). All these algorithms are applied to relevant data collected from both controlled settings and in-field measurements.

Golf Alarm

The current standard default method for detecting anomalous radiation signals in time-series data compares the deviation of the gross counts of the most recent measurement(s) with the expected gross counts based on the mean and variance of previous—but recent—measurements.

The Golf Alarm algorithm is constructed by the following steps:

1. Compute the mean and standard deviation of the gross counts of the set of background spectra.
2. Compute the gross counts of the foreground spectrum.
3. Compute the number of standard deviations that the foreground differs from the background.
4. Compute the alarm metric by taking the logarithm (base-2) of the standard deviations.

This Golf Alarm approach is straightforward to interpret in the presence of stochastic (normally distributed) data, but the natural environment is inherently non-Gaussian; therefore, this alarm algorithm can lead to a high false-alarm rate. Furthermore, this algorithm makes no attempt to use the information contained in the energy spectra collected by the instrument. For example, it is preferred to ignore a strong source of NORM but to alarm in the presence of a weak source of, say, special nuclear material.

NSCRAD

The NSCRAD algorithm is widely available in field-deployable tools. While we have little knowledge of the algorithms and methods employed by NSCRAD, we nonetheless use it as a benchmark by which we may judge our newly developed methods.

Kolmogorov-Smirnov

The Kolmogorov-Smirnov test is a well-established statistical method for testing the probability that two distributions are drawn from the same parent. The test uses the maximum difference between the cumulative distribution functions of two observed datasets to analytically calculate a p-value. This test does not make assumptions about the parametric form of the parent distribution but is only sensitive to the overall *shape* of the distribution.

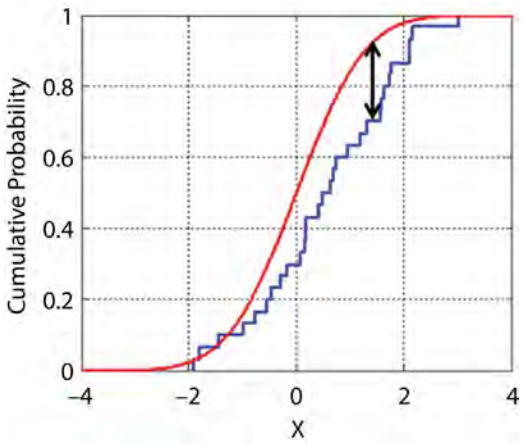

Figure 1. A schematic illustration of the Kolmogorov-Smirnov test. Note that this plot does not show observed spectral data.

The Kolmogorov-Smirnov algorithm (Figure 1) is constructed by the following steps:

1. The cumulative distribution function for the background and the foreground is computed (red and blue curves, respectively).
2. The maximum distance between the functions is determined (black arrow).

3. A p-value, which gives the probability that the background and the foreground are drawn from the same mother distribution, is computed.

4. An alarm is triggered if the p-value is less than a pre-determined value.

WAVRAD

The WAVRAD algorithm was developed by NSTec for comparing spectra at different energy scales by transforming the channel data into a non-standard topological vector space (the specific L^p-norm, the topological vector space, can be adjusted). The metric distance between the spectra in the transformed space enhances the difference in *shape* between the spectra and can be used to robustly differentiate a signal from typical background variations (Figure 2).

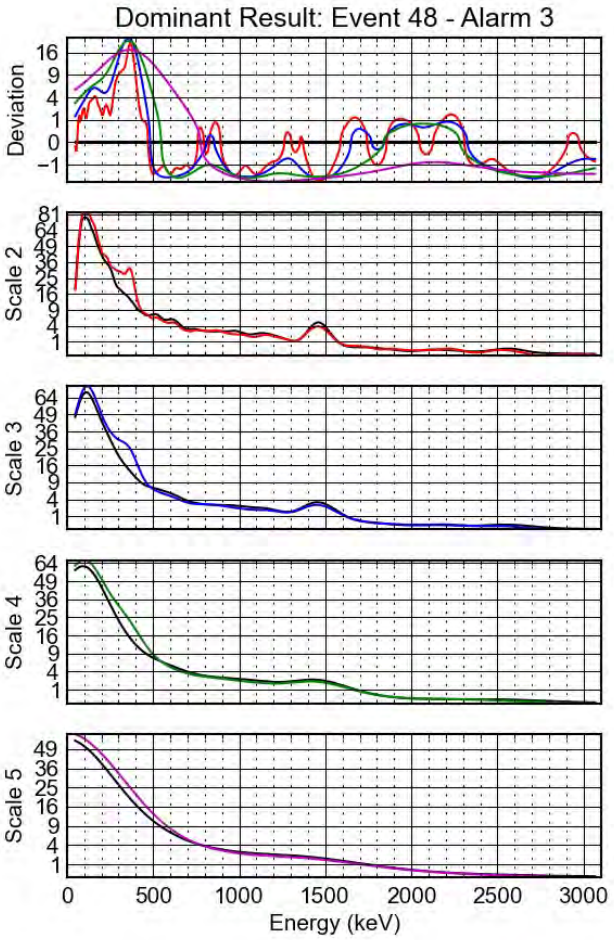

Figure 2. A schematic illustration of the intermediate output of the WAVRAD algorithm. The top plot shows the deviation of the foreground spectrum from the background spectrum at four different characteristic energy scales. The four plots below it show the background in black and the foreground in color at each of the relevant energy scales. The deviations from background at each scale reveal information relevant for an alarming metric.

Algorithm Comparison Results

We compared the performance of the four aforementioned algorithms on representative datasets of (1) no source, a dataset indicative of normal "background" data; (2) ^{133}Ba, a barium-133 source present; (3) ^{60}Co, a cobalt-60 source present; (4) uranium ore, which represented an elevated NORM; and (5) Washington, D.C. mobile, which simulated "real" data collected in Washington, D.C., by a mobile system.

The first four datasets were collected with a vehicle-mounted mobile system in a controlled setting (Figure 3). This was done in order to know in advance both exactly which isotopes were present and the temporal/spatial location of the sources. This, in turn, allows for a fair and known comparison between the algorithms. The controlled dataset that was known not to contain a source (no source) can be used to understand false positive rates of algorithms, including illustrating the drawbacks of the often deployed Golf Alarm (Figure 4). Data collected by a mobile system in the city of Washington, D.C., was obtained and used as a "real-world" example of how the algorithms might perform (Figure 5). Table 1 shows results of the algorithm comparisons on all five datasets.

Results

The algorithm development and the implementation of the testing produced over 20,000 lines of code. The algorithms were validated and their parameters adjusted based on their performance. We can conclude that the WAVRAD and Kolmogorov-Smirnov algorithms perform exceptionally well when compared to previously deployed algorithms. We can also conclude that Kolmogorov-Smirnov outperforms the Golf Alarm algorithm and that the WAVRAD algorithm outperforms both Kolmogorov-Smirnov and NSCRAD (though it is only marginally better than the latter).

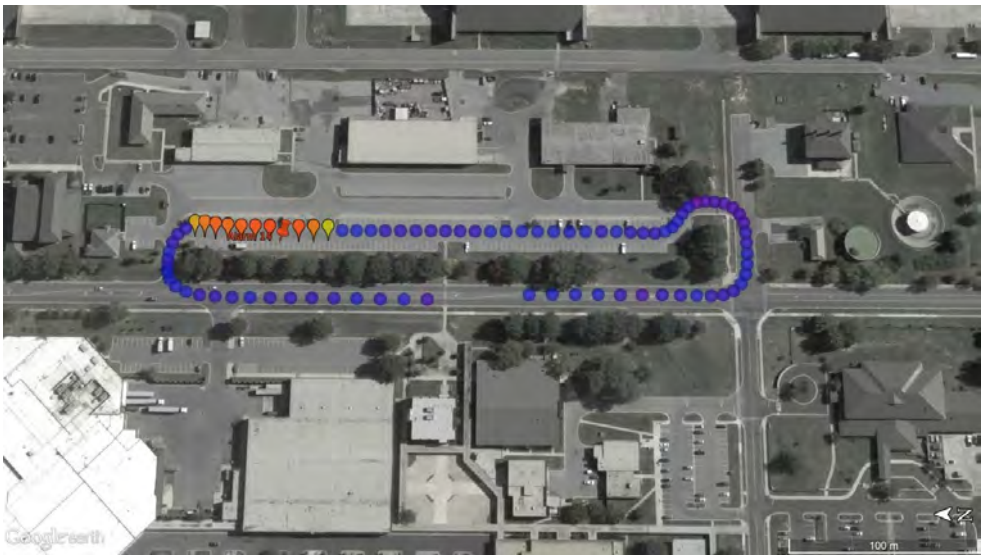

Figure 3. An example of test data collected in a controlled setting. The source is present near the orange and red points.

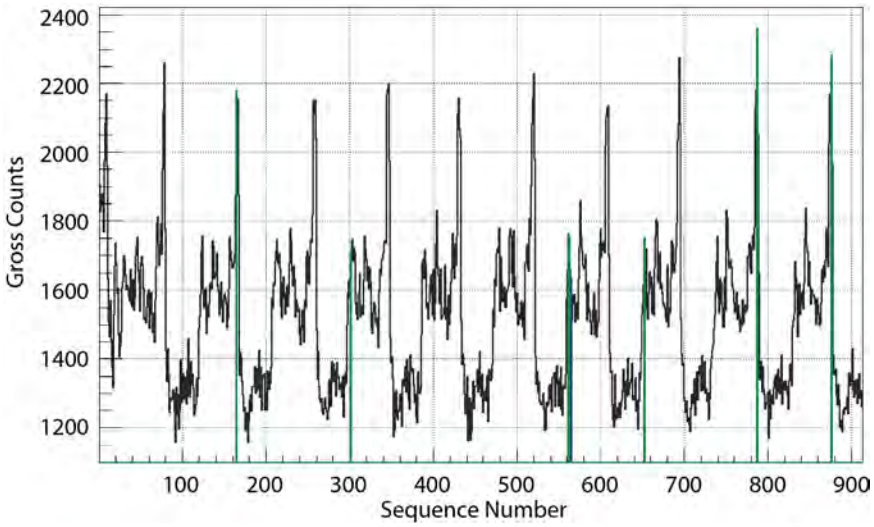

Figure 4. Gross counts versus sequence number for the no source dataset (e.g., natural background only). There is regular variation in the counts, and the Golf Alarm algorithm triggers on this variation, even though there is no source present in the data.

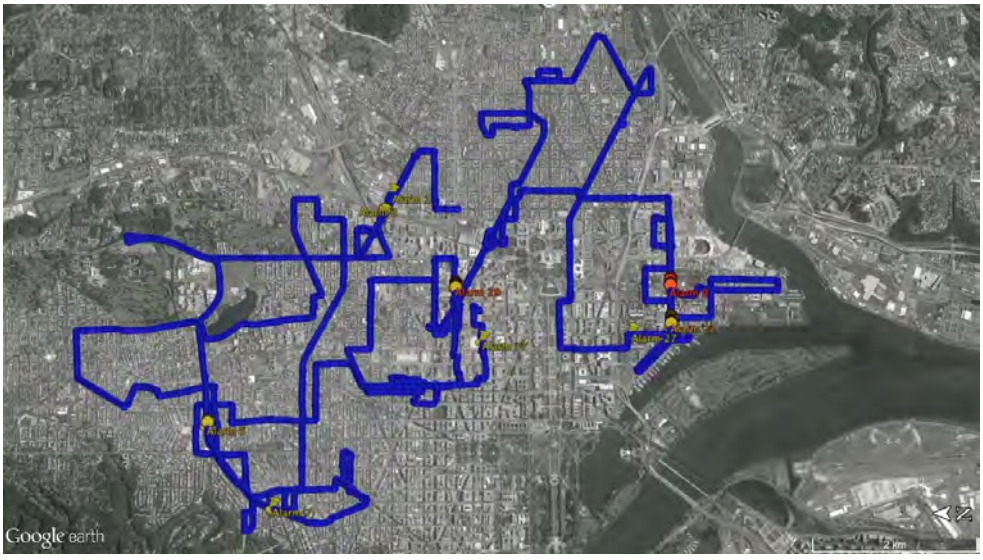

Figure 5. Georeferenced data collected by a mobile system in Washington, D.C. The WAVRAD alarms are the yellow and red colored points.

Table 1. A summary of comparing algorithm performance based on the data available for this study

Data	# Sources	# True Alarms / # False Alarms			
		Golf	Kolmogorov-Smirnov	WAVRAD	NSCRAD
No source	0	0 / 6	0 / 0	0 / 0	0/0
^{133}Ba	5	1 / 0	3 / 0	5 / 0	0/0
^{60}Co	5	0 / 1	2 / 0	5 / 0	5/0
Uranium ore	5	2 / 0	5 / 0	5 / 0	4/0
Washington, D.C.	Unknown	**140+** total alarms	**3** total alarms	**9** total alarms	**9** total alarms

Spatial Analysis and Uncertainty Quantification

In radiological emergency response, a standard data visualization technique is to create an interpolation map of gross counts from a radiation spectrum to understand the location, and extent, of ground deposition. Some standard interpolation methods, such as linear interpolation, lack an inherent process for estimating error in the predictions, while other methods, such as kriging, provide point-wise error estimates for the predictions. However, in terms of an emergency response application where decisions need to be made in a timely manner, kriging has drawbacks; it is a time-consuming process that requires an experienced scientist to manipulate the data to ensure assumptions are met before a spatial interpolation may be created. Based on the exploration of real data in this study, our aim is to provide guidance that generalizes an approach to kriging, applicable from event to event, that allows an untrained scientist to apply kriging in an informed manner. The method we developed to address this need, adapting kriging to quick kriging, is described below.

Quick Kriging

The kriging predictions are based upon a model that describes a variance structure in the data. In practice, before kriging is performed and before the variance is modeled, exploratory data analysis is used to determine if a transform of, and/or the removal of trend from, the data is necessary to satisfy Gaussian assumptions. In aerial radiological applications, it is not unrealistic to assume there is an underlying distribution that describes a family of data; for example, all data of natural background counts likely come from the same parent distribution, regardless of its physical location in the world. This is tested by comparing the distribution of counts from various data and their corresponding semivariograms, a graphical representation of the degree of spatial continuity.

The sample semivariogram γ for a given distance between two data locations, or lag h, is defined as half the variance of the difference between two random variables, expressed mathematically as

$$\gamma(h) = \frac{1}{2n(h)} \sum_{(i,j)|h_{ij}=h} \left(y_i - y_j \right)^2, \quad (1)$$

where $n(h)$ is the number of data points h units apart, $h_{ij} = s_i - s_j$ is the vector connecting points s_i and s_j—given that s_i is the location of the ith observation, and y_i is the observed response of gross counts at site s_i. In practice, the sample semivariogram is computed for a discrete number of lags, and a model is fit to describe the semivariance at any given lag h. This model is used to incorporate the covariance structure of the data into weights necessary for the predictions made by the kriging algorithm.

Many models exist to describe the behavior of a semivariogram, and these models are fully defined by three parameters. The variance of an observation with itself is defined to be 0; in other words, $\gamma(h) = 0$ when $h = 0$, but, in practice, as the distance between any two observations decreases (i.e., $h \rightarrow 0^+$), the sample semivariance approaches $a > 0$, where a is referred to

as the nugget. The second parameter of semivariogram models is the sill, σ^2, the semivariance value at which observations are nearly uncorrelated. The range, r, is the distance beyond which observations are approximately uncorrelated. Of the datasets examined here, a universal parameter set would be one that would serve as initial estimates for the parameters as they are fit by a specified model to any data satisfying some requirement.

We considered six datasets for comparing semivariograms, each of which are listed in Table 2, along with the flight altitude and number of data observations collected. The data were gathered such that flight altitude was as similar as possible from set to set, and the radiation behavior on the ground was composed of deposition or solely natural background counts so as to minimize confounding variables in our analysis. Point source data were not used, as this type of collection would most generally require detrending.

Table 2. Characteristics regarding the datasets used for testing a quick kriging approach

Survey Data	Flight Altitude (ft)	# Data Points
Armory	150	223
Distributed Source	100	2061
Hyde Ares	100	1034
Las Vegas (Urban)	300–600	6024
Natural Background	150	2870
Washington, D.C.	150	11,267

The images in Figure 6 indicate the spatial location of all observed gross counts for each dataset. Gross counts are collected over a time interval and can be on the order of 1,000 for natural background radiation, with values in the tens of thousands for radioactive material.

Fitting routines typically have difficulty with large-valued data and result in fitting errors. By reducing the magnitude of the observations, the data are better behaved and fitting routines provide more robust estimates. In this application, a transform to reduce the magnitude of the data will prove useful when we begin modeling the covariance structure. In addition, exploration of the data suggests that a logarithm transform of the counts tends to provide a more Gaussian distribution, one of the kriging assumptions. Histograms of the logarithm-transformed data are given in Figure 7. Most generally, the distributions appear fairly normal, with the Armory Survey appearing the least normal; this data also has the fewest counts observed. The Distributed Source Survey demonstrates a minor right skew, and the Washington, D.C., Survey is heavy tailed, but neither is strikingly non-normal. Given these six datasets, a log transform may be appropriate for all background and deposition data to satisfy one of the kriging assumptions.

A second assumption of the standard kriging method is that there is no trend in the data. Some methods of kriging allow for trend removal or trend estimation, but we continue with simple kriging (Cressie 1993). See Figure 8 for a linear interpolation of the data to visualize its spatial behavior. The Armory Survey shows the strongest trend, with higher gross counts in the southwest corner and lower values in the northeast corner.

After verifying that the logarithmic transform returns approximately normal distributions in most cases and detrending is not necessary for these data, we consider the semivariance computed at regular distances, given by the open circles in Figure 9. The semivariogram of the Natural Background Survey indicates a hole effect, where the semivariance increases but then decreases with increasing lag; this behavior is common in geostatistical data.

For each semivariogram, initial estimates for the nugget, range, and partial sill, ($\sigma^2 - a$), were obtained by eye from the plots in Figure 9. An exponential semivariance model was chosen as the best universal model for these data, and it is defined by

$$\hat{\gamma}(h) = \begin{cases} 0 & h = 0 \\ a + (\sigma^2 - a)\left(1 - e^{-3\|h\|/r}\right) & h > 0 \end{cases}. \qquad (2)$$

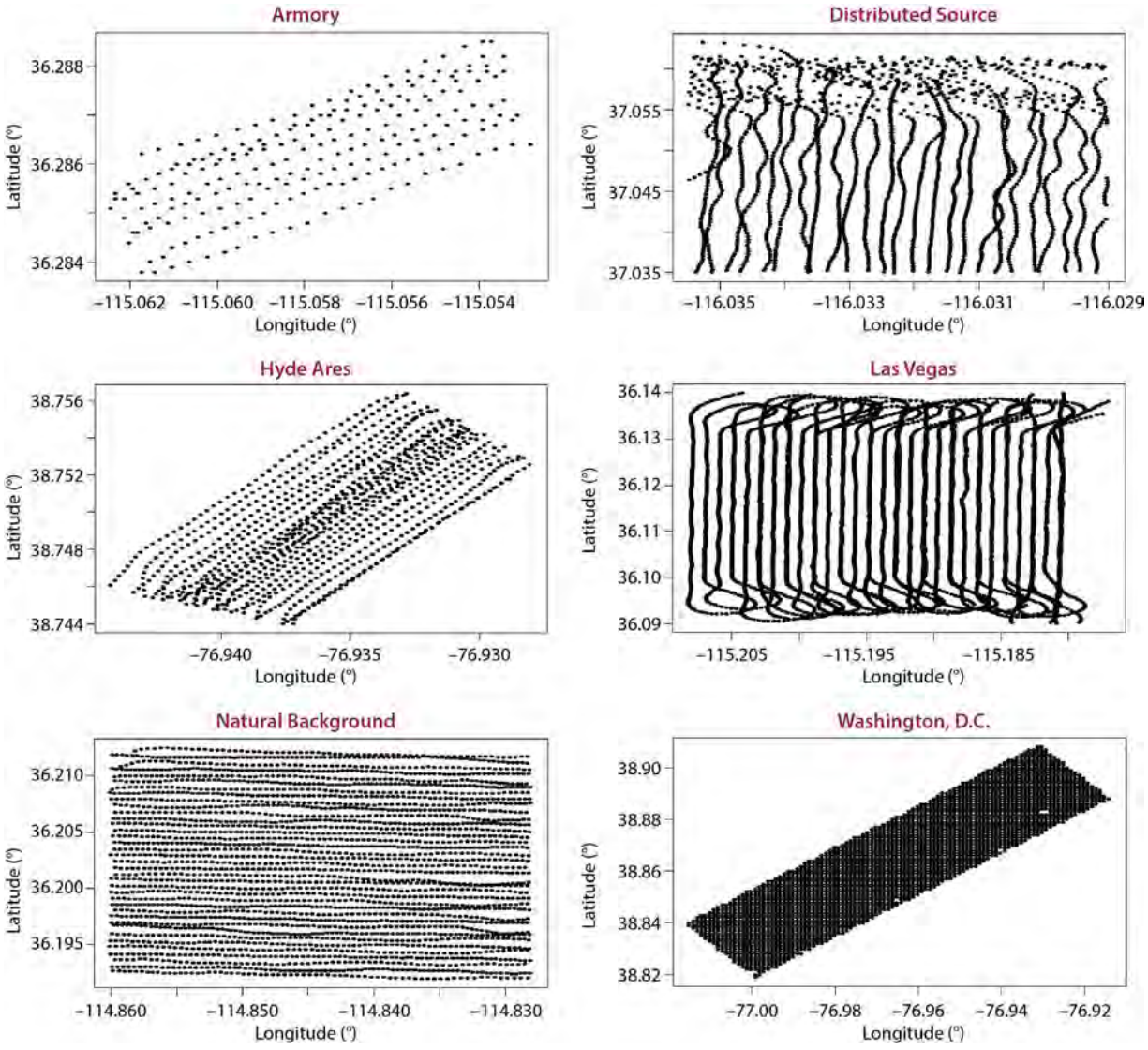

Figure 6. Locations of all observed gross count values for datasets

The parameters were fit in the R software package using a weighted least squares routine, and both the initial parameter estimates and the final fitted parameters are given in Table 3. The fit of each model is also given in Figure 9 (blue lines).

From comparing the fitted parameters in Table 3, it was noted that the values for each of the three parameters seem to be similar, as though the covariance structure is similar from dataset to dataset. A universal set of seed parameters was chosen based on the fitted parameters in Table 3, where $(\sigma^2 - a) = 0.01$, $r = 0.003$, and $a = 0.0005$, and the model was fit again with the R software package using a weighted least squares routine. The resulting parameters are given in Table 3, and we note that these are very similar to the previous fitted parameters, with the exception of the Armory data. For visual comparison, the resulting model fit is shown in Figure 10. Visually, all of the fits are nearly identical, with the exception of the Armory data, which has been an exception nearly this entire process. The Armory dataset is one that would likely be discarded early in the preprocessing stages of data manipulation because it does not have enough spatial coverage in the northwest-southeast direction (see Figure 6), thereby creating too few lags (open circles in Figure 10) to properly fit a semivariogram model.

Table 3. Semivariogram parameters for the exponential model. The initial estimates were used to seed the weighted least squares fitting routine, from which the fitted parameters were calculated. The universal fit are the resulting parameters from the model seeded with estimates ($\sigma^2 - a$) = 0.01, r = 0.003, and a = 0.0005.

Survey Data	Initial Estimates			Fitted Parameters			Universal Fit		
	$\sigma^2 - a$	r	a	$\sigma^2 - a$	r	a	$\sigma^2 - a$	r	a
Armory	0.0015	0.0010	10^{-8}	0.0431	0.0629	0.0004	0.0047	0.0062	0.0004
Distributed Source	0.1000	0.0040	0.0010	0.0107	0.0034	0.0011	0.0103	0.0031	0.0010
Hyde Ares	0.0300	0.0040	0.0001	0.0390	0.0043	0.0003	0.0454	0.0054	0.0007
Las Vegas	0.0250	0.0060	0.0200	0.0198	0.0030	0.170	0.0197	0.0031	0.0171
Natural Background	0.0320	0.0060	0.0010	0.0310	0.0027	$<10^{-8}$	0.0299	0.0024	$<10^{-8}$
Washington, D.C.	0.0090	0.0040	0.0020	0.0103	0.0026	0.0001	0.0102	0.0027	0.0002

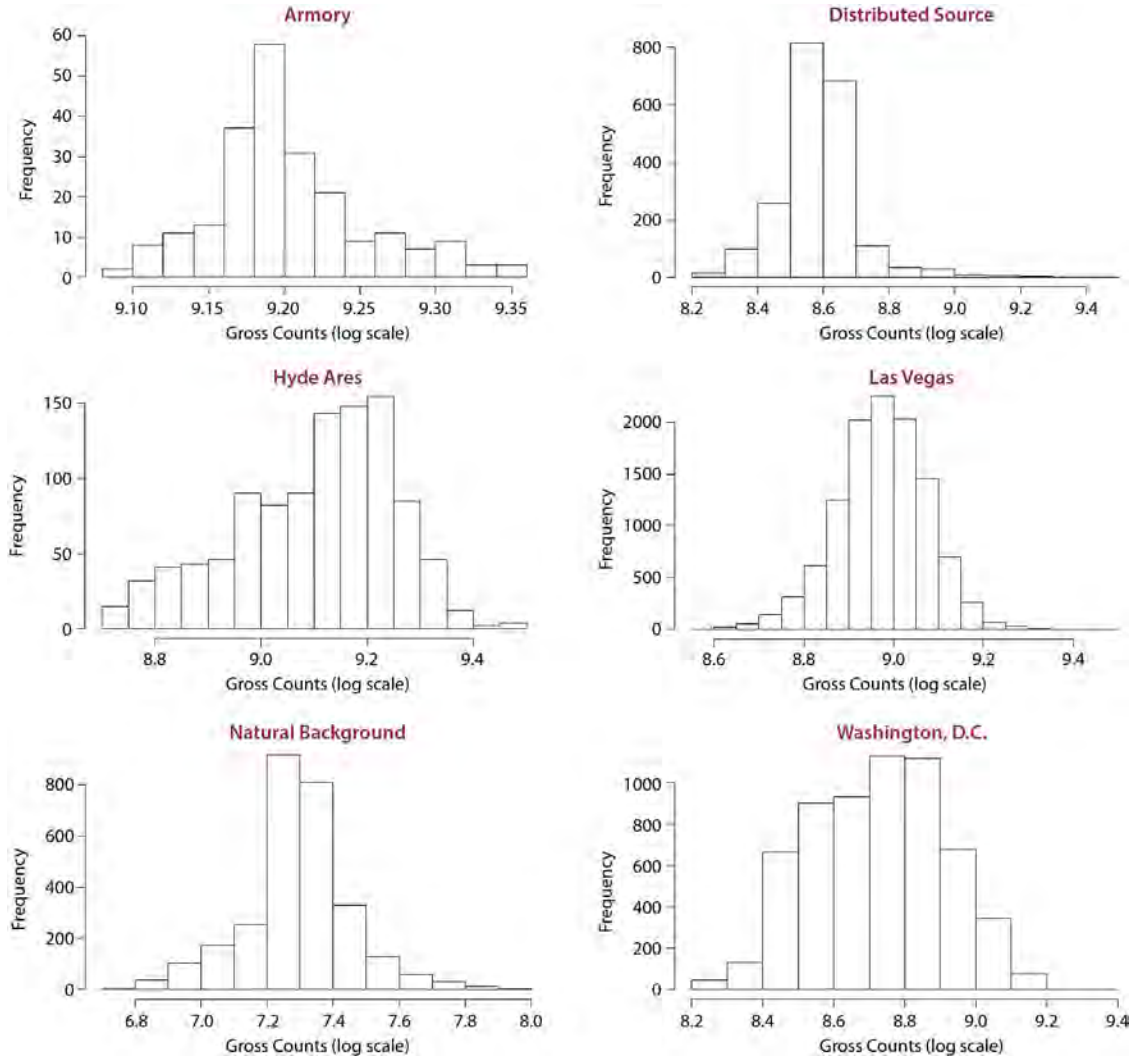

Figure 7. Histogram of log (gross counts) for six datasets

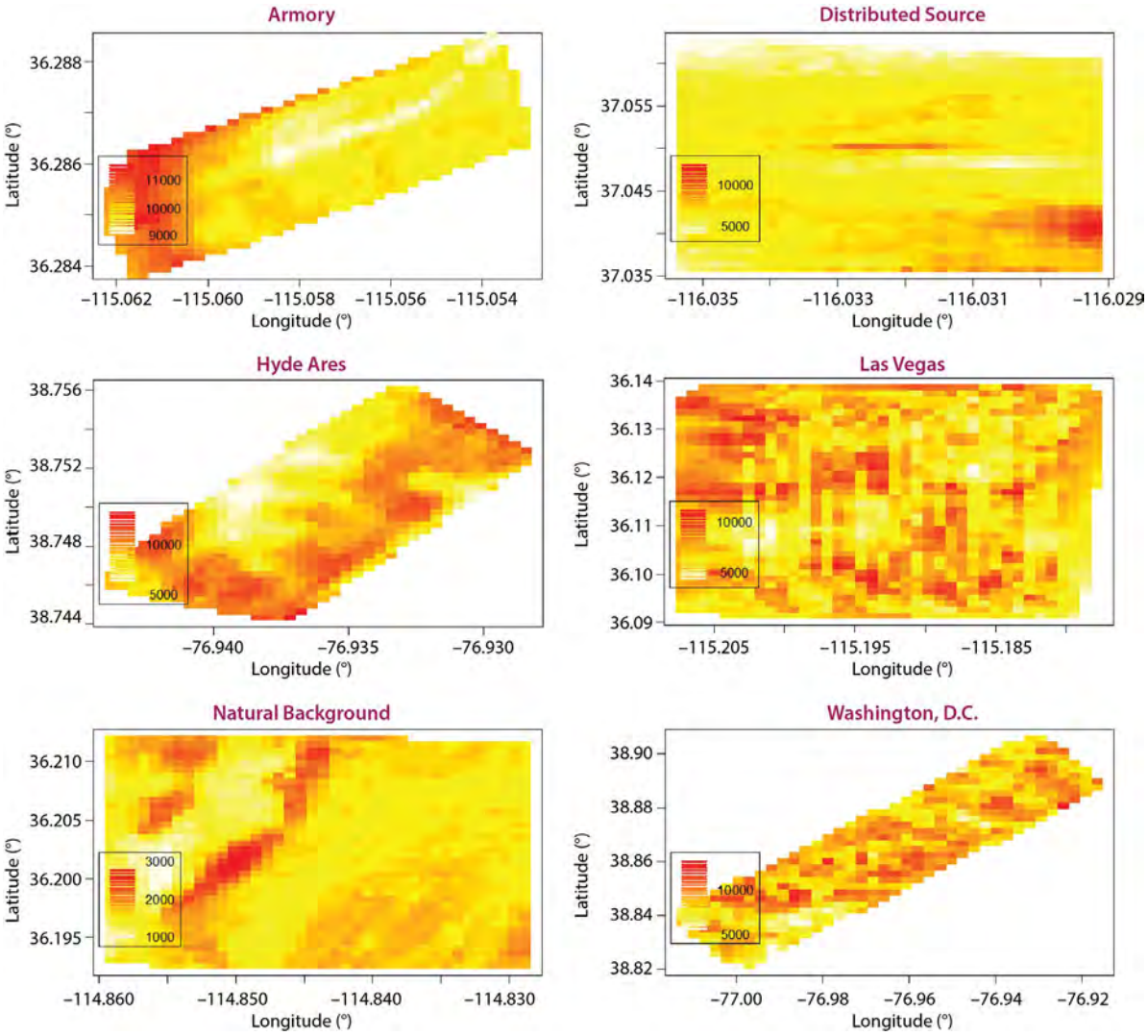

Figure 8. Linear interpolation plots of gross counts to visualize trend, or lack thereof, in the data

Proceeding forward, a log transform of distributed source or natural background data provides a fairly Gaussian distribution. Without a point source, it is less likely that trend needs to be removed prior to semivariance modeling and interpolation. For the five reasonable datasets presented, we found a universal parameter set for fitting an exponential model to the semivariance, indicating that there is great potential for speeding up preprocessing necessary for producing kriging estimates and that an expert in data manipulation is not needed. These results are for aerial data collected within a few hundred feet of the ground altitude and for which sufficient data was collected in perpendicular directions. In addition, these data are of natural background counts or deposition; they do not include data with point sources, which would likely require detrending. Extrapolation of this technique beyond these data characteristics should proceed with caution.

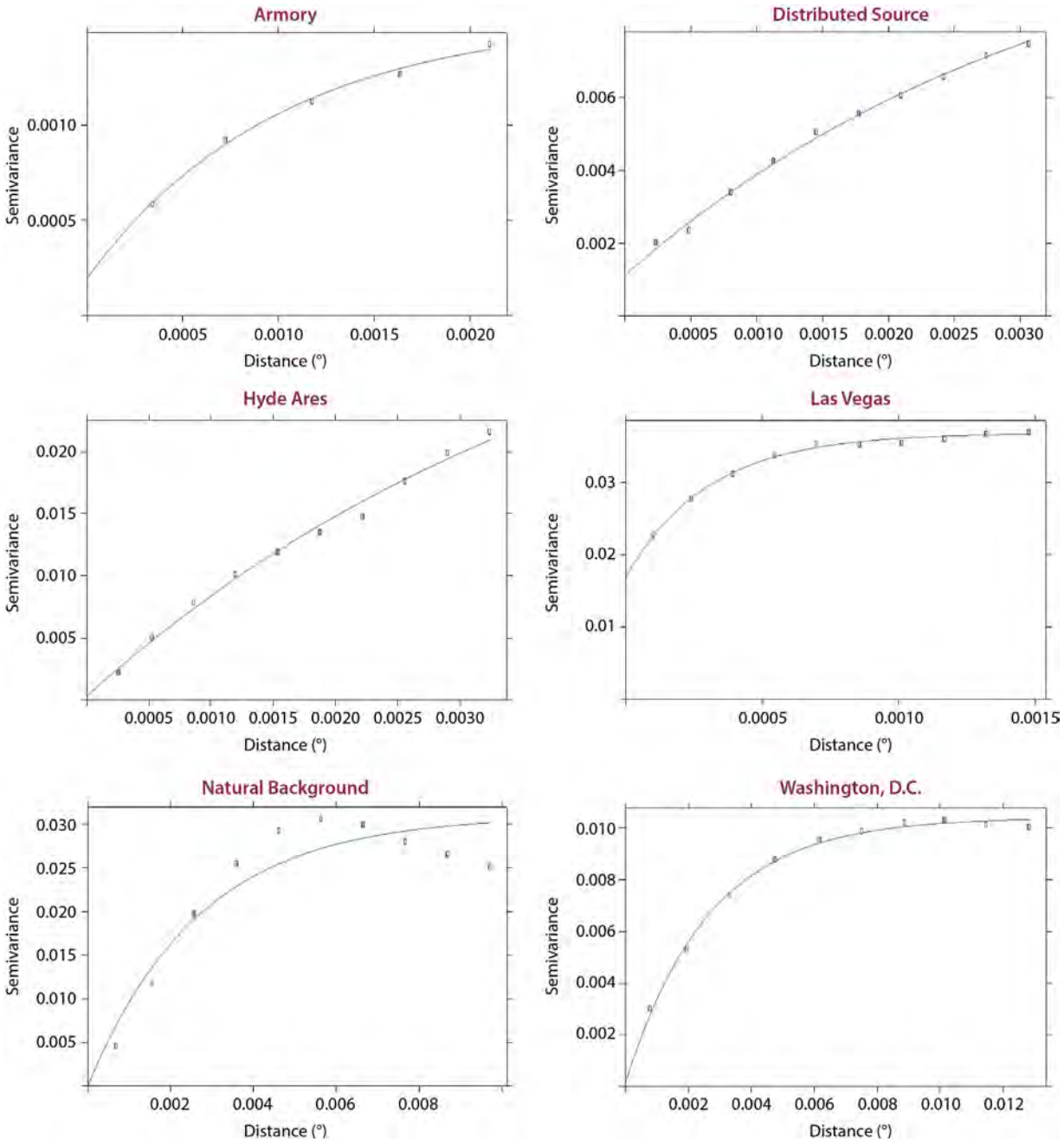

Figure 9. Calculated semivariance for each dataset (open circles) with a fitted exponential model (line)

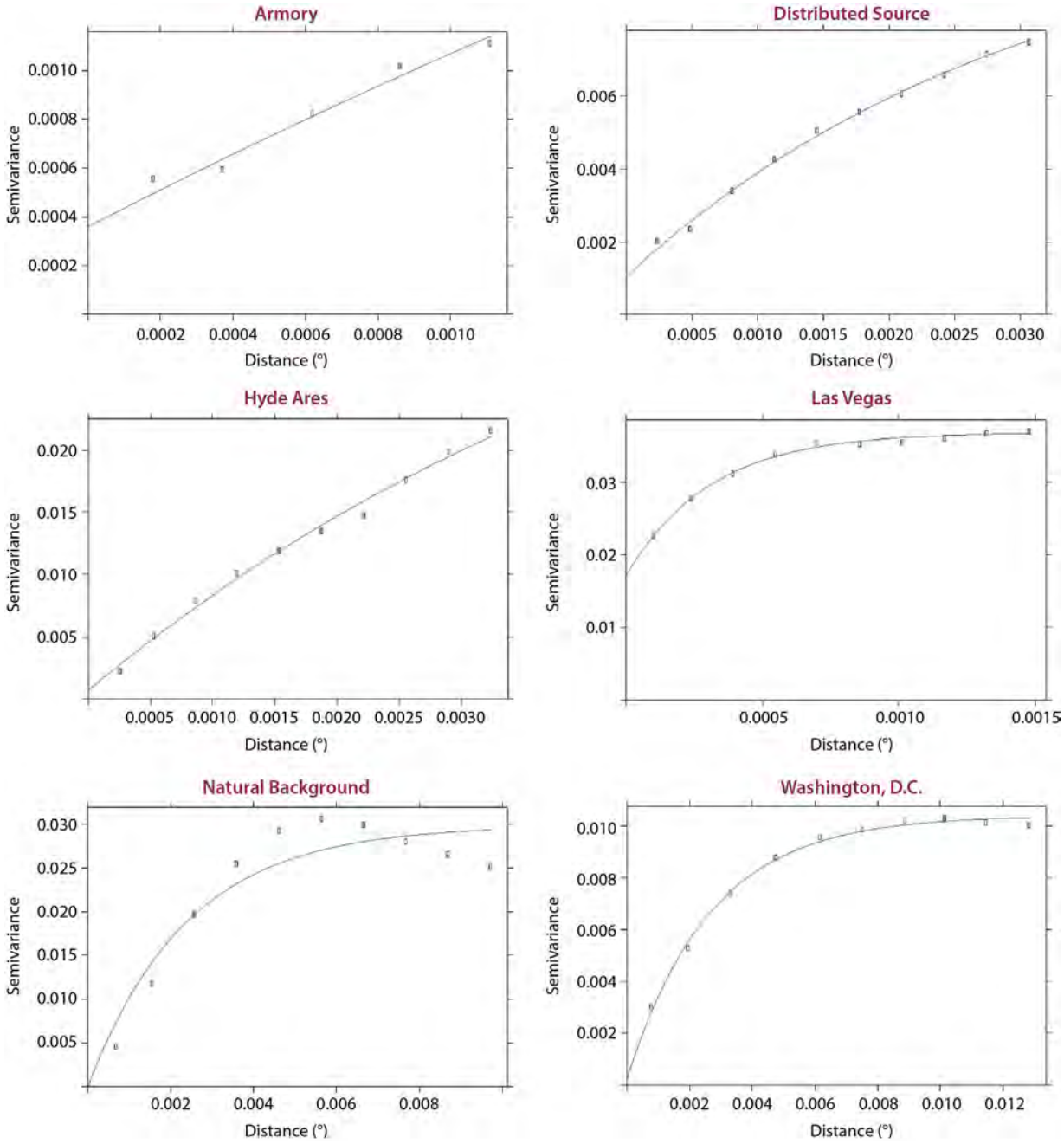

Figure 10. Calculated semivariance for each dataset (open circles) with a fitted exponential model (line), seeded with the universal parameter set ($\sigma^2 - a$) = 0.01, r = 0.003, and a = 0.0005

Conclusion

In the second year of this project, we have completed the studies of superior spectral anomaly detection as well as spatial analysis and uncertainty quantification. In each of these areas, we have worked to decrease noise and variance in the data collection and analysis processes.

References

Cressie, N., *Statistics for Spatial Data, Revised Edition*, John Wiley & Sons, Inc., New York, 1993.

Turk, J., J. D. Hague, M. Howard, A. Luttman, M. Mazur, T. McCullough, "Advanced modeling and uncertainty for the Aerial Measurement System," in *Site-Directed Research and Development*, FY 2014, National Security Technologies, LLC, Las Vegas, Nevada, 2015, 169–174.

Development of a Hybrid Magneto-Hydrodynamic/Particle-in-Cell Modeling Technique Applicable to High Plasma Densities and Long Timescales

SO-03-15 | Continued from FY 2014 (NLV-18-14) | Year 2 of 2

Nichelle Bennett,[1,a] Tim Meehan,[b] and Dale Welch[c]

The dense plasma focus (DPF) device is being developed by NSTec as a highly repeatable, high-fluence neutron source. An improved modeling capability is needed to increase our understanding of the device physics involved, improve hardware designs, and optimize pulsed power drivers. Because conventional particle-in-cell (PIC) and magneto-hydrodynamic (MHD) codes have limitations, we have developed a hybrid modeling capability in which the first phase of the DPF operation may be modeled using an MHD code and the second and third phases are modeled using PIC.

[1] bennetnl@nv.doe.gov, 505-845-9588
[a] New Mexico Operations–Sandia; [b] North Las Vegas; [c] Voss Scientific, LLC

Background

The dense plasma focus (DPF) device, which has long been considered a compact source for neutron production, is being developed by NSTec as a highly repeatable, high-fluence neutron source for future experiments (Mather 1964, 1965; Bernard 1977). While NSTec is a world leader in the development and operation of DPF devices (Goldin 2010, Hagen 2013), an improved modeling capability is needed to increase our understanding of the physics involved, improve hardware designs, and optimize pulsed power drivers.

The DPF device is a coaxial accelerator with a blunt anode termination filled with a low-density gas, typically deuterium. As the accelerator is pulsed, the gas is ionized and accelerated through the $\mathbf{J} \times \mathbf{B}$ force to the end of the anode (run-down phase), where it pinches (run-in and pinch phases) on axis. The challenges to simulating the DPF device are numerous: (1) the microsecond timescales required to ionize the gas and transport the plasma down the anode in the "run-down" phase, (2) the high plasma densities achieved when the plasma collapses in the "run-in" to the "pinch" phases, (3) the dominance of kinetic effects in beam-target fusion, and (4) the presence of instabilities. Magneto-hydrodynamic (MHD) codes have been used successfully to model the run-down phase where fluid approximations are an acceptable trade-off for enabling larger time steps and lower spatial resolution. However, MHD has not been able to reproduce the observed neutron yields, especially on the smaller DPF devices (Potter 1971; Kueny 2009; Welch 2009, 2010). Particle-in-cell (PIC) codes can treat particles kinetically, allowing for binary collisions and charge separation that are essential to reproducing the pinch physics but require spatial resolution near ~100 μm and correspondingly small time steps.

To reduce computation times, we have developed a hybrid modeling capability in which the run-down phase may be modeled using an MHD code, such as the 3-D high-energy-density plasma code ALEGRA (Robinson 2008). The plasma distributions, fields, and circuit parameters are recorded from the MHD simulation after run-down and transitioned to the fully 3-D

relativistic PIC code LSP, which is a large-scale plasma simulation code (Hughes 1999; Welch 2004, 2007). LSP then models the run-in phase, the pinch, and fusion processes.

Project

We have developed a hybrid modeling capability in which the DPF run-down phase may be modeled using ALEGRA, GORGON (a hybrid MHD-based code developed by Imperial College London), or other MHD code, and the run-in, pinch, and fusion processes may be modeled using LSP. The first year's effort (Meehan 2015) set up the ALEGRA simulations and the model for the Gemini DPF. In this second year, we created the software that enabled the hybrid technique. The FY 2015 effort included developing an algorithm in LSP to accept cell field values as initial conditions and developing a method to initialize the LSP circuit model from the final state of the ALEGRA circuit. To perform the transition from ALEGRA to LSP, we constructed an ALEGRA simulation mesh that is optimized for transitioning fields to a cylindrical PIC grid, mapped the ALEGRA fields to the LSP grid, and verified that the EXODUS file format used to record the ALEGRA fluid densities, nodal velocities, and internal energies can be read by the existing LSP interpreter routine. To increase the accuracy of the simulations, we modified the circuit model of the pulsed power driver to achieve the best match possible to measured currents. In addition, we calculated an electron-deuterium cross section table from Monte Carlo codes and an electron-copper cross section table from experimental data. Finally, we developed a transition criterion to determine when the MHD is no longer valid. Because the DPF timescales necessitate an implicit field solver, we used the two-step alternating direct implicit method (Welch 2004).

Hybrid Modeling Algorithms

In the MHD-LSP hybrid technique, the time-dependent field and circuit values are exported from the MHD mesh and interpolated onto the LSP grid and circuit. The values of (x,y,z), (E_i, E_j, E_k), and (B_i, B_j, B_k) are recorded for each MHD mesh position and combined into a single import file. The circuit parameters, current in each element and voltage at each node, are written to a separate file. A new module was written for LSP (***importFields.c***) that reads these import files and interpolates the data into the LSP grid and circuit. This is a significant advancement over previous efforts in that the field values are stored in the dynamic field variables of the grid cells instead of static variables. The static-variable kluge cannot generate an accurate result.

The file from which the fields and current densities are imported is called ***fieldInput.dat***. The data structure is assumed to be $x \times$ sizeOfY $\times$ sizeOfZ + $y \times$ sizeOfZ + z, where x, y, and z are the mesh positions and sizeOfY and sizeOfZ are the number of y and z positions, respectively.

In the ***importFields.c*** module, the interpolation routine loops over each cell in the LSP grid and identifies the MHD mesh field values that are nearest in $\pm x$, $\pm y$, and $\pm z$. This is two mesh positions in 1-D, four mesh positions in 2-D, and eight in 3-D. The mesh values are then weighted by their distance from the cell field position and averaged. The 1-D representation of the weighting is

$$E_x = \frac{x_2 - x}{x_2 - x_1} E_{x1} + \frac{x - x_1}{x_2 - x_1} E_{x2}, \quad \textbf{(1)}$$

where E_{x1} and E_{x2} are the fields at mesh positions (x_1) behind and (x_2) in front of the grid field position x. The implementation in ***importFields.c*** is 3-D. The fields are stored in different physical locations inside each cell, as shown in Figure 1, where the subscript h indicates the half-cell positions. After the fields are imported to the grid, boundary conditions are enforced.

The remaining error that is difficult to correct is the initialization of guard cells in the LSP grid. These cells exist outside the boundary of the simulation space and, therefore, their field values are typically inaccessible as output, even in PIC codes. Our solution is to use the nearest grid values.

Of the two available circuit models in LSP, we use the one based on the BERTHA circuit (Hinshelwood 1983),

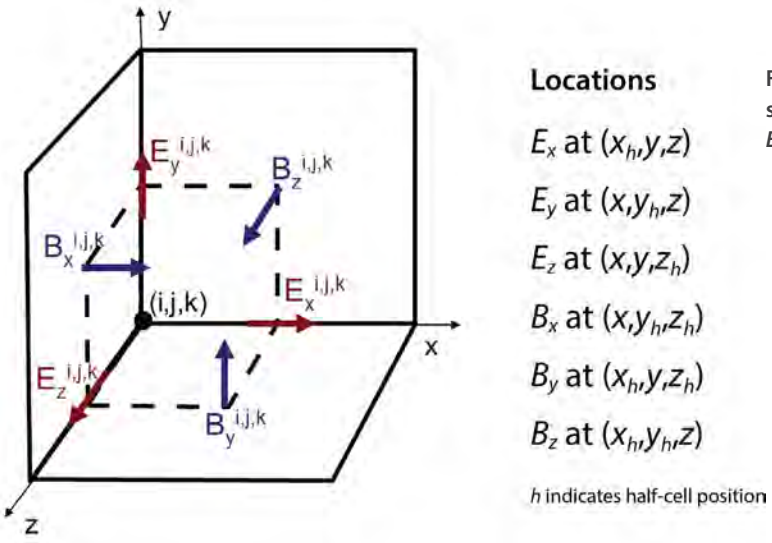

Figure 1. Yee grid diagram of a simulation cell showing staggered *E* and *B* field positions

which follows the telegraphers' equation treatment. As implemented in LSP, the length of the segments between the circuit nodes is specified in nanoseconds, and each segment is then divided into n intervals based on segment length/time step. A static impedance is assumed for the segment. Forward-going and backward-going voltages in each interval are denoted as $V0[\mathrm{i}]$ and $V1[\mathrm{i}]$, respectively, and all of these segment intervals must be initialized in the hybrid technique.

The circuit import routine reads the forward-going and backward-going voltages and currents at each node in the circuit, from the file ***circuitInput.dat***, and calculates the segment voltages via

$$\begin{aligned} V1[0] &= \frac{1}{2}(V_{out} - I_{out}Z) \\ V1[1] &= \frac{1}{2}(V_{in} - I_{in}Z) \\ V0[0] &= \frac{1}{2}(V_{in} + I_{in}Z) \\ V0[1] &= \frac{1}{2}(V_{out} + I_{out}Z). \end{aligned} \quad (2)$$

Criterion for Transitioning from MHD to PIC

The criterion for when particles need to transition from a quasi-neutral to a fluid or kinetic treatment is based on the instantaneous maximum local charge separation of the plasma. Clearly if the plasma is becoming non-neutral, then the assumption of quasi-neutrality no longer holds and the ions and electron particles must evolve separately. If the final particles are kinetic, this transition requires that a thermal Maxwellian distribution be sampled, necessitating more kinetic particles to maintain energy conservation.

In sample simulations, the transition from quasi-neutral particles to kinetic occurs when the transition criterion of 100 μC/cc is reached. After the transition to inertial fluid, and if Poisson correction is enabled, the code slowly corrects for the maximum residue density, where the residue is defined as the difference $\nabla \cdot \mathrm{E} - \rho/\varepsilon$, or the violation of Gauss' Law.

Key quantities to check for simulation accuracy through the migration from quasi-neutral to kinetic particle treatments are the continuity of total field energy, total particle energy, but particularly the electron energy. Too few electron pairs will result in a rapid energy loss. Too late a migration when the residue is very large can result in energy growth.

Test Results

To test the import technique, a DPF-like simulation was performed in LSP in 2-D cylindrical coordinates. The geometry was that of the upstream portion of the DPF, including a Pyrex insulator sleeve, as shown in Figure 2. The original simulation was run to 6 ns, with

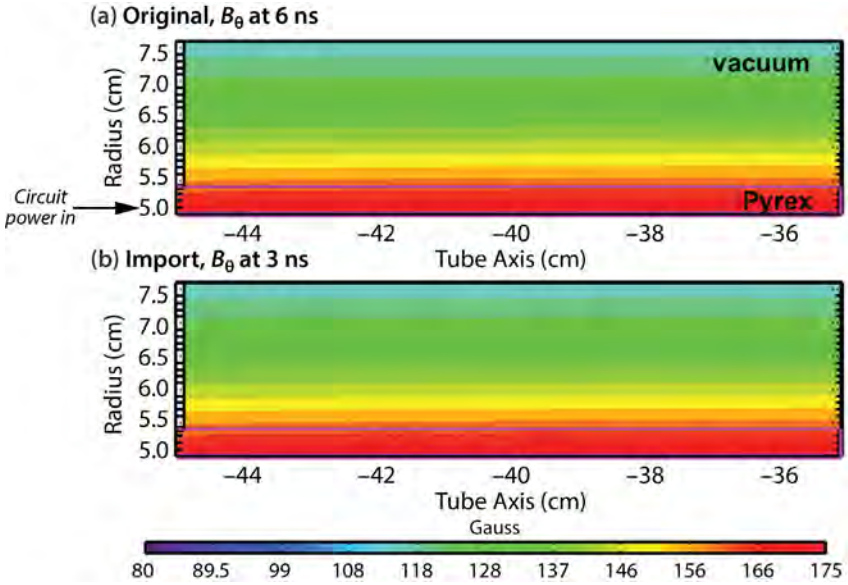

Figure 2. Comparison of B_θ from (a) the original 6 ns simulation and (b) the imported 3 ns simulation. The imported 3 ns simulation was initialized using the values of the original 6 ns simulation dumped midway through the run. Power is injected at the left radial boundary through the Pyrex, between 5 and 5.4 cm.

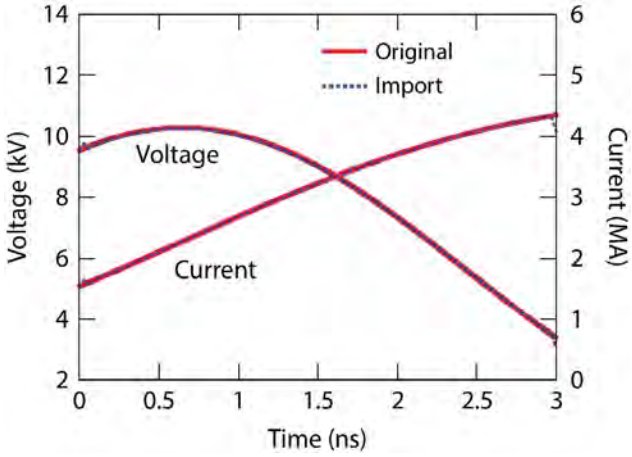

Figure 3. Comparison of circuit parameters for the simulations in Figure 2

the circuit parameters, fields, and current densities recorded at 3 ns. The import simulation was initialized using those fields, currents, and circuit parameters and run for 3 ns, such that the final field contours for the two simulations should be identical. We note that the imported fields were not on the same grid as the original simulation. The B_θ contours recorded at the final step of both simulations are compared in Figure 2. We note that perfect agreement was achieved when rapid variation in the guard-cell fields could be avoided, and that the agreement in Figure 2 suffers near the power-injection boundary. The currents and voltage of the original and import simulation are compared in Figure 3.

The second test incorporated particles. To reduce computation time, the original simulation was run to 2 ns, with the circuit parameters, fields, current densities, particle densities, and particle velocities recorded at 1 ns. The import simulation was then run for ~1 ns. The particle temperatures are compared in Figure 4.

Modeling Results

As part of this effort, new electron-copper cross section tables for impact ionization, energy loss, and momentum transfer frequency were compiled from published experimental results. The electron-deuterium (e^-/D) tables were provided by Voss Scientific. The two are compared in Figure 5.

Because copper ionizes much more rapidly than deuterium (Figure 5), we explored the impact of copper contaminants on the gas-breakdown phase of the DPF. Because these simulations are necessarily kinetic, we used LSP instead of the hybrid technique and limited the simulation space to the region around the insulator sleeve, as illustrated in Figure 6. The downstream boundary is a symmetry boundary since an open outlet causes numerical instabilities in the field solution. Once the plasma is pushed to the symmetry boundary (~1.5 μs), the simulation has reached the limits of its validity. The grid resolution is Δr = 100 μm and Δz = 200 μm, and the physics models used are impact ionization of deuterium and copper, binary collisions,

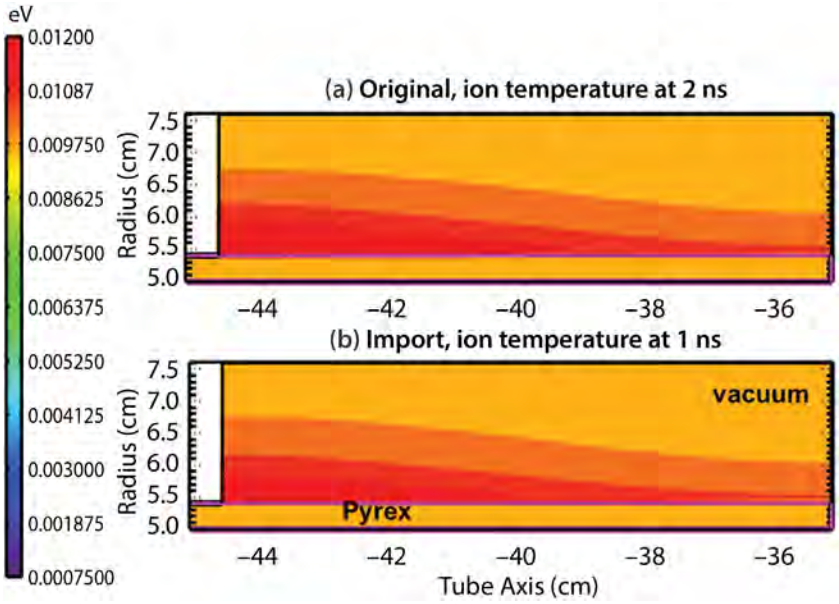

Figure 4. Comparison of ion temperature for (a) original and (b) imported simulations

and Child-Langmuir (CL) electron emission from the cathode surface when the local electric field stress exceeds 60 kV/cm. The power is injected into the simulation using a BERTHA circuit (Hinshelwood 1983) at the insulator boundary (z = –45 cm). The circuit parameters are C = 432 mF, L = 50 nH, R = 0.0178 Ω, and V = 37.5 kV.

The gas initialization for all of the kinetic simulations is neutral deuterium at 2.4×10^{17} cm^{-3} density (3.8 Torr). In the baseline simulation, a seed e^-/D^+ plasma of 10^{11} cm^{-3} density is used to initiate avalanche ionization (supplementing the CL emission). In the copper contaminant test simulation, a seed e^-/D^+ plasma of 10^{11} cm^{-3} density is again used to initiate avalanche ionization, but 10^{15} cm^{-3} of the neutral deuterium is replaced by neutral copper. A third simulation, in which the seed plasma density is increased to 10^{13} cm^{-3}, was also completed in this series. This is a test of simulation sensitivity and a precursor to tests of a pre-ionization scheme.

Figure 6 shows the density contours of the neutral deuterium and the electrons at 1.1 µs into the pulse. Of note are the long time to achieve gas-breakdown and conduction and the relatively wide (4–5 cm) plasma sheath that forms. These are in contrast to an MHD or MHD-like simulation in which the gas is assumed to be fully ionized prior to pulse injection.

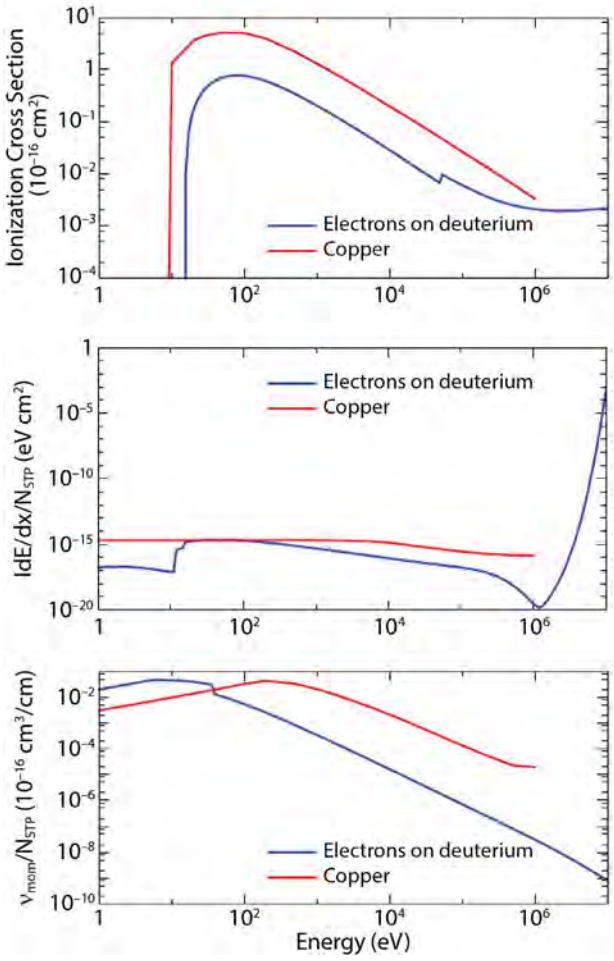

Figure 5. Ionization, energy loss, and momentum transfer frequency cross sections for electrons on deuterium and copper as functions of electron energy; copper ionizes much more rapidly than does deuterium

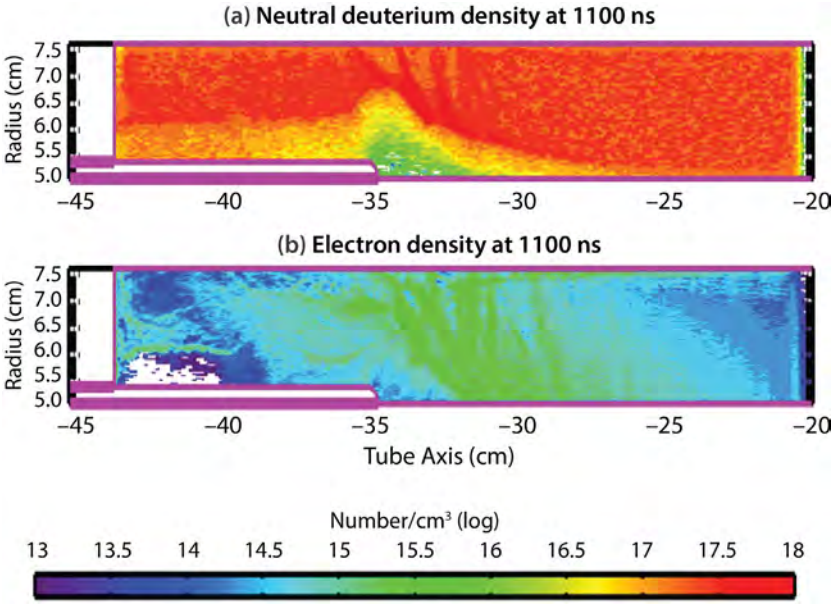

Figure 6. Density contours shown at 1100 ns into a kinetic gas-breakdown simulation of a 2 MJ DPF. (a) Neutral deuterium density and (b) electron density are plotted on a log scale. Only the final 25 cm of the anode and cathode are modeled. The anode has a 5.08 cm outer radius, and the cathode has a 7.62 cm inner radius. Power is injected along a Pyrex sleeve, which covers $-45 < z < -35$ and $5.08 < r < 5.40$ cm.

An example of an MHD-like result is shown in a quasi-neutral simulation in which the electron density at t = 0 is 2.4×10^{17} cm^{-3}. The geometry is illustrated in Figure 7. (The speed of this solution enables the full device to be modeled in 2-D.) The density contour plotted in Figure 7 is a snapshot at 1.1 μs into the pulse, as in Figure 6. When the gas is fully ionized, the conductivity is high and the current follows a path from the anode at the end of the insulator, upstream through the plasma above the insulator, to the cathode back (mounting) plate. By contrast, in the gas-breakdown simulations, the resistivity is high initially and the conductivity increases as the plasma density increases. The current density is distributed across the radial gap and does not follow the insulator surface. The plasma is created in filaments, which is characteristic of avalanche ionization.

The gas-breakdown simulations have shown that the time to breakdown is ~1 μs for the 4" anode tube geometry at 37.5 kV. The gas ionizes primarily above the dielectric sleeve, and is concentrated near the end of the sleeve, such that there is residual neutral gas upstream. A longer sleeve results in faster run-down and more material pushed radially outward. The peak density at the end of the sleeve extends for ~3–5 cm. The breakdown time, currents, and plasma velocity compare well with measured currents and velocities. Contaminants at the 2% level do not impact the measured current.

Because the gas-breakdown studies were conducted inside a limited volume, the quasi-neutral studies, which covered the entire volume, have been modified to hold the plasma particles fixed for 1 μs. The simulation geometries are the 4" OD anode, as shown in Figure 7, and the 6" OD anode, as shown in Figure 8.

Simulations of the run-down phase showed the potential for current loss across the transmission line, especially with a solid cathode, and that the flat anode has a slightly longer run-down time. The longer dielectric sleeves demonstrated faster run-down times with more plasma accelerated outside the cathode bars. Simulations agreed with the experimental observation that, at a given charge, higher pressure slows the run-down velocity so the pinch may occur closer to peak power. An observation that requires further testing is that partial ionization (decreased q/m) did not impact run-down time.

Agreement with current magnitude will improve as we continue to develop the circuit model of the pulsed power driver.

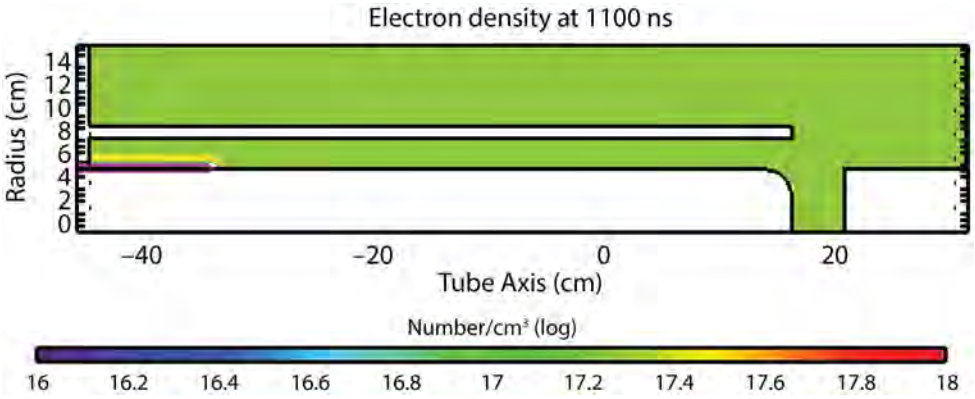

Figure 7. Electron density contour at 1100 ns into a quasi-neutral simulation of a 2 MJ DPF with a 4″ OD anode. The log scale lower limit is 10^{16} cm^{-3}. The full device is modeled in 2-D.

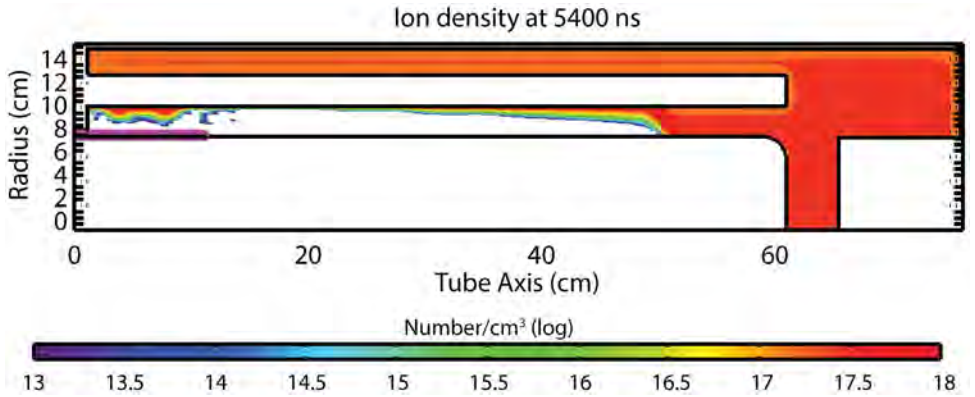

Figure 8. Ion density contour at 5400 ns into a quasi-neutral simulation of a 2 MJ DPF with a 6″ OD anode

Conclusion

This SDRD project has enabled NSTec to grow a robust modeling effort. The new hybrid tool is collaborative. The ALEGRA code is less useful for this purpose because the electric fields are no longer accessible as field dumps; however, importing from GORGON or other codes may be possible. The simulations have provided significant insight into the breakdown and run-down stages of operation as well as DPF electrical characteristics.

Acknowledgment

We would like to thank Chris Mostrom of Voss Scientific for making the latest version of LSP available.

References

Bernard, A., P. Cloth, H. Conrads, A. Coudeville, G. Gourlan, A. Jolas, Ch. Maisonnier, J. P. Rager, "The dense plasma focus—A high intensity neutron source," *Nucl. Instrum. Methods* **145**, 1 (1977) 191–218.

Goldin, F. J., B. T. Meehan, E. C. Hagen, P. R. Wilkins, "Time-resolved spectra of dense plasma focus using spectrometer, streak camera, and CCD combination," *Rev. Sci. Instrum.* **81**, 10 (2010) 10E531.

Hagen, E. C., D. Lowe, R. O'Brien, S. Molnar, B. T. Meehan, "PPPS-2013: Observed multi-decade DD and DT Z-pinch fusion rate scaling in 5 dense plasma focus fusion machines," *Plasma Science (ICOPS)* (2013).

Hinshelwood, D. D., "BERTHA – A versatile transmission line and circuit code," NRL Memorandum Report 5185, Naval Research Laboratory, Washington, D.C., 1983, http://www.dtic.mil/dtic/tr/fulltext/u2/a135024.pdf, accessed October 20, 2015.

Hughes, T. P., S. S. Yu, R. E. Clark, "Three-dimensional calculations for a 4 kA, 3.5 MV, 2 microsecond injector with asymmetric power feed," *Phys. Rev. ST Accel. Beams* **2** (1999) 110401-1–110401-6.

Kueny, C. S., D. G. Flicker, D. V. Rose, "ALEGRA-HEDP simulations of the dense plasma focus," SAND2009-6373, Sandia National Laboratories, Albuquerque, New Mexico, 2009, http://prod.sandia.gov/techlib/access-control.cgi/2009/096373.pdf, accessed October 20, 2015.

Mather, J. W., "Investigation of the high-energy acceleration mode in the coaxial gun," *Phys. Fluids* **7**, 11 (1964) S28–S34.

Mather, J. W., "Formation of a high-density deuterium plasma focus," *Phys. Fluids* **8**, 2 (1965) 366–377.

Meehan, T., M. Berninger, "Optimizing DPF neutron output using particle-in-cell and MHD models," in *Site-Directed Research and Development*, FY 2014, National Security Technologies, Las Vegas, Nevada, 2015, 203–209.

Potter, D. E., "Numerical studies of the plasma focus," *Phys. Fluids* **14**, 9 (1971) 1911–1924.

Robinson, A. C., et al., "ALEGRA: An arbitrary Lagrangian-Eulerian multimaterial multiphysics code," *Proc. 46th AIAA Aero. Sci. Meeting* 2008, http://www.cs.sandia.gov/ALEGRA/Publications/ALEGRA_Overview_AIAA2008.pdf, accessed October 20, 2015.

Welch, D. R., D. V. Rose, R. E. Clark, T. C. Genoni, T. P. Hughes, "Implementation of a non-iterative implicit electromagnetic field solver for dense plasma simulation," *Computer Physics Communication* **164**, 1–3 (2004) 183–188.

Welch, D. R., T. C. Genoni, R. E. Clark, D. V. Rose, "Adaptive particle management in a particle-in-cell code," *J. Comp. Phys.* **227**, 1 (2007) 143–155.

Welch, D. R., D. V. Rose, R. E. Clark, C. B. Mostrom, W. A. Stygar, R. J. Leeper, "Fully kinetic particle-in-cell simulations of a deuterium gas puff z pinch," *Phys. Rev. Lett.* **103** (2009) 255002.

Welch, D. R., D. V. Rose, C. Thoma, R. E. Clark, C. B. Mostrom, W. A. Stygar, R. J. Leeper, "Kinetic simulation of thermonuclear-neutron production by a 10^7-A deuterium Z pinch," *Phys. Plasmas* **17** (2010) 072702.

Techniques for Access to Large and Dynamic Datasets from Mobile Devices over 4G Networks

RSLN-25-15 | Year 1 of 1

James Essex,[1,a] Michael Reed,[a] and Calder Lane[a]

The goal of this research is to develop a framework for access to large datasets from smart mobile devices with dynamic network bandwidths. Using an efficient bidirectional protocol, we developed a client-server software architecture and implemented it in the Microsoft Azure cloud. The methods of interest used to test and benchmark our framework is from previous work by Reed (2010a, 2010b). Reed developed a radiation transport code and computational tool for computing minimum detectable activity (MDA) and maximum detectable distance metrics for common detection systems in real-world configurations. The research presented here expands on that work to enable the near real-time, dynamic, cloud-based calculation of MDA values for the area around actual sensor observations. The data used in this project replicate actual routes, detectors, and velocities collected by deployed teams, rendered as a geospatially referenced raster dataset.

[1] essexjj@nv.doe.gov, 702-295-8714
[a] Remote Sensing Laboratory–Nellis

Background

Robust implementations exist for transmitting data to central repositories for aggregated analysis, but making disparate datasets available in near real time to the originating node is severely limited or not attempted. This means that field operators cannot efficiently fuse newly acquired data with data previously acquired or data from other operators in real time. The primary limitations to this capability have always been network bandwidth, local storage capacities, and the computing resources of mobile devices. This research is directly applicable to many real-world scenarios and scientific disciplines, including environmental data collection, hazard characterization, and radiological emergency response.

Numerous concepts, techniques, and prototypes exist in the literature, and many are being explored for access to large datasets in the domains of social media and geoinformatics. However, little engineering design work and implementation have been done. Developing and benchmarking intelligent services for server-side data access by mobile devices using the technologies employed here will help define limitations and manage expectations for future efforts seeking to increase the complexity of near real-time analysis.

Project

Architecture

The technical approach to this work relies on a new computation based on an operational transport code (Reed 2010b), an efficient method of transmitting data to the client, and an elastic cloud-hosted server implementation. The type of architecture we envisioned necessitated use of a dynamic computation that could be controlled for both time to compute and the amount of data transmitted.

The implemented architecture also required that we employ a new software protocol that was more efficient than those currently employed. Until recently, the Remote Sensing Laboratory (RSL) used WebServices as the communication standard for transmitting all data to the server from mobile clients in the field. This protocol, while secure and easy to work with, is not bidirectional and comes with a high overhead cost. A new protocol, Websockets [IETF RFC 6455] (Fette 2011), was chosen for this project as a low-overhead, bidirectional, full-duplex messaging alternative to WebServices that, while dependent on multiple variables, is roughly 10x more efficient than WebServices over the domains of interest.

Due to the scalable nature of both the computation and the server transmission bandwidth requirement, an elastic cloud-based server implementation was developed. The cloud-based environment was established and enabled benchmarking of test data that was collected from real platforms.

The architecture consists of three parts (Figure 1). The setup encapsulates the parameters required for calculation of a sensitivity matrix for each isotope and detector combination. The setup component of the architecture is typically performed once per computational model depending on operational requirements. The server uses the sensitivity matrix and an existing repository of client-transmitted sensor observations to calculate a set of geospatially referenced raster datasets of optimal size. The client initiates the server calculation and establishes a long-lived bidirectional WebSocket-based communication channel when making the initial request of the server. The client request includes the detection system, isotope of interest, and bandwidth availability, while the position of the client is updated at regular intervals that trigger new server calculations.

Methods

In order to evaluate our new data aggregation and dissemination technologies, we chose to compute high-fidelity, dynamic, multi-sensor detectability maps. In general, the detectability metrics for an operational scenario are a function of the (a) detection system employed, (b) proximity of source and detector, (c) system velocity, (d) radiation source of interest, (e) algorithm employed, and (f) local

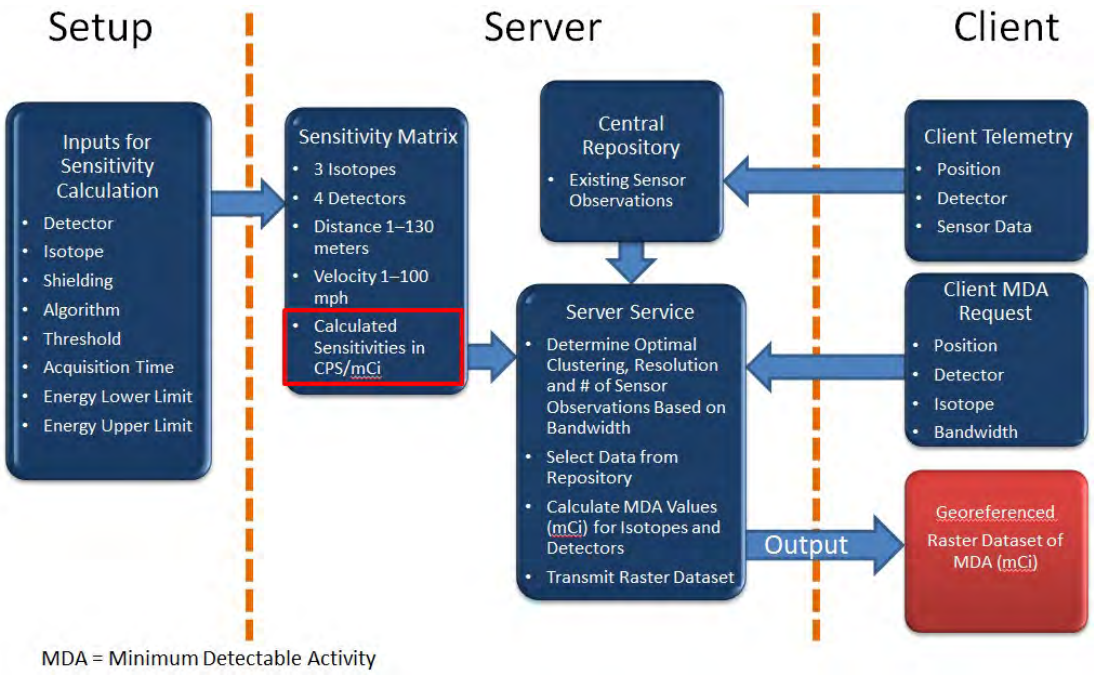

Figure 1. The architecture is composed of a setup, server, and client

background response. For basic scenarios of interest, this problem is separable, whereby source sensitivities may be precomputed for a particular detector/isotope combination. Then, real-time data in the form of tracks, velocities, and local background may be used in conjunction with source sensitivities to estimate the detection ranges associated with data as it is acquired. A simple superposition principle may then be used to resolve the overlap of sensor tracks resulting from systems covering the same area. The final result is a gridded detectability map representing the minimum detectable activity (MDA) present in 2-D space, given the operational parameters employed and the local conditions. This computation is ideal for this test because the underlying rasters can be relatively large (hundreds of megabytes typically), and total computational time required to maintain real-time response easily requires distributed computing.

The generation of a near real-time, dynamic, cloud-based raster dataset is initiated by a client request. The client request includes the position, detector, isotope, and a dynamically generated bandwidth. The bandwidth is based on a client request for a 100 KB data packet that is executed at regular intervals. The timing difference between the request and server transmission to the client is directly proportional to the downlink bandwidth. The position, detector, and isotope are selected by the operator when initializing the calculation. The server then responds with a positional update frequency based on the optimum calculation parameters.

The server starts generating the raster dataset by pulling data from the existing client telemetry repository for the area of interest (AOI) around the current position. The effective area covered by the AOI is determined by querying the database for the number of observations and optimizing the AOI round-trip time. Round-trip time is determined by the "calculation time," which is static and composed of AOI, number of observations, and resolution of the raster dataset, plus the dynamic "time to transmit." Figures 2–4 show results of tests run on individual parameters of the model, including detector, isotope, and resolution. These data were used for rough validation of the computation.

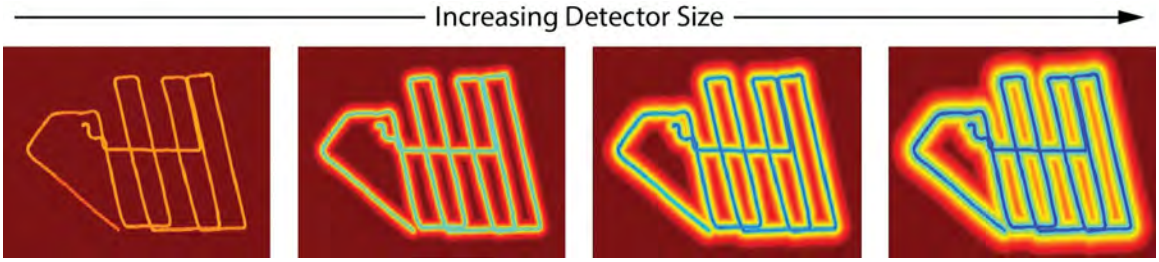

Figure 2. Individual parameters for the MDA calculation were tested to validate the calculation. The four runs rendered in these images vary only the detector size. As expected, there is a clear correlation between detector size and MDA values.

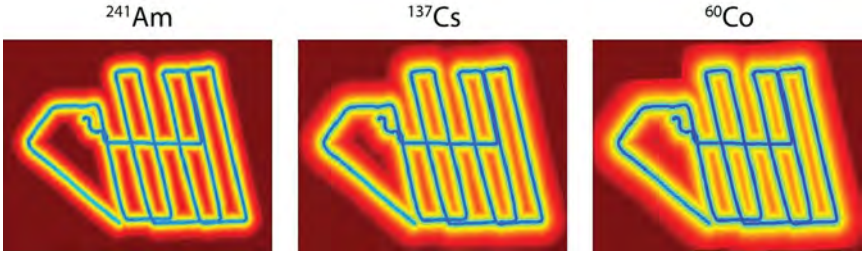

Figure 3. The three runs rendered in these images vary only the isotope of interest. The differences in MDA values represent attenuation differences in air due to photon energy and isotope photon yield.

Figure 4. The three runs rendered in these images vary only the resolution in meters of each raster grid cell. Note the increasing fidelity at increasing computational cost and convergence between 2.5 and 5 meters.

Benchmarking

The benchmarking effort consisted of more than 50 MDA server calculations from a single test dataset to determine the fundamental relationships that govern the architecture. The two main variables of interest are the duration of the server-to-client transmission (transmit time) and the duration required for the server calculation. The objective was to optimize the server calculation by controlling the resolution of the raster and the number of observations such that the total of the two did not exceed common operational requirements.

Figure 5 shows the relationship between the server-to-client transmit time and the resolution of the raster dataset, which is a function of the size of the dataset. Because average server-to-client bandwidth varies widely depending on technology, three commonly leveraged commercial communication technologies are plotted. Figure 6 shows the relationship between the number of sensor observations used in the MDA calculation and both the total round-trip time (calculation + transmit time) and the calculation time.

From the data shown in Figures 5 and 6, a preferred resolution and conservative estimate for sensor velocity and bandwidth was used to determine that a 60-second update interval would be the optimal update frequency. This value allows the server to perform additional calculations as the sensor platform acquires data inside the current AOI and allows the sensor to receive updated calculations as the AOI changes. Ultimately, this indicates that a raster dataset based on approximately 2500 sensor observations could be continuously created and transmitted to the client in under 60 seconds using a 4G network.

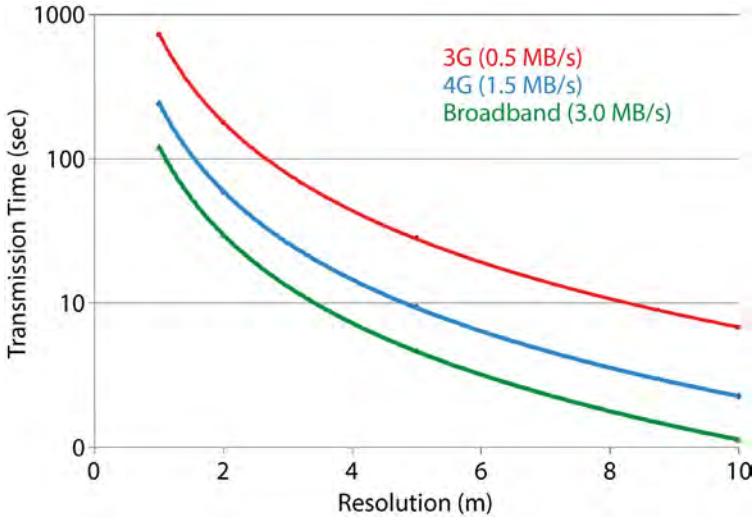

Figure 5. The relationship between time to transmit data and resolution of the calculated raster dataset compiled from 9834 sensor observations

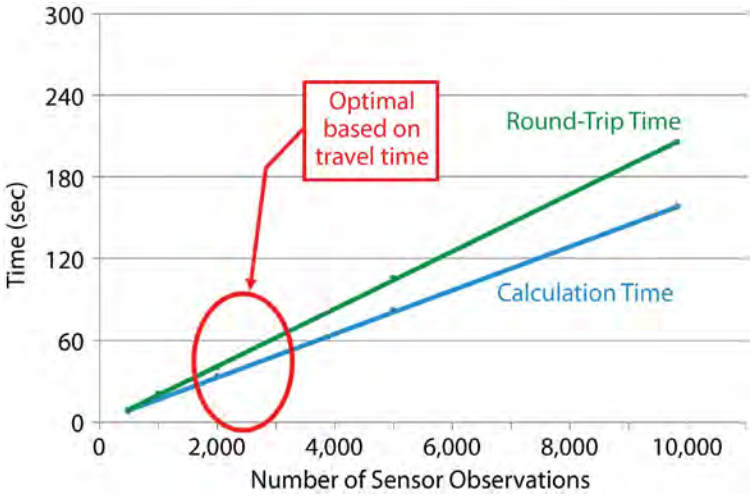

Figure 6. The optimal number of sensor observations per calculation for round-trip and calculation times; the times are based on calculations using a 2.5-meter resolution

Conclusion

This work focused on how complex scientific datasets can be used to effectively visualize data at multiple spatial and temporal resolutions. This effort is relevant to existing requirements in many NNSA, Defense Threat Reduction Agency, Domestic Nuclear Detection Office, and local law enforcement mission spaces, and is applicable to data collection efforts during special events and wide-area or targeted searches. Specifically, all federal and multiple local agencies that perform sensor-based search have an untapped resource—previously collected data. Our study has developed a platform for moving the concepts and theory of big data into real-world applications.

Future research areas include architectural and computational improvements. Improvements that will decrease compute time include (a) decreasing sensor observations based on clustering, (b) adding temporal limitations to the data included in computations, and (c) threading the computation based on detection system. Decreasing computation time is one primary objective, but another strategy would be limiting the bandwidth utilization by only transmitting "pixel" data that has changed recently. Finally, as both cheap computational resources and network bandwidths improve over time, adding the ability to calculate MDA values based on spectral alarming algorithms will enhance our ability to understand detectability in operational settings.

Acknowledgments

We would like to thank the NSTec Cyber Security team, led by Ken Lehman and Chad Lewis, and members of the RSL Software Technologies team, Aaron Morrisett, Dayne West, and Paul Ainsworth, for their contributions to this work.

References

Fette, I., A. Melnikov, "Protocol Overview," in *RFC 6455 The WebSocket Protocol*, Internet Engineering Task Force, December 2011, https://tools.ietf.org/html/rfc6455#section-1.2, accessed October 16, 2015.

Reed, M. S., "Aerial MDA Quantification Tool," in *NA-42 Technical Integration Program Final Report*, National Security Technologies, LLC, Las Vegas, Nevada, 2010a.

Reed, M. S., "Interpreting radiological measurements with inverse transport," in *Nevada Test Site–Directed Research and Development*, FY 2009, National Security Technologies, LLC, Las Vegas, Nevada, 2010b, 165–172.

This page left blank intentionally

Quantifying Uncertainties through Advanced Theoretical Analysis for Image and Signal Reconstruction

NLV-02-15 | Continuing in FY 2016 | Year 1 of 2

Aaron Luttman,[1,a] Marylesa Howard,[a] Kevin Joyce,[a,b] Jesse Adams,[a,c] and Johnathan Bardsley[b]

Linear inverse problems pervade experimental diagnostics analysis—from Radon inversion in neutron time-of-flight studies to deconvolution of radiation detector signals to Abel inversion in radiography—and the primary theoretical shortcoming to all computational approaches for solving such ill-posed problems is the introduction of regularization or priors, imposing potentially incorrect physical assumptions on the computed solution. To quantify uncertainties due to error in prior assumptions, Bayesian reconstruction models with Markov Chain Monte Carlo methods have been developed that allow the data to drive the regularization, giving visually excellent signal reconstructions. The two primary drawbacks to this approach are that it requires the solution of large-scale linear systems and that it introduces additional tuning parameters. In this project we have designed numerical schemes for solving the very large linear systems associated with some of the inverse problems arising in diagnostics analysis and an approach to characterizing the sensitivity of these methods to the choices of tuning parameters. We have also extended this theory to the problem of computing the point spread function (impulse response) of an x-ray imaging system from edge imagery. Results are presented here as applied to the Cygnus pulsed power radiographic imaging source from the NNSS. In FY 2016, our goal will be to combine the components developed in FY 2015 into a single set of computational tools for solving linear inverse problems in a statistical framework with uncertainty quantification.

[1] luttmaab@nv.doe.gov, 702-295-0303
[a] North Las Vegas; [b] University of Montana, Missoula; [c] University of Arizona

Background

It is rare in large-scale experimentation that one has the opportunity to directly measure the quantities that are of interest, so instead one is forced to make indirect measurements. Calling a measurement indirect is a euphemism for measuring a quantity other than that of interest and inferring the desired information from that measurement. For example, in photonic Doppler velocimetry, the goal is to compute the velocity of a moving surface, but, because the velocity is not directly measurable, one measures a voltage induced by the Doppler shift of light reflected off the surface. In x-ray imaging we often wish to measure object densities, the imaging system impulse response, or the shape of the x-ray source, and these are the three target problems addressed in this work. In all three of these cases, we image an object and must compute the quantity of interest from the image data by solving a linear inverse problem of the form

$$b = Au, \tag{1}$$

where b is the measured image data (or is derived therefrom), A is the forward operator describing the

specific application, and u is the solution we wish to compute. The classical variational approach to solving Equation 1 is to solve the optimization problem

$$u = \underset{x}{\operatorname{argmin}} \int_{\Omega} (b - Ax)^2 \, d\Omega + \delta R(x), \tag{2}$$

where Ω is the problem domain, δ is a scale parameter, and R is the so-called regularization, which ensures that the inverse problem is well-posed (Vogel 2002). Rather than solving a variational optimization problem, Equation 1 can be reformulated in a Bayesian framework, with a prior distribution serving a role analogous to the regularization, and this statistical approach allows the estimation of uncertainties associated with computed solution.

Project

As noted above there were three target problems to be addressed in the first year of this project. The first was to extend statistical reconstruction methods to compute the point spread function (PSF) of a high-energy x-ray imaging system from edge images. This is a problem that was first presented in the literature more than 50 years ago, and yet the mathematical foundations of the inverse problem had not been explored. In this work we have developed a mathematical model that is more robust than the classical approach and fits directly into the latest statistical framework developed for uncertainty quantification. The second problem on which we focus in this work is addressing a theoretical gap in how hierarchical Bayesian methods are applied to x-ray radiography. The primary reason for using hierarchical models is that they ostensibly have significantly reduced dependence on and sensitivity to the selection of tuning parameters. This is not obvious at first, as hierarchical models in fact have more parameters than their non-hierarchical counterparts. In this project we use Abel inversion as the primary application for characterizing the sensitivity of our statistical framework to hyperprior parameter selections, and we demonstrate that the mean reconstructions are quite insensitive to the selections of hyperprior parameters. Nonetheless, there is more work to do to explore the dependence of the error bars on the parameter selections. Our final problem in this work is to address one of the primary drawbacks to using Bayesian models with Markov Chain Monte Carlo (MCMC) algorithms, which is that they require solutions to very large-scale linear systems. Here we demonstrate the efficacy of matrix-free methods for solving large-scale linear systems and use the reconstruction of a high-energy x-ray source shape to validate our techniques.

Point Spread Function Reconstruction

One of the most common problems in mathematical imaging is deblurring, which means to deconvolve the impulse response function of the imaging system from a measured image; this is the so-called PSF, or blur kernel. For many systems the PSF can be measured by imaging a source that approximates a point source, a typical example being astronomical imaging where far-off stars approximate point sources. It is also common to model the PSF with a parametric form, so computing the PSF reduces to computing a small number of parameters rather than an entire function (Hansen 2006). In the absence of a known or measured blur kernel, it is also possible to estimate the PSF directly from the deconvolution process, with estimating the blur kernel ahead of time, an approach known as blind deconvolution (Levin 2009). This commonly requires a parametric form for the PSF in order to reduce the number of unknowns being estimated.

In high-energy x-ray imaging, it is not feasible to measure the PSF by imaging a bright, approximately point source, because generating an approximately point source of x-rays is not possible. In DOE applications, such as the Cygnus pulsed power x-ray facility at the NNSS, it is also desirable to eliminate the need for parametric forms of the PSF, as the functional forms designed to match the Cygnus PSF have been phenomenological rather than principled. In what follows we present some of the core ideas behind a new mathematical derivation of computing a PSF from rolled-edge images, as well as the results of a PSF reconstruction for the Cygnus imaging system.

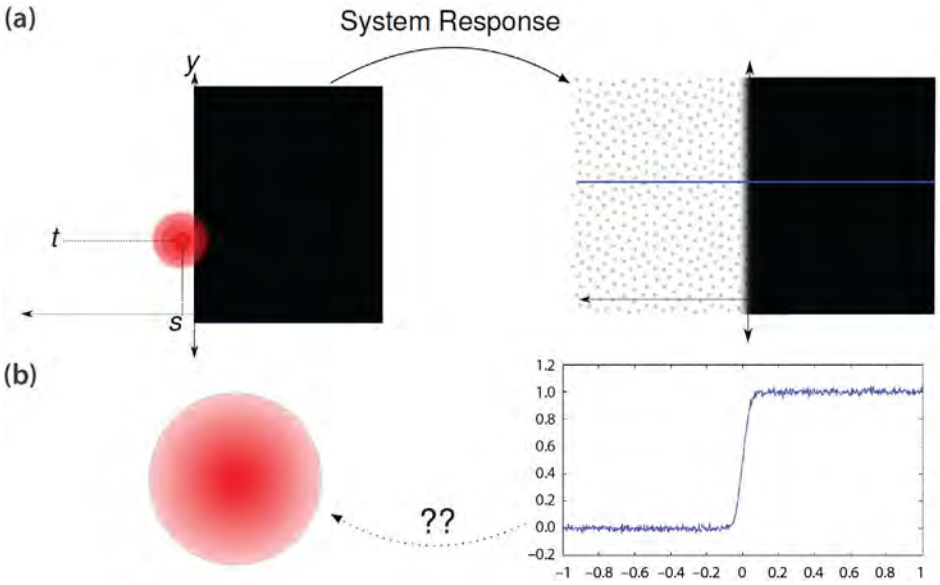

Figure 1. (a) Convolving a black half-plane with the red system response kernel results in a blurred edge along the axis, which in a real imaging system is also contaminated with noise. (b) The inverse problem is to compute the kernel from the blurred edge information.

The basic principle is pictured in the upper left of Figure 1a, which is a cartoon of a thick object (black region on right) and of open space (white region on left), with an imagined radiation source (red) overlaying the edge of the thick object. The forward model leads to image data such as that in the upper right of Figure 1a, with the black and white both contaminated by noise and blurred by the PSF. The inverse problem is to measure the edge image, take a single horizontal cross section—such as that in the lower right of Figure 1b—and reconstruct the blur kernel from the edge data, as shown in the lower left of Figure 1b.

Let $\chi_E(x,y)$ be the characteristic function of the left half-plane (i.e., $\chi_E(x,y) = 1$ for $x \le 0$ and $\chi_E(x,y) = 0$ otherwise). This function represents a vertical rolled edge, an object with a vertical edge in which all light is transmitted to the left of the edge (where $\chi_E(x,y) = 1$) and essentially no light is transmitted to the right of the edge (where $\chi_E(x,y) = 0$). The measured image, b, of such an object is then $\chi_E(x,y)$ convolved with the blur kernel of the imaging system, k, which plays the role of u in Equation 1, so that

$$b(x,y) = \int_{-\infty}^{\infty}\int_{-\infty}^{\infty} k(x-s,y-t)\chi_E(s,t)dsdt. \quad (3)$$

If we assume that the blur kernel has radial symmetry, as is often the case for imaging systems of this type, then we also apply the symmetry of convolution to reduce Equation 3 to

$$b(x) = \int_{-\infty}^{\infty}\int_{-\infty}^{\infty} k(s,t)\chi_E(x-s)dsdt. \quad (4)$$

We thus have the underdetermined linear inverse problem of computing the convolution kernel k from the 1-D measured edge data b. The formulation in Equation 4 does not inherently impose radial symmetry. Nonetheless, it can be shown that, if h is an increasing diffeomorphism of $(0,\infty)$ onto itself, $\tilde{r} = h^{-1}(r)^{1/2}$, and

$$g(x,r) = \begin{cases} 0 & x < -\tilde{r} \\ 2\left(\pi - \cos^{-1}\left(x/r\right)\right) & |x| < \tilde{r} \\ 2\pi & x > \tilde{r}, \end{cases}$$

then Equation 4 further reduces to

$$b(x) = \int_{0}^{\infty} \rho(r)g(x,r)h^{-1'}(r)dr := A\rho, \quad (5)$$

which is a linear Fredholm operator equation of the first kind and of the form of Equation 1.

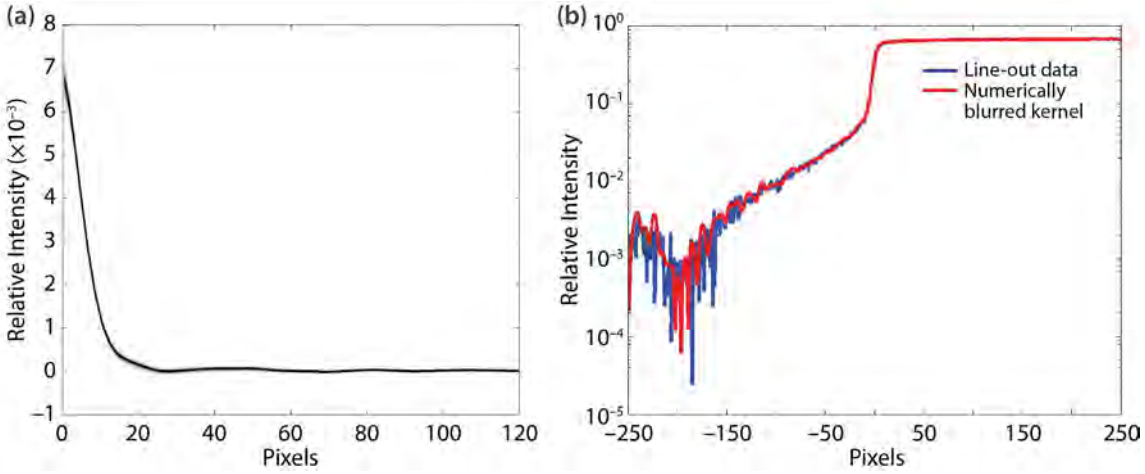

Figure 2. (a) Reconstructed PSF from a measured Cygnus image and (b) a synthetic edge forward blurred with the computed PSF

The blue curve in Figure 2b is measured edge data from a Cygnus image, and in Figure 2a the reconstructed PSF, ρ, is shown as the black line. The red curve in Figure 2b is a synthetic edge convolved with the computed PSF, and the fact that the red and blue curves line up demonstrates that our approach to computing the PSF works well.

The full mathematical formulation of this approach to imposing radial symmetry on linear inverse problems—and in particular to the problem of PSF reconstruction from edge data—along with the details of the radial regularization and numerical discretization can be found in Bardsley (2016). This formulation presents two major innovations. First, we characterize the space of radially symmetric PSFs as a Hilbert space, which means that this problem can be recast within a recently developed statistical framework for uncertainty quantification (Dashti 2016). Therefore, we are able not only to reconstruct the PSF but also to develop a measure of uncertainty on the PSF. Second, our new formulation uses a novel change of variables that allows us to avoid Abel inversion, which has been classically used in PSF reconstruction from edge data. Abel inversion suffers from significant numerical drawbacks, so an Abel-free approach is inherently more numerically stable.

Hyperparameter Sensitivities in Markov Chain Monte Carlo

As noted above, it is desirable to eliminate parameters like δ that must be selected by the user. If such parameters cannot be eliminated completely, then the next best goal is to design algorithms that reduce the sensitivity to the selection of the parameter value.

Specifically, in quantitative imaging, where one attempts to compute real values of object properties like material density from image data, it is essential that the reconstruction methods preserve scale. Rather than simply trying to compute a reconstruction that "looks good," we must develop algorithms that will give correct absolute values. In the case of computing the volumetric density of a radially symmetric object in the image scene, it is common to interpret the image as a single tomographic projection and use the Abel transform as the density transformation. Thus, given image data b', measured in intensity, we first transform the data to areal density, b, which is a quantity with units of g/cm^2. This gives a measure that accounts for both the volumetric density of the material and the thickness of the particular object. Areal density is then converted to volumetric density via the inverse Abel transform, which is a linear inverse problem of the form in Equation 1. In this setting, the

$$
\begin{aligned}
u = \arg\min_x p(x,\lambda,L,\delta \mid b) &= \arg\min_x p(b \mid x)p(x \mid L,\delta,\lambda)p(L,\delta,\lambda) \\
&= \arg\min_x \left|L\right|^{\frac{\nu-n}{2}} \lambda^{\frac{n}{2}+\alpha-1} \delta^{\frac{n}{2}+\theta-1} \exp(-\beta\lambda - \phi\delta)\times \\
&\quad \exp\left(-\frac{\lambda}{2}\left\|b-Ax\right\|^2 - \frac{1}{2}Tr(\Delta^{-1}L) - \frac{\delta}{2}x^T Lx\right)
\end{aligned} \tag{6}
$$

data b are areal densities, the forward operator A is the Abel transform, and we are computing u, the volumetric density of the material with units of g/cm^3.

An alternate, statistical approach to solving Equation 2 is to solve the statistical estimation problem as in Equation 6 where $Tr(\cdot)$ is the trace function. In this formulation, L plays the role of the regularization (or prior), and α, β, θ, ϕ are the so-called *hyperprior parameters* associated with gamma distribution priors on δ and λ (Fowler 2015, Howard 2015). Rather than assuming a fixed form of the prior matrix L, we take

$$L \sim Wishart(\Delta,\nu), \tag{7}$$

where Δ is the scale matrix and ν is the number of degrees of freedom. The Wishart distribution is a standard distribution for matrices and can be thought of as playing the same role that multivariate normal distributions play for vectors. The number of degrees of freedom ν is almost always fixed and not viewed as being selected by the user.

Computing the minimizer in Equation 6 with an MCMC sampling scheme (Fowler 2015, Howard 2015) would, at first, appear to be much worse than solving Equation 2, because Equation 6 has tuning parameters α, β, θ, ϕ, and Δ, rather than the one tuning parameter δ. As will be shown, however, this is a better formulation, because the four tuning parameters and user-selected seed for L are less sensitive than the selection of δ in the variational case.

The initial seed selected for L is the Wishart scale matrix, Δ, which has a form similar to that of the solution. The most direct approach is to compute a solution to Equation 2 for some choice of regularization R and regularization parameter δ, and use that solution to build Δ. In practice, this approach works quite well, and we recommend its use, but it violates the Bayesian assumption of Δ corresponding to prior information, that is, information known independent of the data, and gives a sense of needing to know the answer before you compute the answer, which is obviously undesirable. In order to show that this reconstruction technique is insensitive to the choice of Δ, Figure 3 shows two computed reconstructions of a synthetic density profile, along with 95% credible intervals calculated using MCMC sampling. It also shows the true density profile and the two distinct initial Wishart scale profiles. The scale profiles, referred to as the TV Solution in the figure legend, are shown as dot-dashed lines; TV is an abbreviation for total variation. The scale profile corresponding to Δ_1 in Figure 3a is a constant; the scale Δ_2 in Figure 3b is a step function with jumps at incorrect locations. Despite these two choices for Δ failing to capture any of the structure of the true solution profile (and even containing incorrect structure), the sampling scheme is still able to compute the material densities accurately enough to nearly completely overlay the true solution. Moreover, the true solution lies entirely within the 95% credible intervals of the reconstructions in both cases. This demonstrates that our hierarchical Bayesian formulation in Equation 6 is quite insensitive to the choice of Δ.

As noted above, the formulation in Equation 6 has four more "tuning" parameters (α, β, θ, and ϕ), and we wish to also show that our density reconstructions are insensitive to the choices made for these parameters. Figure 4 contains plots of eight reconstructions, each computed with the same Wishart scale matrix Δ but with different 4-tuples (α, β, θ, ϕ). The parameters for the images are (a) (10^3, 10, 10, 1), (b) (10^4, 10, 10, 10), (c) (10^4, 10, 1, 1), (d) (10^4, 10, 10, 10), (e) (10^4, 10, 10^2, 1), (f) (10^4, 10^2, 10, 1), (g) (10^5, 10, 10, 1), and (h) (10^4, 1, 10, 1).

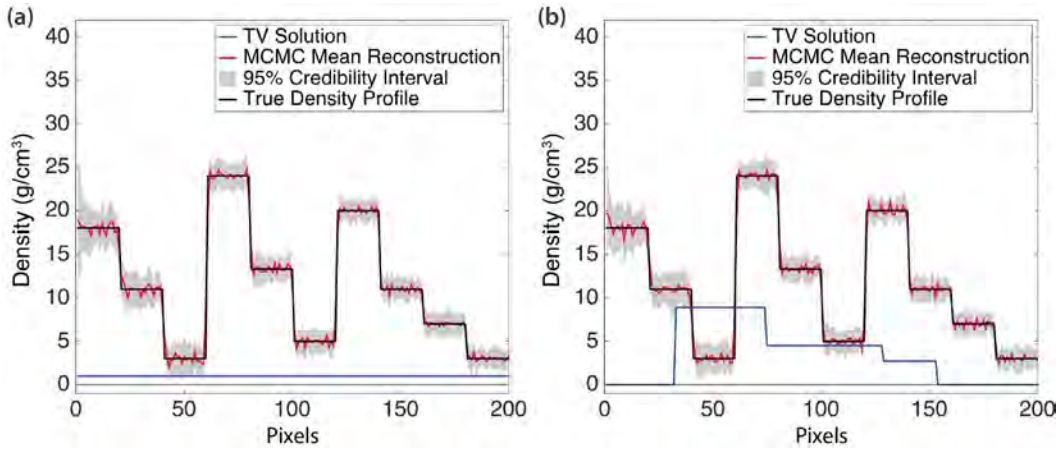

Figure 3. Density reconstructions with L sampling, from two different initial scale matrices (a) Δ_1 and (b) Δ_2

In all cases the density reconstructions are very similar, and all virtually overlay the true solution, which indicates that the mean of the MCMC samples is insensitive to the choices of these parameters. Nonetheless, there are significant differences in these plots with regard to the 95% credibility intervals. These results suggest that the reconstructions obtained using MCMC sampling from Bayesian posteriors are robust to the choices of hyperparameter selection but that it may be difficult to use the variation in the posterior as a quantification of uncertainty in the reconstruction, which is a topic of further study for this project in the second year.

Numerical Methods for Large-Scale Linear Systems in Inverse Problems

One of the greatest difficulties in solving problems of the forms in Equations 1, 2, or 6 is that they can require the solutions of very large–scale linear systems, in some cases as large as $10^6 \times 10^6$, that cannot be solved via direct matrix solvers. It is essential to employ matrix-free numerical methods designed for large-scale systems in order to compute the imaging reconstructions we desire.

In x-ray imaging it is essential to understand the size and shape of the x-ray radiation source, and methods have been developed for reconstructing the shape from images of a calibration object known as an L rolled edge. This process is known as spot reconstruction. The mathematical model for spot reconstruction is

$$b(s,t) := A(u)(s,t) = k\int_{s'}^{s''}\int_{t'}^{t''} u(\eta,\mu)d\eta d\mu, \qquad (8)$$

where k is a constant that depends on the geometry of the scene, and (s',s'',t',t'') are known parameters that define the region of integration. The function u is the source shape, and b is the data from an image of the L rolled edge; as in the problems above, this is of the form given in Equation 1. A statistical formulation for solving this problem is detailed in Fowler (2015), along with results for both the Cygnus x-ray imaging facility at the NNSS and for the RITS-6 facility at Sandia National Laboratories. In both of those cases, however, it was necessary to downsample the measured image data in order to ensure that the linear systems being solved were small enough to store in computer memory. We implemented a conjugate gradient/projected Newton (CG-PN) solver that allowed computing the solutions of the linear systems without explicitly constructing the matrices and yet enforcing non-negativity constraints on the solution.

Figure 5 shows the spot reconstructions for L rolled edge image data from shot 1802 at RITS-6. Figure 5a shows the reconstruction one obtains from a 75 × 75 pixel region of the original image, which is approximately

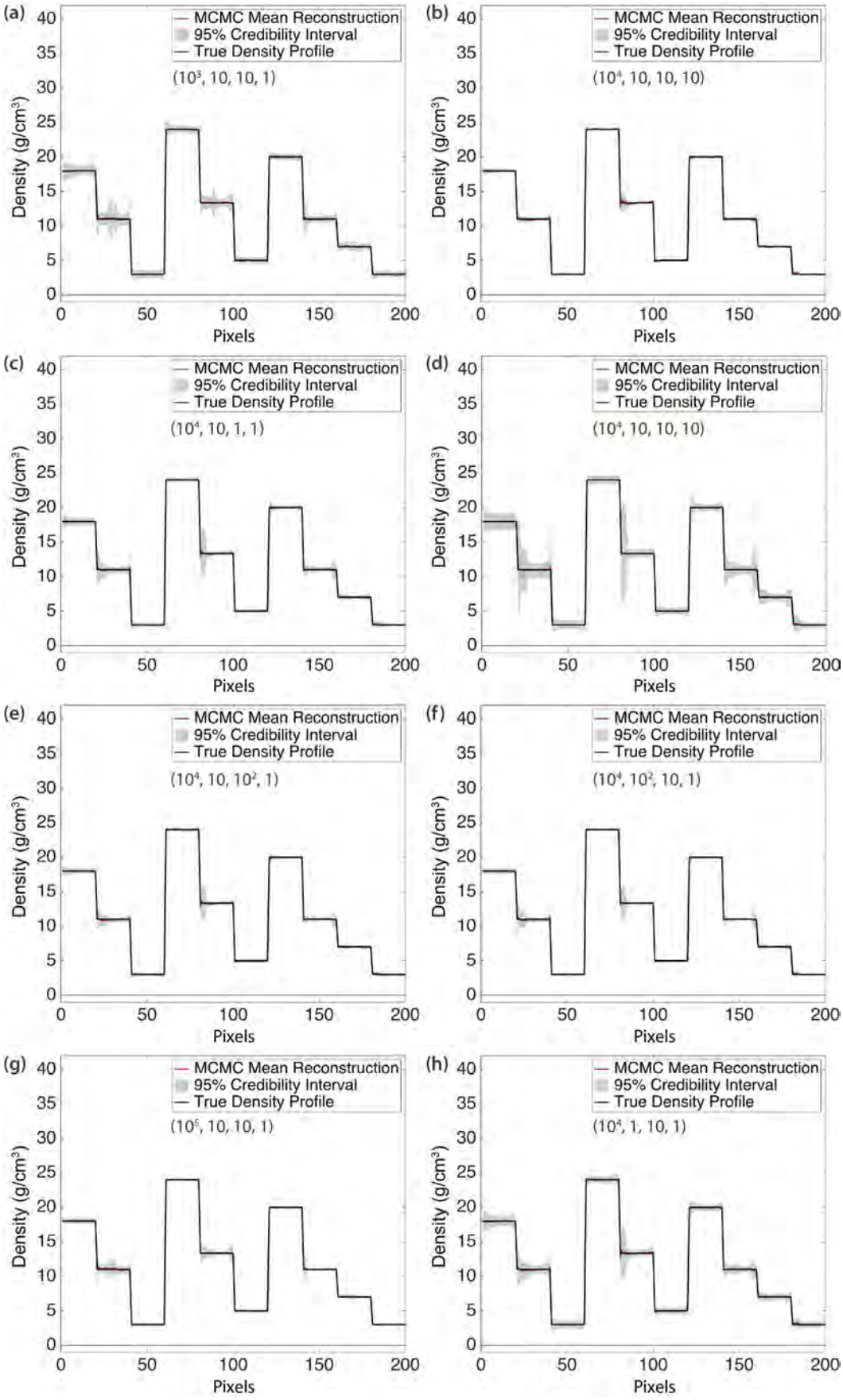

Figure 4. Density reconstructions with error bars for eight different sets of hyperparameters

the size of a reconstruction that could be computed with explicitly constructing the matrix associated with the forward operator. As can be seen, the reconstruction does not resemble the expected approximately round region with central point of highest intensity. Figures 5b and 5c show reconstructions from the same image, using data swaths that are 250 × 250 and 1000 × 1000 pixels, respectively. (Note that Figure 5c was computed from a 1000 × 1000 pixel swath but is zoomed in to 250 × 250 pixels to show the structure of the spot.) Whereas 75 × 75 pixels failed to contain enough information to reconstruct the spot, 250 × 250 pixels is large enough, and the area of 1000 × 1000 pixels contains all the required information. Both of the latter two regions of the measured image contain enough information for a full reconstruction, and our CG-PN approach to solving the associated linear system is able to compute the solutions without numerical pathologies. Thus, our new approach allows us to reconstruct spot shapes that our previous numerical schemes were simply incapable of solving.

Figure 6 shows reconstruction results from two different images of the L rolled edge taken at the NNSS Cygnus dual-axis (axis 2) x-ray facility. For Cygnus, the 75 × 75 pixel region of data is enough to capture almost a complete reconstruction (left images, top and bottom), but the 250 × 250 and 1000 × 1000 pixel reconstructions are required to prove that the smaller 75 × 75 pixel area is large enough. Thus, even though the Cygnus reconstructions could be computed with codes that explicitly construct the forward model matrix, we would not know that such a reconstruction was sufficient without analyzing the larger-scale reconstructions. With our new approach, these computations are trivial, and we are able to calculate the size and shape of the Cygnus spot.

Conclusion

In the first year of this project, we focused on three problems. The first was developing a mathematical theory for computing the PSF of an x-ray imaging system from edge data. While this has been done

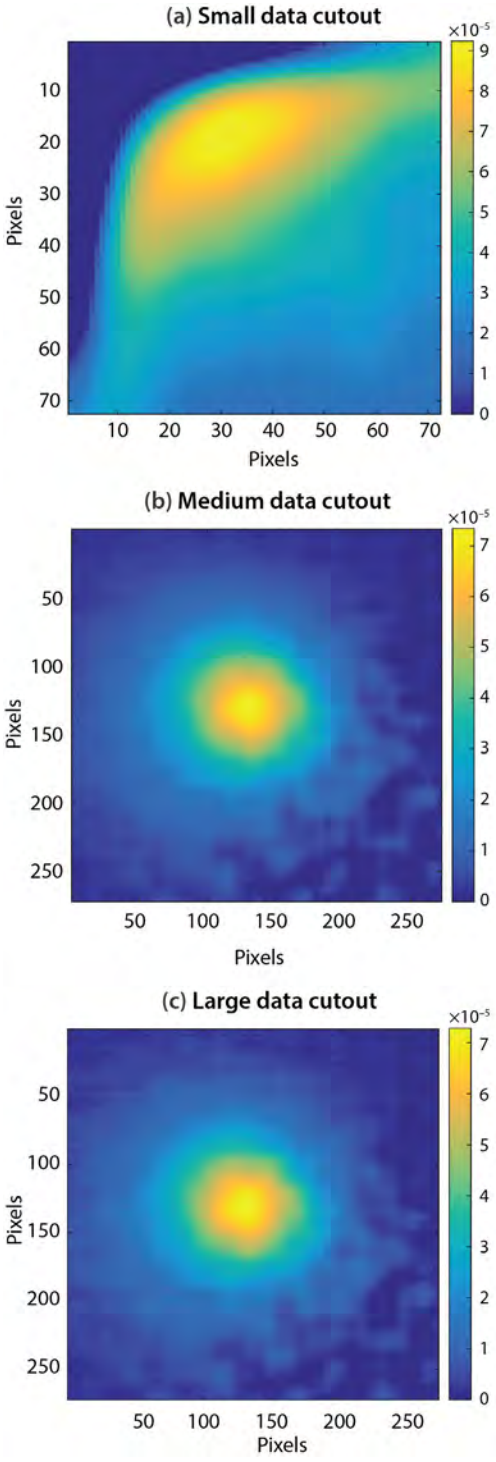

Figure 5. RITS-6 Shot 1802 reconstructions with (a) small, (b) medium, and (c) large data cutouts. (Note that image (c) was computed from a 1000 × 1000 pixel swath but is zoomed in to 250 × 250 pixels to show the structure of the spot.) The color scales are in arbitrary units.

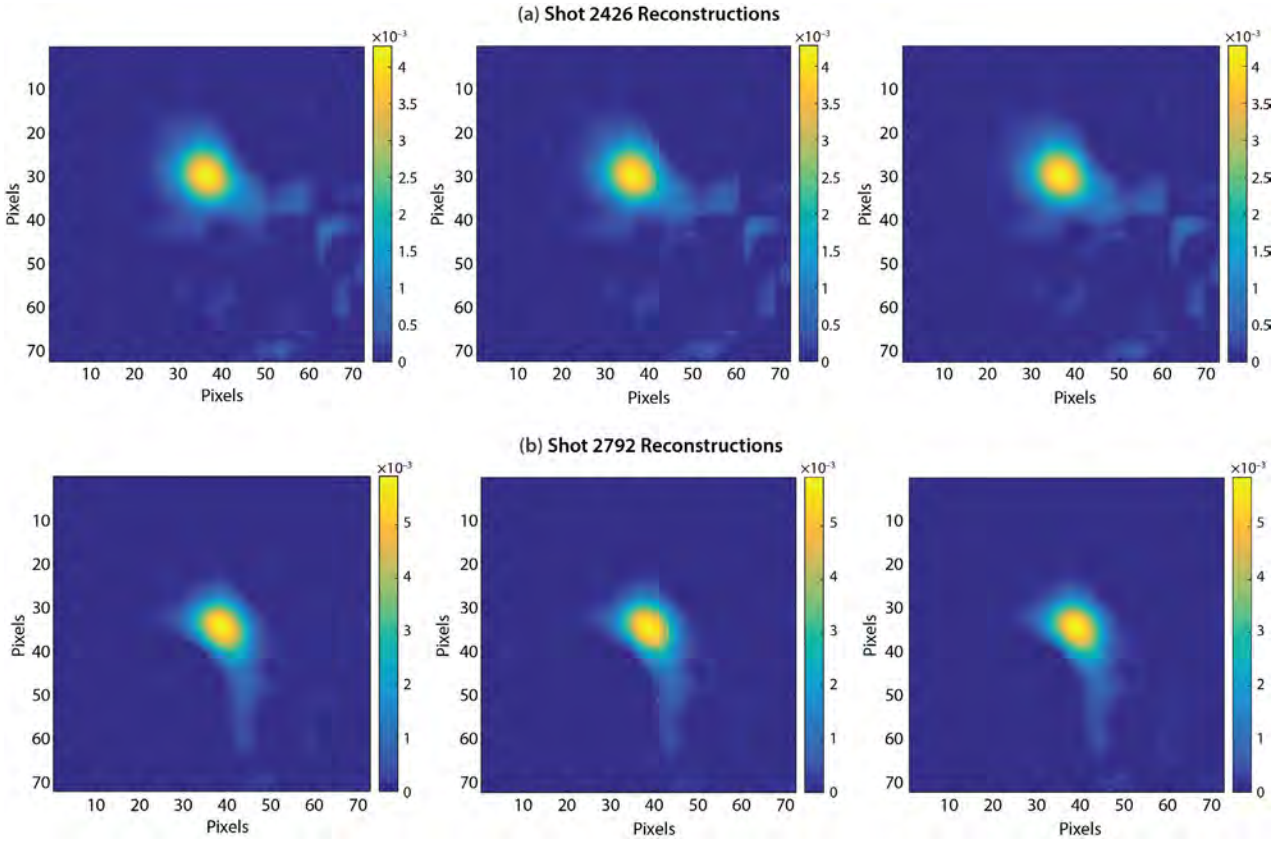

Figure 6. Cygnus source reconstructions from shots (a) 2426 and (b) 2792 with small (left), medium (middle), and large (right) data cutouts. The color scales are in arbitrary units.

for many years for systems like Cygnus at the NNSS, the theory was not well formulated, and there were no methods for directly constructing the PSF without the use of phenomenological parametric models. Our new approach fills this gap, and we have designed an MCMC method to sampling from a posterior distribution of possible solutions, giving a measure of uncertainty to the computation. Such sampling schemes require a theoretical and practical understanding of the behaviors of the built-in tuning parameters, and they require the ability to solve very large linear systems. Addressing these issues, our second and third problems were conducting a sensitivity study of the behavior of hyperprior parameters in an MCMC approach to Abel inversion and implementing matrix-free numerical schemes for solving large-scale linear systems with non-negativity constraints, respectively. Our work on all three problems will continue in the second year, with the goal being to combine the different components into a single set of computational tools for solving linear inverse problems in a statistical framework with uncertainty quantification.

Acknowledgments

The authors would like to thank Dr. Dave Higdon of Virginia Polytechnic Institute and State University and Dr. Earl Lawrence of Los Alamos National Laboratory for helpful guidance and suggestions on the project.

References

Bardsley, J. M., K. Joyce, A. Luttman, "Partially collapsed Gibbs sampler for linear inverse problems and applications to x-ray imaging," DOE/NV/25946--2713, National Security Technologies, LLC, Las Vegas, Nevada, 2016.

Dashti, M., A. M. Stuart, "The Bayesian Approach to Inverse Problems," in *The Handbook of Uncertainty Quantification*, R. Ghanem, D. Higdon, H. Owhadi, eds., Springer, 2016.

Fowler, M., M. Howard, A. Luttman, S. E. Mitchell, T. J. Webb, "A stochastic approach to quantifying the blur with uncertainty for high-energy X-ray imaging systems," *Inverse Probl. Sci. Engineering* (2015).

Hansen, P. C., J. G. Nagy, D. P. O'Leary, *Deblurring Images: Matrices, Spectra, and Filtering*, SIAM Publishing, Philadelphia, 2006.

Howard, M., M. Fowler, A. Luttman, S. E. Mitchell, M. Hock, "Bayesian Abel inversion in quantitative x-ray radiography," DOE/NV/25946--2439, National Security Technologies, LLC, Las Vegas, Nevada, 2015.

Levin, A., Y. Weiss, F. Durand, W. T. Freeman, "Understanding and evaluating blind deconvolution algorithms," in *Computer Vision and Pattern Recognition*, IEEE Conference on Computer Vision and Pattern Recognition, June 20–25, 2009 (2009) 1964–1971.

Vogel, C. R., *Computational Methods for Inverse Problems*, SIAM Publishing, Philadelphia, 2002.

Three-Dimensional Seismic-Attribute Model for Yucca Flat

NLV-24-14 | Continued from FY 2014 | Year 2 of 2

Lance Prothro,[1,a] Heather Huckins-Gang,[a] Sig Drellack,[a] Dawn Reed,[a] Margaret Townsend,[a] Kevin Day,[b] and Todd Kincaid[b]

Based partly on an evaluation using data collected during underground nuclear testing in Yucca Flat of the NNSS, an existing 3-D hydrostratigraphic framework model of Yucca Flat that was developed for groundwater modeling shows considerable promise as a 3-D seismic-attribute model. With relatively minor modifications, the existing framework model has been converted to a 3-D seismic-attribute model and is already being utilized to better understand seismic wave propagation from underground chemical explosive tests being conducted in Yucca Flat. These tests are designed to improve the United States' ability to detect, locate, and characterize underground nuclear explosions conducted anywhere in the world.

[1] prothrlb@nv.doe.gov, 702-295-7745
[a] North Las Vegas; [b] GeoHydros, LLC

Background

The United States has a significant national security interest in improving its ability to detect, locate, and characterize underground nuclear explosions (UNEs), particularly low-yield UNEs, that may be conducted anywhere in the world (Snelson 2013). One of the primary methods for monitoring for UNEs is through the analysis of seismic waves generated by explosions, which propagate outward through the earth from the detonation point to seismic recording sensors located around the globe (Auer 2014). Seismic waves, whether generated by UNEs or other man-made or natural events, propagate through different rock types at differing speeds and with unique characteristics that depend largely on various rock properties and the presence of other geologic features. The earth is a very heterogeneous geologic medium, and the 3-D geologic structure of the earth strongly affects how seismic waves propagate both locally and regionally as they encounter various rock types, faults, and other geologic features, and how they interact with the variable topography of the earth's surface.

The Source Physics Experiment (SPE) is currently being conducted in Yucca Flat of the NNSS by the U.S. DOE NNSA to develop predictive capabilities that will enhance the United States' ability to model and characterize low-yield nuclear tests anywhere in the world (Snelson 2013). The approach of the SPE is to conduct well-characterized chemical explosions at different depths and in diverse geologic media to improve the understanding of how seismic waves are produced and how they propagate in different geologic settings.

Yucca Flat is an excellent site for studying seismic wave propagation from controlled explosive experiments like those conducted for the SPE. The geologic setting of Yucca Flat is diverse, but well understood, with an abundance of geologic and geophysical data from more than 50 years of subsurface characterization activities associated with the U.S. underground weapons testing program (WTP). In addition, and important for improving seismic wave propagation modeling, a 3-D geology-based computer framework model constructed for a

different purpose and under another program already exists for Yucca Flat. We show that with minimal modifications, this existing hydrostratigraphic framework model (HFM) can function as a seismic-attribute framework model (SFM) and thus become a valuable tool for improving seismic wave propagation modeling in and around Yucca Flat.

Project

The project leverages existing seismic property data collected during the WTP in Yucca Flat and an existing 3-D HFM for Yucca Flat to develop a 3-D SFM and an associated seismic properties database. We also test the underlying hypothesis that with minimal modifications the Yucca Flat HFM can function as an SFM.

The Yucca Flat Hydrostratigraphic Framework Model

The Underground Test Area (UGTA) Activity was initiated by the NNSA Nevada Field Office (NFO) to assess the effects of UNEs on groundwater at the NNSS (Navarro-Intera 2013). The UGTA strategy requires the development of sophisticated groundwater flow and contaminant transport computer models to estimate the lateral and vertical movement of radionuclide-contaminated groundwater over the next 1,000 years. Because groundwater flow is mainly controlled by certain physical properties of the rocks through which it flows, the development of 3-D computer framework models of the distribution of subsurface units according to their abilities to transmit groundwater was a critical first step in the development of groundwater flow and contaminant transport models. These 3-D HFMs are the foundation for subsequent numerical flow and transport modeling, and have been successfully used by UGTA for more than 10 years.

The Yucca Flat HFM was constructed for UGTA in 2006 (Bechtel Nevada 2006). It covers 1,250 square kilometers in the northeastern portion of the NNSS and includes all of Yucca Flat proper and portions of the adjacent highlands (Figure 1).

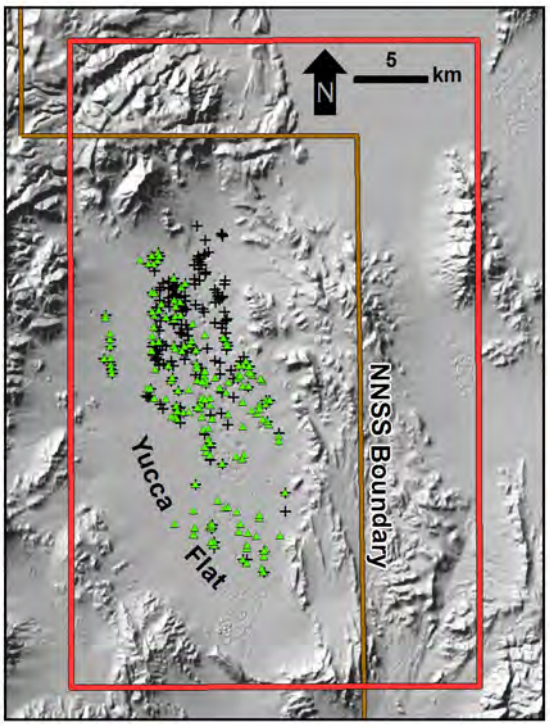

Figure 1. Shaded relief map of Yucca Flat showing the boundaries of the Yucca Flat HFM (red rectangle) and drill holes with working point (WP) medium characteristics (black plus signs) and down-hole geophone data (green triangles)

Vertically, the Yucca Flat HFM extends from the land surface to 5 kilometers below sea level. The HFM is geology-based and incorporates stratigraphic principles and rock properties to group the various rock layers beneath Yucca Flat into hydrostratigraphic units (HSUs) based on their ability to transmit groundwater (Prothro 2009). Thus, HSUs form the main 3-D model volumes, or layers, in the HFM. The Yucca Flat HFM includes 25 HSUs as well as 178 faults that cut and offset the HSUs (Figure 2).

Many of the properties and characteristics that influence a rock's ability to transmit groundwater also influence the transmission of seismic waves (e.g., velocity) through the rock. This is mainly because of the relationships between rock porosity, density, and velocity. Higher porosity typically corresponds to lower density and velocity. Porosity is a fundamental hydrologic property of rocks and typically functions as a major control on a rock's ability to store and transmit

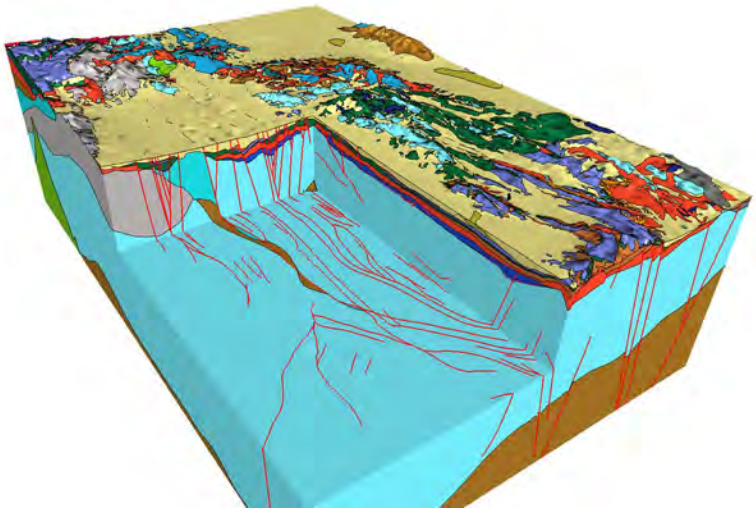

Figure 2. Looking northeast at a cutaway 3-D perspective view of the Yucca Flat HFM. Colored layers are HSUs; red lines are faults.

groundwater. Rocks with higher matrix porosity tend to be categorized as aquifers; rocks having lower porosity are considered to be confining units, or aquitards. Velocity, a fundamental seismic property of rocks, typically decreases with decreasing density and the associated increase in porosity. Thus, in the Yucca Flat HFM, high-porosity, low-density aquifer HSUs, such as the alluvial aquifer (AA) and Timber Mountain lower vitric-tuff aquifer (TMLVTA), have corresponding low velocities (Figure 3).

Porosity, however, is not the only rock property that can impart a substantial influence on a rock's ability to transmit groundwater. The presence of interconnected, open fractures can substantially increase the ability of water to move through a rock volume even though the rock is relatively dense with low matrix porosity. In the Yucca Flat HFM, aquifer HSUs like the Timber Mountain welded-tuff aquifer (TMWTA) and lower carbonate aquifer (LCA) are examples of dense, low-porosity rocks with substantial fracture permeability. These rocks also tend to have higher seismic velocity due to their high density and low matrix porosity, although the intensity of fracturing can affect the overall velocity as well as other seismic attributes.

Additionally, post-depositional alteration of porous low-density volcanic rocks can have significant effects on the hydrologic and seismic properties of these rocks. This is observed in the deeper portions of Yucca Flat where post-depositional zeolitic and quartzo-feldspathic alteration of porous low-density volcanic rocks appears to have choked off the interpore pathways within the rock, thus substantially reducing the ability for these altered rocks to transmit groundwater. Within the Yucca Flat HFM, these altered units are categorized as tuff confining units even though they still retain significant porosity. Two examples of altered HSUs are the lower tuff confining unit (LTCU) and the Oak Spring Butte confining unit (OSBCU). Because zeolitic and quartzo-feldspathic alteration also increases the density of these rocks, they also tend to have higher velocity than in their unaltered states.

In summary, the Yucca Flat HFM groups rock layers beneath Yucca Flat according to their abilities to transmit groundwater, and they are defined by certain hydrologic and physical properties that also have corresponding seismic effects. Thus, the Yucca Flat HFM was expected to be applicable for use in modeling of seismic wave propagation in and around Yucca Flat.

Yucca Flat Site-Characterization Data from the Weapons Testing Program

From 1957 to 1992, 747 UNEs were conducted in the Yucca Flat area (Navarro-Intera 2013). The individual sites for these detonations were typically the subject of intense geological and geophysical characterization. More basin-wide geological and geophysical

investigations were also commonly conducted and, together with individual site-characterization data, resulted in a detailed understanding of the geological and geophysical character of Yucca Flat. These extensive characterization studies in Yucca Flat have produced a diverse set of geological and geophysical data for the basin, including laboratory measurements of rock characteristics (e.g., density, water content, mineralogy), borehole geophysical logs (e.g., bulk density, acoustic impedance, seismic velocity), and field surveys (e.g., seismic reflection and refraction, gravity, resistivity, magnetotelluric, and aerial and ground magnetics).

From this large, diverse assemblage of data, we chose two specific datasets to interrogate and evaluate the applicability of the Yucca Flat HFM to function as an SFM. Both datasets provide field-scale seismic velocity data for distinct subsurface intervals of rock sections beneath Yucca Flat. The first data of interest were extracted during year 1 of our study (Prothro 2015) from detailed site-characterization reports from 150 UNE emplacement holes in Yucca Flat (Figure 1). Of particular interest were data tables that list various physical properties of the rocks within the region of the working point (WP; i.e., depth of detonation). These data tables provided seismic compressional-wave (P-wave) velocity for a specified interval of rock around the WP. In addition, they listed other important interval-specific rock properties such as bulk density and porosity.

In year 1 we also compiled the results from down-hole seismic surveys conducted in many of the emplacement holes drilled to site UNEs in Yucca Flat. These surveys yielded seismic velocity data at 50-foot intervals throughout the depth of the hole. More than 5,400 interval velocity measurements from 188 holes in Yucca Flat (Figure 1) were compiled in FY 2014.

From the original WTP reports and paper logs of down-hole geophysical surveys, we extracted the required data and compiled it in a spreadsheet format. Because the velocity and other data of interest were for specific depth intervals tied to individual holes, information such as hole name, location, surface elevation, and depth to the water table were extracted from existing UGTA databases and included with each interval velocity record.

A critical step in the compilation of the Yucca Flat seismic velocity dataset during year 1 was to correlate each interval velocity in the database with geologic parameters of the interval. These parameters included stratigraphic unit, lithology (i.e., rock type), mineral alteration, and, most importantly, the HSU that the interval represented in the Yucca Flat HFM. Drill hole geologic data were extracted from various WTP-era reports, logs, and data compilations. HSU assignments were determined from Appendix C of the Bechtel Nevada report (2006).

Data Analyses and HFM Evaluation

Linking each of the 5,526 interval velocity measurements within the drill hole database to geologic parameters allowed us to sort, evaluate, and statistically analyze the velocity data relative to stratigraphic unit, lithology, alteration mineralogy, and HSU (Figure 3). Our initial analyses in year 1 showed expected seismic heterogeneity within the rocks beneath Yucca Flat, and a general correlation between seismic properties and HSUs, thus demonstrating that most HSUs in the Yucca Flat HFM can function as seismo-stratigraphic units (SSUs).

Using a subset of the down-hole interval velocity data, we constructed, in year 1, a separate preliminary velocity model independent of the HFM to explore its potential to aid in evaluating the HFM. In particular, we wanted to determine whether lateral velocity changes occur within some HSUs. These initial assessments of the preliminary velocity model indicated that it could provide an additional and efficient method to evaluate the 3-D distribution of velocities beneath Yucca Flat and the seismic character of HSUs.

Thus, in year 2, we constructed a full 3-D velocity property model within the HFM (Figure 4). Velocity data used for the model were the 50-foot interval downhole seismic survey data, which were modeled in three dimensions using a minimum tension gridding algorithm.

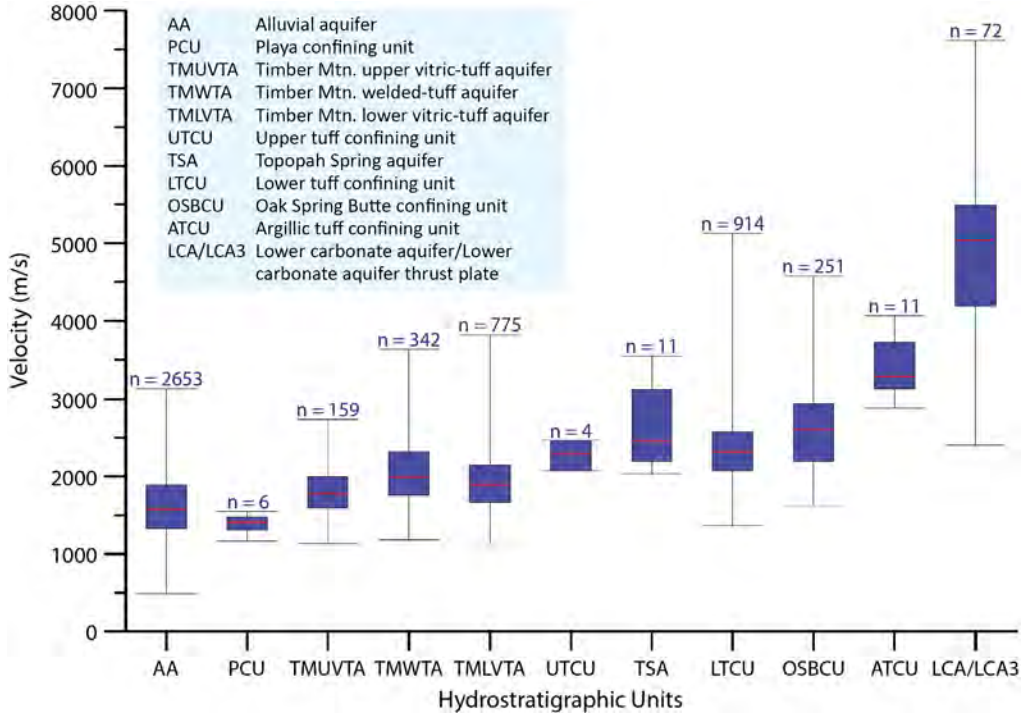

Figure 3. Box-whisker plot of selected HSUs from the Yucca Flat HFM showing velocity heterogeneity within the rocks beneath Yucca Flat; n values indicate measurement counts for particular HSUs

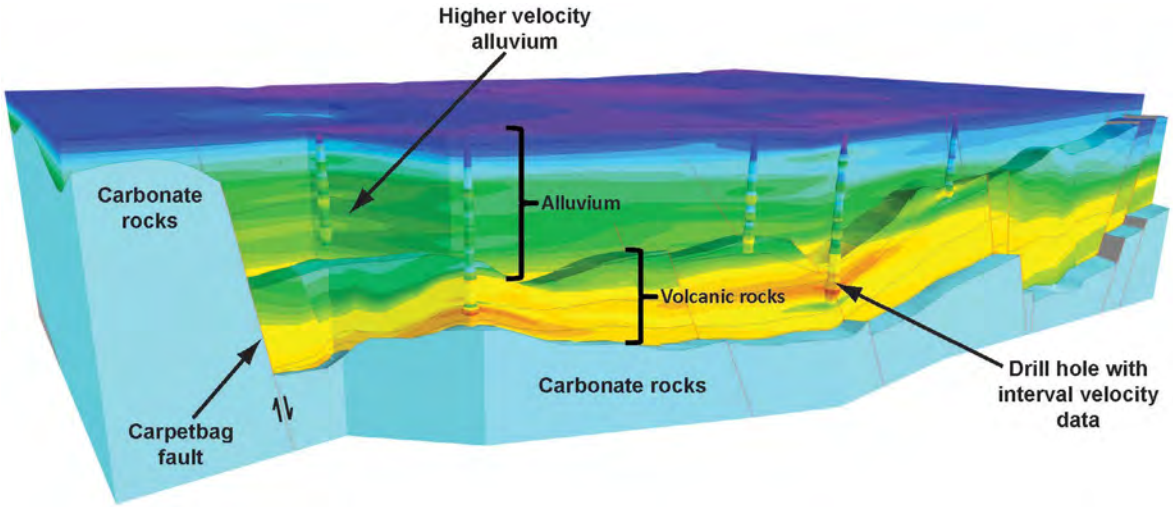

Figure 4. Profile of the velocity model, northern portion of Yucca Flat. View is northeast. Warmer colors are higher velocity.

Higher-resolution and well-constrained geologic data and observations were used to inform the velocity model by vertically grouping seismic data into stratigraphic zones including alluvium, volcanic, and Paleozoic carbonate deposits. This approach preserved hard velocity contrasts where alluvial-volcanic contacts are known to exist and facilitated investigation of contrasts within the stratigraphic zones. Interpolated velocity was adjusted using a z-influence variable to determine the degree of lateral continuity that best honored

the input data and that produced the most geologically realistic results, such as elongated lens-shaped forms characteristic of alluvial deposits. The velocity distribution in the volcanic stratigraphic zone was modeled such that the grids are conformable by fault block, which propagates the dip and dip azimuth of the overlying and underlying surfaces into the velocity model. Conversely, the velocity distribution in the alluvium is non-conformal, preserving the horizontal depositional fabric of these post-volcanic deposits.

One important result of the development of this 3-D velocity model is the recognition of higher velocity in the alluvium in the northwest portion of Yucca Flat adjacent to the Carpetbag fault (Figure 4). This region of high-velocity alluvium is consistent with the geologic setting, which suggests that paleo-exposures of dense carbonate rocks on the up-thrown side of the Carpetbag fault could have resulted in coarse, high-velocity carbonate debris being shed eastward off the high side of the fault and into the developing basin, creating thick lenses of high-velocity alluvium. As a result of the recognition of this region of higher velocity in the alluvium, a new layer was developed that demarcates the higher velocity alluvium. The location of this region is significant because it is in the vicinity of the future site of the SPE Phase II "Dry Alluvium" test bed.

Collapse Chimneys and Damage Zones

Another potential complicating factor in modeling seismic wave propagation in Yucca Flat is the presence of features associated with individual UNEs that may contain locally altered or damaged rocks, resulting in local zones with seismic properties different than those same rocks in their undamaged state. These features include rubble chimneys that form above the WP region when the roof of the cavity created by a UNE collapses, and possible damage zones that surround the WP region. Carroll (1983) discussed the measured changes in velocity associated with damage to the rock from passage of the stress wave from a UNE. Reductions in shear wave velocities are primary indicators of this damage, but changes in P-wave velocity may also be observed very close to the collapse chimney. Carroll (1983) mainly worked in volcanic tuff, but it may be that similar changes occur in alluvium and other rock types beneath Yucca Flat. Because sites of expended UNEs are densely clustered in many places in Yucca Flat, the demarcation of individual collapse rubble chimneys and WP-region damage zones associated with Yucca Flat UNEs could be an important addition to the seismo-stratigraphic framework model by allowing seismic wave propagation modelers to assess the impact of these features.

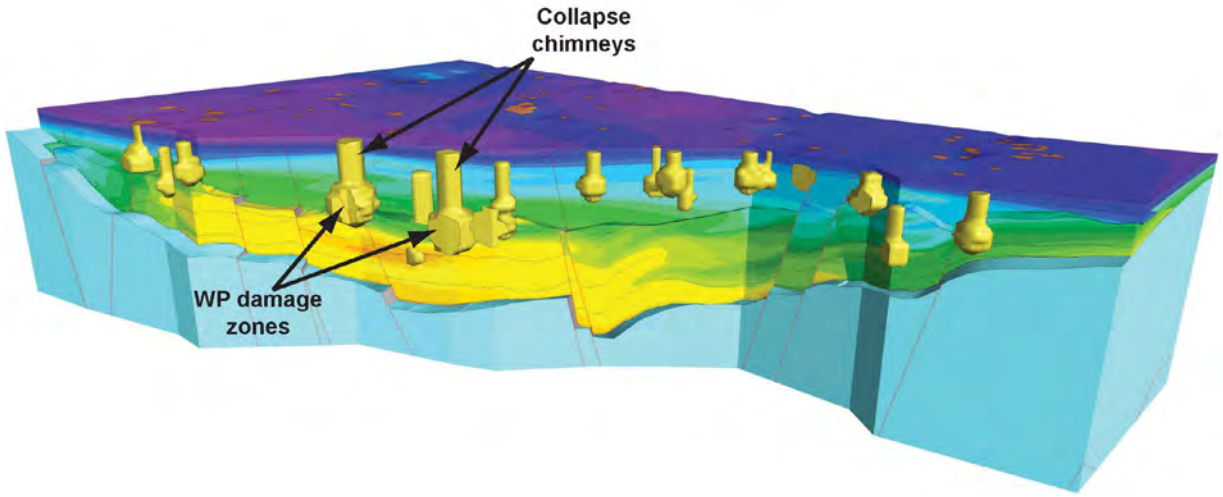

Figure 5. Profile of the velocity model showing collapse chimneys and WP damage zones integrated within the velocity model. View is northeast. Warmer colors are higher velocity.

Using available specifications such as WP depth, cavity radius (based on announced maximum yield), and chimney growth height, we constructed 3-D property models that represent the collapse rubble chimneys and WP damage zones for 747 UNEs in Yucca Flat. Collapse rubble chimneys were modeled as approximate cylinders with a radius equal to the radius of the associated cavity and extending from the WP depth up to the calculated height of chimney growth. WP damage zones were modeled as approximate spheres with radii equal to two times the announced cavity radii. Because the collapse rubble chimneys and WP damage zones were modeled as 3-D property models, they can be integrated with both the seismo-stratigraphic framework model and the velocity model (Figure 5).

Conclusion

Analyses of the seismic data compiled for this investigation indicate that most HSUs in the Yucca Flat HFM directly correspond to SSUs. Therefore, with only minor modifications, the UGTA Yucca Flat HFM can function as a 3-D SFM and be a valuable tool for more precisely studying seismic wave propagation in Yucca Flat. In fact, at the time of writing, these data and model outputs are being used by Sandia National Laboratories to help with interpretation of the Thor 1 seismic-hammer data, a SPE-related surface seismic survey in Yucca Flat.

When we used the down-hole interval velocity data to construct 3-D velocity property models and applied geologic knowledge to inform the modeling process, a region of high-velocity alluvium was revealed near the future location of the SPE Phase II "Dry Alluvium" site in the northwestern portion of Yucca Flat. A new SSU was created within the SFM to represent this high-velocity alluvium. It is anticipated that this will prove to be an important enhancement to the SFM during data analyses of future SPE Phase II tests.

Creating 3-D models of collapse chimneys and damage zones associated with past UNEs in Yucca Flat as separate model elements will allow seismic modelers to assess the impact of these features on seismic wave propagation from SPE tests in Yucca Flat. As with the SFM, modeling of these features is already proving its utility. SFM profiles with collapse chimneys and damage zones were created along the Thor 1 seismic line to help evaluate anomalous recordings in the vicinity of expended UNEs that occur near the Thor 1 line.

Acknowledgments

We would like to thank Cathy Snelson (formerly of NSTec) and Steve Molnar for their contributions to this work. Bill Wilborn, NNSA/NFO, facilitated the use of the UGTA HFM for this project.

References

Auer, M., M. K. Prior, "A new era of nuclear test verification," *Physics Today* **67**, 9 (September 2014) 39–44.

Bechtel Nevada, *A Hydrostratigraphic Model and Alternatives for the Groundwater Flow and Contaminant Transport Model of Corrective Action Unit 97: Yucca Flat–Climax Mine, Lincoln and Nye Counties, Nevada*, DOE/NV/11718--1119, Bechtel Nevada, Las Vegas, Nevada, January 2006.

Carroll, R. D., "Seismic velocity and postshot properties in and near chimneys," in *Proceedings of the Monterey Containment Symposium, Monterey, CA, August 26–28, 1981*, B. C. Hudson, E. M. Jones, C. E. Keller, C. W. Smith, eds., LA-9211-C, Vol. 1, Los Alamos National Laboratory, Los Alamos, New Mexico, February 1983, 379–396.

Navarro-Intera, LLC, *Phase I Flow and Transport Model Document for Corrective Action Unit 97: Yucca Flat/Climax Mine, Nevada National Security Site, Nye County, Nevada*, N-I/28091-080, Navarro-Intera, LLC, Las Vegas, Nevada, September 2013.

Prothro, L. B., S. L. Drellack, Jr., J. M. Mercadante, *A Hydrostratigraphic System for Modeling Groundwater Flow and Radionuclide Migration at the Corrective Action Unit Scale, Nevada Test Site and Surrounding Areas, Clark, Lincoln, and Nye Counties, Nevada*, DOE/NV/25946--630, National Security Technologies, LLC, Las Vegas, Nevada, January 2009.

Prothro, L., M. Townsend, H. Huckins-Gang, S. Drellack, D. Reed, T. Kincaid, K. Day, "Three-dimensional seismic-attribute model for Yucca Flat," in *Site-Directed Research and Development*, FY 2014, National Security Technologies, LLC, Las Vegas, Nevada, 2015, 225–231.

Snelson, C. M., R. E. Abbott, S. T. Broome, R. J. Mellors, H. J. Patton, A. J. Sussman, M. J. Townsend, W. R. Walter, "Chemical explosion experiments to improve nuclear test monitoring," *Eos, Trans., American Geophysical Union* **94**, 27 (July 2013) 237–239.

Predictive Radiological Background Distributions from Geochemical Data

RSLN-23-14 | Continued from FY 2014 | Year 2 of 2

Piotr Wasiolek,[1,a] Russell Malchow,[a] Pamela Burnley,[b] Elisabeth Hausrath,[b] Kara Marsac,[b] Daniel Haber,[b] Racheal Johnsen,[b] and Christopher Adcock[b]

Aerial radiological surveys have a decades-long history of use in prospecting, consequence management, and search applications. Recent experience during the Fukushima nuclear power plant accident exposed the need for better knowledge of the normal radiological landscape before a radioactive release occurs, and modern search algorithms are increasingly making use of a priori data to estimate anticipated background radiation distributions. This project made use of available information in the form of existing geochemical data, geologic maps, remote sensing data, and sparse radiological data to create high-resolution maps of estimated background radiation levels.

[1] wasiolpt@nv.doe.gov, 702-295-8728
[a] Remote Sensing Laboratory–Nellis; [b] University of Nevada, Las Vegas

Background

This project devised a method to use existing geologic data to predict gamma ray background levels as measured during aerial radiological surveys. Foreknowledge of the background is valuable for a variety of homeland security and disaster response purposes. Detectable components of the gamma ray background come from the rocks and soil within the first 40 cm of the earth's surface and should therefore be predictable based on an understanding of the geochemistry of the rocks on the surface. We used geologic maps, remote sensing imagery, the National Uranium Resource Evaluation (NURE) low-resolution national airborne gamma ray spectrometry survey (Duval 2005) database, and bedrock and soil geochemical data from existing databases and the scientific literature to create surface geochemical models. By comparing predicted with observed background values, we refined our modeling strategies in order to produce a protocol that can be used by others.

During an actual consequence management mission, knowledge of pre-contamination background may be limited. The ability to estimate pre-release backgrounds will improve data products that are produced for customers. Benefits for radiological search include providing a location-specific map of natural radiation anomalies to help rule out false positives in direct radiation measurements and delineating spatial variability of radiation to help select optimized search techniques and parameters (Kock 2014).

Project

An ideal background radiation model would predict the gamma radiation point by point across the surface, where the background at each point was modeled independently from each adjacent point. However, such a model would be impractical to construct. Instead, we sought to subdivide the region over which the model extends into geographic units over which

average characteristics can be assigned. For the sake of discussion, these geographic areas are referred to as "background radiation units." The premise of this study is that we can define background radiation units using geologic maps combined with remote sensing imagery and assign radiation characteristics based on available geochemical data. To test this hypothesis, in FY 2014 (Malchow 2015), we chose test areas (Cameron, Arizona; Government Wash, Nevada; and the region around the Aerial Measuring System (AMS) calibration line along the shore of Lake Mohave, Nevada, for which the DOE AMS had pre-existing aerial survey data. The preliminary results from these test areas were used in FY 2015 to target several additional test areas in the Twin Peaks volcanic field in southwestern Utah for which AMS conducted aerial gamma ray surveys.

Test Areas

AMS conducted a radiological survey of the Cameron, Arizona, area in 1997 as part of the Abandoned Uranium Mines Project conducted by the U.S. Army Corps of Engineers and the U.S. Environmental Protection Agency (Hendricks 2001). The region around Cameron consists largely of gently dipping Permian and Triassic sedimentary rocks, partially obscured by Pleistocene and Pliocene basalt flows, overlain by Quaternary alluvial sediments, some of which are associated with the Little Colorado River and its tributaries. Exposure rates in this area range from about 2.4 to 67 µR/hr, with the majority of the area below 12 µR/hr. High exposure rates are associated with localized uranium mineralization within the Triassic sediments.

Government Wash lies just east of Las Vegas, Nevada. This area consists primarily of Quaternary alluvium, which fills a broad valley rimmed by Tertiary gypsum-rich lacustrine sediments interbedded with Tertiary alluvial sediments. The wash area is used for training flights by AMS. Exposure rates in this area range from about 1.11 to 6.89 µR/hr, with an average of 3 µR/hr.

The Lake Mohave calibration line lies on the western shore of Lake Mohave, which is located on the Nevada/Arizona state line south of Lake Mead. The area is entirely composed of alluvial sediments shed from mountains to the west containing crystalline basement and volcanic rocks. In addition to the calibration line that is regularly flown by AMS, an 8.4-square-mile area around the calibration line was surveyed by AMS in the second year of this project. Exposure rates in the area range from about 5.45 to 9.95 µR/hr, with an average of 8.63 µR/hr.

The Twin Peaks volcanic field in west-central Utah contains a wide range of volcanic rocks from basalts to rhyolites. Lower elevations (<5200 ft) in the region were submerged beneath Quaternary Lake Bonneville and covered by varying amounts of lacustrine sediments; some areas are covered by active sand dunes. Localized outcrops of lacustrine limestone deposited ~2.5 million years ago in caldera lakes are also present. Exposure rates in the Twin Peaks area range from 2.3 to 15.3 µR/hr, with an average of 6.7 µR/hr.

Background Radiation Units

For the test areas in Nevada and Arizona, we obtained geographic information system (GIS) shape files from the most recent state geologic maps (Duebendorfer 2003, Billingsley 2007, House 2008), which reasonably captured spatial variation of rock types as seen in the satellite imagery available in Google Earth. For Government Wash, the shape file with the geologic boundaries was corrected so it better followed lithologic boundaries as observed on satellite images from Google Earth. The bedrock units of the Twin Peaks volcanic field in Utah were based partially on maps done at various scales by Haugh (1978) and Crecraft (1981) that were modified and updated at the 1:12,000 scale by Johnsen (2014). Alluvial and lacustrine units were based largely on the Richfield 30' × 60' quadrangle map (Hintze 2003). Although many geologic formations contain only a single rock type and therefore might reasonably be expected to have homogeneous geochemical properties, in some instances there are lithologic variations within geologic formations. This is particularly true of sedimentary bedrock and especially Quaternary alluvial units, which are

mapped by geologists based on their age of deposition rather than composition. In order to subdivide such units into background radiation units, we used multispectral images based on bands that are sensitive to the mineralogy of surficial materials (Sabins 2007). Spectral bands were chosen based on the mineralogy observed using x-ray diffraction on soil samples and geologic unit descriptions that list the lithologies observed within the sedimentary bedrock formations. Band math strategies were developed to maximize the differences in signals coming from various lithologies.

Remote sensing imagery was classified by two methods. In the first method, the images were clipped to the spatial extent of the alluvium and classified into five classes using the Iso Cluster Classification tool in ArcGIS. In Cameron, the images were further subdivided by creating a union between the classified image and the geologic polygons. The second method was devised to reduce the effects of shadows and noise in the images. The pixels were normalized using the histogram equalize tool; tonal differences were then reduced using the Segment Means Shift tool, both in ArcGIS. The image was then classified using the Reclassify tool. An example of the first method is shown in Figure 1, which uses a 2:1 band ratio image.

Data Analysis

AMS Data

Legacy AMS data from the Cameron area consisted of only geolocated exposure rates. Raw geolocated spectral data for Government Wash and Lake Mohave were provided to the University of Nevada, Las Vegas (UNLV). The spectra were corrected for non-terrestrial contributions using flight lines at survey altitude over Lake Mead and Lake Mohave. Altitude spirals were used to correct for air attenuation. Exposure rates were calculated from gross counts, and potassium (K), uranium (U), and thorium (Th) extractions were performed using the technique outlined by the International Atomic Energy Agency (2003). For flights over the Twin Peaks volcanic field, AMS performed non-terrestrial corrections, topographic corrections, and K, U, Th extractions.

In order to compare the predicted exposure rates with the measured exposure rates for each background

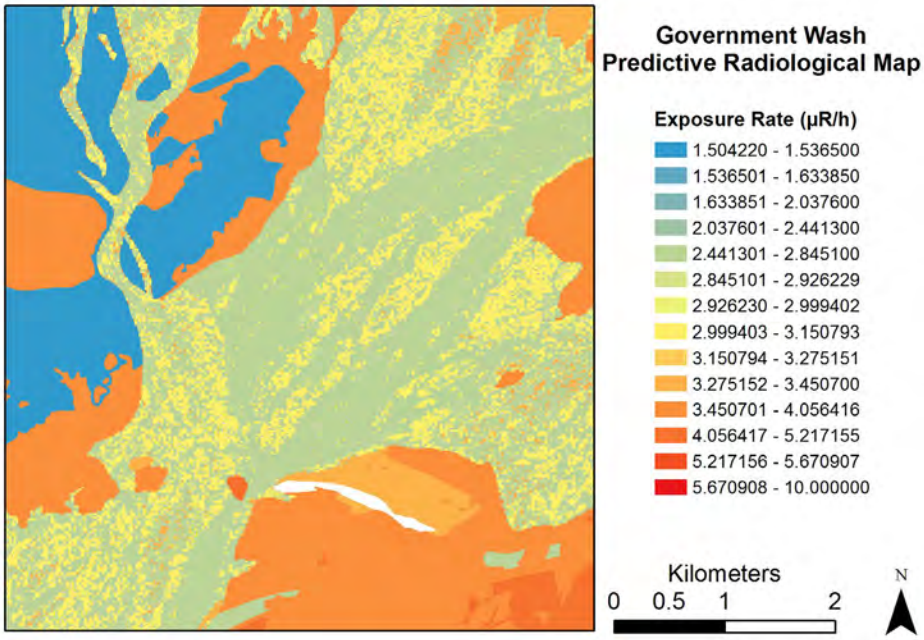

Figure 1. Predictive map based on a geologic map of Government Wash, Lake Mead, Nevada, combined with the remote sensing–derived subunits within the Quaternary alluvium unit

radiation unit, we used GIS shape files to capture the AMS data points. The means and standard deviations of the exposure rates (and K, equivalent uranium [eU], and equivalent thorium [eTh] values, if available) for each unit were calculated and chosen to represent that unit. Here "equivalent" means that uranium and thorium are assumed to be in secular equilibrium with their daughter isotopes.

Geochemical Data

For the test areas in Arizona and Nevada, we obtained geolocated geochemical analyses of K, U, and Th in geologic formations relevant to each area from national databases (U.S. Geological Survey [USGS] 2008, Max Planck Institute of Chemistry [MPIC] 2014, Interdisciplinary Earth Data Alliance [IEDA] 2015) and private industry (Turner 2013). We evaluated the metadata attached to each analysis as well as the geochemical data (USGS 2008, Turner 2013, MPIC 2014, IEDA 2015) itself for consistency with the mapped rock types at the reported location (Duebendorfer 2003, Billingsley 2007, House 2008); data that did not meet these criteria were discarded. The remaining analyses were grouped according to the geologic unit in which they occurred. For some units in Cameron, Arizona, the distribution of U content in bedrock units contained extremely high outliers. Therefore, for units with multiple analyses, the median values of K, U, and Th were used to calculate an exposure rate for each unit. For the Twin Peaks volcanic field, we obtained geochemical analyses from published material, including Crecraft (1981) and Johnsen (2010, 2014). Because the units are homogeneous, we were able to use the mean values of K, U, and Th.

NURE Aerial Survey Data

Another source of geochemical information is the NURE national airborne gamma ray spectrometry survey, which gives K and equivalent U and Th values (Duval 2005, Hill 2009). The survey covers much of the United States with flight lines spaced between 1 and 10 km. We used ArcGIS to capture the NURE data into the background radiation units and then calculated the mean and standard deviation for K, U, and Th for each unit. In the Cameron study area, there are eight east/west NURE flight lines and one north/south flight line. Two NURE flight lines cross the immediate vicinity of Government Wash, and nine lines are located over the western shore of Lake Mohave. Data from five flight lines are available in the Twin Peaks volcanic field.

Exposure Rate Calculation

Exposure rates for each background radiation unit were calculated from K, U, and Th geochemical analysis as well as from K, eU, and eTh values from the NURE survey using the relationship from Grasty (1984) as updated by Duval (2005):

$$D = 1.32K + 0.548eU + 0.272eTh. \quad \textbf{(1)}$$

With the concentrations K in percent potassium, and eU and eTh in ppm of equivalent uranium and equivalent thorium, respectively, D will be in µR/hr. We used MCNP to investigate the effect of variations in composition and density of basalt, gabbro, granite, rhyolite, limestone, and gypsum-rich siltstone and found that the changes in the coefficients were insignificant for this range of material. Therefore, to be consistent with other work, we continued to use the coefficients from Duval (2005).

Results and Discussion

In order for a background model to be useful, it needs to predict the probability of obtaining a given exposure rate at any particular location. Thus, the predictive background models can be evaluated on two separate criteria: (1) how close the predicted average exposure rate over a given background radiation unit is to the measured average exposure rate and (2) how small the standard deviation of exposure rates, both predicted and observed, is over the background radiation unit to which the predicted average is applied. With regard to the first criterion, our goal is to model the average exposure rate within ±1 µR/hr. With regard to the second criterion, we reason that if the standard deviation of the exposure rate over a background radiation unit is smaller than the standard deviation of exposure rates over the larger region in which the background

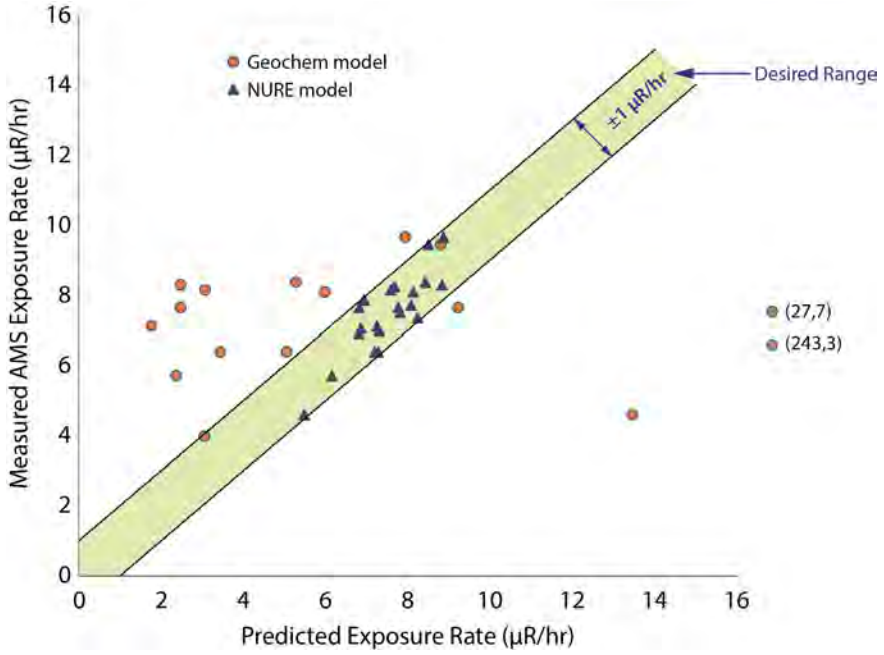

Figure 2. Predicted exposure rates from (1) geochemical data (circles) and (2) median K, eU, and eTh values over geologic units reported by the NURE survey (triangles), plotted against measured exposure rates over geologic units in Cameron, Arizona. For the two outliers that fall beyond the range of the plot, the predicted and measured exposure rates are noted beside the data points.

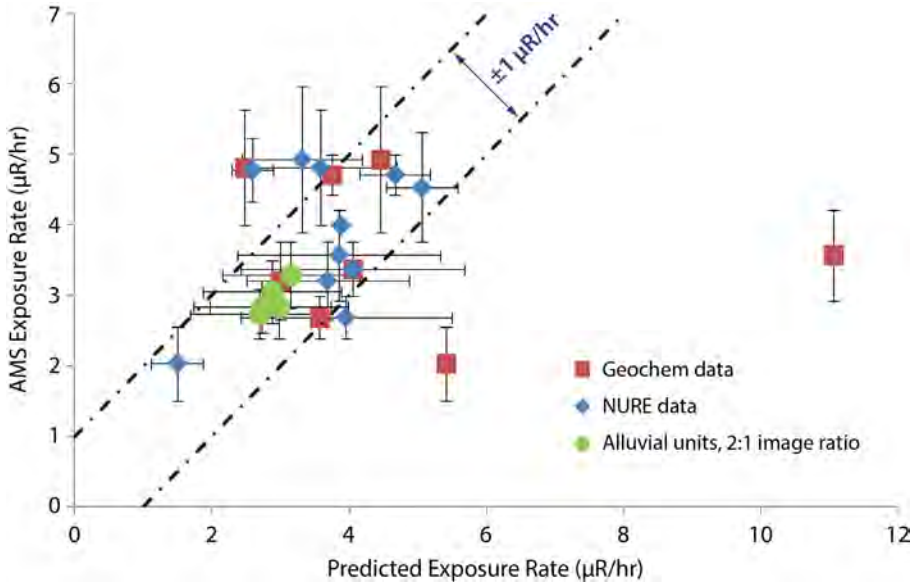

Figure 3. Predicted exposure rates calculated from (1) geochemical data (squares), (2) median K, eU, and eTh values over geologic units reported by the NURE survey (diamonds), and (3) alluvial units only from classified images having a 2:1 ratio from ASTER (Advanced Spaceborne Thermal Emission and Reflection Radiometer) data (circles), plotted against measured exposure rates in Government Wash, Lake Mead, Nevada. Error bars are 1 standard deviation.

radiation unit sits, then the background radiation unit has achieved some degree of homogeneity over a random division of the larger area into subunits.

Figures 2–5 compare predicted and observed median exposure rates for radiation background units in each of the test areas.

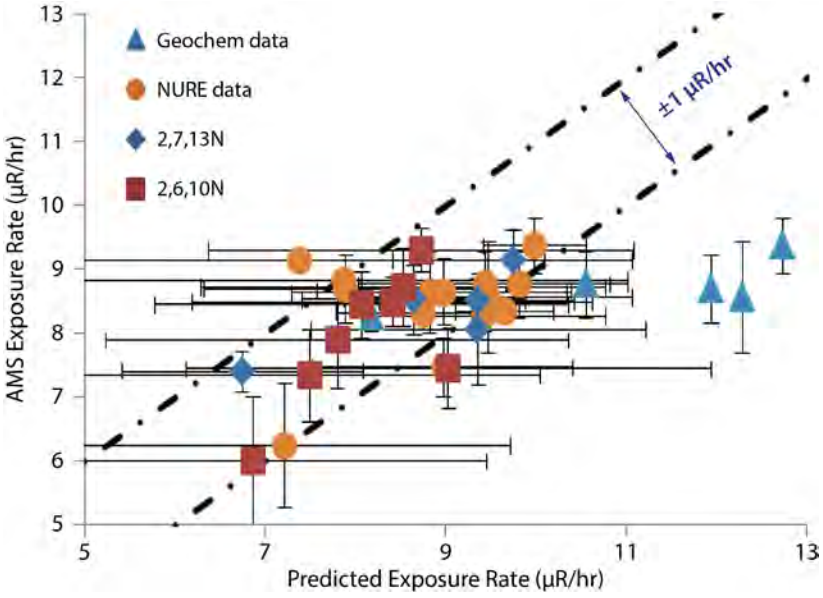

Figure 4. Predicted exposure rates calculated from (1) geochemical data (triangles), (2) median K, eU, and eTh values over geologic units reported by the NURE survey (circles), (3) NURE data segmented by a 2,7,13 ASTER band combination (diamonds), and (4) NURE data segmented by a 2,6,10 band combination (squares), plotted against measured exposure rates over geologic units at Lake Mohave, Nevada. Error bars are 1 standard deviation.

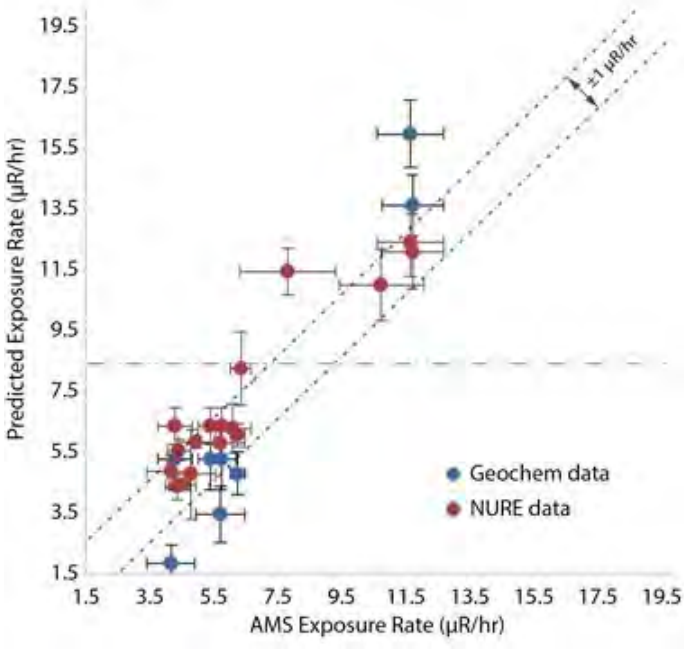

Figure 5. Predicted exposure rates calculated from (1) geochemical data (blue circles) and (2) median K, eU, and eTh values over geologic units reported by the NURE survey (red circles), plotted against measured exposure rates over geologic units in the Twin Peaks volcanic field, Utah. The dashed line at 8.4 µR/hr indicates exposure rate of regional dust calculated from geochemistry as reported by Reheis (2009). Error bars are 1 standard deviation.

In all areas studied, NURE data are able to predict the average exposure rate over most geologic units to within 1 µR/hr, whereas predictions from geochemical data are far less reliable. Over alluvial units, predictions can be improved by combining classification of remote sensing band math imagery with the NURE data. A

variety of problems, including poor geolocation and lack of metadata, generates challenges for predictions from bedrock geochemistry. However, these issues cannot account for differences between predicted and observed exposure rates in the Twin Peaks volcanic field in Utah, where we have precise field location information and metadata. The elimination of this type of problem in the Twin Peaks study area allows us to examine the underlying causes of difference between bedrock chemistry and surface chemistry—the desert soil–forming processes, eolian deposition, and weathering. By examining Figure 5, it can be noted that for units with high exposure rates, the chemical data over-predict the exposure rate; in contrast, for units with low exposure rates, the geochemical data under-predict the exposure rate. Using Equation 1, the chemistry of regional eolian dust as reported by Reheis (2009) translates to 8.4 µR/hr. For all but two units, the observed exposure rate can be generated from a combination of the bedrock geochemistry and the dust geochemistry.

Conclusion

Over the course of this 2-year project, we have determined that the application of geochemical data from the literature to predicting background radiation using Equation 1, while qualitatively similar, does not constrain backgrounds quantitatively at the desired levels. We have, however, demonstrated a successful method for extrapolating low-resolution NURE background radiation survey data using background radiation units based on a combination of geologic maps and remote sensing.

Acknowledgments

We gratefully acknowledge the assistance of Ralf Sudowe of UNLV, Jez Stampahar of the Remote Sensing Laboratory–Nellis, and the DOE AMS for the use of their data.

References

Billingsley, G. H., S. S. Preist, T. J. Felger, *Geologic Map of the Cameron 30′ × 60′ Quadrangle, Coconino County, Northern Arizona*, U.S. Geological Survey, 2007.

Crecraft, H. R., W. P. Nash, S. H. Evans, Jr., "Late Cenozoic volcanism at Twin Peaks, Utah—Geology and petrology," *Journal of Geophysical Research* **86**, B11 (1981) 10303–10320.

Duebendorfer, E. M., *Geologic Map of the Government Wash Quadrangle, Clark County, NV*, Nevada Bureau of Mines and Geology, Reno, Nevada, 2003.

Duval, J. S., J. M. Carson, P. B. Holman, A. G. Darnley, "Terrestrial radioactivity and gamma-ray exposure in the United States and Canada," 2005-1413, U.S. Geological Survey Open-File Report, 2005, http://pubs.usgs.gov/of/2005/1413/, accessed September 19, 2014.

Grasty, R. L., J. M. Carson, B. W. Charbonneau, P. B. Holman, "Natural Background Radiation in Canada," *Geo. Surv. Can. Bull.* **360** (1984).

Haugh, G. R., "Late Cenozoic, cauldron-related silicic volcanism in the Twin Peaks area, Millard County, Utah," *Brigham Young University Studies* **25**, 3 (1978) 67–82.

Hendricks, T. J., "An aerial radiological survey of abandoned uranium mines in the Navajo nation," DOE/NV/11718--602, Bechtel Nevada, 2001.

Hill, P. L., R. P. Kucks, D. Ravat, "Aeromagnetic and aeroradiometric data for the conterminous United States and Alaska from the National Uranium Resources Evaluation (NURE) Program of the U.S. Department of Energy," 2009-1129, U.S. Geological Survey Open-File Report, 2009.

Hintze, L. F., D. D. Fitzhugh, P. D. Rowley, C. G. Cunningham, T. A. Steven, G. C. Willis, *Geologic Map of the Richfield 30′ × 60′ quadrangle, southeast Millard County and parts of Beaver, Piute, and Sevier Counties, Utah*, Utah Geological Survey Map 195, 2 plates, 2003.

House, P. K., J. E. Faulds, *Preliminary Geologic Map of the North Half of the Spirit Mtn. Quadrangle, Clark County NV and Mohave County AZ*, Nevada Bureau of Mines and Geology, 2008.

Interdisciplinary Earth Data Alliance (IEDA), EarthChem, 2015, http://www.earthchem.org, accessed May 1, 2014.

International Atomic Energy Agency, "Guidelines for radioelement mapping using gamma ray spectrometry data," International Atomic Energy Agency, 2003.

Johnsen, R. L., E. I. Smith, R. F. Biek, "Subalkaline volcanism in the Black Rock Desert and Markagunt Plateau volcanic fields of south-central Utah," *Utah Geological Association Publication* **39** (2010) 109–150.

Johnsen, R. L., E. I. Smith, J. D. Walker, "The 2.7–2.1 Ma Twin Peaks Caldera: Stratigraphy and petrogenesis," *Utah Geological Association Publication* **43** (2014) 617–638.

Kock, P., "On background radiation gradients—The use of airborne surveys when searching for orphan sources using mobile gamma-ray spectrometry," *J. Environ. Rad.* **128** (2014) 84–90.

Malchow, R., P. Burnley, E. Hausrath, K. Marsac, D. Haber, C. Adcock, "Predictive radiological background distributions from geologic data," in *Site-Directed Research and Development*, FY 2014, National Security Technologies, LLC, Las Vegas, Nevada, 2015, 193–201.

Max Planck Institute of Chemistry (MPIC), *Geochemistry of Rocks of the Oceans and Continents*, http://georoc.mpch-mainz.gwdg.de/georoc/, accessed May 1, 2014.

Reheis, M. C., J. R. Budahn, P. J. Lamothe, R. L. Reynolds, "Compositions of modern dust and surface sediments in the Desert Southwest, United States," *Journal of Geophysical Research* **114** (2009) F01028.

Sabins, F. F., *Remote Sensing: Principles and Interpretation*, 3rd edition, Waveland Press, Long Grove, Illinois, 2007.

Turner, L., DIR Exploration, Inc., Palisade, Colorado, 2013.

U.S. Geological Survey (USGS), "Geochemisty of rock samples from the National Geochemical Database," U.S. Geological Survey, Reston, Virginia, 2008.

Ultrafast All-Optical Framing Technology

LAO-02-2013 | Continued from FY 2014 | Year 3 of 3

Daniel Frayer,[1,a] Gene Capelle,[b] Daniel Marks,[a] and Aaron Bernstein[c]

Current methods of recording multiple-frame images at short timescales are limited by electro-optic tube physics and radiometry. We developed a novel all-optical methodology for the capture of a high number of quasi-continuous effective frames of 2-D data at very short timescales (from $<10^{-12}$ to $>10^{-8}$ seconds), with potential improvement over existing framing camera technology in terms of short recording windows and effective number of frames. Our concept combines a chirped laser pulse that encodes temporal phenomena onto wavelength, a strong hyperchromatic lens to map wavelength onto axial position, and a recording technology, such as holography or plenoptic imaging, to capture the resultant focal stack in both spatial (imaging) and longitudinal (temporal) axes. The third year of this project focused on demonstrating algorithmic feasibility and further development of the discretized pulse technique. A considerable effort was also made to develop a separate, analogous technique, compressed ultrafast photography, based on coded masks.

[1] frayerdk@nv.doe.gov, 505-663-2090
[a] New Mexico Operations–Los Alamos, [b] Special Technologies Laboratory, [c] University of Texas at Austin

Background

Many methodologies are currently available for capturing optical phenomena at ultra-short timescales (less than 1 ns), but they suffer from a number of limitations. The temporal resolution of framing cameras employing electro-optic tubes is limited by tube physics, in the case of single-tube imaging, and radiometry, in the case of multiple-path configurations using either tubes or microchannel plates. The temporal resolution of electro-optic streak cameras can be substantially higher but with the loss of an entire dimension of spatial data. Recent innovations using different phenomena offer improvements over these methods. Time-resolved imaging of non-repeating events with a megahertz frame rate, using a broad-spectrum illumination source and dispersive optics, has been demonstrated by Goda (2009); time-resolved imaging of repeating phenomena with picosecond resolution, using an ultrafast streak camera in a time-of-flight configuration, has been demonstrated by Velten (2011). The viability of a methodology for recording a pair of frames with 50 fs spacing has been demonstrated by Günther (2011). Nakagawa (2014) published a methodology employing a discretized chirped laser, in combination with beam splitters and an imaging sensor, to actively illuminate and record multiple frames of femtosecond phenomena. Finally, Gao (2014) published a method for using streak cameras and coded masks to produce 2-D movies of dynamic events at very high effective frame rates.

We have developed a novel all-optical methodology for the capture of a high number of quasi-continuous effective frames of 2-D data at very short timescales (from $<10^{-12}$ to $>10^{-8}$ seconds), with potential temporal improvement over existing technologies, for specific application in light-matter interaction studies and potential application in broader dynamic studies. This

methodology combines three essential components: (1) A chirped laser pulse interacts with a dynamic experiment, mapping temporal information from the experiment onto wavelength. (2) A hyperchromatic lens, designed to maximize the change in the position of its focus as a function of incident illumination wavelength, images this light to create a focal stack of images of the experiment, such that each narrow slice along the optical axis contains an image from a narrow slice of time. (3) An integrating 3-D recording technology captures the focal stack with axial position information in toto; this technology may be a plenoptic camera or a hologram (digital or film). The scheme is illustrated in Figure 1.

Compared to the method developed by Nakagawa (2014), we expect our use of a diffraction-limited hyperchromatic lens (rather than high-f/# optics and beam splitters) to offer improved spatial resolution, and our use of a 3-D recording mechanism (rather than either multiple image sensors or a single long sensor) potentially improved temporal resolution. However, as our method maps time onto space, improving either resolution would detriment the other. In recent years, hyperchromatic lens systems have been developed for use in several fields, including confocal microscopy (Garzon 2004, Carrasco-Zevallos 2011, Hillenbrand 2012a), topography (Mikš 2007), and hyperspectral imaging (Hillenbrand 2012b). However, to our knowledge, our methodology is the first to employ hyperchromats in ultrafast imaging. Additionally, published hyperchromatic designs have been relatively simple, with low longitudinal chromatic aberration, whereas our method requires much higher longitudinal chromatic aberration and therefore substantially higher complexity.

Project

During this project's first year (Frayer 2014a), the three described components of the technology (hyperchromatic lens, chirped laser, and recording system) followed three separate, parallel paths of inquiry: (1) Design and fabrication of the hyperchromatic lens resulted in a final system design with a peak longitudinal chromatic aberration of nearly 9 mm/nm, reducing demands on input illumination bandwidth. A complete description, including the dispersion curve for the final system and the complex optical design, is available in Frayer (2014b). (2) Investigation into laser sources with appropriate specifications concluded that our requirements could be met through substantial development, or at a large research-grade laser facility already employing pulse chirping in chirped-

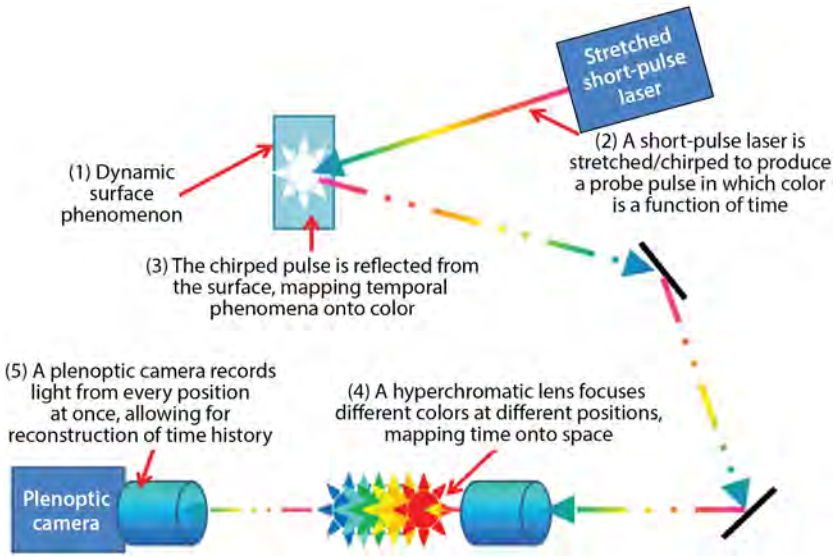

Figure 1. The ultrafast all-optical system experimental and recording methodology

pulse amplification. (3) Investigation into recording methods concluded that focusing plenoptic imaging, as employed in cameras produced by Raytrix GmbH of Kiel, Germany, would offer the most straightforward and likely path to data capture and reconstruction. We purchased a custom R29 camera from Raytrix in the same year.

The second year of this project (Frayer 2015) saw investigation along similar lines: We worked with laser physicists and manufacturers to investigate alternatives for laser sources, and developed a novel technique for producing discretized quasi-chirped pulses. We initiated a subcontract with the University of Texas at Austin (UTA) for preliminary validation experiments at their laser facilities. We worked with Raytrix GmbH towards modification of their reconstruction algorithm to allow for complete reconstruction of captured data. Additionally, we investigated modes of extending our methodology into non-active illumination experiments.

In the project's current and final year, we (1) worked closely with our Raytrix collaborators, internal subject matter experts, and additional external researchers to modify the Raytrix algorithm to reconstruct captured data; this work also included extensive calibration and characterization of the hyperchromatic lens. (2) We continued development of the discretized-pulse illumination scheme towards possible fielding on an ablation experiment in a shadowgraphy configuration at the NSTec Special Technologies Laboratory (STL). (3) We also investigated Gao's methods (2014) and developed a preliminary technique that improved upon the published work and offered the potential for implementation in the x-ray regime.

Algorithm Development for Data Reconstruction

Throughout FY 2015, we worked with Raytrix GmbH towards enabling their proprietary data capture and reconstruction algorithm to capture and reconstruct the kind of focal stacks produced by a chirped illumination pulse and the hyperchromatic lens. Raytrix's software operates on the underlying assumption that the scene that is recorded is opaque and spatially unique (i.e., each point in (x,y) contains data in focus only at a unique (z) position). Our methodology violates this assumption, however, as the hyperchromat may produce a focused image of one or more points within the recorded scene over an axial extent Δz for a single (x,y) position, indicating no apparent change at (x,y) over some temporal extent corresponding to Δz. During FY 2014, company representatives expressed confidence in Raytrix's ability to modify their algorithm to capture and reconstruct data, and this work continued into FY 2015.

After we found that no affordable tunable laser sources with the required bandwidth and center wavelength were commercially available, we developed a method for characterizing the performance of the hyperchromatic lens with a chirped pulse, using a continuous-wave monochromatic laser source. This method consisted of mapping wavelengths across the required spectrum to equivalent positions at the object plane of the lens, thus exchanging a spectrum of illumination light focused at a single object position for a single wavelength of illumination light focused over a range of object positions. This method, in conjunction with basic image math, also proved capable of producing representative surrogate focal stack datasets that were sent to Raytrix for baselining reconstruction attempts in their development effort (Figure 2). Using surrogate datasets provided an advantage over real datasets insofar as real datasets are captured using an integrating recording device, so individual slices in the focal stack must be reconstructed to be seen. Surrogates, on the other hand, are effective focal stacks produced by first recording slices and adding them, thereby providing a built-in method for checking any reconstruction. At the same time, we pursued the possibility of recording datasets from actual experiments at UTA, but due to facility shutdowns and upgrades, this possibility was not realized.

Unfortunately, Raytrix determined at the conclusion of their effort that producing a viable algorithm would require resources beyond this project; consequently, we discontinued the effort. Shortly after, however, Raytrix located recent research done by a radiography

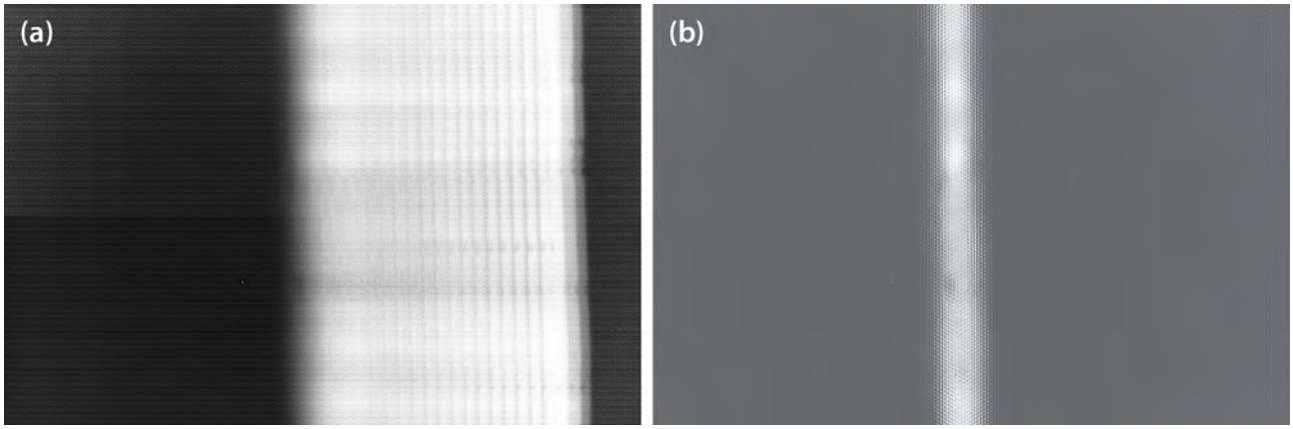

Figure 2. (a) A representative surrogate dataset produced by adding discrete "slices" and (b) exemplar slice

group at the University of Laval (Goulet 2014) that held promise. Goulet describes the use of a Raytrix plenoptic camera to capture data from a 10 × 10 × 10 cm^3 scintillating volume irradiated by a linear accelerator, and reconstruct the shape of the volume with 2 × 2 × 2 mm^3 resolution, a volumetric resolution more than adequate for our purposes. Dr. Archambault, a coauthor and researcher at the university, expressed interest in a potential collaboration despite the limited time available, and indicated that, although the Laval algorithm had not been optimized, it was developed for spatially non-unique datasets similar to ours. Raytrix delivered several surrogate datasets that fit communicated requirements to Dr. Archambault. Unfortunately, we have been unable to make further progress in this collaboration due to the project timeline. We may also conclude from these conversations that our methodology is more sound than previously thought and implementing the described technique should in principle be possible. It should be noted that a patent application for the hyperchromatic lens for recording time-resolved phenomena (Frayer 2016) was submitted to the U.S. Patent and Trademark Office, and we await the outcome of the application process.

A Method for Producing Discretized Pseudo-Chirped Pulses

In addition to algorithm development, we pursued development of the discretized pseudo-chirped pulse method invented in FY 2014. In this method, output from an untuned dye laser is focused onto the slit of an imaging spectrograph, and a linear fiber array is positioned at the output plane of the spectrograph. The fiber bundle is connected to fiber extensions of varying lengths such that each fiber along the linear array is incrementally longer than the previous fiber; thus, the transit time of light in each successive fiber is longer than that in the previous, so output from the sum of discrete fibers mimics a discretized chirped pulse.

We determined that a shadowgraph of a laser ablation of a surface would provide the simplest way to demonstrate the technique in conjunction with the 3-D imaging technology generally pursued under this project. We first assembled a basic shadowgraph system as follows. A Big Sky Nd:YAG laser at 1064 nm, pulsed, about 12 ns FWHM pulse width was focused (f = 8 cm) onto various ablation targets, including a bare aluminum rod and the same rod wrapped with burn paper. The 532 nm output from the same laser was initially split off and run through a delay line for backlighting illumination before implementation of the described dye-based technique. Light from the experiment was captured using a 6-megapixel Nikon SLR camera and an f = 500 mm catadioptric lens with extension tubes at a 44.5" standoff. It should be noted that, whereas the 532 nm light produced noticeable speckle and diffraction effects, these were obviated by the broader spectral content of the dye-based illumination.

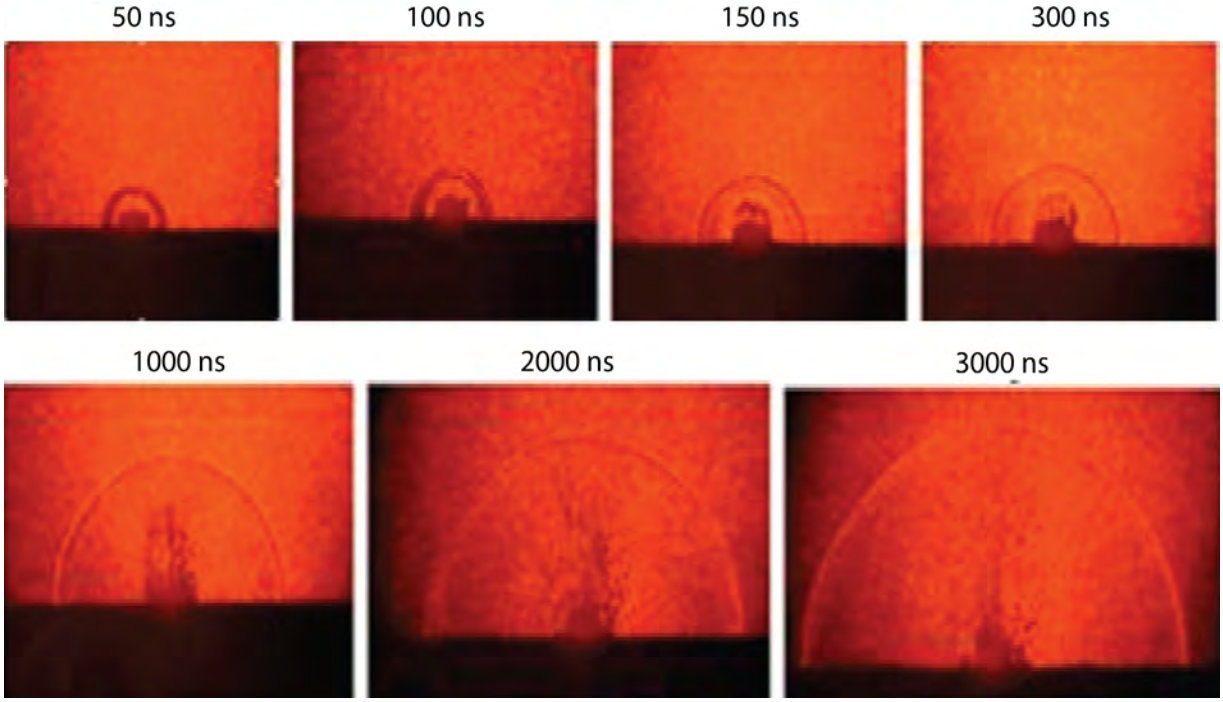

Figure 3. Images captured at delay times from 50 to 3000 ns from the ablation pulse. At 50 and 100 ns, a mass of ablated material in the center is surrounded by a shock wave. By 150 ns particulates appear.

The dye-based technique was implemented by coupling a single 100 µm core fiber to the imaging spectrograph, and butt-coupling the far end to a 400 µm core fiber to emulate a single channel of a larger multichannel system in which the larger fiber collects and mixes light from the individual channels to produce a common illumination path for the pseudo-chirped pulse. The larger fiber was terminated in a Thorlabs fiber collimator to provide illumination for the experiment. The laser energy emerging from the single-channel system was 0.2 µJ; additional bandpass filters between the target and the detector, used to remove generated light from the ablation plasma, reduced the light to the camera to ~50 nJ. The illumination pulse was run through a delay leg to mimic, over the course of multiple experiments, the presence of multiple spectral channels. Images captured at different delay times over multiple experiments using burn paper are contained in Figure 3. Although the scheme was successfully demonstrated, it was implemented shortly after we discontinued algorithm development; therefore, a multichannel system was never implemented with the hyperchromatic lens and Raytrix camera. A provisional patent application for the long-pulse-width variable-wavelength chirped laser pulse (Capelle 2015) was submitted to the U.S. Patent and Trademark Office.

Compressed Ultrafast Photography in the X-Ray Regime

Gao's paper (Gao 2014) on compressed ultrafast photography (CUP) describes a method for imaging non-repetitive dynamic phenomena by combining a coded spatial mask and a streak camera. The CUP technique was not the first technique in which streak cameras were used to capture 2-D information using 1-D detectors, as NSTec (Bender 2007) and others have developed optical tomographic systems towards similar ends, but it appeared to obviate shortcomings of tomographic methods. We realized both the potential applicability to dynamic experiments of interest to the weapons complex and NSTec's historical strength in streak camera development and operation, but also the complementarity of CUP to that investigated under this project. As such, given the apparent risks

associated with the Raytrix development effort, we began to explore the method's applicability, usefulness, strengths, and weaknesses. We determined that the CUP technique was well suited for NSTec's historical strengths and experimental needs, and could be readily applied to both near-term and long-term development efforts; some potential applications were presented at the 2015 IEEE Pulsed Power Conference (Marks 2015a). The improvements we developed include the incorporation of multiple views, using either rotation or non-identical mask matrices, to substantially improve reconstruction; we also developed recommendations for further improvements realizable in future work. A provisional patent application for these improvements (Marks 2015b) was submitted to the U.S. Patent and Trademark Office. Our advancements in the CUP technology were featured in a successful FY 2016 SDRD proposal for the project "Multi-Frame X-Ray Imaging Using a Streak Camera with Patterned Photocathode" (LAO-008-16).

Recommendations for Future Work

A collaboration between NSTec, Raytrix, and the University of Laval (or associated entity) could prove fruitful in applying the techniques developed successfully by Goulet (2014) to our methodology. In addition, the energy output and channel count of the current pseudo-chirped pulsed generator configuration needs to be substantially increased to make it a viable illumination source for this or similar systems (such as a diagnostic developed using our modified CUP approach).

Conclusion

During this project's final year, we made progress in developing a novel algorithm for capturing and reconstructing data. We successfully demonstrated a single channel of the discretized pseudo-chirped pulse illumination scheme on an ablation shadowgraphy experiment at STL. We built upon the work of Gao (2014) and developed a preliminary technique that improves substantially upon the published work and offers the potential for effective implementation in the x-ray regime. We did not successfully demonstrate our described ultrafast optical recording technique from experiment through data capture and reconstruction; however, we have good reason to believe that it is possible, given research published by Goulet (2014). This work resulted in one patent application, two provisional patent applications, and one SDRD project in FY 2016.

Acknowledgment

We would like to thank Christian Perwass of Raytrix GmbH for his significant contributions to this effort.

References

Bender, H., C. Carlson, D. Frayer, D. Johnson, K. Jones, A. Meidinger, C. Ekdahl, "Quasianamorphic optical imaging system with tomographic reconstruction for electron beam imaging," *Rev. Sci. Instrum.* **78**, 1 (2007) 013301.

Capelle, G. A., D. K. Frayer, "Long-pulse-width variable-wavelength chirped laser pulse," U.S. Provisional Patent 62,236,096, filed October 1, 2015.

Carrasco-Zevallos, O., R. L. Shelton, C. Olsovsky, M. Saldua, B. E. Applegate, K. C. Maitland, "Exploiting chromatic aberration to spectrally encode depth in reflectance confocal microscopy," *Proc. SPIE* **8086** (2011).

Frayer, D., "Ultrafast all-optical framing technology," in *Site-Directed Research and Development*, FY 2013, National Security Technologies, LLC, Las Vegas, Nevada, 2014a, 207–213.

Frayer, D. K., M. I. Kaufman, G. A. Capelle, "A hyperchromatic lens for recording time-resolved phenomena," *Proc. SPIE* **9193** (2014b).

Frayer, D., G. Capelle, A. Bernstein, "Ultrafast all-optical framing technology," in *Site-Directed Research and Development*, FY 2014, National Security Technologies, LLC, Las Vegas, Nevada, 2015, 233–239.

Frayer, D. K., "A hyperchromatic lens for recording time-resolved phenomena," U.S. Patent 14,850,838, filed January 8, 2016.

Gao, L., J. Liang, C. Li, L. V. Wang, "Single-shot compressed ultrafast photography at one hundred billion frames per second," *Nature* **516**, 7529 (2014) 74–77.

Garzón J., J. Meneses, G. Tribillon, T. Gharbi, A. Plata, "Chromatic confocal microscopy by means of continuum light generated through a standard single-mode fiber," *J. Opt. A: Pure Appl. Opt.* **6**, 6 (2004) 544.

Goda, K., K. K. Tsia, B. Jalali, "Serial time-encoded amplified imaging for real-time observation of fast dynamic phenomena," *Nature* **458** (2009) 1145–1149.

Goulet, M., M. Rilling, L. Gingras, S. Beddar, L. Beaulieu, L. Archambault, "Novel, full 3D scintillation dosimetry using a static plenoptic camera," *Medical Physics* **41**, 8 (2014) 082101.

Günther, C. M., et al., "Sequential femtosecond x-ray imaging," *Nature Photonics* **5** (2011) 99–102.

Hillenbrand, M., B. Mitschunas, C. Wenzel, A. Grewe, X. Ma, P. Feßer, M. Bichra, S. Sinzinger, "Hybrid hyperchromats for chromatic confocal sensor systems," *Advanced Optical Technologies* **1**, 3 (2012a) 187–194.

Hillenbrand, M., A. Grewe, M. Bichra, B. Mitschunas, R. Kirner, R. Weiß, S. Sinzinger, "Chromatic information coding in optical systems for hyperspectral imaging and chromatic confocal sensing," *Proc. SPIE* **8550** (2012b) 85500D.

Marks, D., D. Frayer, "Compressed streak imaging beam diagnostic," *IEEE Pulsed Power Conference (PPC)* (2015a) 1–6.

Marks, D. G., "Compressed sensing improvements," U.S. Provisional Patent 62,238,648, filed October 7, 2015 (2015b).

Mikš, A., J. Novák, P. Novák, "Theory of chromatic sensor for topography measurements," *Proc. SPIE* **6609** (2007) 66090U.

Nakagawa, K., et al., "Sequentially timed all-optical mapping photography (STAMP)," *Nature Photonics* **8** (2014) 695–700.

Velten, A., R. Raskar, M. Bawendi, "Picosecond camera for time-of-flight imaging," *Imaging Systems Applications, OSA Technical Digest*, Optical Society of America, Toronto, Canada (2011).

This page left blank intentionally

Exploration of High Miller-Index Crystals as High-Energy X-Ray Imaging Optics

LO-02-2015 | Year 1 of 1

Jeffrey A. Koch,[1,a] Joshua J. Lee,[a] and Michael J. Haugh[a]

Near normal–incidence spherically bent crystals are widely used as x-ray imaging optics for a variety of applications, including high energy-density physics (HEDP) applications at Sandia's Z machine, the Omega Laser Facility, and short-pulse laser laboratories worldwide. Geometrical optics requires these crystals to operate near normal–incidence, and inter-atomic spacings are limited to at least several angstroms, so these crystals are generally only useful for x-ray energies up to several keV. Higher energies, above 10 keV, have previously required high-order reflections where the lattice $2d$ happens to match an integral number of wavelengths. We instead explored high Miller-index crystals, operated in the first diffraction order, as an alternative to high-order reflections from low Miller-index crystals. We tested a flat germanium (15,7,7) crystal and compared its performance to calculations. We find good agreement with one calculation, benchmarking our ability to calculate the reflectivity of uncommon high Miller-index crystals, as well as to measure crystal reflectivity at high x-ray energies suitable for HEDP experiments. This lays the groundwork for new spherically bent imaging applications at high x-ray energies.

[1] kochja@nv.doe.gov, 925-960-2525
[a] Livermore Operations

Background

Near normal–incidence spherical, toroidal, and ellipsoidal bent crystals are widely used for quasi-monochromatic x-ray imaging applications (Pikuz 1995, Aglitskiy 1998, Uschmann 2000, Koch 2003, Akli 2011, Stoeckl 2012). These systems can provide very large–collection solid angles when the angle of incidence is close to normal and the crystal quality is high, and can be very efficient when used with narrow-band emission line sources (Koch 1998). Applications include high-energy density physics (HEDP) plasma imaging in the light of bright lines, either in emission or absorption geometries, with Bragg angles $\theta_B > 80°$, following the Bragg equation $n\lambda = 2d\sin\theta_B$.

Typical interatomic spacings d are several angstroms, so efficient common crystal plane reflections with θ_B close to 90° are matched to wavelengths λ of several angstroms, or up to several keV x-ray energy. Such matches are coincidental and discrete, and are improbable for any particular x-ray line of interest. At higher x-ray energies, the Bragg condition cannot be satisfied with low-order (n = 1) reflections from common crystal planes having low Miller indices (h,k,l), so typically one resorts to using high-order (n > 1) reflections from common crystal planes (Pikuz 1995, Koch 2003, Akli 2011). This can allow imaging at higher x-ray energies, but does not increase the likelihood of chance matches having θ_B close to 90°. It also ensures that lower-energy x-rays matching the Bragg condition in lower orders will also reflect, complicating interpretation of monochromatic imaging data.

An alternative approach to near normal–incidence imaging at high x-ray energies is to utilize uncommon crystal planes having high Miller indices, operated in first-order (n = 1). In principle, there are a large number of such planes available, with closely spaced Bragg angles as (h,k,l) become large, but these uncommon planes are generally untested and have unverified reflectivities. Exploration of this alternative approach to high-energy x-ray imaging, specifically with near normal–incidence bent germanium (Ge) crystals, provided the motivation for this research.

Project

We obtained a flat Ge crystal, 12.5 × 40 × 0.1 mm in dimensions, cut with the (15,7,7) plane parallel to the surface by Inrad Optics, from Lawrence Livermore National Laboratory. The crystal was bonded to a flat 50 mm diameter laser mirror substrate to aid handling. Ge is a diamond-cubic structure crystal, with an interplanar spacing d determined by Fraenkel (1990),

$$d = \frac{5.6576\text{Å}}{\sqrt{h^2 + k^2 + l^2}}, \quad (1)$$

and with allowed reflections having (h,k,l) either all odd, or all even with $(h+k+l)$ being an integer multiple of 4. The (15,7,7) cut therefore has $2d$ = 0.6296 Å, corresponding to 19.693 keV at normal incidence. This would be a close match for imaging highly ionized ruthenium (Ru) He-α ($^3P_1$ upper state) at 19.717 keV with a Bragg angle of 87°.

To measure the integrated reflectivity of the crystal, we set the mounted crystal in front of a fluorescent-foil high-energy x-ray source, the HEX (Lee 2012). The geometry is shown in Figure 1. The fluorescing foil was silver (Ag), which emits primarily Ag K-α and K-β lines superimposed on a bremsstrahlung continuum, with additional contributions from Compton-scattered Ag lines on the low-energy wings, through an 11.3 mm collimator and an adjustable slit aperture. The system was aligned using an autocollimating alignment telescope, and the angle of incidence along the principal ray intersecting the center of the crystal was set using a precision rotation stage relative to normal incidence as determined by the alignment telescope.

Significant effort was required to mitigate Ag K-line x-rays that scattered off the walls, optical table, optics mounts, and the x-ray collimator aperture on the HEX source. Adequate mitigation required substantial lead shielding and the use of a tantalum slit aperture between the source and the crystal (Figure 1). Exposures were from 16 to 90 hours total due to the low brightness of the source and to the narrow rocking curve of the crystal, putting a stringent requirement on maximum acceptable background levels. Long exposure durations were controlled by turning the source on and off, while short (~ seconds) exposures

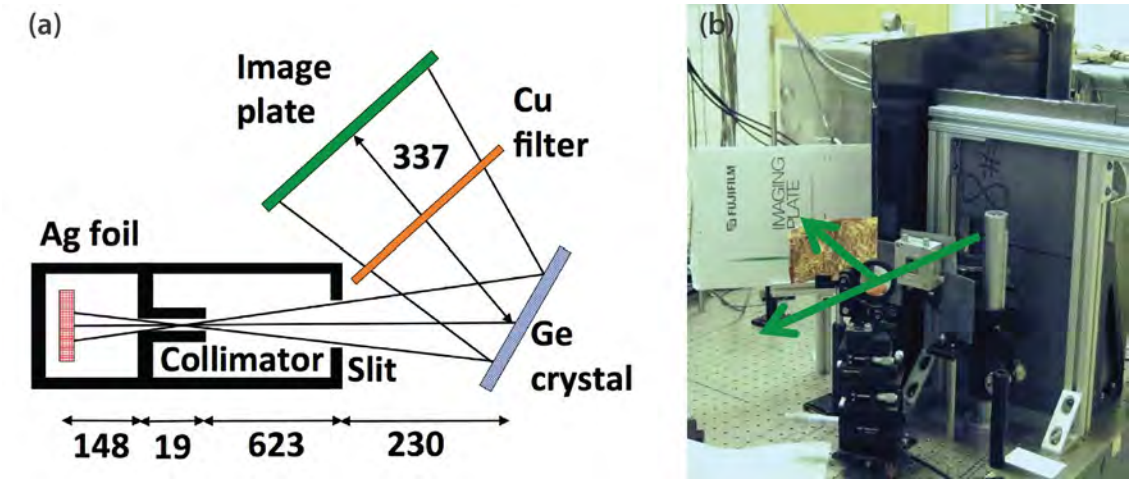

Figure 1. (a) The HEX source experimental geometry (dimensions in mm) and (b) a commercial x-ray tube (not shown) illuminates a large Ag foil with x-rays, and the foil fluoresces primarily in Ag K-α

were controlled by a thick beam block serving as a 50 ms shutter. We used a 25 µm copper foil as an x-ray filter between the Ge crystal and the detector (Figure 1), primarily to reduce Ge K-α fluorescence backgrounds.

The detector for all experiments was an SR-type image plate that was characterized previously (Maddox 2011), and exposures were scanned using 200 µm pixels on a General Electric Healthcare Typhoon FLA 9500 flatbed image plate scanner. A characteristic of image plates is that the accumulated signal fades over time, so a correction must be applied to account for fade due to both the duration of the exposure and to the unavoidable delay between the end of the exposure and the start of scanning (Maddox 2011). Image plates can be absolutely calibrated for exposure in photostimulated luminescence (PSL) units, but because our system is not yet absolutely calibrated, we work throughout with the squares of the (square-root compressed) .gel file outputs from the scanner. These exposure units are proportional to PSL units when the scanner settings are unchanged, which was the case for these experiments.

The large effective source size (11.3 mm) and large divergence sufficed to illuminate the crystal at multiple angles along its length, providing a source-broadened spectrometer geometry that illuminates multiple crystal planes at the correct Bragg angle simultaneously. In convenient coordinates, the normal vector for any plane (h,k,l) is

$$\vec{n} = \langle h,k,l \rangle, \quad \textbf{(2)}$$

so that as (h,k,l) become large, there are increasingly many planes that are nearby in angle and have similar $2d$ values. This results in a number of reflected x-ray spots on the image plate detector, from K-α_1 and K-α_2 as well as K-β, in a complex pattern.

Reflected exposure measurements (I, K-α_1 off the crystal) were combined with direct beam exposure measurements (I_0, direct spectrally integrated exposure with the crystal removed) to calculate the integrated reflectivity, as described below. The spectral content of the I_0 exposure was measured with an Amptek XR-100T-CdTe spectrometer and convolved with the spectral response curve of the image plate (Maddox 2011) and the transmission curve of the copper (Cu) filter (Henke 1993) to obtain the I_0 exposure fraction 0.73 from K-α alone. The relative fraction of K-α_1/(K-α_1 + K-α_2) was assumed to be 0.65 (Kortright 2001), negligibly different from the ⅔ value expected based on upper-state multiplicity alone, because the Amptek measurements could not resolve the K-α_1 and K-α_2 lines individually.

Representative image plate data are shown in Figure 2. The (15,7,7) plane reflects K-α_1 and K-α_2 near the center of the image plate, and numerous other reflections from different planes of Ge are also evident in a complex pattern, superimposed on a non-uniform background exposure likely caused by crystal and filter fluorescence, filter transmission variations, and residual Compton-scattered Ag K-line x-rays. All lines except the K-α_1 reflection from (15,7,7) reflect from off-center regions of the crystal surface, and so are clipped to

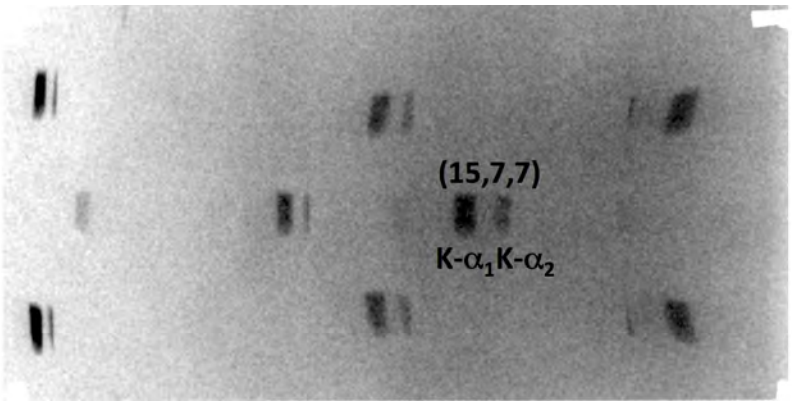

Figure 2. Image plate data from the experiment. The center of the 200 × 400 mm image plate was offset from the principal ray axis (K-α_1 of (15,7,7)) to record additional reflections on the far left.

varying degrees by either the edge of the crystal or the edge of the slit aperture, depending on system alignment.

We simulated the expected pattern of reflections with a custom Monte Carlo ray trace program written specifically for this purpose. Random source points and ray angles are propagated through the system for each of three emission lines (K-α_1, K-α_2, and K-β, each with E/ΔE = 2400 relative line width), and are allowed to reflect off any Ge crystal planes that happen to match the Bragg condition within rocking curve widths calculated by X0h (X0h 2015) and averaged for unpolarized light. We used Equations 1 and 2 to determine the $2d$ spacing and normal vector for each reflection plane, relative to the (15,7,7) normal vector that is the surface normal. The geometry of Figure 1 was used with the correct dimensions and angles, under the assumption that the crystal was flat and aligned exactly, and relative intensities for the source lines were obtained from Kortright (2001).

Figure 3 shows a grayscale simulated image plate exposure from this ray trace, which is in good agreement with the experimental data shown in Figure 2. This agreement allows us to identify each of the reflected patterns as being due to a specific (h,k,l) plane and emission line wavelength. In addition to (15,7,7), we observe (15,5,7), (15,7,5), (15,5,5) = 5th order of (3,1,1), as well as (14,8,2), (14,2,8), (14,4,2), (14,2,4), (14,10,8), (14,8,10), and (16,4,4) = 2nd order of (8,2,2). Many additional reflections would be visible on a larger image plate. Slight differences between the measured vs. simulated patterns are likely due to differences between the actual system alignment and the ideal alignment. The mounted crystal is also slightly curved. As mounted, we measured a large (several meter) concave radius of curvature that does not significantly affect subsequent analysis, but that will slightly shift the line positions on the image plate.

The largest angular term in our spectral measurements is source broadening from the 11.3 mm collimator aperture. This implies that with careful alignment, the widths of the crystal rocking curve and the K-α_1 emission line are negligible, and the source size does not enter into the integrated reflectivity calculation. This is confirmed by ray tracing. Therefore, the rocking curve width cannot be measured with this system because it is too narrow, but the integrated reflectivity over the full rocking curve is simply

$$R_{\text{int}} = \frac{I\ (\text{total reflected exposure in PSL/s for K-}\alpha_1)}{\phi I_0\ (\text{mean incident exposure in PSL/s/Sr for K-}\alpha_1)}$$

$$\phi = \frac{\text{sagittal crystal width}}{\text{collimator to crystal distance}}. \qquad \textbf{(3)}$$

In the numerator I, we sum the image plate exposure in a region of interest (ROI) containing the (15,7,7) reflection of K-α_1, subtract a background sum obtained from a nearby ROI of the same size containing only background, divide by the exposure duration, and correct for image plate fade during the exposure and between the conclusion of the exposure and the start of scanning. In the denominator I_0, we determine a mean image plate exposure in a ROI in the center of

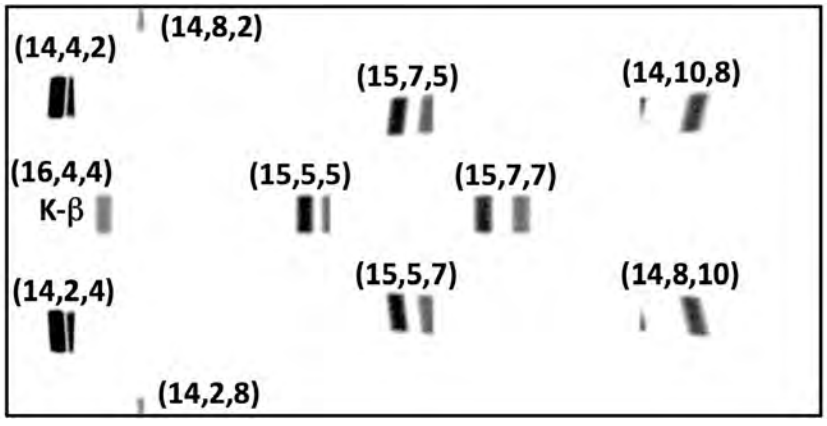

Figure 3. Grayscale, pixelized simulated image plate exposure (200 × 400 mm) generated by a custom ray trace program using the experimental geometry and source and crystal parameters

the field, subtract a background mean obtained from a nearby ROI containing only background, divide by the exposure duration, divide by the solid angle subtended by a pixel at the image plate distance, correct for the measured K-α_1 fraction of the incident spectrum, and correct for image plate fade during the exposure and between the conclusion of the exposure and the start of scanning.

Four I exposures and four I_0 exposures were obtained, with the entire system being realigned between each I exposure to ensure that alignment uncertainties were captured in the error bars. The resulting mean integrated reflectivity is 0.16 µrad for Ge (15,7,7) at Ag K-α_1, with ±20% error bars. The errors are dominated by variations in exposures and background exposures depending on the image plate data and ROIs used, with additional errors from uncertainty in the image plate fade correction (Maddox 2011) and the K-α_1 fraction in I_0. This compares with 0.10 µrad calculated by X0h and 0.56 µrad calculated by XOP (XOP 2015). The lower bound of the data range is 30% higher than the X0h calculation, while the upper bound is 66% lower than the XOP calculation. The reasons for the discrepancy between the X0h and XOP calculations are not known, and exploration of the discrepancies is outside the scope of this research, but either calculation suffices for better than order-of-magnitude estimates of the integrated reflectivity of a flat Ge crystal, even for obscure and untested crystal planes such as (15,7,7).

Conclusion

We have measured the integrated reflectivity of Ge (15,7,7) at Ag K-α_1 using a large-area, divergent x-ray source in a source-broadened spectrometer geometry. We find a value of 0.16 µrad ±20%, which compares to a calculated 0.10 µrad from X0h or 0.56 µrad XOP. We also observe many additional reflections of Ag K-α_1, K-α_2, and K-β from a variety of nearby crystal planes, and all have comparable reflectivity consistent with ray trace simulations that are in good agreement with the data.

Ge (15,7,7) would be a candidate for near normal–incidence bent-crystal imaging in the light of Ru He-α at 19.7 keV, with a Bragg angle of 87°. Scaling with $\tan\theta_B$, we would predict an integrated reflectivity of 1.6 µrad at this energy. An additional increase would be expected due to the bending of the crystal to a few-hundred millimeter radius of curvature (Haugh 2015), potentially bringing the integrated reflectivity up to >10 µrad, a level that is well-suited for practical applications when the emission line is suitably bright. One potential application is monochromatic imaging of hot imploded plasma at the National Ignition Facility (Miller 2004).

Demonstration of approximate (much better than order of magnitude) agreement between data and calculations for the integrated reflectivity of this obscure high Miller-index crystal plane of Ge provides support for the idea of expanding the probability of chance matches between other emission lines of interest and arbitrary crystal planes. High-order reflections from common low Miller-index planes are one option for high-energy x-ray imaging with Bragg angles near 90°, but a superior option is the use of nearby first-order reflections from high Miller-index planes that provide comparable reflectivity, greater flexibility in tuning the Bragg angle, and elimination of lower-order signal that would otherwise superimpose a lower-energy x-ray background and complicate monochromatic image data interpretation.

During the course of this project, we submitted two Technology Abstracts: “Germanium crystals for krypton helium-alpha line emission microscopy” (August 20, 2014) and “Method for imaging bulk motional velocities in plasmas” (March 16, 2015). The first of these is being prepared as patent application NSTec 14-A-17, and the second has been filed as provisional patent 62/142,985. Both relate to specific applications of high-energy monochromatic crystal imaging using high Miller-index crystals. This work also led to a new 3-year SDRD project, “X-Ray Doppler Velocimetry,” funded for 2016 as LO-004-16. An invited talk on the work was given by J. Lee at the SPIE Optics and Photonics conference in San Diego in August 2015 (Lee 2015), and a journal article (Koch 2015) summarizing the work was submitted to *Applied Optics* in September 2015.

Acknowledgments

We thank W. Hsing, O. Landen, B. Remington, and R. Stewart at the Lawrence Livermore National Laboratory for their contributions and early support.

References

Aglitskiy, Y., et al., "High-resolution monochromatic x-ray imaging system based on spherically bent crystals," *Appl. Opt.* **37**, 22 (1998) 5253–5261.

Akli, K. U., et al., "A novel zirconium Kα imager for high energy density physics research," *Rev. Sci. Instrum.* **82** (2011) 123503.

Fraenkel, B. S., Z. H. Kalman, "Monochromatic imaging of an x-ray synchrotron source," *Physica Scripta* **41**, 4 (1990) 400–403.

Haugh, M. J., J. J. Lee, K. D. Jacoby, C. Christensen, G. Loisel, "Determining the diffraction properties of a cylindrically bent KAP(001) crystal from 1 to 5 keV," *Proc. SPIE* **9591** (2015) 95910K.

Henke, B. L., E. M. Gullikson, J. C. Davis, "X-ray interactions: Photoabsorption, scattering, transmission, and reflection at *E* = 50-30,000 eV, Z = 1-92," *Atomic Data and Nuclear Data Tables* **54**, 2 (1993) 181–342.

Koch, J. A., et al., "High-energy x-ray microscopy techniques for laser-fusion plasma research at the National Ignition Facility," *Appl. Opt.* **37**, 10 (1998) 1784–1795.

Koch, J. A., et al., "4.5- and 8-keV emission and absorption x-ray imaging using spherically bent quartz 203 and 211 crystals," *Rev. Sci. Instrum.* **74** (2003) 2130.

Koch, J. A., J. J. Lee, M. J. Haugh, "High Miller-index germanium crystals for high-energy x-ray imaging applications," *Appl. Opt.* **54**, 34 (2015) 10227–10231.

Kortright, J. B., A. C. Thompson, "X-ray emission energies," in *X-ray Data Booklet*, A. C. Thompson, D. Vaughan, eds., 2nd edition, Lawrence Berkeley National Laboratory, Berkeley, California, 2001.

Lee, J. J., M. J. Haugh, G. LaCaille, P. Torres, "Calibrating of x-ray detectors in the 8 to 111 keV energy range and their application to diagnostics on the National Ignition Facility," *Proc. SPIE* **8505** (2012) 850508.

Lee, J., M. Haugh, J. Koch, "Exploration of High Miller Index Ge crystals in flat and bent geometries for imaging high-energy x-rays," *SPIE Optics + Photonics 2015*, San Diego, California, August 9–13, 2015.

Maddox, B. R., H. S. Park, B. A. Remington, N. Izumi, S. Chen, C. Chen, G. Kimminau, Z. Ali, M. J. Haugh, Q. Ma, "High-energy x-ray backlighter spectrum measurements using calibrated image plates," *Rev. Sci. Instrum.* **82** (2011) 023111.

Miller, G. H., E. I. Moses, C. R. Wuest, "The National Ignition Facility," *Opt. Eng.* **43**, 12 (2004) 2841–2853.

Pikuz, S. A., V. M. Romanova, T. A. Shelkovenko, T. A. Pikuz, A. Ya Faenov, E. Förster, J. Wolf, O. Wehrhan, "Use of higher-order reflection from mica crystals in x-ray spectroscopic investigations at 0.1–0.3 nm," *Quantum Electronics* **25**, 1 (1995) 16.

Stoeckl, C., G. Fiksel, D. Guy, C. Mileham, P. M. Nilson, T. C. Sangster, M. J. Shoup III, W. Theobald, "A spherical crystal imager for OMEGA EP," *Rev. Sci. Instrum.* **83** (2012) 033107.

Uschmann, I., K. Fujita, I. Niki, R. Butzbach, H. Nishimura, J. Funakura, M. Nakai, E. Förster, K. Mima, "Time-resolved ten-channel monochromatic imaging of inertial confinement fusion plasmas," *Appl. Opt.* **39**, 31 (2000) 5865–5871.

X0h, http://x-server.gmca.aps.anl.gov/x0h.html, accessed August 2015.

XOP 2.4, http://www.esrf.eu/Instrumentation/software/data-analysis/xop2.4, accessed August 2015.

Ultra-High-Sensitivity Fiber-Optic Links

STL-32-14 | Continued from FY 2014 | Year 2 of 2

E. Kirk Miller,[1,a] Kevin Lee,[a] and Eric Larson[a]

We have developed analog fiber-optic data links based on high-sensitivity electro-optic modulators, in order to improve recording of small voltage signals in electrically noisy environments. During the second year of the project, we continued work with Professor Nadir Dagli at the University of California, Santa Barbara, to improve the fieldability of novel modulator structures developed in his laboratory. We also made significant improvements in the demodulation and recording of small signals that will enable the fielding of improved fiber links across a broad range of experimental facilities.

[1] millerek@nv.doe.gov, 805-681-2237
[a] Special Technologies Laboratory

Background

Current analog fiber-optic links commonly use Mach-Zehnder (M-Z) electro-optic modulators, for which drive voltages are typically 3–5 V. Recent innovations in modulator design using III-V semiconductors, such as those used by Professor Nadir Dagli's group (Dogru 2013, Dagli 2015, Kim 2015) at the University of California, Santa Barbara (UCSB), have demonstrated drive voltages well below 0.5 V, opening up a new regime of sensitivity to small signals. Such devices have been demonstrated in the laboratory, but they have not been available as packaged components suitable for experimental use. Other technologies such as electro-optic polymer devices have been investigated (Buckles 2012) but are also not readily available.

Diagnostics currently struggling to record small signals in noisy environments include electrical conductivity measurements at the Joint Actinide Shock Physics Experimental Research facility, gamma and x-ray measurements at the National Ignition Facility (NIF) and the Sandia National Laboratories' Z machine, and RF recording systems used on high-explosives experiments at the National Center for Nuclear Security. All of these measurements and experiments would benefit from the significant increase in sensitivity from a new generation of optical modulators for long-distance data transmission along low-cost, lightweight, fiber-optic cable systems.

Our ultimate goals are to be able to detect small voltages output from detectors of various types and relay those signals via fiber-optic cables to remote digitizers. The existing systems employed at various sites across the complex are capable of peak-to-peak noise floors from ~2 mV at 100 MHz up to 20 mV at 10 GHz. A diagram of noise-floor values plus associated applications is shown in Figure 1. The fieldable improvement that we developed this year is a combination of higher light power and much higher RF amplification to improve small-signal recording capability by a factor of approximately 5 over previous generations. This insight will likely lead to improvements in other small-signal recording applications, including multiplexed photonic Doppler velocimetry (MPDV) and others.

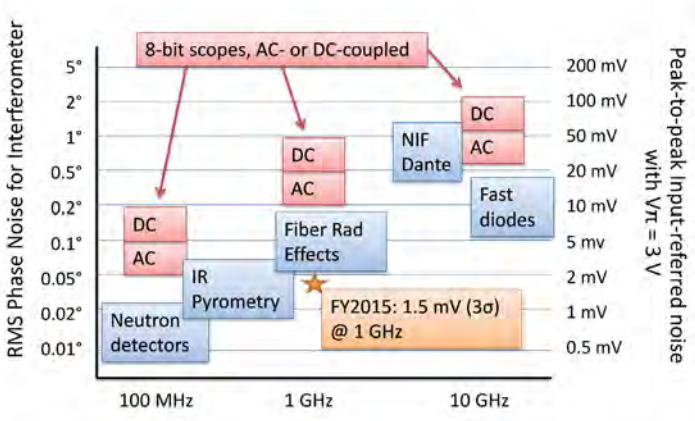

Figure 1. Past and current noise floor limitations for Mach-Zehnder fiber-optic links

Project

UCSB Modulator Development

The modulator architecture employed by UCSB is distinct from traditional modulator designs in that the electrodes providing the electric field are transparent to the 1550 nm light in the waveguide and, hence, can be in intimate contact with the waveguide. Traditional designs use a dielectric material, such as lithium niobate or electro-optic polymers with metallic electrodes patterned on top but separated from the waveguide by a buffer layer to avoid absorption by the metal. Typical spacing between the patterned electrodes is 20 µm. The UCSB design allows much higher electric fields to be applied across the waveguide, thus creating a strong electro-optic effect at a lower voltage. These "sandwich" electrodes are shown as n-type and p-type indium gallium arsenide (InGaAs) layers in Figure 2.

The primary task remaining on the path to a fieldable device based on this modulator design was to reduce the optical coupling loss between fiber input, semiconductor waveguide, and fiber output. Laboratory losses are typically ~25 dB; these devices would not be usable in the field, as only one part in three hundred of the launch light would make it through the modulator. To decrease the coupling losses, Professor Dagli's group undertook the design of a novel waveguide structure that uses well-known tapered structures to transition between waveguides of different mode-field diameters, and uses dielectric waveguides for light transport and for the light-splitting "Y-branches."

Optically, the device is bidirectional. Light is brought to the chip on an optical fiber with an optical mode approximately 9 µm in diameter. From there it couples to a polymer waveguide, using a well-characterized, thermally cured polymer known as SU8, which is well-matched to telecommunications fiber. Next, the light is transferred to a smaller silicon nitride (Si_3N_4) waveguide using a taper; the nitride waveguide is higher-index than the polymer, and so is better for making the Y-branches, which require stronger mode confinement. After the Y-branches, the light is transitioned into the semiconductor waveguide using another taper; the semiconductor structure is where the electric fields are applied to modulate the phase of the light and, hence, the intensity of the output of the M-Z interferometer. The conceptual structure is diagrammed in Figure 3.

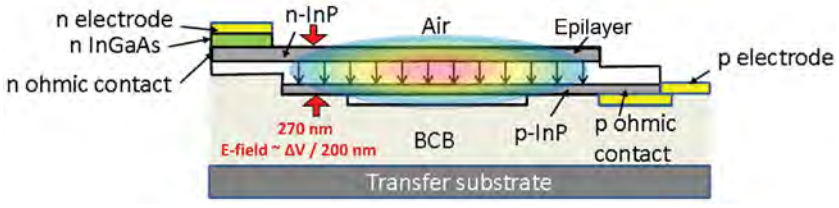

Figure 2. Sandwich electrode architecture on an InP waveguide used in UCSB modulators

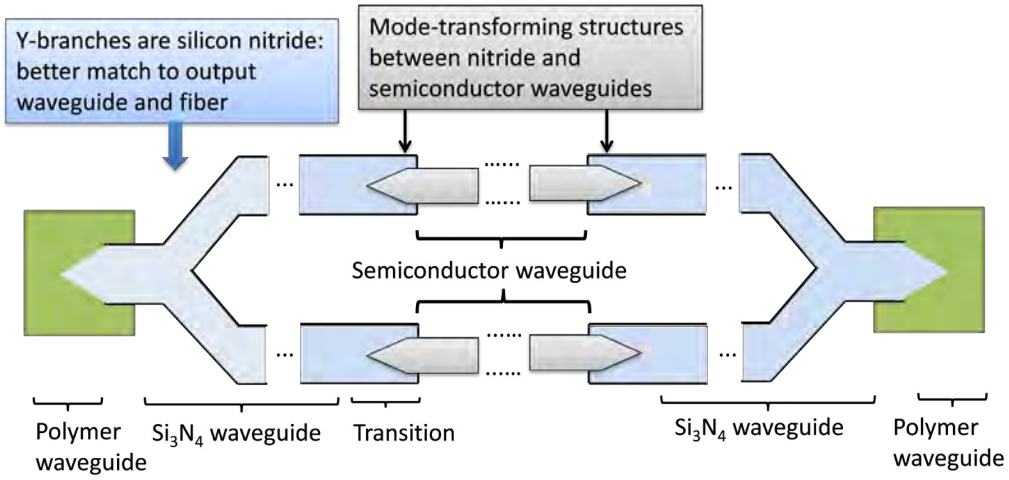

Figure 3. Conceptual diagram of the reduced insertion–loss modulator architecture being developed at UCSB

Progress during FY 2015 included the design, fabrication, and characterization of the taper structures between the polymer and the nitride waveguides, as well as design of a thermally tuned M-Z interferometer as a demonstration test bed. Unfortunately, the goal of a completed, chip-scale device suitable for packaging and field testing was not achieved, though some important elements of the design have been worked out and in future will be integrated with the other, more mature parts of the design, such as sandwich electrodes patterned in a traveling-wave RF configuration for high bandwidth.

To characterize the losses of the polymer-to-nitride transitions, hybrid structures were fabricated with straight waveguides and bent waveguides, plus varying numbers of tapered transitions. The straight waveguide structures were repeatedly measured and cleaved to determine the waveguide loss for each material. The polymer waveguide loss was measured at 4.6 dB/cm, and the nitride waveguide loss was 3 dB/cm. The high loss value for the polymer may be due to subsequent high-temperature curing of a different polymer, known as BCB, which is used as a mechanical member to facilitate material handling; a more common propagation loss value for the SU8 polymer waveguides is 2.4 dB/cm. The test structures are diagrammed in Figure 4. Three different taper-lengths were tested, ranging from 500 to 1200 µm; the longest taper typically gave the highest loss, though between 500 and 1000 µm the dependence on taper-length was weak. Another set of measurements on higher-quality samples will be made to isolate the effect of varying taper-length from the

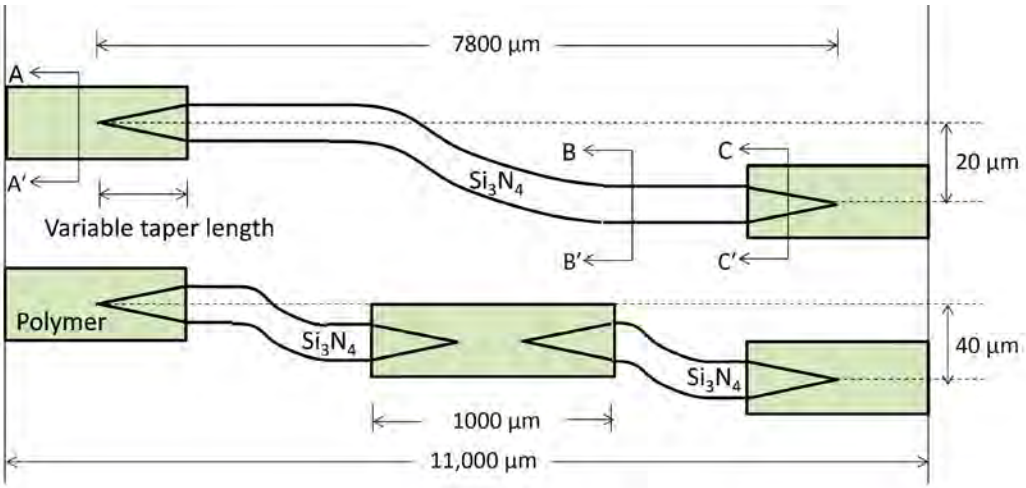

Figure 4. Test structures for characterizing tapered transitions between polymer and nitride waveguides

losses related to curing of the different polymers. UCSB will continue work on improving the processing of these structures to eliminate excess loss and integrate RF electrodes.

NSTec Improvements to Recording Systems

Any modulated light signal must have a high-quality recording system to accurately digitize the signal before data can be post-processed. While UCSB was making progress on improving modulator sensitivity, we made significant improvements in our understanding of the recording of optical signals that will positively impact all analog fiber links. Two important advances are discussed below: (1) improved small-signal response that will allow smaller signals to be recorded with existing fiber links and (2) a little-known demodulation scheme for phase-modulated signals that should allow more straightforward bias-free operation of fiber links.

The sensitivity of fiber links based on different configurations of M-Z modulators can be compared by normalizing the signal-to-noise ratio to the sensitivity of the (possibly voltage-attenuated) modulator. The sensitivity of a modulator is typically parameterized by its "half-wave voltage," denoted by V_π, the voltage required to shift the output intensity from minimum to maximum (i.e., through π radians of phase). A useful metric for the recording system of an analog M-Z link is the ratio of V_π to the RMS noise after "unfolding" the sinusoidal transfer function, V_π/RMS. This ratio quantifies the amount of noise relative to the recordable signal, in essence the available dynamic range of the link (assuming the full modulation can be recorded accurately).

With applications in the 10 GHz regime at a high technology readiness level, we focused on emerging applications with recording bandwidth requirements in the 1 GHz regime. Higher bit-count digitizers are starting to become available in this range, but the majority of the recording systems still employ 8-bit recorders. One unexpected observation was that by going to very high–gain photoreceivers, we can see smaller input signals above the overall noise floor.

A particularly good case study is the Thorlabs PDB-480C-AC, which is specified from 30 kHz to 1.6 GHz, with a conversion gain of approximately 12 V/mW. The amplifier output is linear to approximately 1.5 V (into 50 Ω), and for small modulation the receiver can be operated with DC light up to approximately +2 dBm (1.6 mW) single-ended or +5 dBm (3 mW) as a balanced receiver. The noise matched the vendor's specification of approximately 9 mV RMS total. The step-response, measured in single-ended configuration, showed a 1/*e* recovery time of approximately 4 µs, typical of a 250 kHz low-frequency cutoff, which is much higher than the specified 30 kHz low-frequency cutoff. The as-measured performance is summarized in Table 1.

Table 1. Performance of Thorlabs PDB-480C-AC Photoreceiver

Thorlabs PDB-480C-AC measured performance	
Conversion gain, single-ended, 1550 nm	~12 V/mW
RMS noise, 1 GHz bandwidth	~9 mV
DC light level max for small-signal linearity (single-ended)	~+2 dBm
DC light level max for full-modulation linearity (single-ended)	~–10 dBm
DC light level max for small-signal linearity (balanced)	~+5 dBm
Amplifier output linearity	~±1.5 V (specification is 1 dB compression at +16 dBm out)
Low-frequency cutoff	~250 kHz (specification is 30 kHz)

Small-Signal Recording

With the high gain of this receiver, we were able to record small signals at significantly better signal-to-noise ratio than is achievable using our more familiar receivers, with the NewFocus 1544B (conversion gain 1 V/mW) being the most common. We generated a step pulse that was then attenuated to approximately 14 mV amplitude for testing. The pulse was directly recorded using a Tektronix DPO4104 digitizer with 1 GHz analog bandwidth at 5 GS/s sampling rate. Then the same pulse was used to modulate an M-Z modulator with V_π of 5 V, and the recorded data were unfolded to return the input waveform. Figure 5 shows a small-amplitude input pulse, plus unfolded M-Z recordings using a NewFocus 1544B receiver and a PDB-480C-AC receiver. The signal-to-noise ratio is noticeably better with the very high–gain PDB receiver compared to the New Focus receiver. Also in Figure 5 is a plot of several different conditions and receivers that shows the increase in V_π/RMS as the effective DC light level is increased by different combinations of optical power and RF gain.

The improvement is significant and may prove valuable for other recording needs, such as MPDV or PDV. While adding more RF gain to an already amplified signal is not customarily done, it may be useful in driving the front end of high-bandwidth digitizers, so that the noise floor of the optical-to-electrical conversion can be driven up above the noise floor of the digitizer. With the noise floor set *before* the digitizer, more options open up for configuring the digitizer sensitivity to cover either smaller signals at high signal-to-noise ratio or larger signals by further reducing the sensitivity.

True, Instantaneous Optical Quadrature

One problem that has been addressed repeatedly in the open literature (e.g., Choma 2003) as well as in several previous SDRD efforts (Marshall 2007; Miller 2007, 2008) is the demodulation of a phase-encoded signal into optical quadratures (i.e., interferometric outputs that are locked at 90° out-of-phase) for recording. Modern telecommunications systems have quadrature demodulation devices, but these are designed as tightly integrated systems for digital demodulation, so are not well suited for laboratory

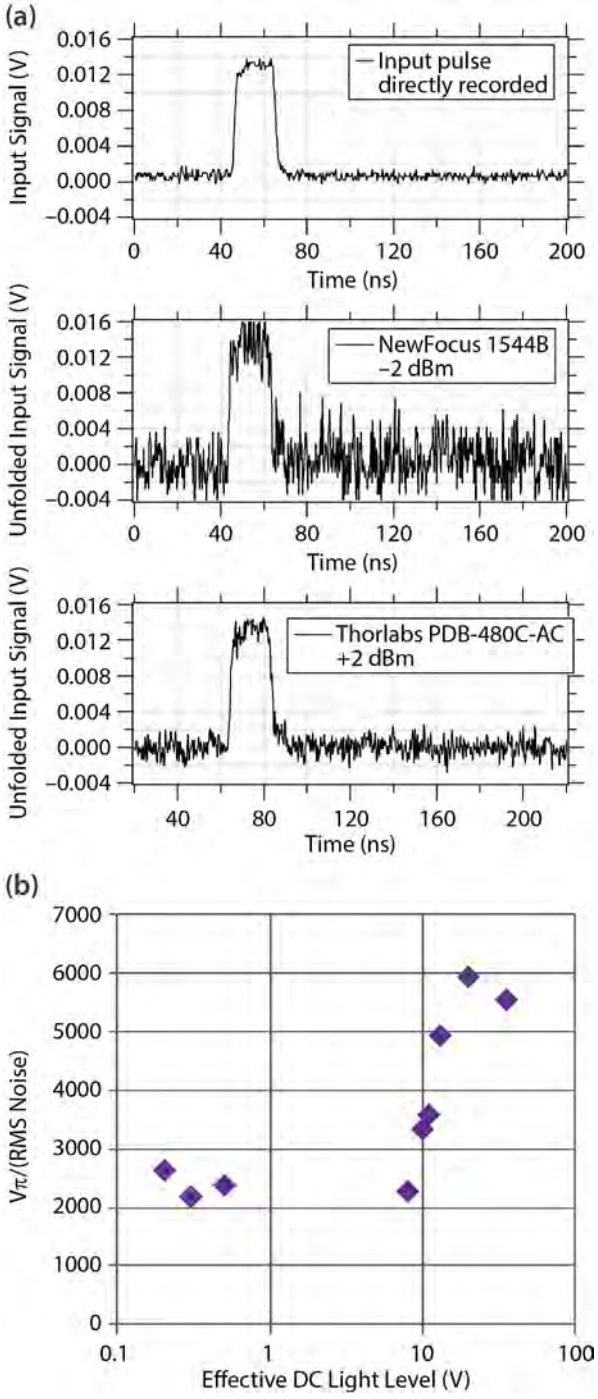

Figure 5. (a) Input signal and unfolded output signal and (b) V_π/RMS values for different effective DC light levels

use (Ip 2008). For laboratory applications requiring quadrature, the scientific and patent literature has a variety of contraptions that use polarization control, heated fibers, and other means of tweaking phase, usually with active feedback required to deliver reliable quadrature demodulation. Where simplicity is of the essence, researchers have repeatedly turned to the technique of using well-balanced 3×3 optical couplers to record three signals, each 120° out-of-phase with the others, and then computing the in-phase and quadrature signals algebraically. Such computation is not complicated, but if real-time data are required, or if analog RF techniques are to be used, then true quadrature is necessary.

The effect that we have uncovered is straightforward and flexible, and it should permit researchers to immediately generate quadrature signals for recording in a variety of applications from velocimetry to optical-coherence tomography. The technique is suitable to a wide range of wavelengths, bandwidths, and sensitivities, using off-the-shelf components. An interferometer based on a 3×3 coupler with well-matched outputs will have 120° phase shifts between its three outputs. For the time-varying part of the recorded intensity (i.e., in the limit that the reference and signal amplitudes are stable and not of specific interest), the difference between any two of those three outputs will be locked at 90° to the third. This technique is not entirely original, but the only direct reference to it in the literature that we uncovered is a paper by J. Pietzsch (1989). This new way of recovering quadratures, compared with the more computationally intensive three-channel system, is diagrammed in Figure 6.

To demonstrate this system, we used a pair of the Thorlabs PDB-480C-AC balanced receivers, one operated single-ended and the other operated in balanced mode to create the difference signal, together with a conventional 3×3 coupler, as diagrammed in Figure 6. The reference input was a laser with fixed frequency, and the signal was a separate laser whose frequency was offset by approximately 500 MHz from the signal and then modulated by approximately ±400 MHz with a period of approximately 5 µs. The heterodyne signal is then a variable frequency sine wave ranging from less than 100 MHz to more than 900 MHz.

One cycle of the modulation is shown in Figure 7a, with the spectrogram (top) showing the rapid change in frequency and the interferogram (or scope record, bottom) showing the signal amplitude compressing slightly as the signal frequency approaches the 3 dB bandwidth of the digitizer. To visualize the data, the points from 1.7 to 3.5 µs are color coded from purple to red. The same color coding applies in the X-Y Lissajous plot in Figure 7b, in which we plot the two

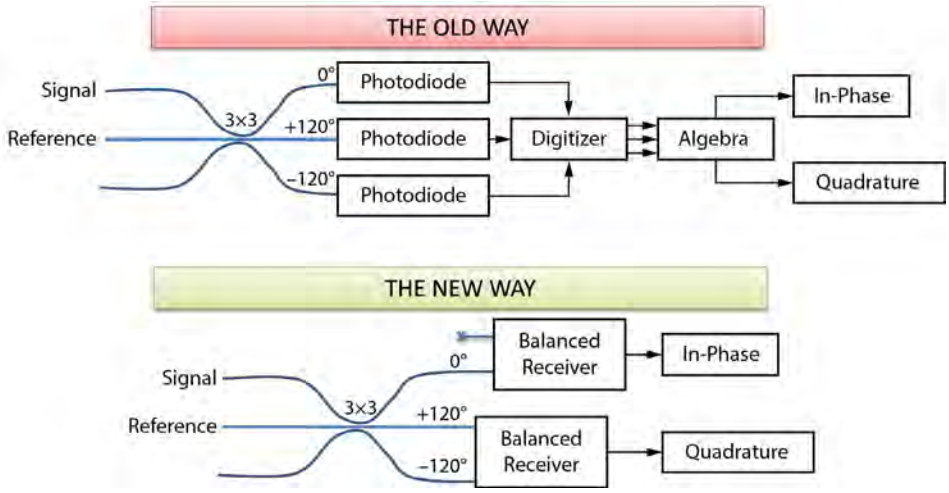

Figure 6. Diagrams for systems delivering quadrature signals using 3×3 couplers

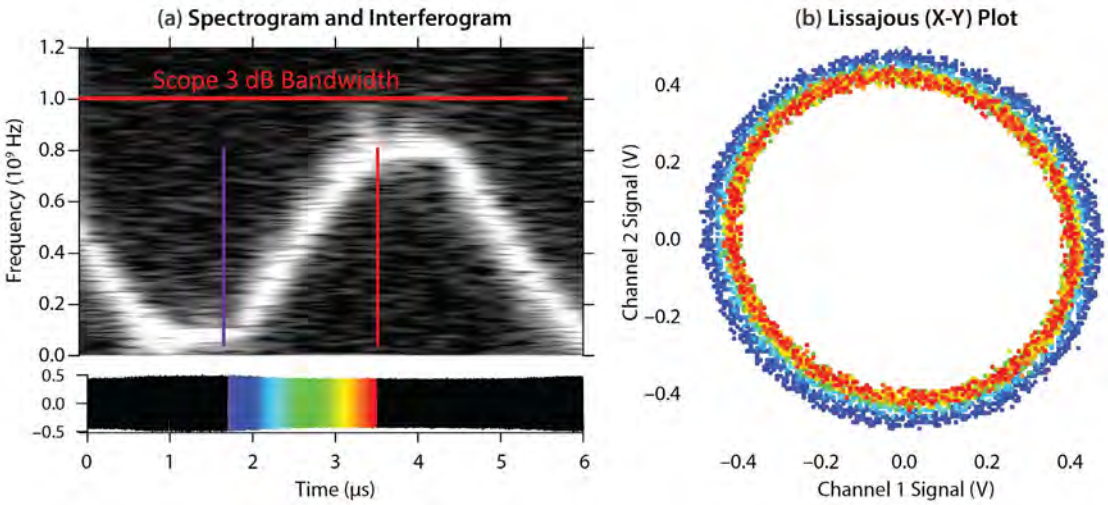

Figure 7. (a, top) Spectrogram and (bottom) one-channel interferogram, plus (b) X-Y Lissajous plot for frequency-modulated signal directly recorded using the new quadrature technique

recorded outputs of the photoreceivers against one another. As is evident, the phase is nearly 90° and quite stable across a heterodyne frequency range from 100 to 900 MHz, indicating that the quadrature is not an artifact of a time delay. The smaller radius of the red points is again caused by the reduced amplitude near the digitizer's bandwidth limit.

At this point, we believe that the phase offset from 90° is due to slight imbalances in the particular coupler, though for many applications, this offset might be tolerable. This technique will be useful for operation with, for example, a delay interferometer and phase modulator in analog electro-optic links where uniform signal-to-noise ratio is required over a large range of signals, or where supplying a DC electrical bias to an M-Z modulator is problematic.

Conclusion

We have made important advances in high-sensitivity electro-optic links in collaboration with Professor Nadir Dagli's research group at UCSB. Novel light-transport and delivery mechanisms for integration with high-sensitivity modulators have been developed and demonstrated on test structures, with the next step being integration into a fully functioning modulator with low optical-insertion loss. In addition, we have used high-gain receivers to achieve a factor of ~5 improvement in small-signal sensitivity recording that is compatible with all existing and future links. Finally, we have rediscovered and demonstrated a very useful technique for demodulating a phase-encoded signal to true, instantaneous optical quadratures using simple, robust components.

Acknowledgments

We would like to thank Professor Nadir Dagli and Mr. Prashanth Bhasker for the support at UCSB.

References

Buckles, R. A., E. Dutra, "Ultrafast Mach-Zehnders with chromophore polymers," in *Site-Directed Research and Development*, FY 2011, National Security Technologies, LLC, Las Vegas, Nevada, 2012, 245–257.

Choma, M. A., C. Yang, J. A. Izatt, "Instantaneous quadrature low-coherence interferometry with 3×3 fiber-optic couplers," *Opt. Lett.* **28**, 22 (2003) 2162–2164.

Dagli, N., N. K. Kim, P. Bhasker, S. Dogru, "InP based very-low voltage electro-optic intensity modulators in conventional waveguides," paper IM2B.2, in *Advanced Photonics 2015*, OSA Technical Digest, Optical Society of America, Boston, Massachusetts, 2015.

Dogru, S., N. Dagli, "0.2 V drive voltage substrate removed electro-optic Mach-Zehnder modulators with MQW cores at 1.55 μm," *J. Lightwave Tech.* **32**, 3 (2013) 435–439.

Ip, E., A. P. T. Lau, D. J. F. Barros, J. M. Kahn, "Coherent detection in optical fiber systems," *Opt. Express* **16**, 2 (2008) 753–791.

Kim, N. K., P. Bhasker, S. Dogru, N. Dagli, "Very low voltage InGaAlAs/InAlAs MQW core electro-optic modulators fabricated with conventional processing," paper MC3.2, *Proc. IEEE*, Reston, Virginia, October 4–8, 2015, 92–93.

Marshall, B., "Displacement interferometry," in *Nevada Test Site–Directed Research and Development*, FY 2006, National Security Technologies, LLC, Las Vegas, Nevada, 2007, 345–353.

Miller, E. K., "Quadrature optical modulator," in *Nevada Test Site–Directed Research and Development*, FY 2006, National Security Technologies, LLC, Las Vegas, Nevada, 2007, 369–375.

Miller, E. K., "Hybrid electro-optic links," in *Nevada Test Site–Directed Research and Development*, FY 2007, National Security Technologies, LLC, Las Vegas, Nevada, 2008, 303–309.

Pietzsch, J., "Scattering matrix analysis of 3×3 fiber couplers," *J. Lightwave Tech.* **7**, 2 (1989) 303–307.

Laser-Generated Ultra High–Energy Density Plasma for Fast Neutron Pulse Production and Neutron Diagnostic Development

LAO-04-15 | Continued in FY 2016 | Year 1 of 3

James Tinsley,[1,a] Alden Curtis,[b,c] and Jorge Rocca[c]

This project is developing a pulsed neutron source using intense femtosecond laser pulses to generate an ultra high–energy density plasma that is rich in deuterium. Plasma densities that approach that of solid material are obtained through the interaction of the laser with arrays of aligned nanowires. Simulations indicate that ~10^9 neutrons may be generated in a pulse of 1 ps duration. This year we developed procedures to fabricate ordered arrays of deuterated polyethylene nanowires. Particle-in-code simulations for various irradiation intensities were run. High-temperature, dense (~0.2–0.3 times solid matter) plasmas were generated with these targets, and we obtained the first emission spectra and time-of-flight ion spectra of polyethylene and deuterated polyethylene nanowire plasmas. Lastly, the principal diagnostics that we will need for the work in FY 2016 were designed. Next year we will increase the laser energy incident on the nanowire targets, calibrate a Thomson spectrometer and use it to optimize the laser pulse parameters to produce hotter and denser plasmas, and bring the shielded neutron detectors on line to monitor neutron production. We will continue to develop better nanowire targets that will couple with the incoming laser beam more effectively.

[1] tinslejr@nv.doe.gov, 805-681-2282
[a] Special Technologies Laboratory; [b] New Mexico Operations–Los Alamos; [c] Colorado State University

Background

The interaction of powerful lasers and solid materials is limited by the barrier to further light penetration that occurs when the critical electron density has been reached. This limits the laser penetration to a thin surface layer and the plasma density to (typically) 0.1% of the solid density. By replacing a solid material surface with an array of nanowires, a much stronger coupling of the incident laser radiation and the target material is possible. The overall goal of this project is to develop a pulsed neutron source using intense femtosecond laser pulses to generate an ultra high–energy density plasma that is rich in deuterium. To that end we are leveraging work done by Professor Jorge Rocca and his collaborators at Colorado State University (CSU) who have produced high-temperature, high-density plasmas through the interaction of high-power density laser pulses and aligned arrays of metal nanowires. CSU researchers have reported electron densities approximately 100 times that of the critical density, multi-keV temperatures, extremely high degrees of ionization, and gigabar pressures using this technique (Purvis 2013). By substituting highly deuterated polyethylene (CD_2) nanowires for the metals, we hope to produce fast, intense pulses of neutrons through deuterium-deuterium fusion.

This project addresses a variety of project needs for subcritical experiments and high-energy density physics (HEDP). Specifically, neutron-diagnosed subcritical experiment (NDSE) capabilities need a fast

neutron source for detector calibration. Additionally, NDSE will benefit from diagnostic development for improved time-of-flight (TOF) and neutron discrimination measurements, which will be necessary for the plasma characterization. HEDP experiments at the National Ignition Facility and the Sandia Z machine will benefit similarly from the development of a diagnostic that can be used for studying neutron burn, TOF, and neutron discrimination.

Project

The central concept in this project is illustrated in Figure 1. In contrast to a laser pulse hitting a flat surface, a pulse incident on an ordered array of nanowires is able to couple to a much larger volume of material before the free electron density becomes so high that it reflects any more incident laser energy. This makes possible plasmas that have densities close to that of the solid material, very high ionization levels (e.g., Au^{52+}), and gigabar pressures produced with 0.5–0.6 J laser pulses (Purvis 2013). Under such conditions, a plasma containing a sufficient number of deuterons should be capable of fusing to produce a useful number of neutrons in a pulse on the order of 1 ps duration.

We performed particle-in-cell (PIC) simulations of a 0.6 J laser pulse of 50 ps duration focused to a 4 µm spot size. They show that 10^8–10^9 2.45 MeV neutrons may be generated per shot via the reaction

$$d + d \Rightarrow {}^3He + n + 3.27\ MeV. \quad (1)$$

Results of simulations, displayed in Figures 2a and 2b, show the electron and ion energy densities as predicted for the plasma at 60 fs and 140 fs after the front edge of the beam hits the target.

Target Fabrication

The first order of business in this project was the fabrication of suitable arrays of CD_2 nanowires. The nanowires are formed by forcing heated raw material into a matrix of holes in a suitable mold. The mold is then dissolved and its material removed using a supercritical drying process that leaves the desired material intact in the form of nanowires attached to the substrate (Figure 3).

Due to the relatively high cost of the CD_2 material, the earliest targets were made using polyethylene (CH_2) plastic. (These targets are also useful in the laser experiments for such things as setup and parameter optimization before running experiments with the CD_2 targets.) After gaining some experience, we began CD_2 target fabrication. The nanowires made with polycarbonate molds are 400 nm in diameter and 10 µm long.

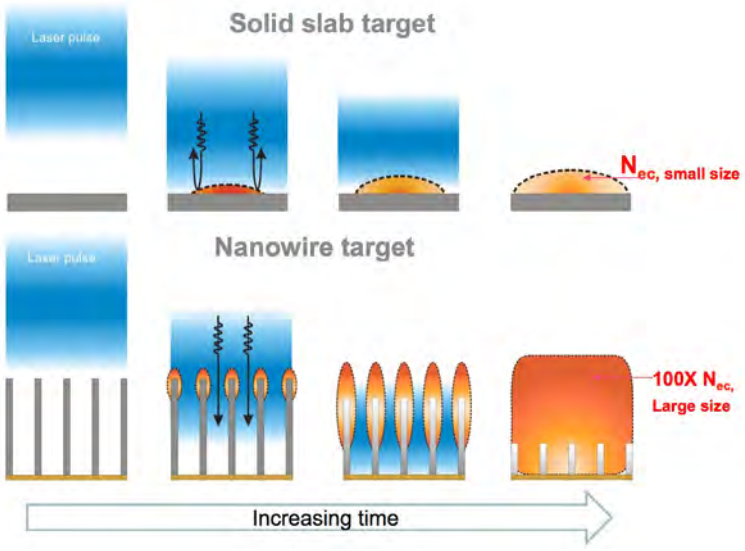

Figure 1. The difference between laser interaction with a solid surface and with a bundle of nanowires; ultimately the nanowire condition enables fusing to produce a useful number of neutrons in a pulse on the order of 1 ps duration (Purvis 2013)

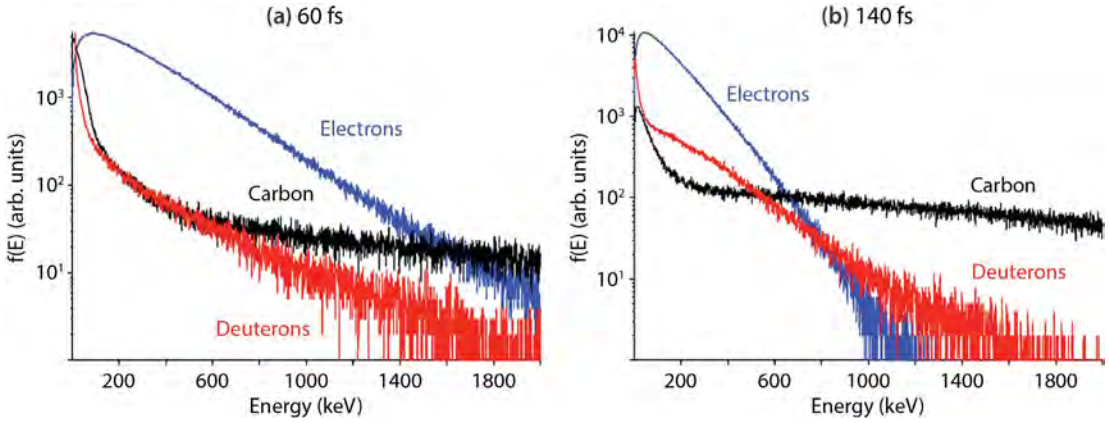

Figure 2. Simulation of the energy spectrum for ions and electrons at (a) 60 fs and (b) 140 fs after a laser pulse hits a nanowire target

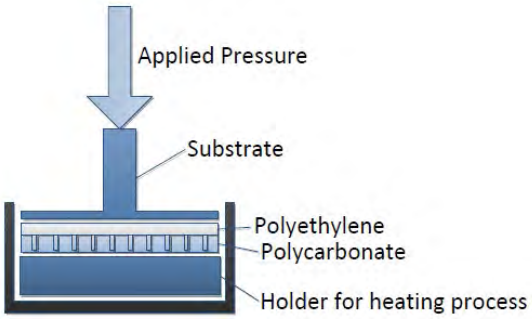

Figure 3. The process of forming arrays of nanowires. The polycarbonate is later dissolved.

Some of the targets we fabricated early on, both CH_2 and CD_2, suffered from having a thin film covering some fraction of the nanowire array. This layer could be removed by plasma etching, but it left the nanowires somewhat in disarray. A scanning electron microscope (SEM) image of a film-covered target before and after etching is shown in Figures 4a and 4b. SEM images are taken of all targets after fabrication to grade them for quality and provide feedback as the fabrication process is improved. A SEM image of a more recent target, shown in Figure 5, shows the improvements made in the process over the course of the year.

Recently, we have begun using alumina molds. The minimum size holes that can be had in polycarbonate molds is 400 nm. For alumina molds, the *maximum* diameter is 200 nm, and diameters down to 20 nm can be obtained. These molds seem to give better results, and they permit us another variable: that of nanowire diameter. One interesting observation is that the CH_2

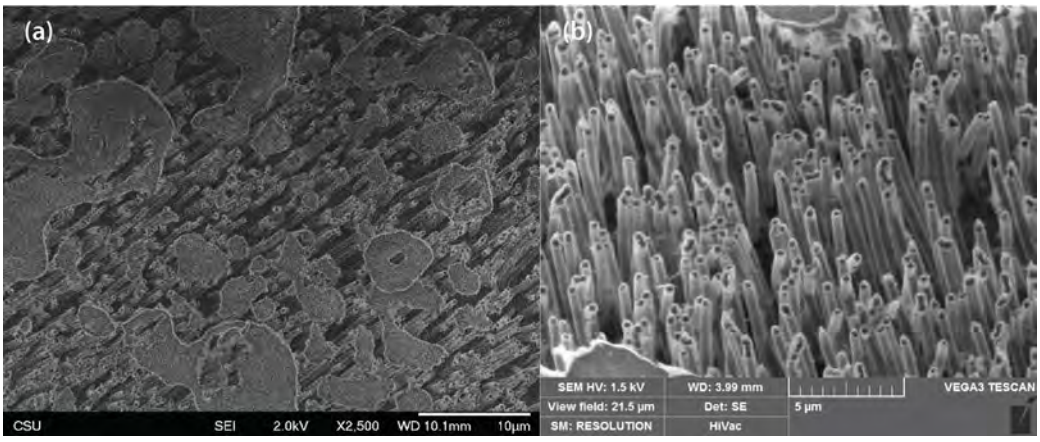

Figure 4. A SEM image of an early CD_2 target array (a) before and (b) after plasma etching; while the film covering the wires could be removed with etching, the result was not yet optimal

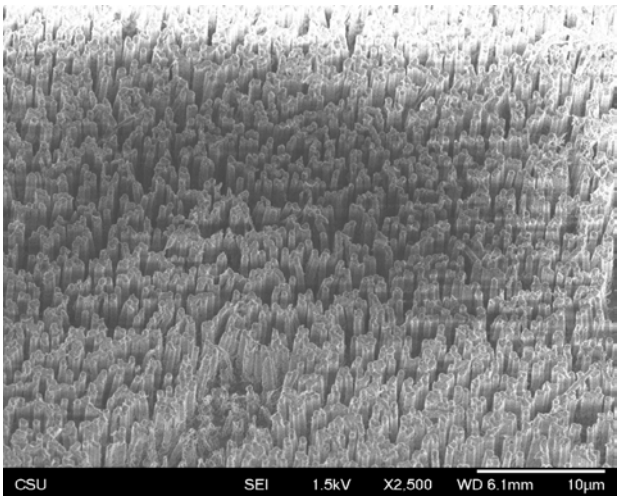

Figure 5. A SEM image of a more recently made target, after the fabrication process was improved, shows closely packed, uniform nanowires

and CD_2 targets made with the new molds look black, whereas the previous ones looked white (as does CH_2). There has been speculation that the white targets did not absorb as much of the laser radiation incident on them as did earlier metal targets, which were dark. The new targets will be tested in laser experiments early in our second-year research.

Laser System

The laser system used in this project is a high-power Ti:Sapphire laser that can produce 32 J uncompressed (Figure 6) power. For this work, the beam is compressed to 50–60 fs in duration in order to maximize the instantaneous power delivered to the target. The power density is further maximized using a deformable mirror to reduce the wavefront error to <20 nm RMS. With this mirror, the beam spot size on the target can be reduced from 10–12 µm FWHM to ≤4 µm FWHM.

The contrast ratio of the 800 nm laser beam is about 2×10^{-7}. In earlier nanowire experiments, it became clear that this contrast is inadequate at the power density levels required to create high-temperature, high-density plasmas. To improve the beam contrast, a beam doubling system using a KDP (potassium dihydrogen phosphate) crystal was installed. This halves the beam wavelength from 800 nm to 400 nm, and, because the efficiency of the doubling goes as the square of the incident beam intensity, the contrast ratio improves to ~10^{-12}. Dichroic mirrors are used to pass the 400 nm light and reflect the 800 nm light. The increase in contrast greatly improves the beam-

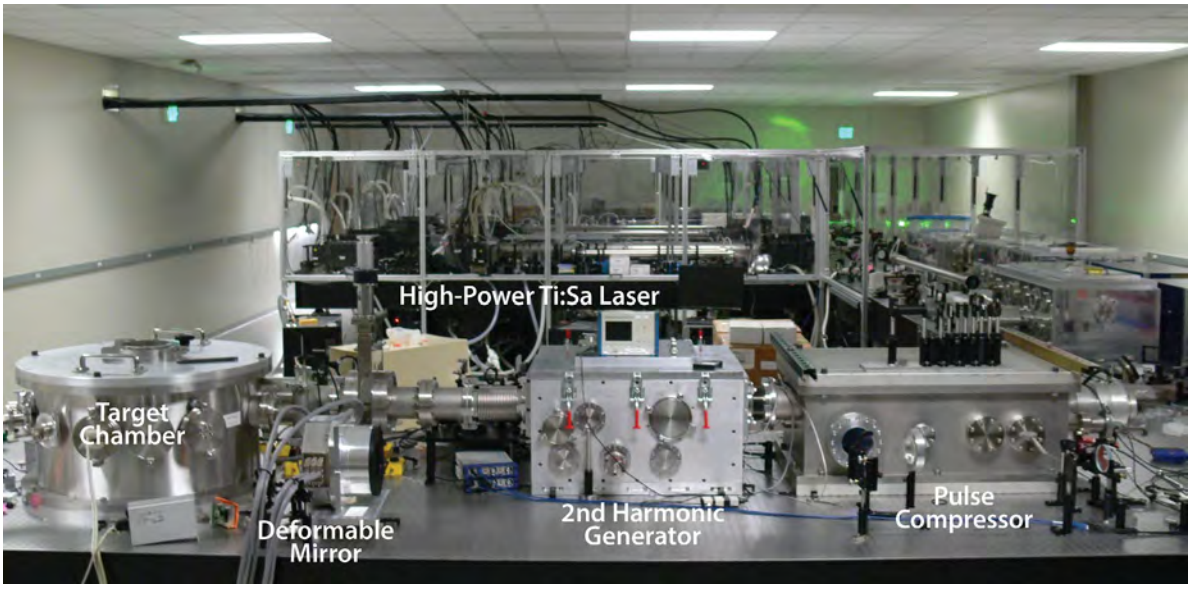

Figure 6. Layout of the experimental apparatus

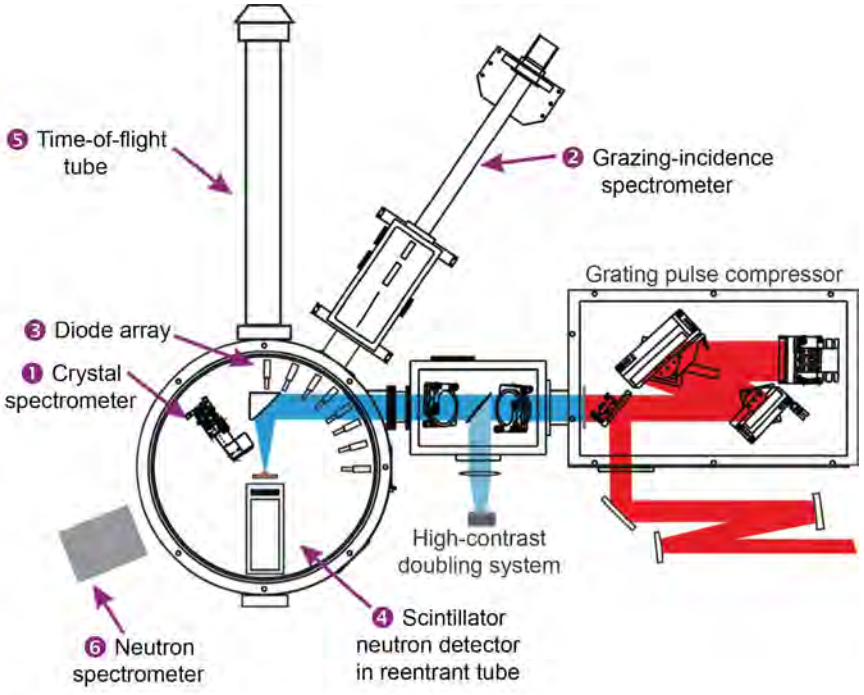

Figure 7. Schematic of major laser system components

target interaction. A schematic of these components is shown in Figure 7. The net beam energy on the target after doubling can be as high as 0.5–0.6 J/pulse, and the power density as high as a few times 10^{19} W/cm^2.

In the final quarter of the year, the 6.5 cm pulse compressor was replaced with another one whose optics support a 9 cm diameter beam. This new compressor will pass four times more beam energy than the old compressor could without damaging the optics. In FY 2016 we will incorporate the Thomson spectrometer (described below) into the setup and at that time will also begin using this enhanced power capability. Because we were trying to bring the Thomson spectrometer online, we have not yet shot targets with this enhanced power capability.

An existing target chamber was used to house the target apparatus, a 3-axis positioner on which the individual targets were mounted in a 3×4 array. Each 1 cm diameter target can be "shot" multiple times since each shot destroys an area of only 1–1.5 mm in diameter. The chamber is evacuated to at least 10^{-6} atmospheres during experiments. The beam is steered and focused on the target using a parabolic mirror. A hole in the middle of the mirror allows the passage of plasma to a port behind it on which the TOF spectrometer is mounted.

Diagnostics

An array of x-ray diodes, a grazing-incidence spectrometer, and a TOF spectrometer comprise the existing set of diagnostics we used for the first experiments. We added to this two neutron detectors. One is a 2" × 2" EJ-410 scintillator that is sensitive to neutrons while being very insensitive to gammas coupled to a cooled photomultiplier tube (PMT). This detector was set just outside the chamber at a location where it has a fairly clear line of sight to the target (other than the chamber wall). The second detector is a 2" × 2" EJ-228 scintillator coupled to a Hamamatsu H2431 PMT assembly. This very fast scintillator and fast PMT pair is designed to separate any x-ray signal from the later neutron signal. The detector is placed in a reentrant tube that is set directly behind the target array; it can be set so that its front face is as close as 3" to the target location (if no shielding is placed in front of it) and as far as ~11".

Another instrument built for this project is a Thomson spectrometer. The fabrication and installation of this device is one of the major milestones for this year, and it is just coming online as the year closes. A Thomson spectrometer uses crossed electric and magnetic fields to separate ions according to momentum and charge state (Cobble 2011), which will allow us to measure the momenta (thus the energy) of the hydrogen, deuterium, and carbon ions that we generate. This diagnostic replaces the TOF spectrometer on the port that faces the front of the target (Figure 7, item 5) so it can intercept some of the plasma emitted after a laser shot.

Data Acquired

In Figure 8 we show x-ray spectra taken for laser pulses incident on flat pieces of polyethylene, an array of polyethylene nanowires, and an array of CD_2 nanowires. The much greater amplitudes of the signals from the nanowire targets illustrate the much higher plasma densities generated using these targets (as schematically shown in Figure 1) versus a flat solid target. The identified peaks illustrate the high ionization level achieved.

A TOF spectrum of the plasma emitted from a CD_2 nanowire target is shown in Figure 9. Just after the large spike that represents x-rays incident on the TOF sensor, a small peak can be seen that we attribute to deuterium ions; the later, larger signal is due to the slower carbon ions. To verify this interpretation, another shot was taken with a very thin aluminum foil in front of the TOF sensor. The large structure was much more attenuated than the smaller, earlier peak—just as one would expect highly charged carbon ions to be stopped more easily than deuterium ions. The results of a PIC simulation of a laser pulse on CD_2 overlaid on the portion of the TOF spectrum attributed to deuterium is also shown. The timing of the peak implies a deuteron energy of about 400 keV, corresponding to a fusion cross section near 100 mb.

The direct detection of neutrons using the scintillator detectors has eluded us thus far. In early attempts to make these measurements, we discovered that there exists a much higher flux of very energetic x-rays—on the order of 100 to 200 keV—than anticipated. Later attempts with added shielding were frustrated when the PMT on the detector failed. A new detector has been built, and in early FY 2016 we will continue this effort.

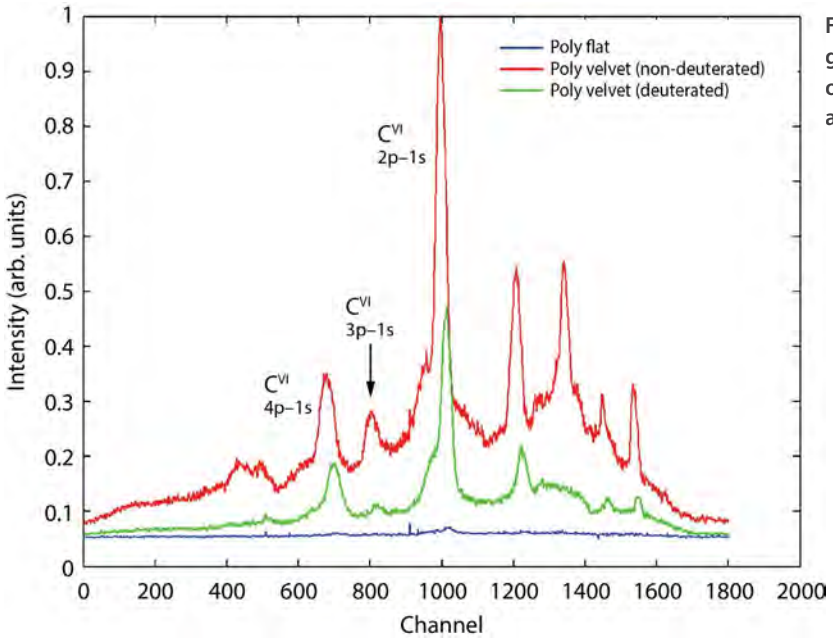

Figure 8. X-ray spectra of the plasma generated by laser pulses on a flat piece of CH_2 (blue), a CH_2 nanowire array (red) and a CD_2 nanowire array (green)

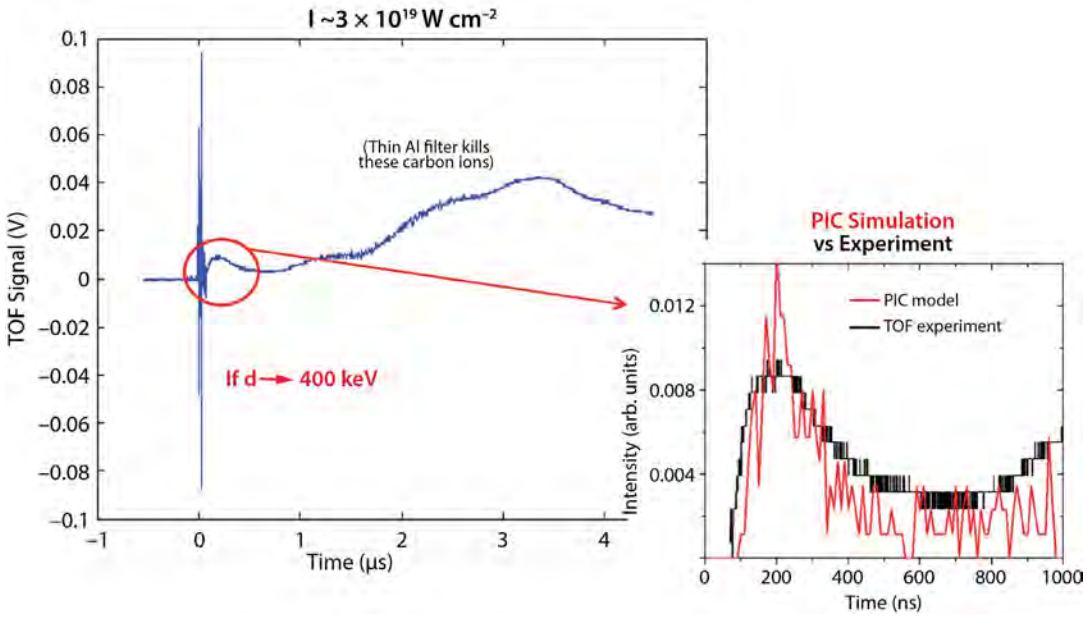

Figure 9. TOF spectrum of plasma generated by a laser pulse on CD_2, indicating the energy of the deuterium ions

Conclusion

During this first year of research, we have developed procedures to fabricate ordered arrays of deuterated polyethylene nanowires. We have performed PIC simulations for various irradiation intensities to guide the experimental program. We have also generated high-temperature, dense (~0.2–0.3 times solid matter) plasmas with these targets and obtained the first emission spectra and TOF ion spectra of CH_2 and CD_2 nanowire plasmas. Lastly, we have fabricated the principal diagnostics that we will need for the work ahead.

In FY 2016, we will increase the laser energy incident on the nanowire targets, calibrate the Thomson spectrometer and use it to optimize the laser pulse parameters to produce hotter and denser plasmas, and bring the shielded neutron detectors online to monitor neutron production. We will also continue the development of better nanowire targets that will couple with the incoming laser beam more effectively.

Acknowledgments

We thank Reed Hollinger, Clayton Bargsten, and C. J. Buss, all of CSU, for their contributions to this work.

References

Cobble, J. A., K. A. Flippo, D. T. Offermann, F. E. Lopez, J. A. Oertel, D. Mastrosimone, S. A. Letzring, N. Sinenian, "High-resolution Thomson parabola for ion analysis," *Rev. Sci. Instrum.* **82** (2011) 113504.

Purvis, M., et al., "Relativistic nanophotonics for ultrahigh energy density plasma physics," *Nature Photonics* **7** (2013) 796–800.

This page left blank intentionally

Site-Directed Research and Development

Appendixes

This page left blank intentionally

In SDRD we have continued to use a suite of basic metrics such as intellectual property, technology needs addressed, and technology transfer to our programs. We also consider the importance of other factors, such as follow-on programmatic or external funding received, new methods developed that effectively save costs, and overall enhanced staff capabilities. These are further indicators of innovation productivity and are also a direct measure of investment return. SDRD provides our staff with opportunities to explore and exercise creative motivations that ultimately lead to new knowledge and realized technologies. The traditional metrics we have used over the past years are tabulated below and are a broad measure of R&D performance.

Invention Disclosures

Invention disclosures are the first step in our intellectual property pursuit and are often followed by patent applications when deemed appropriate. SDRD has generated well over half of all inventions disclosed company-wide since FY 2002, and continues to do so to this day. On average, about one-third of our projects generate new invention disclosures, which is a reasonably high ratio given that projects can vary widely from basic concept, low technical readiness, to much higher more applied development efforts. In fact, our programs benefit from a high rate of technology utilization precisely due to this diverse project mix. A relatively high percentage of projects, roughly 40%, produce technology that is subsequently adopted by a direct NNSS program. Another measure of program effectiveness and alignment with missions is how well projects address technology needs, as identified in the annual NNSS *Technology Needs Assessment*. The ratio of needs addressed to total projects is also indicative of a trend that aligns efforts strategically with the NNSS mission. In addition, a number of projects, though still small in percentage, are targeting emerging fields (of the *Needs Assessment*), which are new initiatives intended to incorporate higher risk and seek to explore opportunities for enhanced mission outside of traditional NNSS areas of expertise.

Needs Addressed

The NNSS *Technology Needs Assessment* document continues to be an effective tool for proposal submitters and reviewers. It provides a roadmap and guidance for technology gaps and challenges facing mission areas. As mentioned, our directed research emphasis areas were similar to last year, and they targeted key investment needs, including nuclear security, information security/assurance, high-energy density physics diagnostics, integrated experiments, advanced analysis, and safeguarded energy. The *Needs Assessment* is developed from a broad base of input from the national security complex, including laboratories, NNSA, and other external agencies. Significant revisions to the assessment were made again this year; most notably the “Emerging Areas and Special Opportunities” section was expanded, as were sections on new challenges and “Breaking Barriers” in cyber security, advanced radiography, energy security, and materials in the extremes. The *Needs Assessment* itself is now in the twelfth year of revision, and its utility and effectiveness continue to improve year to year.

Publications

Publications are another indicator of R&D output and provide an archival record of the investments made that are then available to the broader scientific and technical community. We have placed a renewed emphasis on high-quality, high-impact journal publications, and many are highlighted in the annual reports past and present. We are actively targeting about half of all SDRD projects to publish in a given year; growth in follow-on publications has been noted, and expectations are that it will improve further in time.

Technology Transfer

We continue to strive to have SDRD effectively contribute new technology into key programmatic efforts as quickly as possible. New strategic efforts are also providing greater emphasis on forward-looking needs efficiently coupled with long-term visionary goals. As always, SDRD looks to be "ahead of our time by design" and push for SDRD innovations to intersect future and evolving missions with the most impact possible.

SDRD Program Performance Metrics											
Year	FY05	FY06	FY07	FY08	FY09	FY10	FY11	FY12	FY13	FY14	FY15
Number of projects	55	50	37	27	23	25	26	24	24	25	28
Invention disclosures	21	11	9	6	11	9	7	8	7	7	6
	38%	22%	24%	22%	48%	36%	27%	33%	29%	28%	21%
Technology adopted by programs	12	8	8	8	10	10	9	10	9	10	11
	22%	16%	22%	30%	44%	40%	35%	42%	38%	40%	39%
Gap or need addressed*	18	17	18	15	15	13	13	11	14	11	10
	33%	34%	49%	56%	65%	52%	50%	46%	58%	44%	36%
"Emerging Area & Special Opportunity" effort*	--	--	--	--	--	--	--	--	3	5	5
	--	--	--	--	--	--	--	--	13%	20%	18%
Journal publications	3	2	7	3	6	6	5	7	9	8	7

*per NNSS R&D *Technology Needs Assessment*

Livermore Operations (LO)
P.O. Box 2710
Livermore, California 94551-2710

Nevada National Security Site (NNSS)
P.O. Box 98521
Las Vegas, Nevada 89193-8521

New Mexico Operations (NMO) (Los Alamos and Sandia offices)
182 East Gate Drive
Los Alamos, New Mexico 87544

North Las Vegas (NLV)
P.O. Box 98521
Las Vegas, Nevada 89193-8521

Remote Sensing Laboratory–Andrews (RSL-A)
P.O. Box 380
Suitland, Maryland 20752-0380
(Andrews Air Force Base)

Remote Sensing Laboratory–Nellis (RSL-N)
P.O. Box 98521
Las Vegas, Nevada 89193-8521
(Nellis Air Force Base)

Special Technologies Laboratory (STL)
5520 Ekwill Street
Santa Barbara, California 93111-2352

This page left blank intentionally

1-D	one-dimensional
2-D	two-dimensional
3-D	three-dimensional

A

AA	alluvial aquifer
AC	alternating current
ADC	analog-to-digital converter
ADR	adiabatic demagnetization refrigerator
AFRL	Air Force Research Laboratory
Ag	silver
Al	aluminum
Al_2O_3	aluminum oxide
AlO	aluminum monoxide
Al(g)	gaseous neutral aluminum
ALEGRA	an MHD simulation code (Sandia National Laboratories)
^{241}Am	americium-241
AM	additive manufactured
AMS	Aerial Measuring System
AOI	area of interest
API	application programming interface
Ar	argon
ARES	Airborne Radiological Enhanced-Sensor System
ASI	Applied Spectra, Inc.
ASTER	advanced spaceborne thermal emission and reflection radiometer
Au	gold
AVID	Advanced Visualization and Integration of Data

B

^{10}B	boron-10
Ba	barium
^{133}Ba	barium-133
B_z	magnetic flux density
$Ba_2TiSi_3O_8$	fresnoite
BCT	body centered tetragonal

BCU	base control unit
BLR	broadband laser ranging

C

Ca	calcium
Caltech	California Institute of Technology
$CaMoO_4$	calcium molybdate, scheelite
CaO	calcium oxide
$CaWO_4$	calcium tungstate, powellite
CCD	charge-coupled device
CD_2	deuterated polyethylene
CdTe	cadmium telluride
^{252}Cf	californium-252
CG-PN	conjugate gradient/projected Newton (solver)
CH_2	polyethylene
CL	Child-Langmuir (electron emission)
CN	cyano-radical
^{60}Co	cobalt-60
CONOPS	conduct of operations
cps	counts per second
CPU	computer processing unit
CPW	coplanar waveguides
^{137}Cs	cesium-137
CSU	Colorado State University
CTBT	Comprehensive Test Ban Treaty
CTBTO	Comprehensive Test Ban Treaty Organization
CTH	A Sandia National Laboratories–developed radiation-diffusion hydrodynamics code derived from the one-dimensional 1969 "Chart D," which was extended to two dimensions in 1975 (and named CSQ = (Chart D)^2), and then to three dimensions in 1987, and renamed CTH = (CSQ)$^{3/2}$
Cu	copper
Cu:Pb	lead-doped copper
CU	University of Colorado, Boulder
CUP	compressed ultrafast photography
CWDM	coarse wavelength division multiplexing filter
CZT	cadmium zinc telluride

D

DAC	data acquisition
DASL	Drones and Autonomous Systems Laboratory
DC	direct current
DCF	dispersing compensating fiber
DFT	density functional theory
DJI	Da-Jiang Innovations Science and Technology Co., Ltd.
DNDO	Domestic Nuclear Detection Office
DNN	Defense Nuclear Nonproliferation
DOE	U.S. Department of Energy
DPF	dense plasma focus
DTEC	differential total electron content
DTRA	Defense Threat Reduction Agency

E

EBAM	electron beam additive manufactured
EDS	energy-dispersive x-ray spectroscopy
EM	electromagnetic
EMP	electromagnetic pulse
EO	electro-optical
EOS	equation(s) of state
eTh	equivalent thorium
Eu	europium
eU	equivalent uranium
EXAFS	extended x-ray absorption fine structure

F

FAA	Federal Aviation Administration
FFT	fast Fourier transform
FISR	flash lamp integrating sphere reflectance (experiment)
FOV	field of view
FPGA	field-programmable gate array
FWHM	full-width at half-maximum
FY	fiscal year

G

Ga	gallium
GaAs	gallium arsenide
GBq	gigabecquerel
^{153}Gd	gadolinium-153
GDI	graded density impactor
Ge	germanium
GEANT4	particle simulation software
GFLOP	giga floating-point operations per second
GIS	geographic information system
GMAC	gigabyte multiply-accumulate operations
GNSS	Global Navigation Satellite System
GORGON	hybrid MHD-based code developed by Imperial College London
GPS	global positioning system

H

H, H_2	hydrogen
H_2O	water
HASS	high-activity sealed radioactive sources
He	helium
^{3}He	helium-3
HE	high explosive(s)
HEDP	high energy-density physics
HEL	Hugoniot elastic limit
HET	high-explosive testing
HEX	high-energy x-ray (source)
HFM	hydrostratigraphic framework model
HPGe	high-purity germanium
HSU	hydrostratigraphic units
HTS	high-temperature superconductors

I

IAR	ionospheric Alfvén resonator
ICCD	intensified charge-coupled device
IAEA	International Atomic Energy Agency
IFOV	intermediate field of view
IMS	International Monitoring System (AFRL)

InGaAs	indium gallium arsenide
^{192}Ir	iridium-192
IR	infrared
IS	integrating sphere
ISR-2	Intelligence and Space Research (LANL)

K

K	potassium
KDP	potassium dihydrogen phosphate

L

LANL	Los Alamos National Laboratory
LAO	Los Alamos Office (NSTec New Mexico Operations)
LCA	lower carbonate aquifer
^{6}Li	lithium-6
LIBS	laser-induced breakdown spectroscopy
LiF	lithium fluoride
$LiInSe_2$	lithium indium selenide
LLNL	Lawrence Livermore National Laboratory
LO	Livermore Operations (NSTec)
LS-DYNA	(general-purpose finite element program)
LSP	large-scale plasma simulation code (Alliant Techsystems Operations, LLC)
LTCU	lower tuff confining unit
LWIR	longwave infrared

M

MCA	multichannel analyzer
MCMC	Markov Chain Monte Carlo
MCNP	Monte Carlo N-Particle transport code
MCNP5	Monte Carlo N-Particle transport code, version 5
MCNPX	Monte Carlo n-Particle Extended
MDA	minimum detectable activity
MDD	maximum detectable distance
MHD	magneto-hydrodynamic (code)
MKID	microwave kinetic inductance detector
Mo	molybdenum
MO_3	(M = Mo, W)

MPDV	multiplexed photonic Doppler velocimetry
MPIC	Max Planck Institute of Chemistry
MSS	multispectral scanner
MT	mechanical transfer
m/z	mass-to-charge ratio
M-Z	Mach-Zehnder

N

N	nitrogen
NA-22	NNSA's DNN Office of Research and Development (a nuclear materials security and safeguards program)
NA-42	NNSA's DNN Office of Emergency Response
NaI	sodium iodide
NaI:Tl	thallium-doped sodium iodide
NASA	National Aeronautics and Space Administration
NDA	non-destructive assay
NDSE	neutron-diagnosed subcritical experiment
Nd:YAG	neodymium-doped yttrium aluminum garnet
NFO	NNSA Nevada Field Office
NIF	National Ignition Facility
NIR	near infrared
NIST	National Institute of Standards and Technology
NLV	North Las Vegas (NSTec)
NMO	New Mexico Operations (Los Alamos and Sandia) (NSTec)
NNSA	U.S. Department of Energy, National Nuclear Security Administration
NNSS	Nevada National Security Site
NORM	naturally occurring radioactive material(s)
NRAT	Nuclear/Radiological Advisory Team
NSCRAD	nuisance-rejection spectral comparison ratio anomaly detection (algorithm)
NSTec	National Security Technologies, LLC
NURE	National Uranium Resource Evaluation

O

O	oxygen
O_2	dioxygen
OD	outer diameter
OSBCU	Oak Spring Butte confining unit

P

PCS	Poisson Clutter Split (algorithm)
PDV	photonic Doppler velocimetry
PIC	particle-in-cell (code)
PIN	positive, intrinsic, negative (photodiode with p-layer, intrinsic layer, and n-layer)
PMT	photomultiplier tube
PSF	point spread function
PSI	Physical Sciences, Inc.
PSL	photostimulated luminescence
PTRAN	phase transition
^{239}Pu	plutonium-239
P-wave	seismic compressional wave

Q

QE	quantum efficiency

R

R&D	research and development
RAP	Radiological Assistance Program
RF	radio frequency
RF-SQUID	radio frequency–superconducting quantum interference devices
RITS-6	Radiographic Integrated Test Stand (generation 6)
RMS, rms	root mean square
RNSG	Radiological Nuclear Search Group
ROC	receiver operating characteristic
ROI	region of interest
RSI	Radiation Solutions, Inc.
RSL	Remote Sensing Laboratory
RSL-A	Remote Sensing Laboratory–Andrews
RSL-N	Remote Sensing Laboratory–Nellis
Ru	ruthenium
RVBXI	Ionospheric Hazards Section

S

SDR	software-defined radio
SDRD	Site-Directed Research and Development
SEM	scanning electron microscope

SFM	seismic-attribute framework model
Si	silicon
Si_3N_4	silicon nitride
Si:Li	lithium-doped silicon
SLR	single-lens reflex (camera)
SNM	special nuclear material
SO	Sandia Office (NSTec New Mexico Operations)
SOI	silicon on insulator
SPE	Source Physics Experiment
SPH	smoothed-particle hydrodynamics
SpUD	Spectral Unattended Detector (NSTec RSL)
SQUID	superconducting quantum interference devices
Sr	strontium
SSU	seismo-stratigraphic unit
STL	Special Technologies Laboratory (NSTec)
sUAS	small unmanned aircraft system
SWaP	small size, weight, and power consumption
SWIR	shortwave infrared

T

Tc	technetium
^{99}Tc	technetium-99
^{99m}Tc	metastable technetium-99
TEC	total electron content
TES	transition edge sensor
Th	thorium
Ti	titanium
TMAC	tera multiply-accumulate operations
TMLVTA	Timber Mountain lower vitric-tuff aquifer
TMWTA	Timber Mountain welded-tuff aquifer
TNT	trinitrotoluene
TOF	time-of-flight
TV	total variation

U

U	uranium
^{235}U	uranium-235
^{238}U	uranium-238
UAS	unmanned aircraft system
µCal	microcalorimeter
UCSB	University of California, Santa Barbara
UGTA	Underground Test Area
UNE	underground nuclear explosion
UNLV	University of Nevada, Las Vegas
UO_2	uranium dioxide
USB	universal serial bus
USGS	U.S. Geological Survey
UT	universal time
UTA	University of Texas at Austin
UTC	coordinated universal time
UTK	University of Tennessee, Knoxville
UV	ultraviolet
UV-Vis	ultraviolet-visible

V

VASP	Vienna ab initio simulation package
VISAR	velocity interferometer system for any reflector
VNIR	visible and near infrared
VTEC	vertical total electron content
VTOL	vertical takeoff and landing

W

W	tungsten
WAVRAD	wavelet-assisted variance reduction for anomaly detection (algorithm)
WONDY	a one-dimensional Lagrangian wave propagation code
WP	working point
WTP	weapons testing program

X

XANES	x-ray absorption near edge structure
XAS	x-ray absorption spectroscopy
XSC	XStream compatible

This page left blank intentionally

SDRD
SITE-DIRECTED RESEARCH & DEVELOPMENT

This work was done by National Security Technologies, LLC, under Contract No. DE-AC52-06NA25946, and supported by the Site-Directed Research and Development Program.
Report Date: April 2016

Sorry, something went wrong

An unexpected error has occurred.

TECHNICAL DETAILS

GO BACK TO SITE